Thesis

submitted for the degree of

Doctor of Philosophy in Applied Sciences

Presented by

Liliana GRAMEGNA

Hydromechanical behaviour of bentonite seals in the context of nuclear waste disposals: contributions for engineered barriers evaluation

October 2021

JURY

Prof. Tristan GILET (President)	ULg
Prof. Robert CHARLIER (Supervisor)	ULg
Prof. Frédéric COLLIN	ULg
Prof. Anne-Catherine DIEUDONNÉ	TU Delft
Prof. Bertrand FRANÇOIS	ULB
Dr. Jean TALANDIER	Andra
Prof. Lidija ZDRAVKOVIC	Imperial College

ACKNOWLEDGEMENTS

Among all the people who helped me during this very long walk, I want to acknowledge my supervisor Professor Robert Charlier. Supervisor-PhD student interaction is anything but linear and cannot be described via the already existing strongly coupled constitutive models. Nevertheless, nowadays, I admit that I could not have met a better scientific and, especially, human guidance and that the wonderful impression that I had during our first interview was correct. Robert allowed me fulfilling dreams that I did not dare to have and for this I will always be grateful to him.

ABSTRACT

Several nuclear waste disposal conception designs employ bentonite-based materials to seal underground galleries and shafts, thanks to the bentonite properties, mainly its very low permeability and its high swelling under hydration.

The fundamental goal of a multitude of experimental campaigns and constitutive models development has been to make sealing structures safety assessment and material behaviour long-term reliable predictions.

All this research has shown that the multi-porosity bentonite structure has an undeniable influence on the highly coupled hydro-mechanical processes that occur during water saturation.

Hence, in this research work, by evaluating increasing scales of interest, the topic is examined in a systematic and gradual manner.

First, the multi-level porosities of MX80 and Febex bentonite are presented and analysed. For each observation level, the main structures, mechanisms and processes are presented. Differences between pore structures distribution are highlighted with special regards to the existence of distinct but strongly interacting porosity domains.

Therefore, water retention, water permeability and mechanical behaviour are investigated for numerous conditions, which aim to reproduce all the phenomena occurring for real in-situ sealing.

The feasibility of existing constitutive models is tested for the two analysed assembly types (i.e. the "*classical"* compacted bentonite and the *"contemporary"* pellets mixtures).

Finally, experimental tested are modelled thanks to the finite element code LAGAMINE. Various heterogeneity sources are analysed and investigated at the light of the performed numerical analyses, which span from modelling laboratory tests to reproducing in-situ barrier structures.

Along these lines, the major contributions of this PhD thesis include:

- the identification of the most important properties of pellet mixtures and compacted block and their comparisons. This allowed for the determination of differences (such as in compressibility properties as well as in permeability discrepancies) related not only to dry density but also to multi-level porosities distributions. The presented numerical analyses succeeded in the reproduction of the responses of the two assembly types not only in terms of final state, but also with respect to the non-monotonic properties evolution.

- BBM constitutive model's capabilities were tested on a variety of stress pathways. The model's performance was exploited for oedometer test conditions analysis and methodology validation on many lab tests. The BBM parameters of bentonites were calibrated, compared, and analysed. This allowed for the analysis of a variety of boundary problems including the presence of bentonite sealing of various size (from a few centimetres to several meters).

- The numerical modelling and analysis of laboratory and large-scale in-situ experiments, as well as the in-depth study of experimental results, all contributed to a better understanding of bentonite behaviour. It was demonstrated that the effect of hydration boundary conditions and friction development account for the development of heterogeneous hydro-mechanical characteristics.

CONTENTS

LIST OF SYMBOLS

In the following, the most significant and repeated symbols of the manuscript are reported.

ROMAN SYMBOLS

a	Parameter of Van Eekelen model
A	Parameter of the macrostructural water retention model
b	Parameter of Van Eekelen model
c	Cohesion
C_{ads}	Parameter of the microstructural water retention model
CEC	Cation exchange capacity
e	Void ratio
e_m	Microstructural void ratio
e_{m0}	Microstructural void ratio of dry material
e_M	Macrostructural void ratio
e_w	Water ratio
e_{wm}	Microstructural water ratio
e_{wM}	Macrostructural water ratio
f	Yield surface
f	(x) Pore size density function
g	Gravity acceleration
g	Flow surface
G	Shear modulus
H	Sample height
J_2	Second invariant of the deviatoric stress tensor
J_3	Third invariant of the deviatoric stress tensor
k	Parameter describing the increase in cohesion with suction
k_g	Gas permeability
k_{rg}	Gas relative permeability
k_{rw}	Water relative permeability
k_w	Water permeability
K	Elastic bulk modulus
K_N	Penalty coefficient for normal contact
K_s	Bulk modulus for changes in suction

LIST OF SYMBOLS

K_T	Penalty coefficient for shear contact behaviour
K_w	Water permeability for fully saturated conditions
K_{w0}	Reference water permeability measured at the reference porosity -0
m	Parameter of van Genuchten water retention model
M	Slope of the critical state line
n	Parameter of van Genuchten water retention model
n	Parameter of Van Eekelen model
n_{ads}	Parameter of the microstructural water retention model
n_k	Parameter of the relative permeability law
p	Mean net stress
p_0	Preconsolidation pressure at current suction
p_0^*	Preconsolidation pressure for saturated conditions
p_c	Reference stress in Alonso et al.
p_s	Left intercept of the LC yield surface
q	Deviatoric stress
r	Parameter defining the minimum soil compressibility (at infinite suction)
r_C	Reduced radius for axisymmetric triaxial stress path of compression
r_E	Reduced radius for axisymmetric triaxial stress path of extension
R	Universal gas constant
RH	Relative humidity
$\boldsymbol{s}$	Deviatoric stress tensor
s_{AE}	Air
SP	Swelling pressure
S_r	Degree of saturation
S_r*	Threshold degree of saturation in the mechanical model
S_{rm}	Degree of saturation of the microstructure
S_{rM}	Degree of saturation of the macrostructure
$S_{r,res}$	Residual degree of saturation
s_0	Hardening parameter of the Suction Increase yield surface
t	Time
u_a	Air pressure
u_{atm}	Atmospheric pressure
u_g	Gas pressure

u_w	Water pressure
w	Gravimetric water content

GREEK SYMBOLS

α	Parameter of van Genuchten water retention model
β	Parameter controlling the swelling tendency of aggregates
β_0	Parameter of the microstructure evolution
β_1	Parameter of the microstructure evolution
ε_d	Deviatoric strain
ε_v	Volumetric strain
ε_v^e	Elastic volumetric strain
ε_v^p	Plastic volumetric strain
κ	Elastic compressibility coefficient for change in net stress
κ_s	Elastic compressibility coefficient for change in suction
$\lambda(0)$	Plastic compressibility coefficient for change in net stress at suction 0
$\lambda(s)$	Plastic compressibility coefficient for change in net stress at suction s
μ	Friction coefficient
ρ_d	Dry density
ρ_s	Solid density
ρ_w	Water density
σ_v	Total vertical stress
φ	Friction angle
ϕ	Porosity
ϕ_0	Reference porosity
ϕ_m	Microporosity
ϕ_M	Macroporosity
ω	Parameter controlling the rate of increase of soil stiffness with suction

CHAPTER 1: INTRODUCTION

1.1 General context

Deep geological repositories are often regarded as the best solution for radioactive waste disposal; as such technologies allow radioactive waste being isolated from the biosphere for extended periods of time. Those often consist in an extended gallery network excavated several hundred meters under the ground level ($\sim 500\ m$ for the French concept), in which the harmful waste has to be stored and sealed. Depending on the waste activity level, the gallery diameter can reach values between few decimetres in the case of High-level waste (HLW) to several meters for Intermediate-level waste (ILW). The waste radioactivity decay defines:

- Long-lived intermediate-level waste having a lifetime of several thousand to several hundred thousand years.
- High-level long-lived waste having lifetime of several thousand to several hundred thousand years.

Different disposal concepts are proposed depending on the country, but a common element of all designs is a reliance on the multi-barrier system. The target of the multi-barrier system is to safely isolate the radioactive substances avoiding water flow within the repository (Sellin and Leupin 2014). In order to ensure waste isolation, the multi-barrier concept includes the use of the combination of natural and artificial barriers briefly listed below (Fig. 1.1 and Fig. 1.2):

- The ***chemical barrier*** is made up of vitrified solid waste, which is also stable, long-lasting, and chemically inert;
- The ***physical barrier*** is generally represented by a high-corrosion-resistant canister in which the vitrified wastes are contained;
- The ***geological barrier*** is comprised of the hosting geological medium where the entire system is placed. The host rock is selected according to high-mechanical properties and low permeability features. Indeed, granite (Finland and Sweden) or clay and clay-stone (France and Switzerland) are often preferred;
- The ***engineered barrier*** can be built up of a succession of chambers, shafts, and drifts into which the canisters are inserted, which are filled or further isolated by concrete and/or clay components.

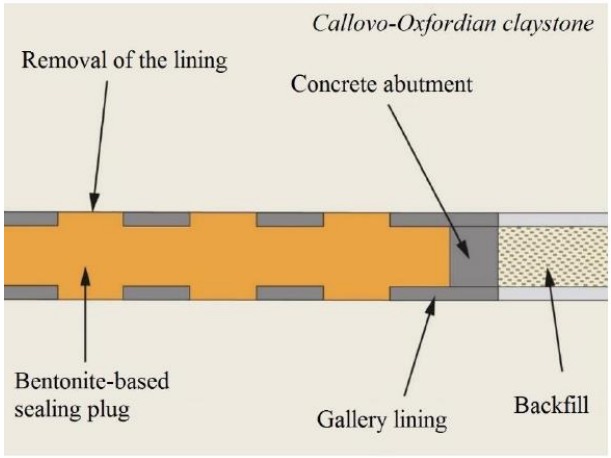

Fig. 1.1: Bentonite employment in French concept of radioactive waste disposals.

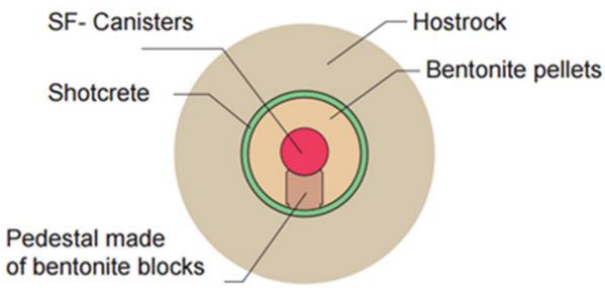

Fig. 1.2: Bentonite employment in Swiss concept of radioactive waste disposals (Sellin et al. 2020).

In all concepts design, bentonite-based materials are selected as crucial elements for the construction of reliable engineered barriers sealing system. This material results particularly suitable for engineered barriers purposes due to:

- high exchange capacity, and thus high ion adsorption capability in the event of radioactive emission;
- swelling capabilities that are translated in volume increase upon hydration and possibly swelling pressure development in case of constraint;
- very low permeability (i.e. decreasing groundwater percolation). This is due to the fact that hydrogeological transport is the primary radioactive transfer mechanism;
- ease in transportability, handling and casting to the underground gallery (pellets and/or block technologies).

The present work was developed in strong collaboration with ANDRA (the French national radioactive waste management agency) (Andra 2005) and within the European project BEACON (Sellin et al. 2020). The complex and strongly coupled multi-scale processes characterising bentonite are widely recognised. Yet, their correct prediction and reproduction are still challenging.

Due to this, the major concern of ANDRA and BEACON is to improve the understanding of bentonite behaviour in order to obtain reliable predictions with respect to its in-situ response. Thus, this thesis work was developed with this aims especially thanks to the Finite Element Code LAGAMINE (Charlier 1987). LAGAMINE suitability for a broad number of phenomena occurring in soils mechanic was demonstrated in numerous studies (Cerfontaine et al. 2015; Collin 2003; Laloui and François 2009), among others.

This PhD thesis is developed as part of the BEACON European project, which has as its major goal the evaluation of existing tools for safety assessment and the evolution of bentonite sealing structures in nuclear waste disposals. The repository's safety is the motivating factor behind this project, as are waste management organizations' demands that the material selection and initial state design satisfy long-term performance requirements.

Emphasis is put on the evaluation of heterogeneities sources, which derive not only from the interaction with the surrounding environmental but also from the intrinsic nature of bentonite components. Indeed, bentonite can be employed in different forms. If on one hand, classical compacted bentonite blocks have been intensively investigated in the past decades (Cui et al. 2008; Saba et al. 2014; Villar 2005; Wang et al. 2013 among many), pellet mixtures are gaining increasing interesting in recent years (Dardé 2019; Van Geet, Volckaert, and Roels 2005; Hoffmann, Alonso, and Romero 2007; Imbert and Villar 2006; Molinero et al. n.d.).

Pellet mixtures can be defined as the combination of high-density bentonite granules of various shape and dimensions (in general between 1 and 35 mm) and fine-grained powder obtained by crushed pellets. Such bentonite assembly type is often preferred after compacted blocks due to in-situ casting operational efficiency and suitability for technological gaps elimination. Pellet mixtures hydro-mechanical response upon hydration remarkably differs with respect to compacted blocks one. Thus, pellet mixtures different structural nature represents an evident heterogeneity source in terms of initial, intermediate and final states, as well as, features development and evolution upon saturation. Bentonite components evolving characteristics account for disparate interactions with in-situ system, which are also central for disposals safety assessment.

MX80 and Febex bentonites are studied among other bentonite types. The remarkable swelling properties deriving from the high montmorillonite content and very low permeability have been extensively demonstrated during years, following deep experimental investigations conducted by numerous European universities and research centres.. Thus, these bentonites will be employed in the European French and Swiss

disposals projects as engineered barriers components. Their precise characterisation and behaviour reproducibly are a major concern for waste disposals safeness assessment.

1.2 Objectives

Hence, the objectives of this thesis can be summarised as follow:

- Comparing the coupled hydro-mechanical behaviour of block and pellet mixtures bentonite assemblies under environmental conditions is crucial. Sealing performances have to respond to the specific nuclear waste disposals requirements. Their deep understanding is necessary for a reliable prediction for long time terms behaviour. The analysis of the transient behaviour of bentonite seals under hydration is also central.

- Large scale bentonite structures (several cube meters) are designed on the basis of laboratory characterisations and investigations (few centimetres). The capability of numerical models to reproduce both observation scales and phenomena has to be assessed

- Properties and physical state heterogeneity of bentonite barriers have to be carefully predicted and minimised. Those can weaken the barrier performances and represent a preferential path for radioactive waste leakage. Thus, initial heterogeneity and hydration induced heterogeneity have to be clarified and reproduced.

1.3 Outline

This thesis is composed of 8 Chapters.

In Chapter 2 bentonite multi-level structure is presented. Dominant components and porosity structures are identified at each observation level. Their specific features are clarified as they are accountable for higher level scale characteristics and behaviour (such as swelling pressure development, permeability evolution and retention properties, among others). In particular, MIP experimental results are presented emphasising structural evolution of several bentonite assemblies' types (pellets, granular and compacted block bentonite) subjected to various hydro-mechanical loading paths. The micro-structure evolution constitutive model adopted for describing such experimental observations is presented.

Chapter 3 considers the hydraulic response of bentonite based materials in terms of water retention properties and permeability evolution. This chapter aims to present the most significant hydraulic features at the light of the different structural domains interactions and evolution knowledge. With respect to this, it is shown how multi-porosities distributions account for different hydraulic behaviour together with material dry density and interacting fluid nature. The double porosity dry density dependent hydraulic constitutive model (Dieudonné, Della Vecchia, and Charlier 2017) adopted in this work is described.

Chapter 4 is dedicated to the experimental and numerical characterisation of bentonite mechanical behaviour. Relatively simple experimental stress paths are analysed and completed with experimental tests performed during a 3 months' stage in CEA (Commissariat à l'Énergie Atomique et aux Énergies Alternatives). Successively existing mechanical constitutive models are recalled, among which BBM (Alonso, Gens, and Josa 1990) capabilities to reproduce a broad number of phenomena are underlined. Therefore, BBM parameters for different bentonites are calibrated, compared and discussed. Finally an alternative strategy is proposed to overcome some BBM limitations and compared to other recent strategies.

In Chapter 5, a combined experimental and numerical approach is adopted to study the hydro-mechanical response of MX80 bentonite samples characterised by the same global dry density, but different multi-porosity distributions (i.e. 35-mm and 7-mm pellets mixtures and compacted block) and sample sizes.

Accordingly the numerical constitutive model validity for heterogeneous structure is validated not only in terms of final stabilised state but especially in the transient hydration phases.

Chapter 6 is devoted to the further investigation of multi porosity assemblies' combinations at laboratory scale. Namely, the combination of Febex pellets and blocks of compacted bentonite is considered. The initial dry densities and structures of such components noticeably differ. Several materials configurations and hydration boundary conditions also at intermediate saturation states are investigated. The employment of an interface element considering friction between material samples and cell becomes essential for the explanation of unexpected experimental discrepancies.

In Chapter 7, the large scale demonstration test EB is modelled. Bentonite components are subjected to various hydro-mechanical conditions and to the interaction of several other barrier elements. Thus, .unavoidable larger complexity has to be considered. Consequentially, this test permits an improved comprehension of the complicated bentonite response with special regards to real in-situ conditions and to the limitation of constitutive models.

Chapter 8 concludes this work with summary, major contribution and recommendations for future research

CHAPTER 2: ON THE MULTI-POROSITIES STRUCTURE OF UNSATURATED SWELLING CLAYS

CHAPTER 2: ON THE MULTI-POROSITIES STRUCTURE OF UNSATURATED SWELLING CLAYS

2.1. Introduction

The suitability of bentonite-based materials as component of engineering barrier in the context of underground nuclear waste disposals depends intrinsically on their characteristics at several observation scales. Accordingly, the goal of this chapter is to provide a clear framework on the multi-porosity structures characterising bentonite. At each observation level, a dominant component and porosity structure can be observed and their features are responsible for some higher level scale characteristics and behaviour.

Starting from the atomic scale, the unit clay particle and particles aggregation (i.e. platelets and tactoids scales) are firstly presented. Successively, clay grain scale is described and, finally, laboratory and engineering scales are introduced Fig. 2.1. For each observation level, emphasis is given both to some relevant features and to the role of the interaction between water and components. In particular, at the laboratory scale, the important topic of pellet/powder mixture and compacted block difference is introduced.

Then, the experimental techniques that allow investigating each of the proposed observation scales are then briefly shown paying careful attention to the bentonite behaviour and related issues. Among the presented experimental methods, the relevance of the mercury intrusion porosimetry technique is underlined for the description and classification of bentonite dominating pore structures. This topic results into a substantial portion of the chapter. In particular, Febex and MX80 bentonites MIP results are analysed.

The analysed complex processes and interactions occurring between all the structural and pore levels need to be tackled by a specific constitutive models in order to take them into account for the repositories design. Thus, the micro-structure evolution constitutive model, specifically implemented in LAGAMINE, is described and subsequent conclusions are finally drawn.

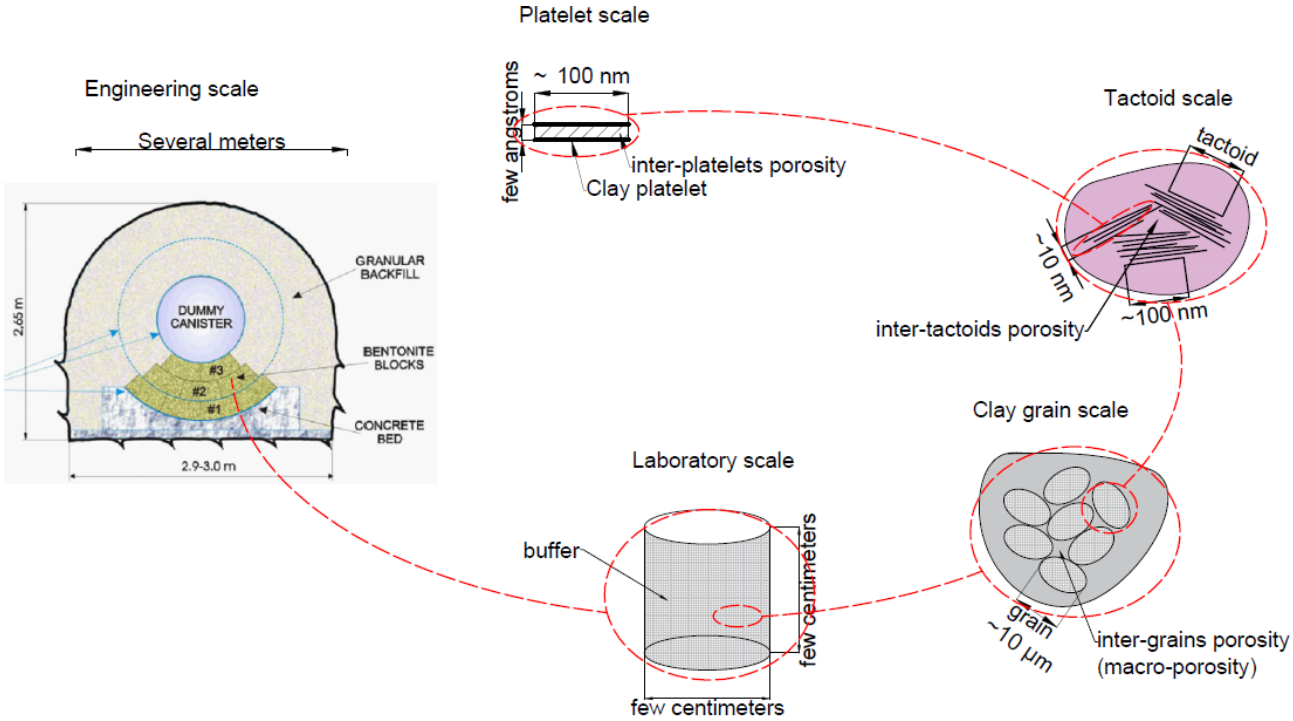

Fig. 2.1: Multi-scale structure of bentonite based materials (modified after (Sauzeat et al. 2001)).

2.2. Observation scales and properties

2.2.1. Platelets and tactoids scale

Starting from the atom scale it is possible to affirm that the crystal-chemical structure of clay minerals is lamellar. Thus, they belong to ***phyllosilicate group*** (*phyllon*=leaf). The different silica structures (i.e. silica tetrahedral $(SiO_4)^{-4}$, Fig. 2.2) are determined by how they mix or remain separated. In general, the silicon atom is centred, and four oxygen atoms are arranged at the vertices. Each tetrahedron has three oxygen atoms in the same plane shared with other tetrahedrons forming tetrahedral rings and sheets (T).

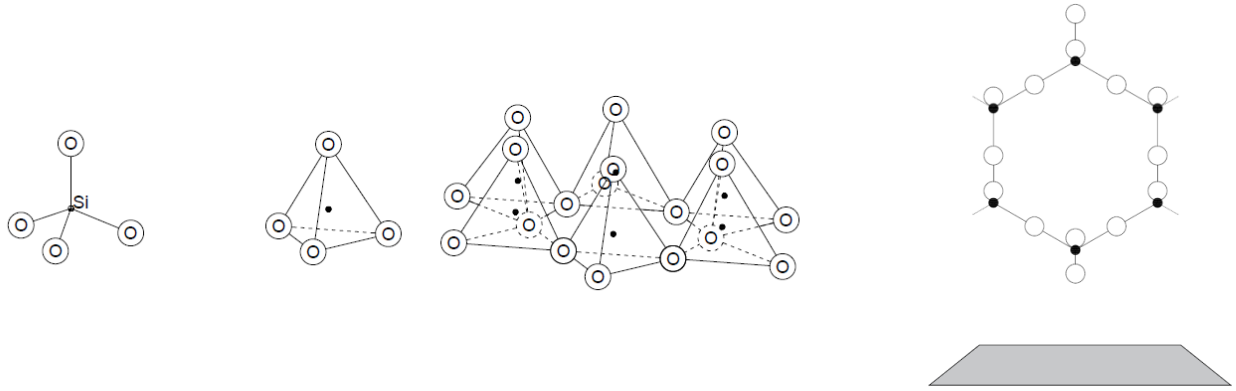

Fig. 2.2: Silica tetrahedron, tetrahedral sheet and schematic representation of the tetrahedral sheet.

Similarly, when Aluminium (Al^{3+}) or magnesium (Mg^{2+}) ions bonded with six oxygen atoms or hydroxyl groups are arranged such as three vertices lay on the same plane and the other three on the parallel one, octahedral units are formed. Also octahedron can combine in order to develop hexagonal rings, which together form the octahedral sheet (O) (Fig. 2.3).

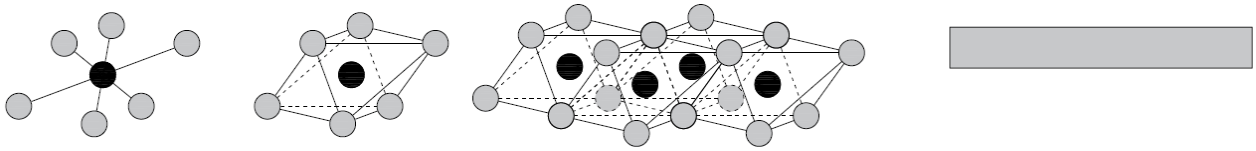

Fig. 2.3: Aluminium or magnesium octahedron, octahedral sheet and schematic representation of the octahedral sheet.

Tetrahedral and octahedral sheets arrange together and combine the typical clay layers via ionic type bonds. Those consist in 1:1 structures (i.e. T-O structures, Fig. 2.4), 2:1 structures (T-O-T structures, Fig. 2.4) and also 2:1:(1) structures (T-O-T(O) structures). Hence, the clay structures present different thickness (i.e. spacing), which is of the order of few Angstrom.

Fig. 2.4: Schematic representation of T:O and T:O:T structures.

These clay structures (i.e. the ***platelets***) result into negative charges distribution on the top and bottom faces and positive charges distribution on the lateral one (Fig. 2.5). The features of the various clay minerals, particularly their behaviour in the presence of water, are determined by the type of layers and the nature and combination of the interlayer. Let us focus, for instance, on the T:O:T structure of Illite and Montmorillonite

(i.e. the most common phyllosilicates composing bentonite-based materials) Fig. 2.5. Among, other features, the inter-platelets distance depends on the nature of the exchangeable cations (2 Å for Na-montmorillonite or 5 Å for Ca-montmorillonite and 3.5 Å for K-Illite), which also determine the number of water molecules that can be stored (i.e. the soil water retention capacity). With respect to the montmorillonite, the bonds between the clay platelets and these ions are quite weak. As a result, the inter-plateles ions can be relatively easily substituted by lower valency ions resulting into an excess of negative charge at the layer surface (***isomorphous substitution***). This feature is the so called "***Cations-Exchange Capacity***" (CEC) and it is defined as the number of positive charges per dry mass of clay that can be exchanged.

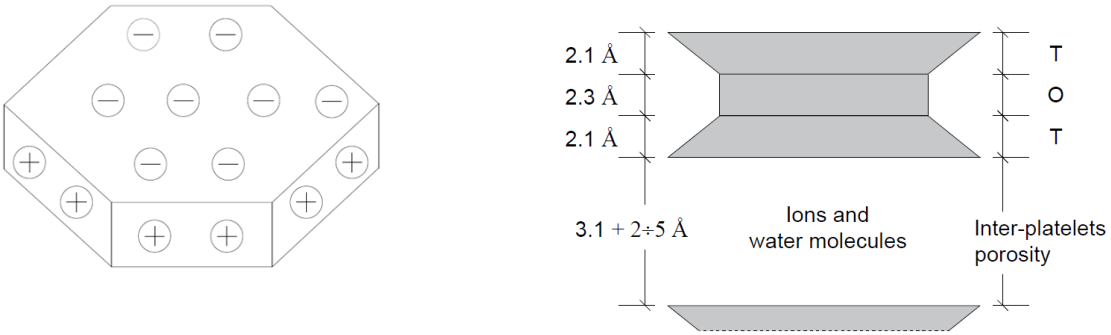

Fig. 2.5: Schematic representation of charges localisation on the external surface of a clay particle and T:O:T platelets spacing.

Due to the relatively weak bonds between the different platelets, water molecules can penetrate. Thus, the water detected at the platelets scale in the ***inter-platelets porosity*** (few Angstrom) can be distinguished in:

- ***structural water***, which is part of the crystalline structure of the clay particles and it is not possible to displace it without destroying the structure itself;

- ***adsorbed water***. This water is kept by quite strong bonds and can be considered unmovable. It is found at direct contact with the platelets and generates very thin layers of about maximum 100 Å (Saiyouri, Hicher, and Tessier 2000).

The adsorbed water causes evident structural swelling: ***crystalline swelling*** (Stern layer development at low water content) and ***osmotic swelling*** (associated with the Double Diffuse Layer "DDL" interaction depending on the cations' concentration and valency –soils CEC-).

The aggregation of clay ***platelets*** with cations and water molecules results into the formation of ***tactoids (***Fig. 2.6 and Fig. 2.7). The tactoids thickness is not constant. It depends on the number and type of stacked platelets (T:O or T:O:T) and on the inter-platelets porosity. The inter-platelets porosity corresponds to the ***intra-tactoids*** porosity. This latter one depends on the type of ions and of the type of bonds that are stablished but also on the quantity of adsorbed water. Hence, a tactoid thickness is of the order of few nanometers.

Let us analyse the tactoids configuration of Montmorillonite (Fig. 2.6) and Illite elements (Fig. 2.7). Both minerals present T:O:T structures but different inter-platelets cations and bonds. Montmorillonite inter-platelets porosity is characterised by Na^+ and Ca^{2+} cations surrounded by water molecules resulting in very weak bonds (Van der Waals type) between layers. On the other hand, in Illite minerals, the free charges are saturated by K^+ (potassium). In this case, the bonds between platelets are of the ionic type. Therefore, the cations and the bonds types are responsible for the configuration stability of the minerals (number of stacked platelets and inter-platelets porosity). As results, the pure montmorillonite tactoid structure (Fig. 2.6) is characterised by a lower number of stacked platelets and larger inter-platelets porosity with respect to the pure Illite tactoid (Fig. 2.7), which present larger number of stacked particles and smaller inter-platelets

porosity. This results into the very high specific surface of Montmorillonite (that is also indicated as *active clay*). Indeed, the strongly unstable structure of montmorillonite accounts for the swelling phenomena characterising bentonite-based materials, not only due to the mass forces but also to the surface ones. The surface forces indeed allow the strong interactions between particles and fluids.

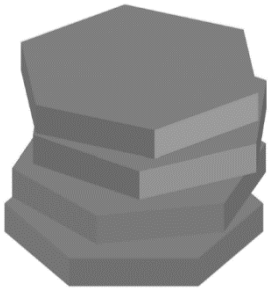

Fig. 2.6: Schematic representation of pure Montmorillonite tactoid (modified after (Dor et al. 2020)).

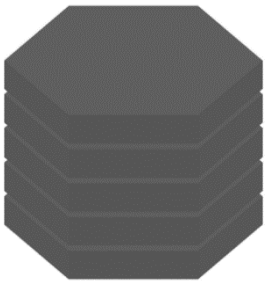

Fig. 2.7: Schematic representation of pure Illite tactoid (modified after (Dor et al. 2020)).

Especially at high water content (i.e. low suction) it is possible to see that the clay platelets number per each tactoid decreases dramatically, namely that the clay particles evidently divide. This leads to the conclusion that in a closed system, on one side, the tactoids thickness tends to increase thanks to the penetration of water molecules, whereas, on the other hand, it tends to decrease due to the decreasing number of stacked platelets, with increasing tactoids number.

Hence, tactoids are surrounded by water, which it can be defined as ***saturation water***. The thickness of this water layer is about 20-200 molecules and it is kept on the external surface of solid particles thanks to polar, electrostatic and hydration forces. This water type is denser than distilled water one, even though it can be relatively easily displaced. As matter of fact, this water is found in the ***inter-tactoids porosity*** (few nanometers).

2.2.2. Clay grain scale

Clay grains (or aggregates) are formed as a result of the aggregation of clay tactoids (Fig. 2.8). The clay grains do not present a constant and well defined thickness. The shape and dimension of clay grains depend among other factors on the clay type and hydro-geological environmental conditions. Let us focus on a general bentonite grain. In general, the bentonite grains present thickness of few micrometres for low hydration levels. With respect to the grains, it is possible to distinguish the ***intra-aggregates*** (intra-grains) porosity (i.e. the sum of the inter-platelets porosity and the inter-tactoids porosity) and the ***inter-aggregates*** (inter-grains) porosity, with dimension comparable to the one of the grains (Fig. 2.8).

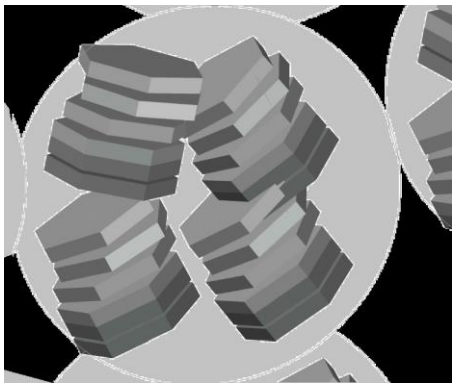

Fig. 2.8: Schematic representation of typical bentonite dry grain (modified after (Dor et al. 2020)). Tactoids (hexagonal structure), inter-tactoids porosity (grey) and inter-grains porosity (in black) are represented.

Pore water can be found in the ***inter-aggregates porosity*** (of the order of few microns). This water type is relatively free and can be removed if capillary forces are not high. Furthermore, in the inter-aggregate pore space, also air and gas phases can be found. Thus, the basic concept of ***soil as multi-phase medium*** can be introduced. In a simplified view, the three phases composing the soils can be distinguished as: solid phase (clay particles), liquid phase (in this thesis framework liquid water) and gas phase (air). The latter two are found in the pore space.

However, it is worth recalling that for high water content level, in highly active clays, it is possible to see that the clay platelets number per each tactoid decreases dramatically, namely that the clay particles evidently divide. This phenomenon causes important structural changes at the clay grain scale. The initial well-defined clay grain increases its volume (i.e. swelling) upon water penetration. The clay fabric undeniably evolves due to clay aggregates flocculation and also dispersion (Lloret, Romero, and Villar 2004). Porosity re-distribution takes place: intra-aggregates porosity (intra-platelets and intra-tactoids porosities) becomes predominant with respect to inter-aggregates porosity, which can also completely disappear under certain conditions (Fig. 2.9). At high hydration level, it becomes quite difficult to indicate the clay structure as composed of grains. Indeed, this strong structure modification can lead to clay gel formation ((Pusch and Yong 2006), (Pusch 2019)).

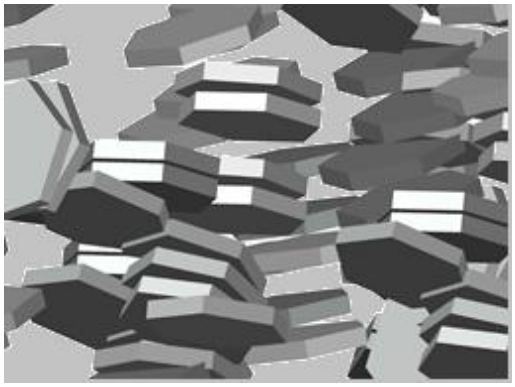

Fig. 2.9: Schematic representation of typical bentonite aggregate at high hydration level. Tactoids (hexagonal structure) and inter-tactoids porosity (grey) are represented.

2.2.3. Laboratory scale

Various aggregation types of clay grains lead to the formation of ***laboratory sample*** (few centimetres, naked eye observation scale) (Fig. 2.11). Most information on which in-situ structure (several cube meters) are designed rely indeed on this observation scale characterisation. The analyses proposed in this thesis are mainly based on laboratory scale experimental tests.

Fig. 2.10: Naked-eye bentonite powder picture.

CHAPTER 2: ON THE MULTI-POROSITIES STRUCTURE OF UNSATURATED SWELLING CLAYS

At the laboratory observation scale a number of useful features can be defined with regards to a given soil sample. For instance, the bulk density (or apparent density or specific mass or density) (Eq. 2.1), ρ, is:

$$\rho = \frac{total\ mass}{total\ volume} = \frac{[kg]}{[m^3]} \qquad \text{Eq. 2.1}$$

The water content (or water ratio) (Eq. 2.2), w, is defined as the weight loss of a sample after drying for 24 h in an oven at 105°C, being equivalent to the mass of the free water contained within the sample, divided by the weight of the dry sample.

$$w = \frac{mass\ of\ water}{total\ mass - water\ mass} = \frac{[kg]}{[kg]} = [-] \qquad \text{Eq. 2.2}$$

In addition, the water saturation degree can be determined as follows:

$$S_r = \frac{w}{\left(\frac{1}{\rho_d} - \frac{1}{\rho_s}\right)\rho_w} = [-] \qquad \text{Eq. 2.3}$$

It is function of water content w, dry density ρ_d, solid density ρ_s and water density ρ_w. The solid density ρ_s is given by the ratio between the solid particles mass and their volume. It is generally determined via helium picnometer (Raynal 2005). In active clay material, the water density ρ_w depends on the storage mechanisms and material saturation degree (Villar 2000). The saturation degree generally ranges between 0 and 11.

With respect to unsaturated soils, such as the most common employment of bentonite-based materials, it becomes relevant to define the dry density ρ_d, determined by the ratio between the dry mass and the total sample volume:

$$\rho_d = \frac{dry\ mass}{total\ volume} = \frac{total\ mass - water\ mass}{total\ volume} = \frac{[kg]}{[m^3]} \qquad \text{Eq. 2.4}$$

The dry density of a given bentonite sample is independent on the grain aggregation type, sample dimension and applied hydro-mechanical loading, as it is the result of global sample quantities. Fig. 2.11 is the schematic representation of MX80 bentonite samples presenting the same dry density but hydration lengths and different assembly types. Despite the comparable samples characteristics, it will be observed in the following chapters of this work how the sample responses can differ one from the other. One major laboratory issue with respect to bentonite sample size concerns the very long testing times. The testing times increase proportionally with the square of the samples hydration length and it can span from several days to few years.

1 Clay materials are never completely desaturated and often present saturation degree higher than 1due to the evolution of water density.

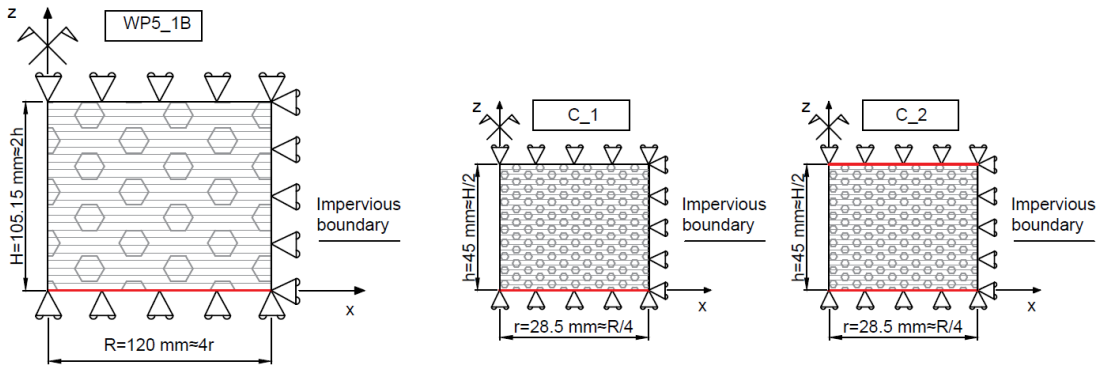

Fig. 2.11: Schematic representation of some laboratory samples with identical dry density

Some different assembly types of which laboratory samples are composed are shown in Fig. 2.12: a) and b) are bentonite pellets of different size (respectively 35 mm and 7 mm), whereas c) is a compacted bentonite sample. Pellets are obtained via pre-heated powder bentonite at low water content level instantaneously compacted in moulds or roller presses. Those present very high initial dry density. Pellets can be mixed with loose bentonite powder (d. Fig. 2.12). The obtained mixtures result into the formation of macroscopically homogeneous samples with heterogeneous dry density components at lower scale. On the contrary, compacted bentonite samples are obtained via static powder compaction at given water content. At lower observation scale, these samples type do not present remarkable denser or looser material components (as the pellet mixtures do).

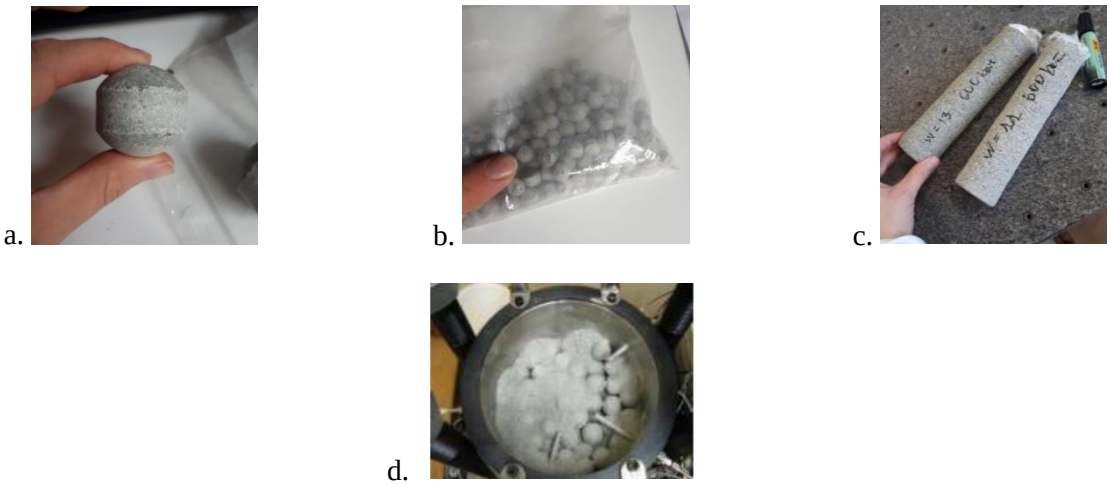

Fig. 2.12: Some bentonite assembly types observable at lab scale.

However, an important characteristic of bentonite pellets mixtures is that the initial heterogeneous dry density and inter-pellets pore space distributions disappear upon water saturation. Fig. 2.13 represents the constant volume hydration of binary Febex mixture (i.e. compacted bentonite on the top and pellets on the bottom) (Villar et al. 2021). Pictures are taken at several hydration states. At the beginning of the hydration, the two layers are clearly separated and distinguishable. Also at naked eye, the top compacted material generally presents a constant and homogeneous density distribution. On the other hand, the pellets layer is evidently characterised by easily detectable inter-pellets pores with dimension comparable to the pellets one. As the saturation front proceeds (from the bottom to the top), the pellets layer immediately homogenises. The large pores structures disappear as the pellets are hydrated. It may be relevant to note that at 1 hour hydration, the saturation front is not regular and smooth but it is strongly affected by the inter-pellets pores space distribution. The inter-pellets space is a preferential path way for hydration at this stage. However, as the saturation continues the water front becomes more regular and smooth. The pellets layer is further

homogenised and at the end of test (1 year) all the inter-pellets pore structures have completely disappeared. The appearance of the pellets layer is similar to the compacted block one at this stage.

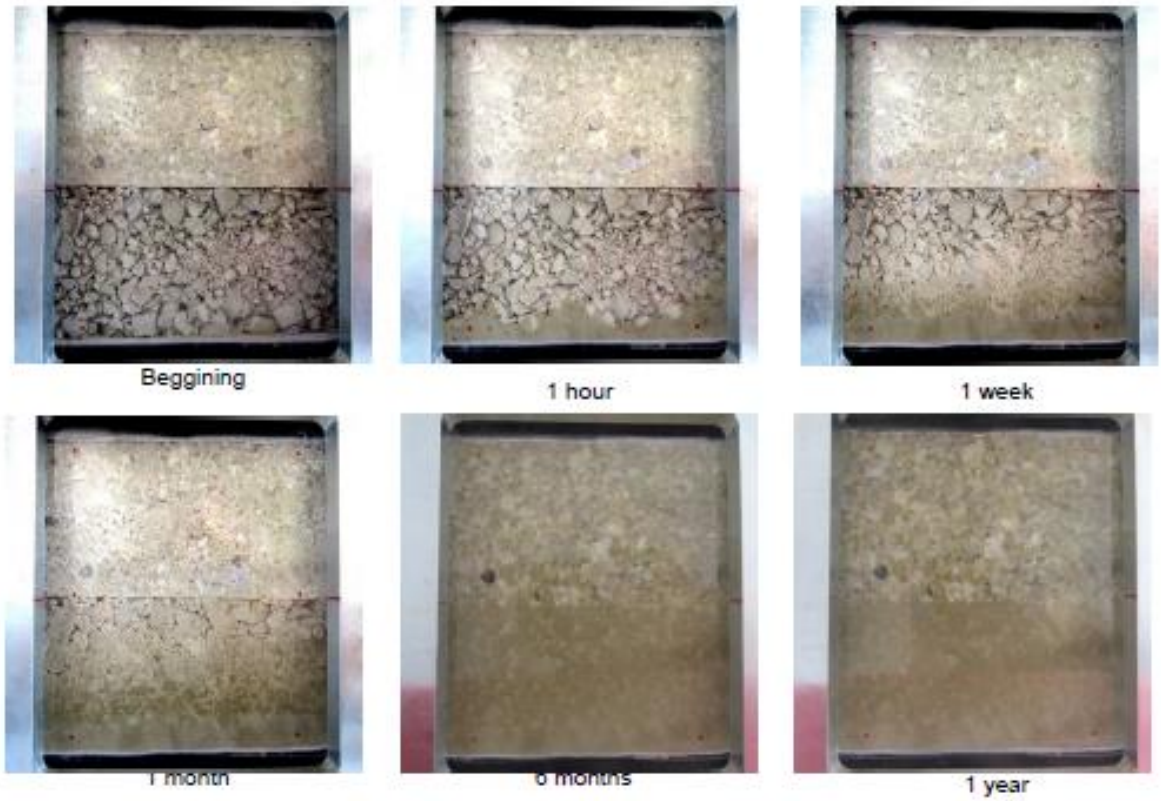

Fig. 2.13: CW1 swelling pressure hydration test performed in a rectangular glass cell on the same assembly analysed in this study (Villar et al. 2021).

As it was observed, the inter-pellets pore space immediately evolves upon hydration. Nevertheless, pores distribution heterogeneities can still be observed thanks to MIP and SEM techniques.

The issue of heterogeneity and homogenisation of pellet mixtures gained increasing relevance during the past decades (Alonso, Hoffmann, and Romero 2010; Bernachy-Barbe et al. 2020; Dardé 2019; Imbert and Villar 2006; Molinero et al. 2017) among others. If on one side, the use of such different assembly types does not allow minimising the laboratory samples dimension, hence reducing the laboratory testing time, it is particularly convenient with respect to real-scale in-situ structure as it will be discussed in the following section.

2.2.4. Engineering scale

For the bentonite large scale structures employment several tons of material are in general involved. This material portion can be not only used to seal drift and shafts but also be placed in direct contact with the radioactive nuclear waste canister (Fig. 2.14) depending on the concept. Thus, the specific bentonite requirements depend on the certain design and safeness assessment, which differ from one Country (and agency) to the other.

For instance, the French CIGEO project (Andra 2005) considers the engineered barrier as sealing component for the excavated galleries and not in direct contact with the radioactive waste. Namely, unsaturated bentonite is placed between concrete confining plugs in order to prevent excessive volume variation (Fig. 2.15). Water is provided by the Callovo Oxfordian (COx) host-rock via concrete liner removals. As saturation takes place, bentonite initially swells closing the technological gaps. When full contact with surrounding confining elements (i.e. concrete plugs, liners and host-rock) occurs, swelling pressure develops. The swelling pressure has to be sufficiently high to close potential fractures caused by the excavation in the host-rock, but reasonably low to avoid further COx damage or concrete plugs displacements.

The reliability of the engineered barrier system depends on all the hydro-mechanical properties development of bentonite. But, it is also necessary to account for the interaction of the bentonite material with the other engineered barrier components, which are usually represented by concrete beds and confining plugs, canisters, and especially by the host-rock. The host-rock is the only bentonite hydration source in all the concepts, however it takes a huge time (some hundreds to few thousands of year for Cigeo). For in situ tests, it is prefer to provide artificially hydration. It affects remarkably the development during time of the above mentioned bentonite characteristics (as it will be explained in the following chapters).

It is consequential that all these features and components are strictly coupled and interacting, therefore, you cannot disregard the study of one to the other.

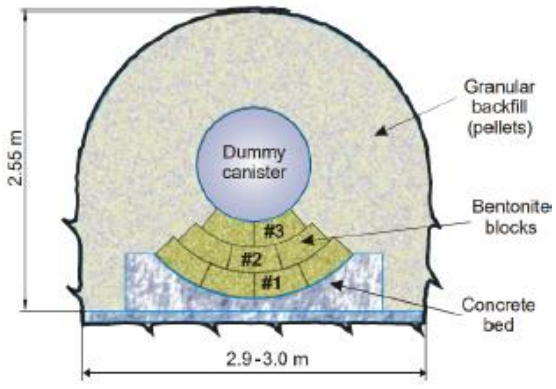

Fig. 2.14: Layout of the EB (Mayor et al. 2005).

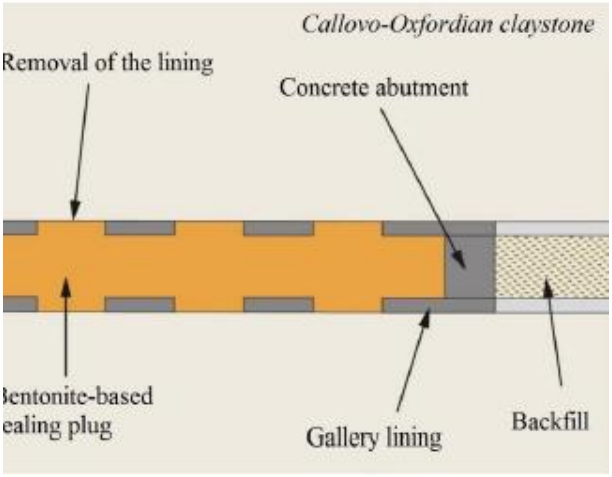

Fig. 2.15: Layout of the French CIGEO project (Andra 2005).

2.3. Experimental techniques and bentonite behaviour

The goal of this section is to take advantage of the presented experimental technique observations in order to clarify the evolving multi-structural phenomena taking place in bentonite-based materials. Even though these technologies have not been directly employed by the author, those are useful to provide qualitative information with respect to the structural modifications undergone from bentonites.

2.3.1. XRD: from platelets to tactoids.

X-ray diffraction (XRD) technique enables the identification of mineral phases in soils samples. Since the 1920s, X-ray diffraction has been the principal method for determining the arrangement of atoms in minerals. A systematic X-ray crystallographic study of the silicates was undertaken in the 1920s. This study showed that, as the Si/O ratio is altered, the silicate crystals exhibit significant changes in their atomic arrangements. (Machatschki 1928) extended these insights to minerals in which aluminium substitutes for the silicon atoms of the silicates.

(Moore and Reynolds 1997) provide a comprehensive description and interpretation guide for XRD results. Thus, this method is feasible to provide qualitative and semi-quantitative descriptions of the nature of clay minerals. Fig. 2.16 shows the XRD outcomes performed on MX80 bentonite provided by ANDRA to ULg. Outcomes interpretation indicates that the material is composed of smectite (77%), micas (1%), quartz (8%), gypsum (1%), calcite (1%) and feldspars (12%) in good agreement with literature results (Table 2.1). The two peaks at 11.7 Å and 1.49 Å are respectively possibly due to a monovalent interchangeable cation (Na+ probably) and to a Di-octahedral smectite. In particular, the value of the first peak at 11.7 Å is close to 12 Å, which suggests the possibility to have illite layers in the tactoids.

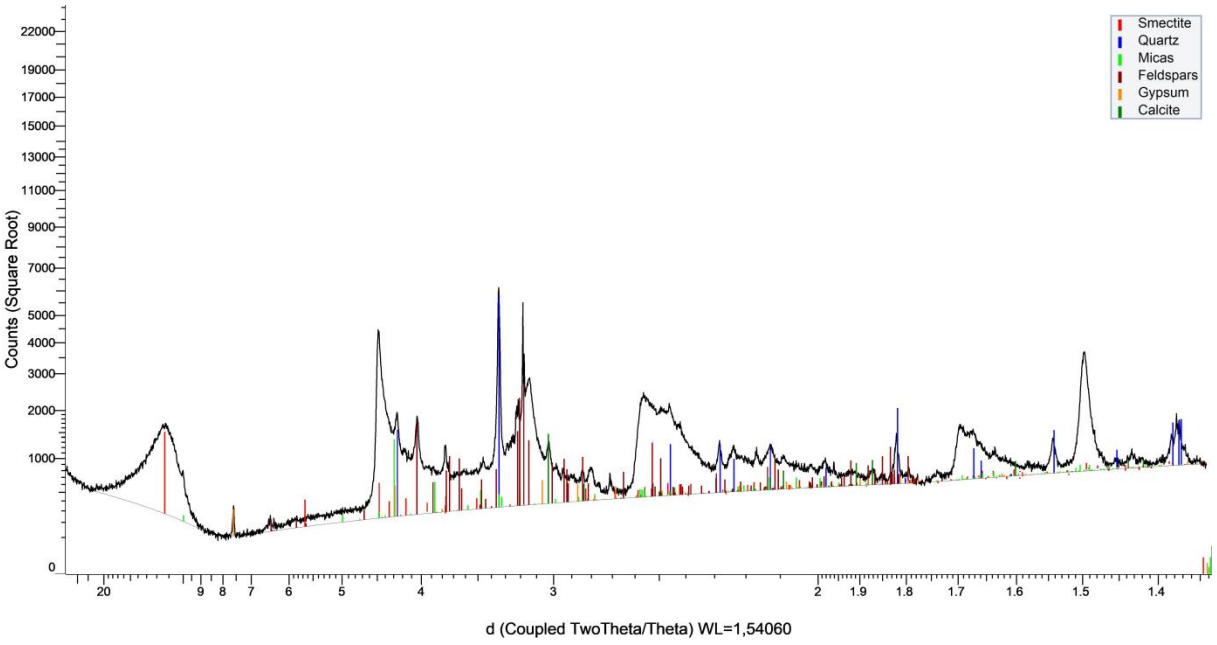

Fig. 2.16: X-ray diffraction analysis on MX80 bentonite performed by Geology department of ULg.

The most common commercial bentonites are made up of a variety of clay minerals, the majority of which are montmorillonite as reported in (Table 2.1).

Table 2.1: Mineralogical composition (main minerals) of the bentonites considered in this work.

Bentonite	Origin	Phyllosilicate	SiO_2	K-feldspar	Plagiocase
Febex [a]	Spain	92% interstratified montmorillonite-illite (10-15% illite)	2%	Traces	2%
MX-80 [b]	USA	75–90% montmorillonite	2.8–15.2%	2–8%	9.2%

[a] (Lloret and Villar 2007a) [b] (Lajudie et al. 1994b) (Madsen 1998) (Montes-H 2002)

This approach can also be used to study the impacts of the hydration process at the platelets and tactoids scales. (Saiyouri, Hicher, and Tessier 2000; Saiyouri, Tessier, and Hicher 2004) obtained thanks to probabilistic analysis the number of water molecules between platelets and the number of clay particles with respect to suction and water content on FoCa and MX80 bentonites (Fig. 2.17). Especially at high water content (i.e. low suction) it is possible to see that the clay platelets number per each tactoid decreases dramatically. Namely that the clay particles evidently divide. This leads to the conclusion that in a closed system, on one side, the tactoids thickness tends to increase thanks to the penetration of water molecules (previous section), whereas, on the other hand, it tends to decrease due to the decreasing number of stacked platelets, with increasing tactoids number.

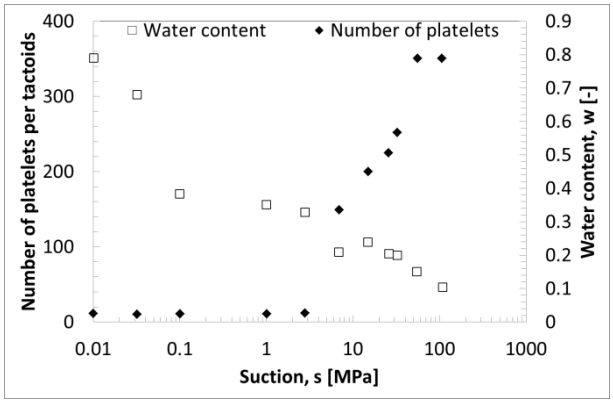

Fig. 2.17: Total water content and number of layers per platelets (layers) per tactoid (particle) with suction evolution for MX80 bentonite during hydration at constant stress (Saiyouri, Tessier, and Hicher 2004).

2.3.2. SEM and MIP: from tactoids to grains.

The clay grains scale can be investigated via Scanning Electron Microscopy (SEM) techniques and Mercury Intrusion Porosimetry (MIP).

Electron microscopy primarily gives qualitative information about pores. Although some quantitative information can be retrieved by employing digital image analysis, structure can be determined utilizing micrographs of the material. Scanning Electron Microscopy (SEM), Environmental Scanning Electron Microscopy (ESEM), and Transmission Electron Microscopy (TEM) are some of the available techniques.

Further qualitative and quantitative information can be provided by mercury intrusion porosimetry (MIP). This technique allows studying the pore size distribution (PSD) of a porous material. This technique principle is based on the mercury injection into a previously dried sample. The mercury injection pressure is linked to the accessible pores dimensions.

(Romero and Simms 2008) provide detailed literature review with respect to the employment of SEM, ESEM and MIP techniques for the investigation of unsaturated soils with a special focus on bentonite behaviour. Some applications of these techniques to study the behaviour of Febex and MX80 bentonites are recalled in the following. The proposed PSD curves are related to unsaturated state when it is not specified differently.

Febex bentonite

(Lloret et al. 2003) performed in-depth analysis on Febex bentonite structure subjected to various hydro-mechanical loadings paths. Among other features, the clay grain scale was investigated via ESEM and MIP techniques. Fig. 2.18 shows the ESEM micrograph of a compacted Febex bentonite sample at dry density ρ_d=1.72 Mg/m^3. Clay aggregates and inter-aggregates pore space are quite clearly distinguished. Aggregates are randomly arranged and also differ for aggregation size. Inter-aggregates pores are consistently of different sizes presenting a detectable maximum equal to approximately 10 to 50 μm. MIP results (Fig. 2.19) agree on the determination of this maximum value for the comparable dry density of ρ_d=1.80 Mg/m^3. MIP results compare the pore size distributions (PSD) of two dry densities: namely ρ_d=1.80 Mg/m^3 (void ratio e=0.520) and ρ_d=1.50 Mg/m^3 (void ratio e=0.830). Two dominant pore families are detected for each of the two densities. The first one corresponds to the intra-aggregates pore space with dominating pore entry diameter equal to 10 nm and that is shared by the two dry densities. The second pore entry diameters are equal to 10 μm for ρ_d=1.80 Mg/m^3 and 40 μm for ρ_d=1.50 Mg/m^3. These values concern the inter-aggregates pore space and differently from the intra-aggregates ones are strongly affected by the compaction level. Thus the compaction level is responsible for the volume change corresponding to void ratio Δe=0.31 between the two densities (grey zone in Fig. 2.19).

Moreover, it is important to underline that MIP cannot investigate pore entry diameter smaller than 6 nm to which corresponds an intra-aggregates pore volume equal to void ratio e=0.32, that is actually the same for the two densities.

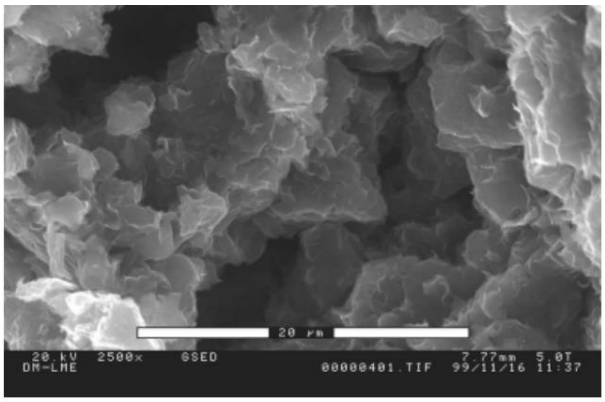

Fig. 2.18: Micrograph of a compacted Febex bentonite sample (dry density 1.72 Mg/m^3) obtained using ESEM (Lloret et al. 2003). Frame width 40 µm.

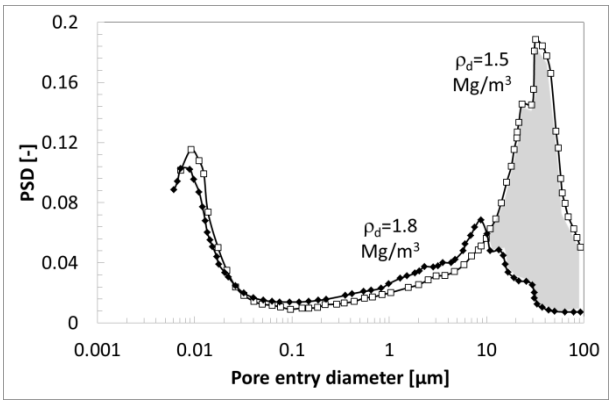

Fig. 2.19: PSD for Febex bentonite compacted at dry densities ρ_d=1.5 Mg/m^3 and ρ_d=1.8 Mg/m^3. MIP results (Lloret et al. 2003).

Recently, MIP analyses have been also performed on Febex pellet mixtures (Alonso, Hoffmann, and Romero 2010; Hoffmann, Alonso, and Romero 2007; Villar et al. 2021). Fig. 2.20 shows the pore size distribution of two different Febex bentonite samples: Febex compacted at dry density ρ_d=1.8 Mg/m^3 and single Febex pellet compacted at ρ_d=1.9 Mg/m^3. Despite, the samples dry densities are quite comparable, the larger dominant pore entry diameters correspond to 2 µm for the single pellet and to 10 µm for the compacted block. This evidence confirms that the larger pore entry diameter is mostly due to compaction process. On the other hand, the smaller pore entry diameters are equal to 10 nm for the compacted block and 13 nm for the single pellet. These values are very close and suggest that the processing taking place inside the clay grains (tactoids scale) are mechanically independent on the ones occurring at the clay grain scale.

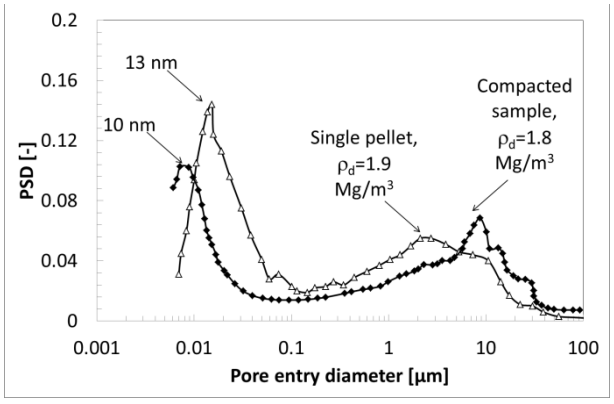

Fig. 2.20: PSD for Febex bentonite compacted at dry densities ρ_d=1.8 Mg/m^3 and single Febex pellet at dry density ρ_d=1.9 Mg/m^3. MIP results (Hoffmann, Alonso, and Romero 2007; Lloret et al. 2003).

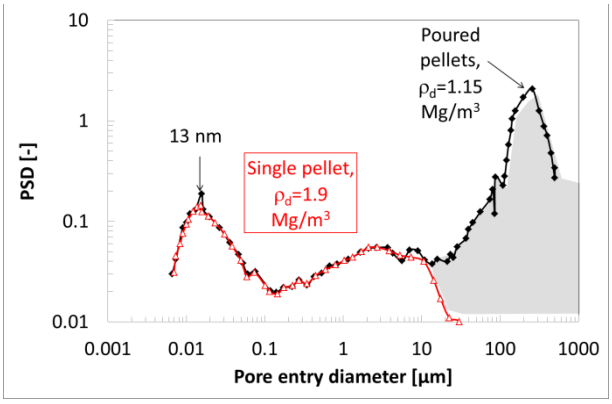

Fig. 2.21: PSD for single Febex pellet at dry density ρ_d=1.9 Mg/m^3 and Febex poured pellet mixture at ρ_d=1.15 Mg/m^3. MIP results (Hoffmann, Alonso, and Romero 2007; Lloret et al. 2003).

MIP analyses on Febex bentonite pellet mixtures are presented in the following. Fig. 2.21 compares the pore size distribution of a single Febex pellet presenting dry density equal to ρ_d=1.9 Mg/m^3 and Febex poured pellet mixture at ρ_d=1.15 Mg/m^3 (Hoffmann, Alonso, and Romero 2007). The two samples have a first PSD peak value at pore entry diameter equal to 13 nm, which corresponds to the intra-aggregates pore space. The second peak at pore entry diameter equal to 3 µm is also detectable for the two samples. The third and last peak related to the intra-pellets pore space has a pore entry diameter equal to 250 µm, which is two orders of magnitude larger than the second peak. This pore family is indeed related to the lowest density component of the mixture. The void ratio difference equal to Δe=0.940 corresponds to this pore space. Similarly to Fig.

2.19, Fig. 2.22 presents the MIP analysis results comparison between Febex pellet mixtures having dry densities of ρ_d=1.35 Mg/m^3, ρ_d=1.45 Mg/m^3 and ρ_d=1.70 Mg/m^3, together with single pellet of dry density ρ_d=1.90 Mg/m^3. The pore entry diameter corresponding to the dominating pores family denoted as "intra-aggregates" pore space is placed at 13 nm. The larger dominating pore entry diameters depend on the dry density also in this case.

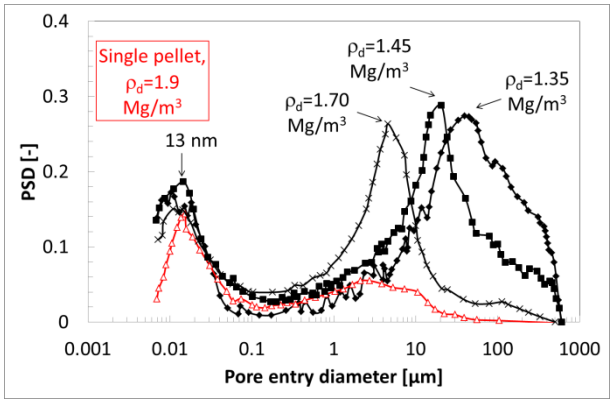

Fig. 2.22: PSD for single Febex pellet at dry density ρ_d=1.9 Mg/m^3 and Febex pellet mixtures at ρ_d=1.35 Mg/m^3, ρ_d=1.45 Mg/m^3 and ρ_d=1.70 Mg/m^3 using static compaction. MIP results (Hoffmann, Alonso, and Romero 2007).

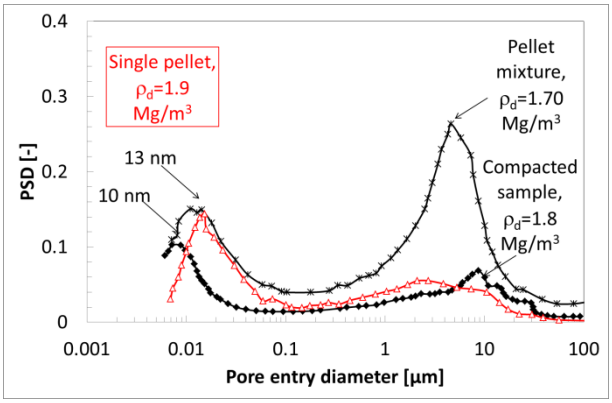

Fig. 2.23: PSD for Febex bentonite compacted at dry densities ρ_d=1.8 Mg/m^3, single Febex pellet at dry density ρ_d=1.9 Mg/m^3 and Febex pellet mixture at dry density ρ_d=1.7 Mg/m^3. MIP results (Hoffmann, Alonso, and Romero 2007; Lloret et al. 2003).

For sake of completeness, Fig. 2.23 compares the PSD of a Febex sample compacted at dry density ρ_d=1.8 Mg/m^3, single Febex pellet at dry density ρ_d=1.9 Mg/m^3 and Febex pellet mixture at dry density ρ_d=1.7 Mg/m^3. Attention has to be paid to the pore entry diameters corresponding to the larger pore families. Even though the pellet mixture at ρ_d=1.7 Mg/m^3 is less compacted than the block with ρ_d=1.8 Mg/m^3, its dominating pore entry size is equal to 5 µm, which is half of the compacted block equal to 10 µm but with a much higher peak. This evidence possibly underlines that pore structure distributions are strongly affected by assembly type and not only on the dry density. Thus, it can also be concluded that the larger pores size of the pellets mixtures are smaller with respect to the compacted block ones but more numerous. The pores network composition undoubtedly accounts for the hydro-mechanical response of the different bentonite assemblies, as it will be discussed in the following chapters.

MX80 bentonite

Among others, EPFL team (Baryla et al. 2018; Seiphoori, Ferrari, and Laloui 2014) conducted extensive experimental campaigns on MX80 granular bentonite under various hydro-mechanical loading paths. SEM and MIP techniques were used to observe the clay grain scale. The SEM micrograph of compacted MX80 granular bentonite sample at dry density ρ_d=1.80 Mg/m^3 is shown in Fig. 2.24 and Fig. 2.25. Micrographs are related to different hydration states. Fig. 2.24 concerns granular MX80 bentonite compacted at ρ_d=1.80 Mg/m^3 at low water content. Clay grains and inter-grains pore space are easily distinguished. Clay aggregates present various sizes with quite well-defined limiting surfaces. The pore space between the clay grains depends on the clay grains aggregation and shape and it is mostly heterogeneous. Fig. 2.25 represents the micrograph of granular MX80 bentonite compacted at ρ_d=1.80 Mg/m^3 after full saturation at constant volume conditions. Clay aggregates seem to have dissolved. It is not possible to distinguish clear boundaries and delimiting surfaces. Accordingly, inter-aggregates pore space is not detectable. This dramatic fabric change is related to the water molecules penetration between tactoids (inside the aggregates) as discussed in section 2.2.2. The fabric state after this type of hydration path cannot be described as grain composition, but it is similar to a quite-homogeneous fabric.

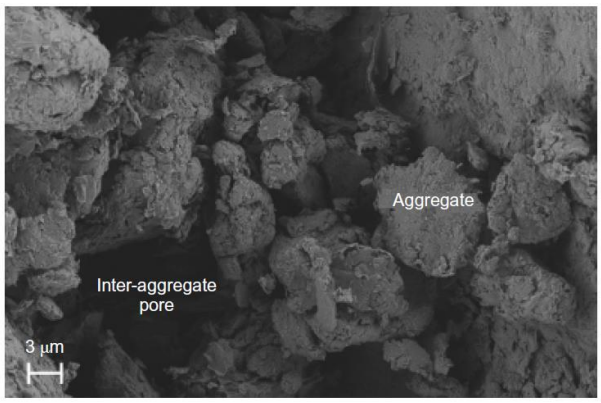

Fig. 2.24: SEM photomicrograph of a sample of dry MX-80 bentonite compacted to a dry density of 1.80 Mg⁄m^3 at the reference scale of 3 µm (Seiphoori, Ferrari, and Laloui 2014).

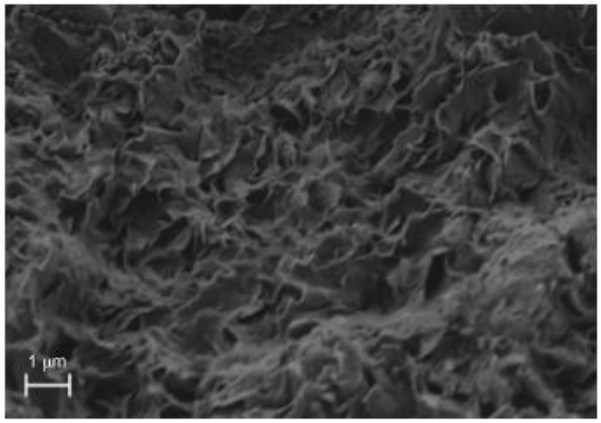

Fig. 2.25: SEM photomicrograph of a sample of MX-80 bentonite compacted to a dry density of 1.80 Mg⁄m^3 hydrated in isochoric conditions at the reference scale of 1 µm (Seiphoori, Ferrari, and Laloui 2014).

A better understanding of the bentonite structure evolution can be provided thanks to the analysis of MIP tests results undertaken after different stress paths (marked with capital letters in Fig. 2.26). The detailed description of each stress path will be discussed in the following chapters. Nevertheless, for sake of clarity, a brief recall is reported:

- point A refers to the initial bentonite state: as poured unsaturated MX80 granular bentonite;

- path AB' corresponds to hydration in constant volume conditions, that is concomitant with the development of swelling pressure due to the volume constrain conditions;

- path AB concerns to hydration performed at constant small vertical stress with sample volume increase;

- path BC is related to sample volume decrease due the application of a given mechanical vertical load.

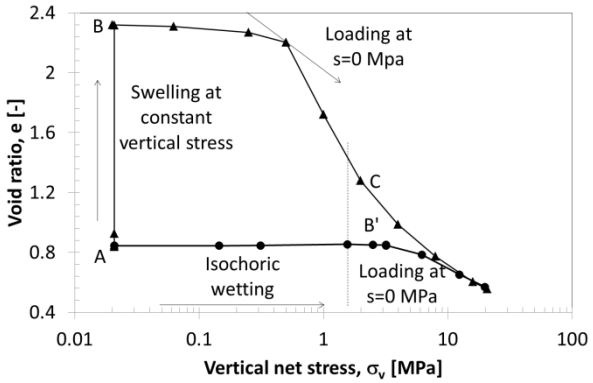

Fig. 2.26: Analysed stress paths. MIP analyses are conducted at points A, B, B' and C (Baryla et al. 2018).

Fig. 2.27 refers to constant volume hydration path (AB'). Small pore family dominating entry diameters are equal to 10 nm at the initial state for the poured material (point A) and equal to 22 nm for the sample hydrated at constant volume conditions (point B'). For this latter case, two further peaks can be distinguished: a first peak at 0.3 μm and a very large second one at 0.1 mm (three orders of magnitude larger than the first). It is assumed that the pore family at pore entry diameter equal to 0.1 mm can be related to experimental dismantling operations2. Consequentially, it can be concluded that upon hydration in constant volume conditions the larger pore space volume decreases due to micro-pores space expansions. The clay pores structure evolution is far from being well-defined. It follows indeed the tactoids separation upon water molecules penetration and clay aggregates consequential dissolution. The inter-aggregates pores volume completely rearranges. More numerous pores with smaller diameters can be observed. This latter feature can depend on the material dry density. Fig. 2.28 shows the MIP results of granular MX80 compacted at dry density ρ_d=1.8 Mg/m^3 before and after water saturation. Comparing the unsaturated compacted state with the as poured unsaturated one it is possible to distinguish the void ratio reduction due compaction, which is equal to Δe=0.30 and corresponds to the pore entry diameter reduction from 15 μm (ρ_d=1.5 Mg/m^3) to 2 μm (ρ_d=1.8 Mg/m^3).

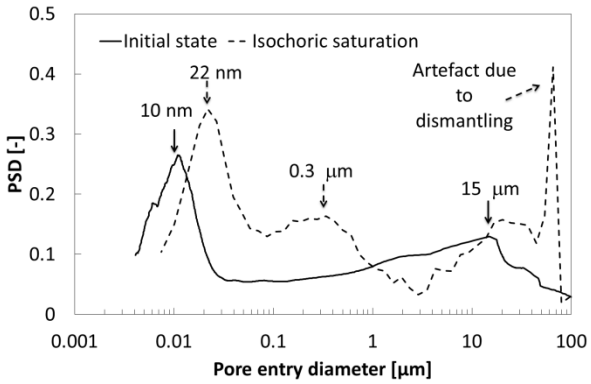

Fig. 2.27: PSD for MX80 granular bentonite as poured at dry densities ρ_d=1.5 Mg/m^3 (Seiphoori, Ferrari, and Laloui 2014) and after hydration at constant volume conditions (Baryla et al. 2018). MIP results at points A and B' in Fig. 2.26.

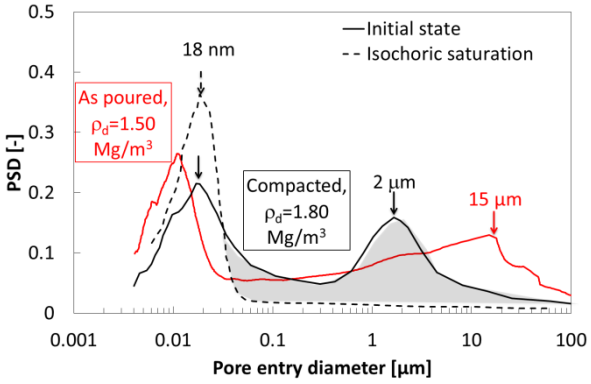

Fig. 2.28: PSD for MX80 granular bentonite as poured at dry densities ρ_d=1.5 Mg/m^3 compared to granular MX80 at compacted dry density ρ_d=1.8 Mg/m^3 before and after saturation (Seiphoori, Ferrari, and Laloui 2014). MIP results.

Fig. 2.29 refers to MIP results related to material state after hydration at constant vertical stress (path AB). The water hydration causes significant swelling phenomena (i.e. volume increase) in active clays such as bentonite. Even through the larger pores family dominating diameter decreases from 15 μm to 1 μm, the larger pores frequency becomes 20 times bigger. The sample volume increase due to hydration is marked grey in Fig. 2.29. This volume increase corresponds to a void ratio difference equal to Δe=1.48 (dry density decrease from ρ_d=1.5 to 0.8 Mg/m^3).

2 It is worth reminding that hydration in isochoric conditions follows swelling pressure's development, which makes the sampling operation more complex. Swelling pressure development will be discussed in the following chapters.

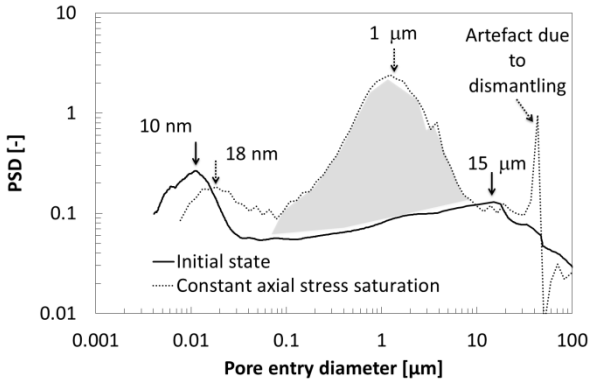

Fig. 2.29: PSD for MX80 granular bentonite as poured at initial dry density ρ_d=1.5 Mg/m^3 (Seiphoori, Ferrari, and Laloui 2014) and after hydration at constant axial stress conditions (Baryla et al. 2018). MIP results at points A and B in Fig. 2.26.

The hydration at constant vertical stress (path AB) and consequential volume increase is followed by the application of mechanical loading up to point C (path AC Fig. 2.26) when full saturation has been reached. During this path, the dominating pore entry diameter equal to 18 nm remains constant. Simultaneously, the larger pores family diameter decreases from 1 μm to 0.4 μm together with its pore frequency (Fig. 2.30). This volume decrease corresponds to a void ratio difference equal to Δe=1 (dry density increase from ρ_d=0.8 to 1.40 Mg/m^3). The larger pore family volume decrease is marked grey in (Fig. 2.30). It may be worth of attention to point out that volume reduction upon mechanical compaction at full saturated state is assumed to be achieved due to water expulsion (Terzaghi consolidation principle). During this process, water saturation degree is constant but water content evolves due to volume reduction.

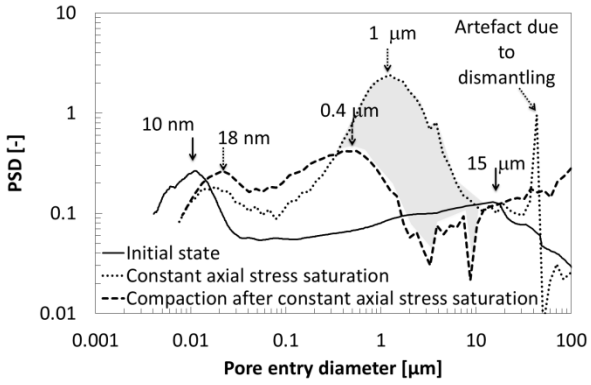

Fig. 2.30: PSD for MX80 granular bentonite as poured at initial dry density ρ_d=1.5 Mg/m^3 (Seiphoori, Ferrari, and Laloui 2014), after hydration at constant axial stress conditions and after compaction following hydration at constant axial stress conditions (Baryla et al. 2018). MIP results at points A, B and C in Fig. 2.26.

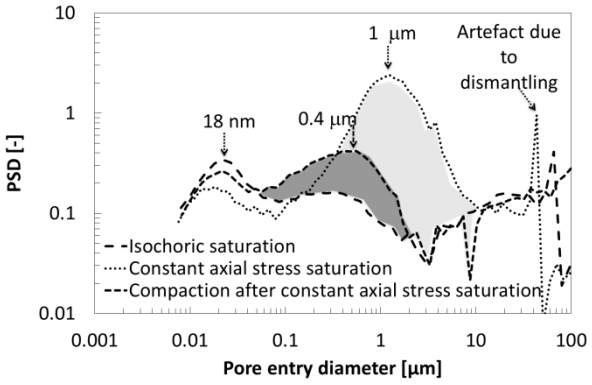

Fig. 2.31: PSD for MX80 granular bentonite at initial dry density ρ_d=1.5 Mg/m^3, after hydration at constant volume condition, after hydration at constant axial stress conditions and after compaction following hydration at constant axial stress conditions (Baryla et al. 2018). MIP results at points B, C and B' in Fig. 2.26.

MIP results at point B, C and B' are reported in Fig. 2.31. All the three points concern the full saturated state but they have different dry density and void ratio (and water content) namely: e^B=2.32, e^C=1.32 and $e^{B'}$=0.830. Moreover, point B correspond to vertical stress equal to 0.02 MPa whereas C and B' to vertical stress equal to 3 MPa. It is interesting to observe that the small pore dominating entry diameter is constant and equal to 18 nm in the three cases with small frequency increase for decreasing dry density. On the contrary, the larger pores dominating family frequency decreases with increasing dry density. The large pore

family diameter is very similar and close to 0.4 μm for e^C=1.32 and $e^{B'}$=0.830 to which the same vertical stress equal to about 3 MPa corresponds. The pores volume differentiating the larger pores families of state B, C and B' is marked light grey and dark grey in Fig. 2.31. This volume corresponds to void ratio, stress state and water content discrepancies between the three cases.

MIP analyses were also performed on MX80 pellets and crushed/powdered pellets as singular components and as homogenised medium after saturation (Baryla et al. 2018; Bernachy-Barbe 2020; Molinero et al. 2017). Fig. 2.32 summarises MIP analyses performed on MX80 different assembly types. As poured granular, compacted bentonite and single MX80 bentonite pellet and crushed/powdered are shown. The smaller pores family entry diameter is between 10 and 20 nm for all the cases. Those differ for the frequency, which is possibly related to the soil water content. The larger pores family entry diameters span of several orders of magnitude. It is particularly relevant to emphasise that for the as poured powdered bentonite the pore entry diameter is of the order of the millimetre. These very large pore structures should account for the very low dry density (ρ_d=0.9 Mg/m^3) and the incredibly high initial permeability. The assembly type (i.e. granular or powdered bentonite) can be distinguished also in Fig. 2.33 that reports the sieve passing percentage of the two poured bentonite types.

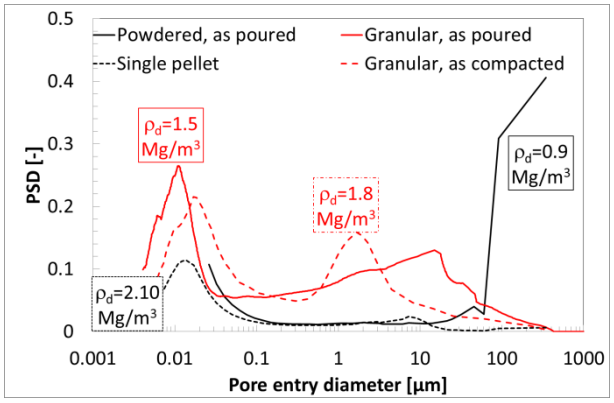

Fig. 2.32: PSD for MX80 granular bentonite as poured (ρ_d=1.5 Mg/m^3) and compacted (ρ_d=1.8 Mg/m^3), single MX80 35 mm pellet (ρ_d=2.1 Mg/m^3) and as poured crushed/powdered pellet (ρ_d=0.9 Mg/m^3). MIP results (Baryla et al. 2018; Gramegna et al. 2020; Seiphoori, Ferrari, and Laloui 2014)

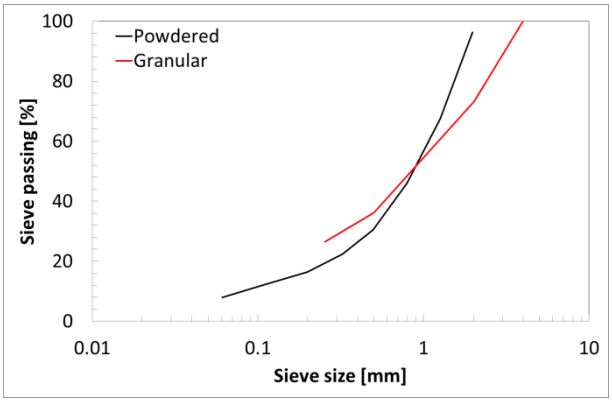

Fig. 2.33: Grain size distribution for granular MX80 bentonite and MX80 crushed/powdered pellet (Baryla et al. 2018; Gramegna et al. 2020; Seiphoori, Ferrari, and Laloui 2014).

Fig. 2.34 represents the MIP analysis results concerning a 35 mm pellet/powder mixture obtained in isochoric conditions. Similarly to the constant volume hydration of granular compacted MX80 (Fig. 2.27 and Fig. 2.28), the small pore diameter structures remain unchanged, while the large pores diameter structures migrates towards smaller pore entry diameter values (namely from 1 mm to 50 μm). This latter pores family does not disappear completely as observed for the higher dry density assembly (Fig. 2.28), but it undergoes a significant frequency (PSD) decrease (i.e. volume reduction). Similar results with respect to Febex bentonite subjected to various stress paths can be found in (Lloret and Villar 2007b). The in-depth analysis of bentonite multi-structure evolution of this assembly type is deeply investigated in the following chapter of this thesis.

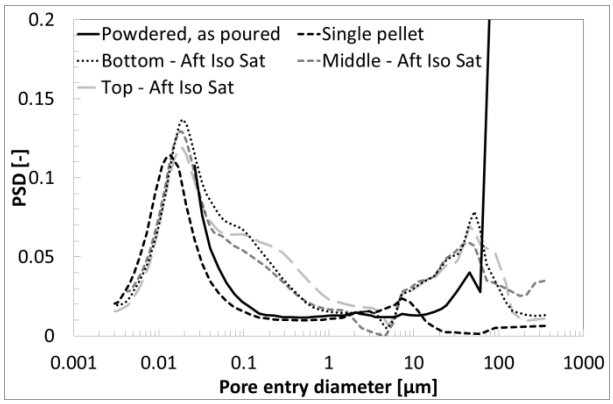

Fig. 2.34: PSD for single MX80 35 mm pellet (ρ_d=2.1 Mg/m^3), as poured crushed/powdered pellet (ρ_d=0.9 Mg/m^3) and pellet/powder mixture (ρ_d=1.5 Mg/m^3) at several location after hydration in isochoric conditions. MIP results (Baryla et al. 2018; Gramegna et al. 2020; Seiphoori, Ferrari, and Laloui 2014)

Remarks on Febex and MX80 MIP results

Fig. 2.35 and Fig. 2.36 show the comparative MIP results for single pellets and compacted samples of MX80 and Febex bentonites. The single pellets structure is similar for the two bentonites: small pores structure diameters are between 10 and 20 nm with comparable pores frequency. The larger pores structures diameters are equal to 10 µm for the MX80 and to 2 µm for the Febex that presents larger pores frequency related to the lower dry density. The compacted samples pores distributions differ remarkably even though those are related to the same materials dry density.

One possible reason of the different behaviour of the single pellets and the compacted samples can be related to the material production. The pellets are in general prepared using pre-heated powder instantaneously compacted in moulds or roller presses at low water content (Alonso, Hoffmann, and Romero 2010; Molinero et al. 2017). The compacted samples are prepared at room temperature. Heat undeniably affects the bentonite structure and response at several observation scales but thermo-hydro-mechanical couplings will not be considered in this work, which focuses on the hydro-mechanical bentonite behaviour.

However, given also the different mineralogical composition of Febex and MX80 bentonites, the MIP results related to compacted samples are not surprising.

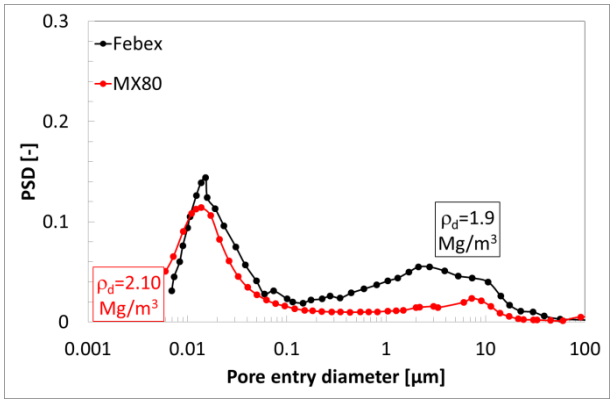

Fig. 2.35: PSD for single MX80 35 mm pellet (ρ_d=2.1 Mg/m^3) (Baryla et al. 2018) and single Febex pellet (ρ_d=1.9 Mg/m^3) (Hoffmann, Alonso, and Romero 2007). MIP results.

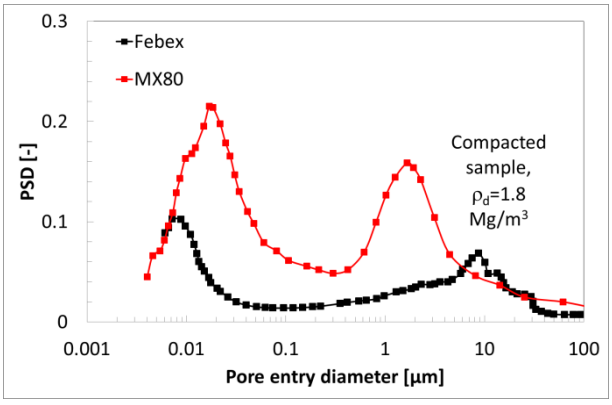

Fig. 2.36: PSD for compacted MX80 bentonite (Seiphoori, Ferrari, and Laloui 2014) and compacted Febex bentonite (Lloret et al. 2003). MIP results.

2.3.3. CT: from grains to laboratory sample

Among other techniques, computed tomography (CT) and micro-tomography (μCT), have been largely employed in recent years for the bentonite samples analysis at laboratory scale (Bernachy-Barbe 2020; Bernachy-Barbe et al. 2020; Van Geet, Volckaert, and Roels 2005; Molinero et al. 2017). CT consists in high-resolution non-destructive 3D observation technique based on the combination of a high number of X-ray images. Apart from qualitative information, CT images can provide significant quantitative information with respect to dry density distribution and evolution inside the sample

This technique is particularly suitable for the reconstruction of bentonite samples dry density field upon hydration. Thus, with respect to the analysis of bentonite pellet mixture (Fig. 2.37), CT allows determining the exact inter-pellets pores space distribution. As the previous section underlined, the very large diameter pore structures account for low dry density components, which is easily detected by CT in the 3D space. Hence, contrarily to MIP analysis, CT is a non-destructive technique that allows continuous tracking of inter-pellets pore space evolution.

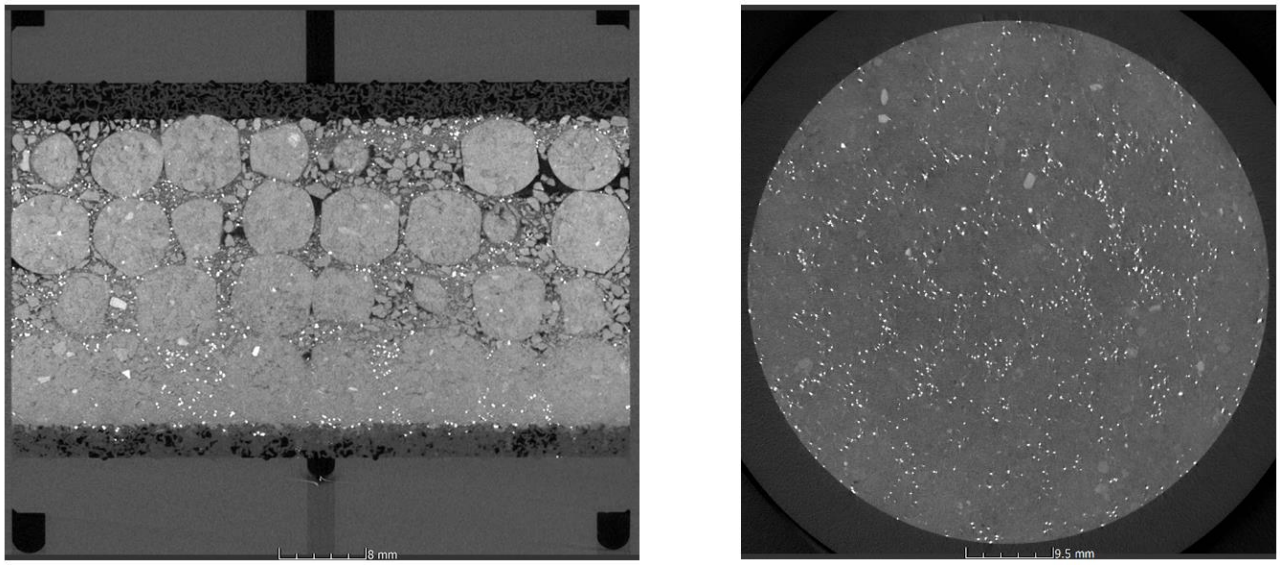

Fig. 2.37: X-ray computed tomography of MX80 pellet mixture vertical and horizontal slices (Baryla et al. 2018).

2.4. Micro-structure constitutive model

The previous sections aimed describing the multi-structural changes taking place in bentonite based materials subjected to various solicitations. In particular, one of this thesis's goals is to focus on the processes occurring from the grain scale to the engineering one. The clay grain observation scale allowed separating the processes occurring into the clay aggregates (intra-aggregate porosity corresponding to smaller pore diameter structure) and the processes taking place between the aggregates (inter-aggregates porosity corresponding to larger pore diameter structure). With this background, the proposed experimental results suggest two main conclusions:

- the smaller pores family diameter is independent on the observed range of mechanical loadings but strongly related to the hydraulic state;
- the larger pores family diameter depends on several features (assembly type, granulometry, dry density, hydration conditions…).

The major complexity of the larger pores family behaviour with respect to the smaller pores one was highlighted. Hence, this section aims to present the adopted constitutive model for the evolution of the small pore diameter structure.

Emphasis was given to the analysis of MIP results, which are capable to provide clear qualitative evidences and, after careful interpretation, quantitative information.

Among others, (Dieudonné, Della Vecchia, and Charlier 2017) rely on the MIP micro-structure analysis interpretation to propose a reasonable constitutive model that is able to describe the small diameter pore family evolution. This micro-structure evolution constitutive model is described in the following via the definition of these quantities:

- the **microporosity** Φ_m, that is defined as the ratio between the micropores volume Ω_m and the total volume Ω:

$$\Phi_m = \frac{\Omega_m}{\Omega} \qquad \text{Eq. 2.5}$$

The microporosity corresponds to the total intra-aggregate porosity comprising both inter- and intra-particles pores.

- the **microstructural void ratio** e_m, that is defined as the ratio between the micropores volume Ω_m and the solid volume Ω_s:

$$e_m = \frac{\Omega_m}{\Omega_s} = \frac{\Phi_m}{\Phi} e \qquad \text{Eq. 2.6}$$

where Φ and e are respectively the (total) porosity and void ratio given as function of the dry ρ_d and solid ρ_s density as follows:

$$e = \frac{\rho_s}{\rho_d} - 1 \qquad \Phi = 1 - \frac{\rho_d}{\rho_s} \qquad \text{Eq. 2.7}$$

the **macroporosity** Φ_M, that is defined as the ratio between the macropores volume Ω_M and the total volume Ω:

$$\Phi_M = \frac{\Omega_M}{\Omega} \qquad \text{Eq. 2.8}$$

The macroporosity coincides with the inter-aggregates pore space or, more in general, with the larger diameter structure pore space.

- the **macrostructural void ratio** e_M, that is defined as the ratio between the macropores volume Ω_M and the solid volume Ω_s:

$$e_M = \frac{\Omega_M}{\Omega_s} = \frac{\Phi_M}{\Phi} e \qquad \text{Eq. 2.9}$$

The total porosity Φ and void ratio e result as:

$$e = e_M + e_m \qquad \Phi = \Phi_M + \Phi_m \qquad \text{Eq. 2.10}$$

(Dieudonné, Della Vecchia, and Charlier 2017) analyse several criteria to distinguish micro and macro porosity. Those criteria are described in (Romero, Gens, and Lloret 1999) and provide similar quantitative results in terms of microporosity evolution tendencies.

Following (Romero, Della Vecchia, and Jommi 2011), (Dieudonné, Della Vecchia, and Charlier 2017) propose a constitutive model for microstructure evolution, which reads as follows:

$$e_m = e_{m0} + \beta_0 e_w + \beta_1 e_w^2 \qquad \text{Eq. 2.11}$$

Where e_{m0} is the microstructural void ratio for the dry material ($e_w = 0$) and β_0 and β_1 are parameters that quantify the swelling potential of the aggregates.

The model is formulated in terms of water ratio e_w:

$$e_w = eS_r \qquad \text{Eq. 2.12}$$

The model is formulated in terms of water ratio e_w, which simultaneously accounts for the saturation degree and dry density of the material.

One possible limitation of this microstructural constitutive model is related to the possibility to obtain a microstructural void ratio e_m higher than the total void ratio e. This issue is overcome assuming as micro-void ratio threshold the total void ratio value, which corresponds to the case in which the complete development of microstructure has occurred (i.e. $e_m = e$).

A relevant feature of the adopted water retention model for bentonite is the distinction between micro and macro structural levels. Moreover, as debated in the previous chapter, the interaction between the different porosities upon hydration, affects undeniably the hydro-mechanical properties. With this background, it becomes necessary to take into account the variation of microstructure upon saturation. Consequentially, among others, the previous equation is considered in the successive water retention model and permeability evolution model.

2.5. Conclusions

The main difficulty of constitutive and numerical modelling of bentonite based materials is related to the strongly coupled hydro-mechanical interactions occurring at several observation scales. The aim of this chapter was to give an overview of all the processes taking place at different observation scales in order to investigate the origins of the most important bentonite features for its employment in the context of nuclear waste repository.

Hence, the atomic/platelets scale (clay unit) and tactoids scale were firstly introduced. Even though, this information is part of any civil engineering school, a brief recall with special regards to bentonite structure and characteristics was unavoidable.

The clay grain scale was also presented in order to show the important structural changes occurring during water hydration, together with the laboratory scale, which is the one on which most of the concept designs rely for the safety assessment needed information.

Finally, the bentonite employment at the engineering scale with its major requirements is recalled with special regards to the French CIGEO concept.

It is particularly relevant to highlight that bentonite based materials are characterised not only by several scale interacting “solid” structures but also, and especially, by the pore structures. These pore structures can be investigated thanks to numerous experimental techniques.

Consequentially, the most used experimental techniques for analysing and distinguishing bentonite based materials and features are indicated. A relevant portion of the chapter is dedicated to MIP results and experimental observations with respect to Febex and MX80 bentonites pore structures.

The experimental evidences help to conclude that the small pore size structures (i.e. pore entry diameter equal to 10-15 nm) are similar in dimension and frequency regardless the assembly type (i.e. compacted or pellet mixtures bentonite). On the other hand, large scale structures present pore entry diameters spanning between several orders of magnitude in both dimension and frequency. Those are remarkably affected by numerous factors such as assembly type, dry density and hydro-mechanical paths, but they also account for different development and evolution of sealing structures hydro-mechanical features. Thus, it is crucial to understand how and to which extend can influence the engineered barriers performances.

At the end, the constitutive model for the description of the bentonite micro-structure evolution proposed by (Dieudonné, Della Vecchia, and Charlier 2017) is presented. This model is implemented in the finite element code LAGAMINE and considered in the double structures water retention and permeability evolution models described in the following. It will be possible to observe how these double porosity models allow the precise reproduction of several bentonite features, which have always been challenging.

CHAPTER 2: ON THE MULTI-POROSITIES STRUCTURE OF UNSATURATED SWELLING CLAYS

CHAPTER 3: ON THE HYDRAULIC BEHAVIOUR OF UNSATURATED SWELLING CLAYS

CHAPTER 3: ON THE HYDRAULIC BEHAVIOUR OF UNSATURATED SWELLING CLAYS

3.1. Introduction

With reference to the radioactive waste isolation concept designs, important radionuclides retardations capacity and extremely low permeability characteristics are required from engineered barriers to prevent harmful substances leakage in the environmental. As a result, bentonite-based materials are chosen as a key sealing structures component for nuclear waste disposals.

Bentonite hydro-mechanical characteristics are strongly related to its multi-level structures that are crucial to understand experimental observations and to build reliable constitutive models.

Thus, following the preceding chapter that aimed to presents the bentonite multi-level structures and porosities, this chapter's goal is to introduce some of the most significant hydraulic features of bentonite-based materials. These features can be profoundly understood only taking advantage of the different structural domains interactions and evolution knowledge.

For this purpose, this chapter is firstly divided in two subsections accounting for bentonite water retention behaviour and water transfer mechanisms. Each subsection implies, after the definitions of some relevant concepts, the introduction of experimental observations and consequential constitutive models explanations.

The experimental results analysis shows that the influence of bentonite structure (i.e. dry density and multi-level porosities distribution) on its hydraulic features is undeniable. Similarly, the coupling with the interacting fluid (liquid water in this work) results into both bentonite and water features modifications.

To complete the framework, taking in consideration the important volumetric change to which bentonite undergoes upon hydration, the effects of volumetric boundary conditions on hydraulic properties are presented taking advantage of some experimental campaigns.

The analysis of the experimental methods generally used to evaluate bentonite hydraulic characteristics is not relevant to the purposes of this thesis, consequentially those are not mentioned.

Most of the presented experimental results are meticulously contemplated in the double porosity dry density dependent water retention and permeability evolution constitutive models adopted in this work. These hydraulic constitutive models proposed by (Dieudonné 2016) also consider the bentonite micro-structural evolution taking place during hydration. As it will be demonstrated in the following numerical analyses, these models result particularly robust and suitable for large scale structure predictions and designs.

3.2.Basic concepts and definitions

In order to better understand the hydraulic processes taking place in bentonite-based materials characterised by various hydration states, fundamental definitions and concepts are recalled and presented in the following.

The ***water content*** (or water ratio) (Eq. 2.2), *w*, is defined as the weight loss of a sample after drying for 24 h in an oven at 105°C, being equivalent to the mass of the free water contained within the sample, divided by the weight of the dry sample.

$$w = \frac{mass\ of\ water}{total\ mass - water\ mass} = \frac{[kg]}{[kg]} = [-] \qquad \text{Eq. 3.1}$$

Accordingly, the ***water saturation degree*** can be defined as follows:

$$S_r = \frac{\Omega_w}{\Omega_v} = [-] \qquad \text{Eq. 3.2}$$

Namely, as the ratio between the volume of water contained in the soil (Ω_w) and volume of pore space (Ω_v). Eq. 3.2 is equivalent to:

$$S_r = \frac{w}{\left(\frac{1}{\rho_d} - \frac{1}{\rho_s}\right)\rho_w} = [-] \qquad S_r = \frac{\rho_s}{\rho_w}\frac{w}{e} = [-] \qquad \text{Eq. 3.3}$$

Where the saturation degree is written as function of water content *w*, dry density ρ_d, (or void ratio *e*), solid density ρ_s and water density ρ_w.

With respect to Eq. 3.3, it can be concluded that the saturation degree can be modified by both hydraulic and mechanical loadings. With regards to this, (Tarantino 2009) introduced the concepts of *hydraulic wetting* (i.e. increase of saturation degree related to an increase of water content) and *mechanical wetting* (namely, increase of saturation degree linked to pore volume decrease).

Moreover, the soil capability to retain a given quantity of water in defined conditions is traditionally related to the definition of ***water potential*** ψ or/and ***suction*** *s*.

(Aitchison, Russam, and Richards 1966) define the potential of water as the amount of work per unit mass of pure water required to transport reversibly and isothermally an infinitesimal quantity of water from a reservoir of pure water at a specified elevation and atmospheric pressure to the point under consideration and it is defined as the contribution of four terms:

$$\psi = \psi_g + \psi_p + \psi_m + \psi_o \qquad \text{Eq. 3.4}$$

Where ψ_g is the gravitational potential (linked to differences in elevation), ψ_p the external pressure potential (related to applied pressure), ψ_m the matric potential (implying capillary and adsorption mechanisms) and ψ_o the osmotic potential (affected by osmotic phenomena and fluid chemistry). In active clays domain, the latter two account for the manifestation of most bentonite features, whereas the former ones are often

considered negligible (Gens 2010). In soils science, it is common to define the water potential as work per unit volume (J/m^3 is homogeneous to a pressure) instead of unit mass (J/Kg).

Moreover, in unsaturated conditions, suction s can be defined as the negative pressurethat water undergoes to be in equilibrium soil water. Therefore, the two definitions are used indiscriminately even though they do not coincide precisely.

Accordingly, the total suction s can be defined as the sum of the matric suction s_m and osmotic suction s_o:

$$s = s_m + s_o \qquad \text{Eq. 3.5}$$

Alternatively, total suction can be expressed as function of relative humidity RH via Kelvin law:

$$s = -10^{-6}\frac{RT}{V_w} ln\left(\frac{RH}{100}\right) \qquad \text{Eq. 3.6}$$

Where R is the ideal gas constant (8.3143 J/mol), T is the absolute thermodynamic temperature (in Kelvin) and V_w is the molar volume of water ($1.80 \cdot 10^{-5}$ m^3/mol).

Even though matric suction is related to both capillary (dominant in granular soils) and absorption phenomena (fluid-minerals electro-chemical interactions dominant in clays), it is defined in this work as the excess of gas pressure, u_g, with respect to water pressure, u_w:

$$s = s_m = u_g - u_w \qquad \text{Eq. 3.7}$$

Thus, in the case of constant gas pressure (as the one studied in this work) suction is considered as negative water pressure and it expresses the degree of attachment of water to clay particles (Gens 2010).

3.3. Water retention behaviour

The relationship between the quantity of water stored in a porous media and suction can be described via the water retention curve. Water content, water ratio, and degree of saturation are indicators that can be used to define the stored amount of water.

3.3.1. Experimental observations

Water storage domains and effect of multi-porosity distribution

The existence of distinct but interacting water retention domains in clays is intrinsically related to their multi-porosity structures accounting for the various water storage mechanisms at each observation level discussed in Chapter 2. Precursor of such conclusion can be identified in Lloret, Villar, Sànchez, et al. (2003); and Romero, Gens, and Lloret (1999), among others. If the latter ones focused on the water retention behaviour of Boom clay (that, similarly to bentonite, also presents bimodal pore size distribution upon compaction at PSD analysis), the former ones investigated the behaviour of Febex bentonite compacted at different dry densities in isochoric conditions (Fig. 3.1). Fig. 3.1 evidently shows that for suction values larger than 12 MPa (w<0.24), water storage mechanism is not affected by the material dry density. On the other hand, for suction lower than 12 MPa (w>0.24), water retention capacity is strictly related to dry density features. Namely, the high suction domain is independent on compaction processes, whereas the low suction one is strongly affected. It may be worth pointing out that water stored between tactoids and inside grains (i.e. adsorbed and saturation water) requires high potential (high suction) to be removed being linked to clay structures by strong physicochemical bonds, whereas water stored between the grains (i.e. pore water) is easily removable also with relatively small forces. Therefore, it is possible to distinguish:

- a water retention domain related to high suction values referring to physicochemical phenomena as adsorption and ***small diameter structures*** (often called as microstructural water retention domain);

- a water retention domain related to low suction values related to capillary phenomena and ***large diameter structures*** (often called as macrostructural water retention domain).

It may be worth to remind that, as it was discussed in Chapter 2, that compaction processes only affect the large diameter pores, whereas the small diameter ones are considered independent, supporting the above-proposed definitions and conclusions.

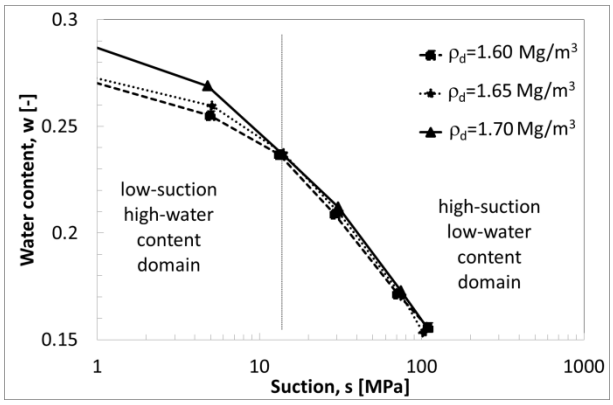

Fig. 3.1: Water retention curve of Febex bentonite compacted at three dry densities obtained in isochoric conditions (Lloret et al. 2003).

Let us focus on the water retention curves of three different samples of MX80 bentonite, presenting identical dry density ρ_d=1.50 Mg/m^3 but different unsaturated pore size distributions (i.e. assembly type: pellets mixture, granular and compacted bentonites) (Fig. 3.2). The differences arising in pore size distribution of sample presenting the same dry density were already debated in Chapter 2. Those basically consist in:

- localised small diameter structures high density components coinciding with pellets and very disperse and large diameter structures low density components corresponding to powder for the pellets mixture;

- more uniform small diameter structures high density components reflecting the single grains components and large diameter structure lower density components corresponding to grains clusters for the granular bentonite sample;

- structure similar to granular bentonite but with smaller large diameter structure for compacted bentonite sample.

It is of particular interest how despite the pore structures of such assemblies remarkably differ especially with regards to larger diameter pores, the three water retention curves correspond quite well. Thus, it can be concluded that the global water retention behaviour of a certain bentonite based material does not depend on the pore-structures distribution but only on the global pore volume.

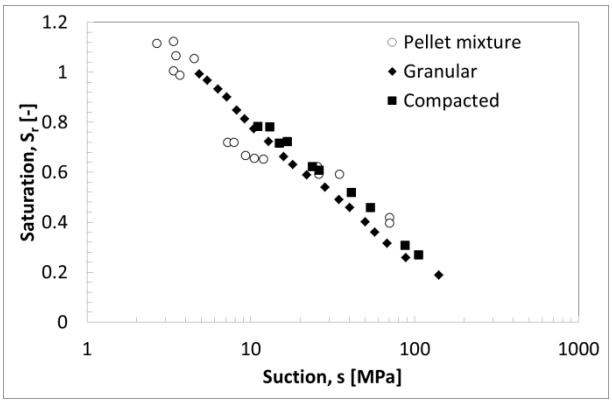

Fig. 3.2: Water retention curve of MX80 bentonite pellets mixture, granular and compacted samples at dry density equal to ρ_d=1.50 Mg/m^3 obtained in isochoric conditions (Molinero et al. 2019; Seiphoori, Ferrari, and Laloui 2014; Villar 2005)

Effect of dry density

Dry density is a key feature to define water retention capabilities of bentonite-based materials. Bentonite dry density indicates not only the degree of compactness of the material, thus, the void volume that can be potentially filled by water, but also, with respect to a given type and bentonite assembly, the quantity and development of large diameter pore structures. Fig. 3.3 and Fig. 3.4 show the water retention curve of MX80 bentonite compacted at different dry density obtained in isochoric conditions (i.e. preventing volume variation upon hydration) by several authors expressed in terms of water content. It appears quite evident that for high suction level (i.e. >30 MPa), the material behaviour corresponds for all the considered dry densities, whereas differences appear when suction decreases following the hydration process. As saturation is approached, it follows that for the lower dry density, larger pore structures occurrence, the higher water content is found. By the observation of the same experimental data in terms of saturation degree (obtained considering constant water density equal to ρ_w=1 Mg/m^3 accordingly to Eq. 3.3), it seems clear that for increasing dry density, increasing potential (suction) is needed to reduce the saturation degree of the material. This conclusion is consistent with the concept of capillarity.

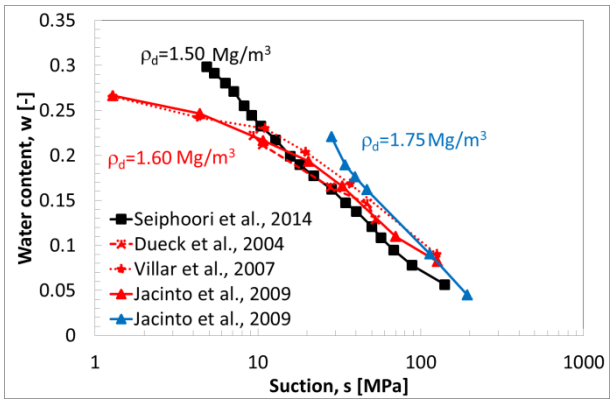

Fig. 3.3: Water retention curve of MX80 bentonite compacted at three dry densities obtained in isochoric conditions by several authors expressed in terms of water content (Dueck and Nilsson 2010; Jacinto et al. 2009; Seiphoori, Ferrari, and Laloui 2014; Villar 2005).

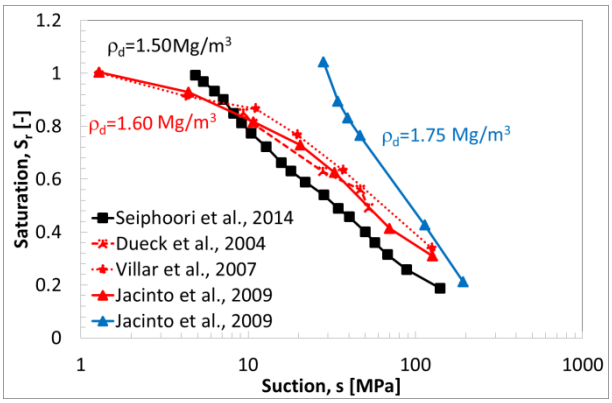

Fig. 3.4: Water retention curve of MX80 bentonite compacted at three dry densities obtained in isochoric conditions by several authors expressed in terms of saturation degree (Dueck and Nilsson 2010; Jacinto et al. 2009; Seiphoori, Ferrari, and Laloui 2014; Villar 2005).

Among other authors, (Seiphoori, Ferrari, and Laloui 2014) studied the water retention behaviour of granular MX80 bentonite compacted at different dry density (Fig. 3.5), with special regards to respect to the air entry value related to each density (Fig. 3.6). The Air Entry value can be defined as the matric suction value that must be exceeded before air recedes into the soil pores. Accordingly to this definition, it is confirmed that the air entry value is mostly related to capillary phenomena. The authors support the previous experimental observation highlighting that for higher dry density, higher suction (potential) is required to obtain water separation from clay particles.

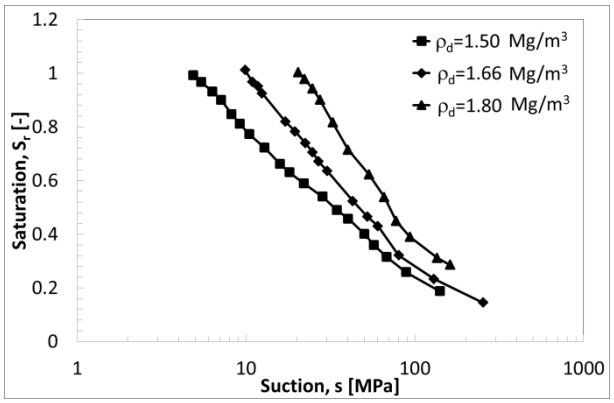

Fig. 3.5: Water retention curve of MX80 granular bentonite compacted at three dry densities obtained in isochoric conditions (Seiphoori, Ferrari, and Laloui 2014).

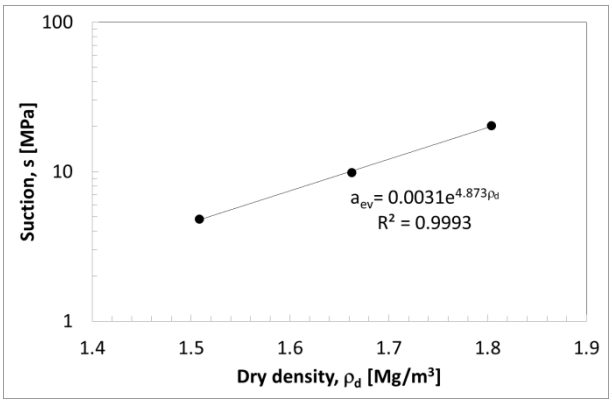

Fig. 3.6: Evolution of the air-entry value as a function of dry density (Seiphoori, Ferrari, and Laloui 2014).

Effect of water density

As it was demonstrated, a significant quantity of water stored in bentonite based materials is related to physicochemical mechanisms implying water molecules attachment to clay particles and layers. This water type is particularly difficult to displace and present a density that is larger than the one of pore water. Numerous experimental results (Jacinto, Villar, and Ledesma 2012; Lloret and Villar 2007a; Marcial 2003; Molinero et al. 2019; Villar 2000) showed that with respect to active clays such as bentonites, the density of water is proportionally increasing with increasing dry density.

Fig. 3.7 and Fig. 3.8 presents the water retention curves obtained for Febex pellets mixtures presenting different dry densities in terms of water content. When normalising to saturation level via Eq. 3.3, it may follow remarkable overestimation of saturation level when considering water density equal to ρ_w=1 Mg/m^3 (Fig. 3.8, black lines). Overestimation may be overcome by considering a relation linking water to soil density, but the exact distribution of water and water density inside the bentonite multi-porosities are not well-known and may result into underestimation for high suction level (Fig. 3.8, red lines).

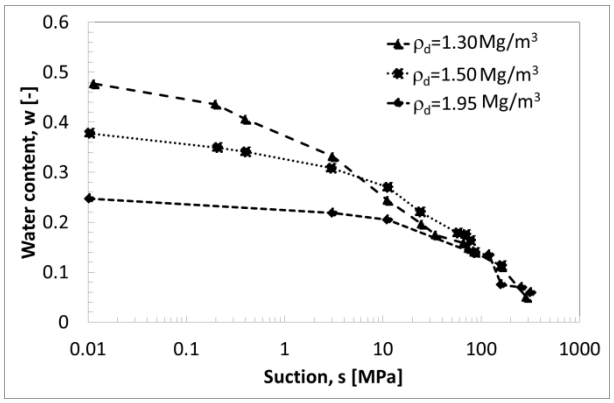

Fig. 3.7: Water retention curve of Febex bentonite compacted at three dry densities obtained in isochoric conditions expressed in terms of water content (Hoffmann, Alonso, and Romero 2007).

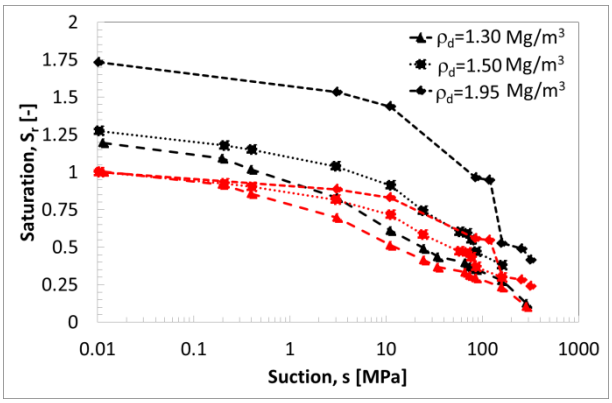

Fig. 3.8: Water retention curve of Febex bentonite compacted at three dry densities obtained in isochoric conditions expressed in terms of saturation. Curves obtained considering water density equal to ρ_w=1 Mg/m^3 (black) and water density increasing with bentonite dry density (red) (modified after Hoffmann, Alonso, and Romero 2007)

Effect of volumetric boundary conditions

Aside from the evolution of fabric and pore structures as a result of water hydration, swelling (i.e. volume expansion) always occurs as a result of water supply (when allowed) in bentonite based materials. water retention curves of MX80 bentonite compacted at initial dry density equal to ρ_d=1.75 Mg/m^3 subjected to hydration in isochoric conditions (Jacinto et al. 2009) and free swelling (Saiyouri, Tessier, and Hicher 2004) are reported. It is possible to observe that for increasing water content up to suction values smaller than 10 MPA, isochoric and free wetting paths correspond quite well (Fig. 3.9). However, it is consequential that as the material dry density decreases, the void ratio increases as well as the material storage capacity, which allows reaching final values three or four times larger than the one related to constant volume conditions. On the other hand, the water supply does not always correspond to saturation increase when dealing with swelling phenomena. Fig. 3.10, indeed, presents the water retention curves in terms of saturation. The sample subjected to free wetting does not show remarkable saturation increase for a suction decrease spanning between 200 and 0.1 MPa, whereas the sample undergoing to isochoric hydration is immediately saturated for very high suction values. With respect to Eq. 3.3, it follows that for the sample undergoing free wetting the water content and the void ratio increases simultaneously at the same rate and that for the sample subjected to volume constraints hydraulic wetting takes place (Tarantino 2009).

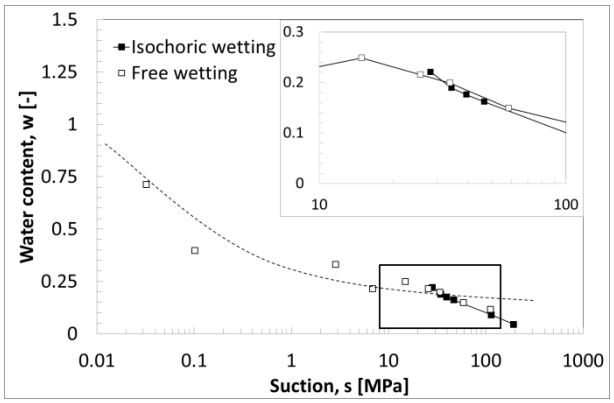

Fig. 3.9: Water retention curve of MX80 bentonite compacted at initial dry density equal to ρ_d=1.75 Mg/m^3 obtained in free swelling and isochoric conditions expressed in terms of water content (Jacinto et al. 2009) (Saiyouri, Tessier, and Hicher 2004).

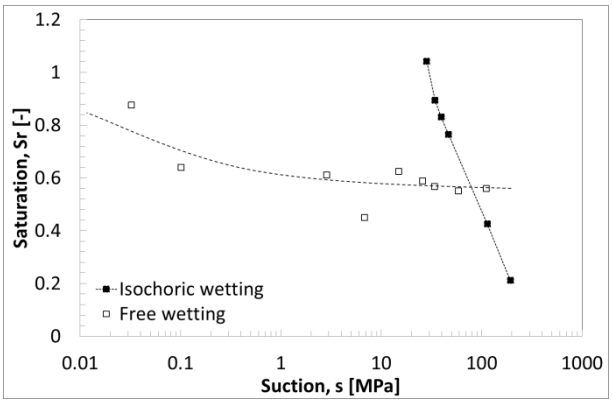

Fig. 3.10: Water retention curve of MX80 bentonite compacted at initial dry density equal to ρ_d=1.75 Mg/m^3 obtained in free swelling and isochoric conditions expressed in terms of saturation (Jacinto et al. 2009) (Saiyouri, Tessier, and Hicher 2004).

For sake of completeness isochoric and free wetting water retention curves are given for Febex bentonite (Lloret et al. 2003) in Fig. 3.11. The two samples are compacted at the same initial dry density equal to ρ_d=1.65 Mg/m^3. For high suction range (s>5 MPa, i.e. small diameter structures domain), the retention responses is the same for the two, whereas for low suction values (s<5 MPa, large pores structure domain) water storage capabilities are strongly affected by density variation. These experimental evidences are in good agreement with the ones related to MX80 bentonite.

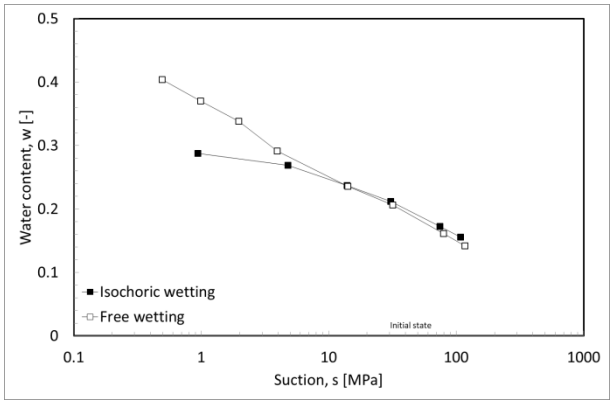

Fig. 3.11: Water retention curve of Febex bentonite compacted at initial dry density equal to ρ_d=1.65 Mg/m^3 obtained in free swelling and isochoric conditions expressed in terms of water content (Lloret et al. 2003)

3.3.2. Constitutive model

The link between water content and suction or saturation and suction is generally described via a unique relationship traditionally described by models such as the ones by (van Genuchten 1980) and/or (Brooks and Corey 1964). These constitutive relationships resulted in satisfactory descriptions of water retention responses of granular and low-activity soils (i.e. materials which do not exhibit remarkable volume or fabric change upon hydration) within a unique set of parameters. Hence, when dealing with highly expansive soils such as bentonite, these classical formulations are not capable to account for the water storage properties evolution with respect to swelling upon hydration (i.e. dry density evolution). Accordingly, the water retention properties dry density dependency is a key feature to provide a better description and reproduction of bentonite-based materials of water storage mechanism.

Hence, a new model is proposed and implemented and it is currently adopted in Liège (Dieudonné 2016; Dieudonné, Della Vecchia, and Charlier 2017). Based on the abovementioned information, the model is formulated in terms of water ratio e_w reference, which is expressed as the superposition of a contribution from the water stored in the micropores e_{wm} and a second contribution from the water contained in the macropores e_{wM}:

$$e_w = e_{wm} + e_{wM} \qquad \text{Eq. 3.8}$$

This model takes into account the evidence of the different water retention mechanisms, namely adsorption in the microstructure (inter-layer porosity and inter-particle porosity) and capillary storage in the inter-aggregate porosity (see Fig. 3.12).

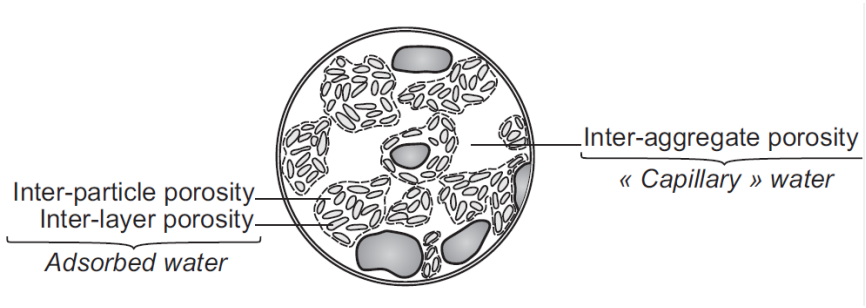

Fig. 3.12: Conceptual representation of the structure of compacted bentonite (in black) and the different water storage mechanisms (in blue) (modified after Gens & Alonso (Gens and Alonso 1992) (Jacinto, Villar, and Ledesma 2012).

The degree of saturation S_r is then expressed as:

$$S_r = \frac{e_w}{e} = \frac{e_m}{e} S_{rm} + \frac{e_M}{e} S_{rM} \qquad \text{Eq. 3.9}$$

where e_m and $e_M = e - e_m$ are respectively the microstructural and macrostructural void rations, and S_{rm} and S_{rM} the microstructural and macrostructural degrees of saturation. The degrees of saturation are therefore not additive, as the global degree of saturation is obtained by the sum of the microstructural and macrostructural degrees of saturation, weighted by the corresponding volumetric fractions.

In the following, thermodynamic equilibrium between the microstructure and macrostructure is assumed. Accordingly, the current value of suction applies to both structural levels.

Microstructural water retention domain

Water in the microstructure is mainly stored by adsorption. Several adsorption isotherms have been proposed in the literature by the community of physicists. Dubinin's isotherm is adopted to describe the water retention behaviour of the microstructure. Its equation takes the following form:

$$\Omega_{wm} = \Omega_m exp\left\{-\left[\frac{RT}{\beta_D E_0} ln\left(\frac{u_v^0}{u_v}\right)\right]^{n_{ads}}\right\} \quad \text{Eq. 3.10}$$

where Ω_{wm} is the volume of water adsorbed in the micropores at temperature T and relative pressure u_v/u_v^0, R is the universal gas constant ($= 8{:}314\, J/mol \cdot K$), and Ω_m is the total volume of the micropores, n_{ads} is a specific parameter of the system, called heterogeneity factor. β_D is termed similarity constant and $E = DE_0$ is the characteristic adsorption energy for the given system. E_0 is the characteristic energy of adsorption for a reference vapour for which $\beta_D = 1$.

By dividing both sides of equation 2.3 by the volume of solid particles Ω_s, it yields:

$$e_{wm} = e_m exp\left\{-\left[\frac{RT}{\beta_D E_0} ln\left(\frac{u_v^0}{u_v}\right)\right]^{n_{ads}}\right\} \quad \text{Eq. 3.11}$$

Moreover, assuming relative humidity RH being function of relative pressure u_v/u_v^0, in terms of suction s:

$$RH = \frac{u_v^0}{u_v} = exp\left(\frac{-sM_w}{RT\varrho_w}\right) \quad \text{Eq. 3.12}$$

where M_w is the molecular mass of water ($= 0{:}018\, kg/mol$) and ϱ_w its density. Gathering the constant parameters, the following expression is finally adopted for the microstructural water retention domain:

$$e_{wm}(s, e_m) = \mathrm{e}_m exp[-(C_{ads}s)^{n_{ads}}] \quad \text{Eq. 3.13}$$

Where n_{ads} and C_{ads} are material parameters controlling respectively the curvature of the water retention curve in the high suction range and the dependency on the rate of desaturation of the soil. C_{ads} also reads:

$$C_{ads} = \frac{M_w}{\varrho_w \beta_D E_0} \quad \text{Eq. 3.14}$$

Macrostructural water retention domain:

The van Genuchten (van Genuchten 1980) water retention model has been successfully used to model the water retention behaviour of a wide variety of soils. It is generally expressed as:

$$S_r(s) = \left[1 + \left(\frac{s}{\alpha}\right)^n\right]^{-m} \quad \text{Eq. 3.15}$$

where m and n are material parameters, and α is related to the air-entry value s_{AE}. Alternatively, the van Genuchten equation may expressed in terms of water ratio e_w:

$$e_w(s,e) = e\left[1 + \left(\frac{s}{\alpha}\right)^n\right]^{-m} \quad \text{Eq. 3.16}$$

In this model, the van Genuchten equation is selected to model the macrostructural water retention domain. Accordingly, the void ratio e is replaced by the macrostructural void ratio $e_M = e - e_m$, and the macrostructural water retention model reads:

$$e_{wM}(s,e) = (e - e_m)\left[1 + \left(\frac{s}{\alpha}\right)^n\right]^{-m} \quad \text{Eq. 3.17}$$

In order to represent the influence of the bentonite structure on the air-entry value, the parameter α is assumed to depend on the macrostructural void ratio. The following law is adopted:

$$\alpha = \frac{A}{e - e_m} \quad \text{Eq. 3.18}$$

where A controls the dependence of the air-entry pressure on the macrostructural void ratio.

Microstructure evolution

In order to take into account the variation of microstructure due to saturation degree change, the following equation is written:

$$e_m = e_{m0} + \beta_0 e_w + \beta_1 e_w^2 \quad \text{Eq. 3.19}$$

Where e_{m0} is the microstructural void ratio for the dry material ($e_w = 0$) and β_0 and β_1 are parameters that quantify the swelling potential of the aggregates.

Eq. 3.19 shows the dependency of the micro-void ratio e_m on the water ratio e_w. The water ratio depends on the total void ratio e and on the global saturation S_r. The total void ratio depends according to the BBM on the suction and on the total stress. Thus, the micro-void ratio e_m depends, among other factors, also on the mechanic stress path and not only on the hydraulic one. Similarly, the micro-void ratio formulation of BExM depends on effective stress, which is given by the total stress (in general few MPa) and suction (often some hundreds of MPa in unsaturated state).

3.4. Water transfer mechanism

Basic concepts and definitions

Fluids transfer mechanisms in porous media are generally described via the Darcy equation (Darcy 1865). The mass fluxes of the liquid and gas phases are written as follows.

$$\boldsymbol{q_l} = -\frac{k_w}{\mu_w}(\nabla u_w + \rho_w \boldsymbol{g}) \qquad \text{Eq. 3.20}$$

$$\boldsymbol{q_g} = -\frac{k_g}{\mu_g}\left(\nabla u_g + \rho_g \boldsymbol{g}\right) \qquad \text{Eq. 3.21}$$

With k_w and k_g representing the relative permeabilities of the liquid (i.e. water) and gas phases of the partially saturated medium, μ_w and μ_g the dynamic viscosities of liquid and gas phases, ∇u_w and ∇u_g are the liquid and gas pressure gradients, while ρ_w and ρ_g are the liquid and gas densities with $\boldsymbol{g}$ the gravity.

As a matter of fact, when dealing with non-active porous materials, the presence of gas phases causes a reduction in cross section responsible for water flow with the amount of water in the porous material. In order to account for this phenomenon, the liquid and gas permeabilities generally read:

$$k_w = K_w k_{rw}(S_{rw}) \qquad \text{Eq. 3.22}$$

$$k_g = K_g k_{rg}(S_{rw}) \qquad \text{Eq. 3.23}$$

Where $\mathrm{k_{rw}}(\mathrm{S_{rw}})$ and $\mathrm{k_{rg}}(\mathrm{S_{rw}})$ are water and gas relative permeabilites accounting for the presence of the other component and, thus, strongly dependent on the water (or gas) saturation[3] degree and $\mathrm{K_w}$ and $\mathrm{K_g}$ are respectively the water permeability in fully saturated conditions (S_{rw}=1) and gas permeability in totally dry conditions (S_{rw}=0).

Even though Darcy equation is extensively used for non-active soils, it was demonstrated that it suits remarkably well the behaviour of low permeability active soils such as bentonite (Lewis and Schrefler 1998), where laminar flow is dominating. Thus, it is selected to account for the partial saturation effect on water flow mechanism. Moreover, it is important to point out that, with regards to the present work, the gas injections, phase changes and temperatures or chemical effects are not considered.

This conclusion allows indicating the permeability as the main feature for the investigation of water transfer in soils.

3 Gas and water saturation degrees are linked via the relation $S_{rw} = 1 - S_{rg}$.

3.4.1. Experimental observations

Effect of dry density

Saturated bentonite permeability has been extensively investigated in numerous experimental campaigns (Bernachy-Barbe et al. 2020; Gatabin, Guillot, and Bernachy-Barbe 2016; Hoffmann, Alonso, and Romero 2007; Imbert et al. 2004; Karnland et al. 2008; Lajudie et al. 1994a; Lloret and Villar 2007a; Pusch 2001; Villar 2005). Experimental results with respect to MX80 and Febex bentonites are recalled in the following. From Fig. 3.13 to Fig. 3.16, saturated bentonite permeability dependency on dry density can be observed. Regardless the bentonite type (i.e. MX80 or Febex) and assembly (i.e. compacted block or pellets) an evident tendency linking decreasing permeability to increasing dry density (i.e. decreasing porosity) on a semi-logarithmic scale is easily observable. Such a feature is undeniably related to variation in large diameter pores upon hydro-mechanical loadings application. The saturated permeability values spans of several orders of magnitude in the range of the analysed dry densities. Moreover, a quite large values scattering up to one order of magnitude for the same density and method is often observed (Fig. 3.13 and Fig. 3.16 in particular). Especially with regard to its role of isolation barrier to radionuclides leakage in the context of nuclear waste disposals, saturated permeability and its evolution need to be extremely carefully accounted.

Effect of multi-porosity distribution

Apart from dry density, which is an important indicator of large pore structures frequency inside the material, the assembly multi-porosity distribution is expected to play also a relevant role. It may be worth reminding that Chapter 2 presented the MIP results comparisons between pellets mixture and compacted block of Febex and MX80 bentonites. It was possible to observe that, regardless the global "void quantity" was the same for the two assembly type, the small-large diameter structures distributions remarkably differed. Namely, those resulted into high density regions characterised by dominating small diameter structures and similarly incredibly low dry density regions characterised by very large dominating diameter structures for pellets and a more homogeneous distribution of densities and structures diameter for the compacted materials.

Exhaustive experimental campaigns have been conducted by Spanish teams UPC and CIEMAT (Hoffmann, Alonso, and Romero 2007; Villar 2002) for Febex bentonite and by the French CEA (Bernachy-Barbe et al. 2020; Gatabin, Guillot, and Bernachy-Barbe 2016) on MX80. Fig. 3.13 and Fig. 3.14 aim to present the effect of such structural distributions with respect to hydraulic conductivity in saturated conditions.

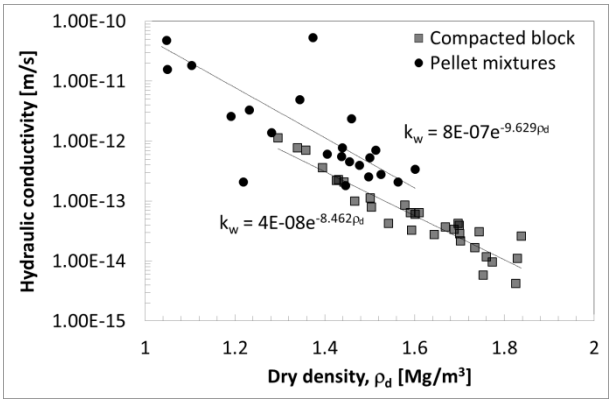

Fig. 3.13: Saturated water permeability with dry density and assembly types Experimental data for Febex bentonite.(Hoffmann, Alonso, and Romero 2007; Villar 2002)

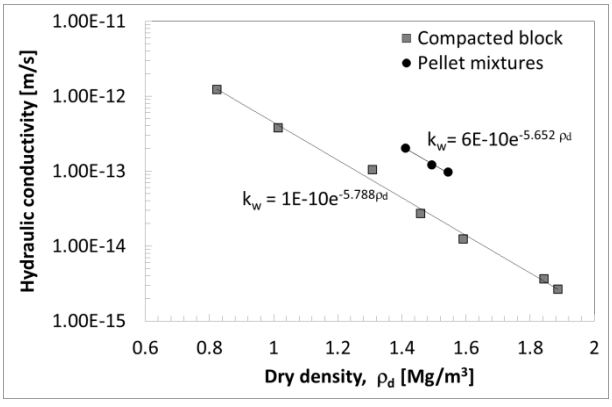

Fig. 3.14: Saturated water permeability with dry density and assembly types Experimental data for MX80 bentonite (Bernachy-Barbe et al. 2020; Gatabin, Guillot, and Bernachy-Barbe 2016)

For the range of investigated density, it appears clear that in the saturated state, pellets mixtures assemblies account for a permeability that is two or three times larger with respect to the one of compacted blocks. This

can affect remarkably the safeness assessment of real in-situ structures, since permeability affects inversely the percolation time inside a porous soil.

Water salinity and other features

It is generally recognised that soils permeability does not depend only on the soil characteristics, but also on the fluid accounted in the transfer mechanism. For instance, the relation between water type and bentonite permeability was deeply analysed by several authors during years (Fig. 3.15 and Fig. 3.16). It is possible to see that the salinity of water (i.e. the amount of salt dissolved in a body of water) allows measuring permeability values, which are in general larger with respect to the ones measured with distilled water and up to two orders of magnitude larger than the ones obtained with colloidal solutions.

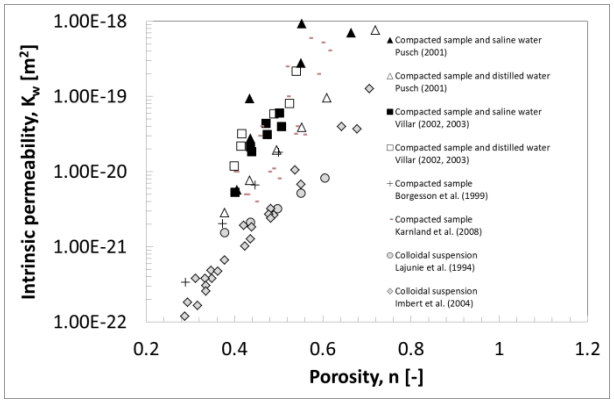

Fig. 3.15: Variation of saturated water permeability with dry density and water salinity. Experimental data for MX80 bentonite.

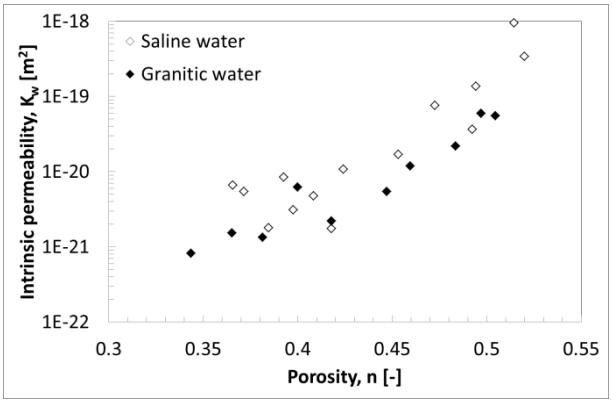

Fig. 3.16: Variation of saturated water permeability with dry density and water salinity. Experimental data for Febex bentonite (Lloret and Villar 2007b).

The influence of salinity is strictly related to the strong activity of bentonite-based materials, which is often expressed via the Cations Exchange Capacity (CEC). Studies on permeability and CEC have also been led by (Ahn and Jo 2009; Dananaj, Frankovská, and Janotka 2005; Narasimha Rao and Mathew 1995) among others.

However, even though, this work focuses only on the dry density and pores size distribution effects on permeability, it may be important to mention that bentonite-based material permeability can depend on montmorillonite content, mixture composition and proportion (i.e. sand or low activity clays components), temperature and material preparation among many other features. (Dieudonné 2016) proposes an extensive overview on some of these topics, giving particular emphasis to the MX80-sand mixture initially accounted in the CIGEO project (Labalette et al. 2009).

Permeability at unsaturated state

It has been mentioned that when dealing with multi-phase porous media, one should account for the presence of a gas phase affecting the water transfer mechanism inside the channel network. Experimental results on non-active soils substantially show that as the water saturation degree inside the soil increases, the gas permeability decreases as a result of the cross section reduction available for gas flow. Similarly, it was also demonstrated that simultaneously to water saturation increase, water permeability consistently increases as a result of the cross section expansion available for water flow. For bentonite based materials, it was demonstrated that only the former definition suits remarkably well the experimental results on gas injection in unsaturated state (ENRESA 2000) (Fig. 3.17), whereas very limited experimental characterisation on water unsaturated permeability is available at the present state.

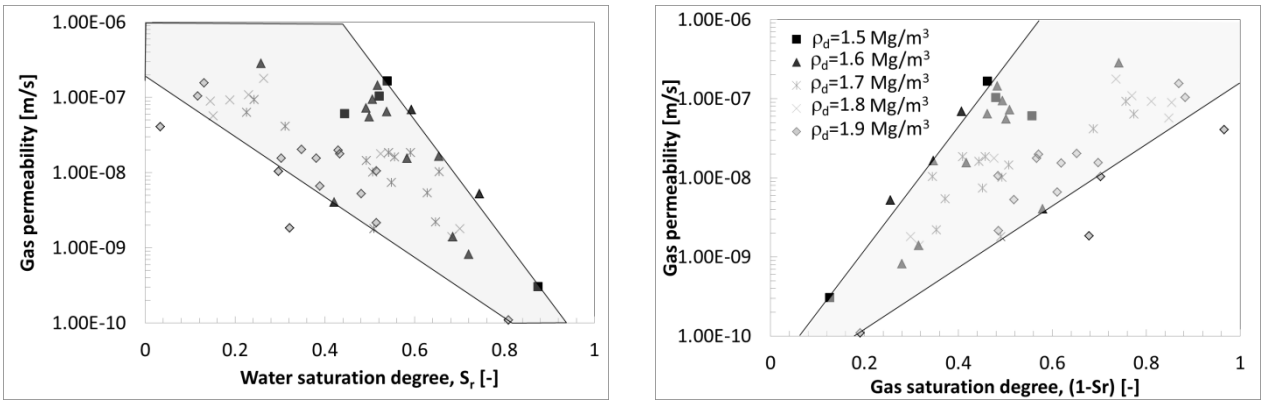

Fig. 3.17: gas permeability as function of water saturation degree and gas saturation degree for Febex bentonite compacted at several dry densities (ENRESA 2000).

However, some attempts have been conducted in the last decades for the evaluation of unsaturated permeability of bentonite based materials (Bernachy-Barbe et al. 2016; Cui 2017). In particular, (Bernachy-Barbe et al. 2016) investigated unsaturated permeability of MX80 bentonite compacted at dry density equal to ρ_d=1.5 Mg/m^3. Fig. 3.18 reports the computed experimental results, which highlights that the unsaturated permeability does not monotonically increase with suction decrease (i.e. saturation increase) in the range of investigated suction. It may be worth comparing this latter experimental outcome with gas permeability evolution as function of water saturation (Fig. 3.19) obtained by (B. Zhou, Sanchez, and Villar 2020). Consistently with results presented for Febex in Fig. 3.17, it appears evident that MX80 gas permeability monotonically decreases. Thus, the non-monotonic water permeability evolution upon water saturation is not only due to the presence and expulsion of gas phases but especially related to the evolution of large diameter pore structures that evolve during hydration.

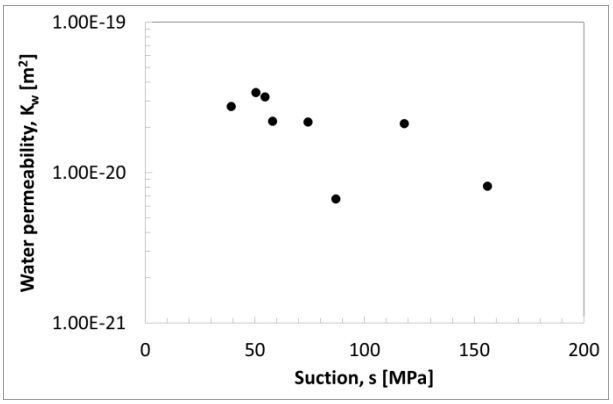

Fig. 3.18: Water permeability as function of suction of MX80 bentonite compacted at dry density equal to ρ_d=1.5 Mg/m^3 (Bernachy-Barbe et al. 2016).

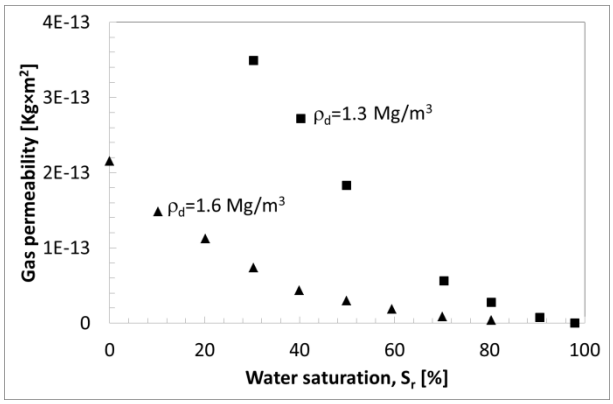

Fig. 3.19: Gas permeability as function of water saturation of MX80 bentonite compacted at different dry densities (B. Zhou, Sanchez, and Villar 2020).

Especially with respect to pellet mixture, (Hoffmann, Alonso, and Romero 2007) computed the water permeability evolution with saturation (Fig. 3.20). After a short initial phase corresponding to low saturation, the permeability immediately decreases for saturation values between 0.6 and 0.7. This abrupt permeability drop is due to the destruction of the large diameter pores structure, whose influence on water flow mechanisms results more considerable than the one related to the saturation dependence.

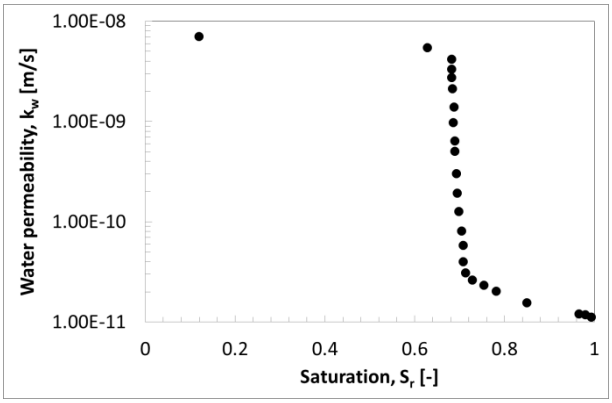

Fig. 3.20: Computed Febex permeability for pellet mixture (Hoffmann, Alonso, and Romero 2007).

The experimental determination of unsaturated permeability is a challenging task and a key issue, which enhances its complexity when such heterogeneous density and structural distributions are considered. At the present state, very few developments have been obtained with respect to this and classical experimental methods do not provide reliable results. However, the combination of image analysis (Fig. 2.13 and Fig. 3.22) with classical measurements techniques may supply an improved understanding.

Fig. 3.21: CW1 swelling pressure hydration test performed in a rectangular glass cell on the same assembly analysed in this study (Villar et al. 2021).

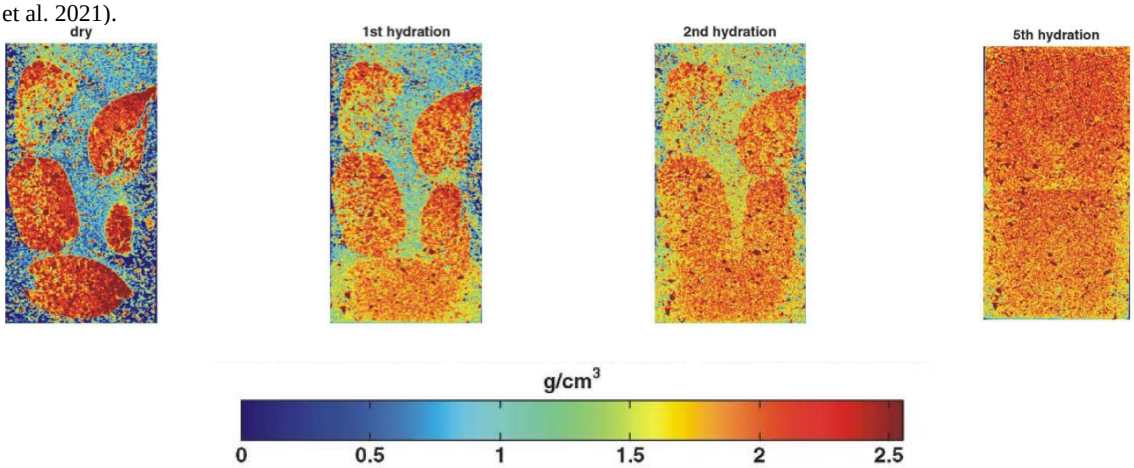

Fig. 3.22: Computed tomography of Fo-Ca bentonite pellets mixture subjected to constant volume hydration (Van Geet, Volckaert, and Roels 2005).

3.4.2. Constitutive model

Geometric permeability

Soils saturated permeability dependency on dry density and dry density evolution is generally considered accordingly to empirical or semi-empirical formulations. The Kozeny-Carman formulation is often adopted to simulate this feature. It can read as follows:

$$K_w = K_{w0}\frac{(1-\phi_0)^m}{{\phi_0}^n}\frac{\phi^n}{(1-\phi)^m} \quad \text{Eq. 3.24}$$

But also as follows:

$$K_w = K_{w0}exp[b(\phi-\phi_0)] \quad \text{Eq. 3.25}$$

Where ϕ is the actual material porosity, K_{w0} a permeability measured with respect to a reference porosity value equal to ϕ_0 and *b*, *m* and *n* material parameters, which are respectively equal to 3 and 2 for granular soils.

Alternatively, (Gerard, Charlier, and Collin 2008) also implemented Eq. 3.26 (based on (Chavant and Fernandez 2005)) to simulate the fluid transfer in clay gallery excavation:

$$K_w = K_{w0}[1+m(\phi-\phi_0)^n] \quad \text{Eq. 3.26}$$

Eq. 3.26, similarly to Eq. 3.24, formulates permeability dry density dependence in terms of the actual material porosity ϕ, K_{w0} a permeability measured with respect to a reference porosity value equal to ϕ_0 and material parameters, *m* and *n*.

Even though such relationships describe remarkably well the water transfer behaviour of a wide range of granular soils, those do not account for the additional complexity characterising multi-structural porosity materials like bentonite.

With this regard, several models were proposed by a number of authors, among those it is worth mentioning (Gens et al. 2011) and (Sanchez, Gens, and Olivella 2012), which modified Eq. 3.25 obtaining:

$$K_w = K_{w0}exp[b(\phi_M-\phi_{M0})] \quad \text{Eq. 3.27}$$

Via the substitution of the global porosity ϕ with the one related to large diameter pores ϕ_M.

On the other hand (Romero 2013) reformulated Eq. 3.24 by introducing the macro-void ratio e_M:

$$K_w = A\frac{{e_M}^B}{(1-e_M)} \quad \text{Eq. 3.28}$$

With *A* and *B* model parameters.

Similarly (Dieudonné 2016) modelled the water permeability evolution considering an Extended Kozeny-Carman model (Eq. 3.29) similar to (Romero 2013), in which the total porosity is substituted by the macro-void ratio e_M. In this way, the experimentally observed evolution of the larger pores will induce a reduction of the permeability.

$$K_w = K_{w0}\frac{(1-e_{M0})^m}{{e_{M0}}^n}\frac{e_M^n}{(1-e_M)^m} \quad \text{Eq. 3.29}$$

Also in this case, K_{w0} is a reference permeability related to a given macro-structural void ratio e_{M0}. The first member of the equation can be also indicated as C_{k0} accordingly to:

$$C_{k0} = K_{w0} \frac{(1 - e_{M0})^m}{{e_{M0}}^n} \qquad \text{Eq. 3.30}$$

However, it is important to underline that such permeability models are formulated for laminar flow regimes generally occurring in limited diameter tubes. Hence, it may happen that for the water flow taking place in large diameter structure such as the one of pellet mixture, further complexity needs to be considered. (Navarro et al. 2020) is pioneering such development accounting for a further porosity level (corresponding to the inter-pellets largest diameter structures) subjected to evolving hydraulic boundary conditions.

Yet, in this study, it will be demonstrated that the formulation proposed in Eq. 3.29 and implemented in LAGAMINE, provides remarkably good results for a wide range of multi-porosity distributions spanning from compacted blocks to pellet mixtures of various dimension.

Relative permeability

In order to consider the influence of partial saturation in water transfer mechanisms, water permeability can be expressed as follows:

$$k_w = K_w k_{rw}(S_r) \qquad \text{Eq. 3.31}$$

The water permeability k_w is given as function of saturated permeability K_w and relative permeability k_{rw} that is function of the saturation degree.

Several models have been proposed, among those the classic Van Genutchen relative permeability model (van Genuchten 1980) has been often selected to simulate the effect of partial saturation on the water transfer mechanisms occurring in clays during excavation (Pardoen 2015):

$$k_r = \sqrt{S_r}\left[1 - \left(1 - S_r^{\frac{1}{\gamma}}\right)^{\gamma}\right]^2 \qquad \text{Eq. 3.32}$$

Where γ is a model parameter.

Alternatively (Collin 2003) considers the semi-empirical relation of (Brooks and Corey 1964) for unsaturated soils such as bentonite, which is written:

$$k_r = S_e^{\frac{2+3\lambda_{BC}}{\lambda_{BC}}} \qquad if\ s > s_c \qquad \text{Eq. 3.33}$$

And:

$$k_r = 1 \qquad for\ s < s_c \qquad \text{Eq. 3.34}$$

Namely accounting for effective saturation S_e and λ_{BC} and s_c as model parameters.

However, it is decided to adopt a relative permeability power law evolution in this analysis (Eq. 3.35), which reads:

$$k_r = S_r^{\gamma} \qquad \text{Eq. 3.35}$$

Fig. 3.23 shows the influence of the model parameter γ on the relative permeability. Note that the parameter calibration is performed on experimental results presented in Chapter 5.

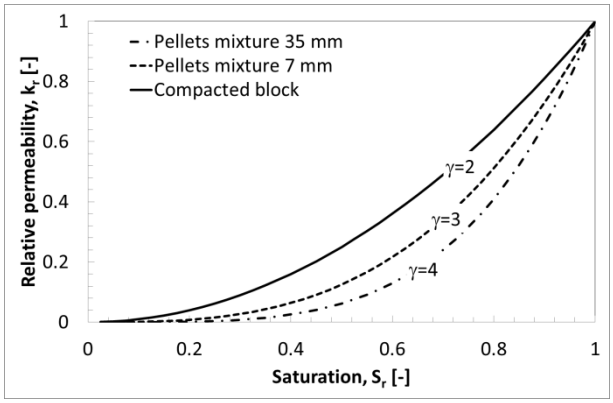

Fig. 3.23: Relative permeability evolution accordingly to Eq. 3.35 for several values of γ.

3.5.Conclusions

The goal of this chapter was to give an overview on the most meaningful hydraulic properties of bentonite-based materials. Water retention behaviour and water transfer response were identified as crucial subjects to evaluate bentonite suitability as one of engineering barrier components in the context of nuclear waste disposals.

Experimental results on water storage and transport mechanisms were investigated at the light of bentonite multi-porosity structures described in Chapter 2.

The impact of bentonite structure (i.e. dry density and multi-level porosities distribution) on its hydraulic properties was highlighted. Furthermore, coupling with the interacting fluid (liquid water in this case) resulting into changes in both the bentonite and the water characteristics was demonstrated.

In particular, with regards to the unsaturated state that characterises bentonite employment in the context of nuclear waste disposals, the very limited experimental characterisation on bentonite unsaturated permeability was shown. The need of more extensive experimental observations was underlined especially with respect to the use of bentonite assemblies presenting strongly evolving structure upon hydration (such as pellet mixtures).

The double porosity dry density dependent water retention and permeability evolution constitutive models used in this study were finally presented. Those strategies carefully consider the majority of the provided experimental results.

The hydraulic constitutive models proposed by (Dieudonné 2016) into account the microstructural evolution of bentonite during hydration. The validation of its parameters can be found in (Dieudonné, Della Vecchia, and Charlier 2017) and will be adopted in the following numerical analyses.

These models are especially resilient and suitable for large scale structural assessments and designs, as shown in the numerical investigations that follow.

CHAPTER 4: ON THE MECHANICAL BEHAVIOUR OF UNSATURATED SWELLING CLAYS

CHAPTER 4: ON THE MECHANICAL BEHAVIOUR OF UNSATURATED SWELLING CLAYS

4.1. Introduction

This chapter is devoted to the experimental and numerical characterisation of the compressibility, swelling capabilities and deviatoric responses of bentonite-based materials. The outline of this chapter is as follows: first, the experimental observations for unsaturated swelling clays are presented. Relatively simple stress paths are analysed. Significant experimental observations on the most important bentonite-based materials features are presented and compared. Advantages and limitations of the presented experimental tests are given. Some of the presented experimental results have been obtained during a 3 months' stage in CEA.

The chapter is continued by presenting a number of existing mechanical constitutive models, especially employed in the BEACON project. Among those, elasto-plastic models such as BBM, ACMEG and BExM are briefly described and compared.

Successively, the Barcelona Basic Model (BBM) that is the mechanic constitutive model adopted and implemented in LAGAMINE is introduced. This model will be used for all the numerical analyses of this thesis. The model is presented with increasing complexity, underlining its capability to reproduce a broad number of experimental observations. BBM parameters for different bentonites are calibrated, compared and discussed. Finally an alternative strategy is proposed to overcome some BBM limitations and compared to other recent strategies.

4.2. Experimental observations

Different hydro-mechanical stress paths can be applied to bentonite shafts and plugs used as underground nuclear waste disposals sealing structures. The bentonite material will be positioned in an unsaturated state in order to develop its swelling capabilities upon hydration. In most concepts, the host-rock formation would result in the major water source allowing bentonite swelling deformation and, successively, swelling pressures development, caused by the establishment of isochoric hydration conditions. Consequentially, it is necessary to envisage that an excessive host-rock deformation would cause bentonite buffer compaction. Hence, in order to assess the safeness of the sealing structure, compressibility properties have to be also investigated.

Thus, laboratory tests along simple stress paths can be conducted to obtain a thorough understanding of the mechanical behaviour of saturated and partially saturated bentonites. These stress paths are in general represented in the space in which specific features can be determined. For example, those can be mean (or vertical) net stress and void ratio (or deformation) to determine compressibility indices and yield loci, suction (or relative humidity) and void ratio (or deformation) to define swelling capabilities upon hydration, but also, deviatoric responses can be determined by the analysis of relatively simple tests.

This section summarizes the most important experimental evidences on the mechanical behaviour of saturated and unsaturated bentonites (which will be also recalled in the model validation paragraph). Although the information on the behaviour of unsaturated soils is quite exhaustive, there is a scarcity of experimental data on bentonites. This lack of information is most likely related to the complexity and time required to perform laboratory tests, which are often affected by several uncertainties. This section aims to underline the most relevant and well-recognised bentonite features in order to better underline the capabilities of the following mechanical models, hence, it is deliberately brief, also due to the fact that numerous comprehensive syntheses already exist.

In this section some relevant features of MX80 and Febex bentonites will be presented, being the bentonite types deeply analysed in the following chapters. Nevertheless, hints are also given with respect to MX80 and sand mixture, which was adopted in the framework of a collaboration with ANDRA and in (Dieudonné 2016) developments.

4.2.1. Mechanic loading under constant suction

Laboratory oedometer tests considering saturated soil samples are commonly used to assess one-dimensional volumetric behaviour of geomaterials. However, bentonite-based materials are generally emplaced in their unsaturated state. Thus, the void ratio (or axial strain) evolution upon vertical loading should be investigated at different water contents (i.e. suction levels) and not only at full-saturation. Furthermore, oedometer tests do not provide details on radial stress evolution during compaction, but due to their simplicity, they are often favoured over triaxial experiments (Gens and Alonso 1992).

Oedometer test experimental results performed by (Wang, Tang, et al. 2013) on MX80 bentonite and sand mixture are presented in Fig. 4.1. The soil sample consists in MX80 bentonite and sand mixture with respective proportion of 70/30 and initial dry density equal to ρ_d=1.67 Mg/m^3. The sample undergoes mechanical loading up to 50 MPa of vertical net stress at constant suction s=38 MPa. The material exhibits a gradual decrease in volume upon loading, with a quasi-bilinear response in the (ln σ_v - e) plane. The formation of irreversible plastic strains, i.e. yielding, is correlated with a shift in slope around a vertical stress of 6 MPa. This stress threshold is called apparent preconsolidation stress (abbreviated as p_0). Beyond the preconsolidation stress, the loading curve corresponds to a virgin (or normal) compression line with slope

equal to λ (plastic compressibility coefficient for change in net stress). Upon mechanic unloading, the sample exhibits swelling with a generally linear response quite parallel to the one of the elastic loading, whose slope is defined by the elastic compressibility coefficient for change in net stress κ. Irreversible (plastic) deformation is developed during this test and it is underlined in Fig. 4.1.

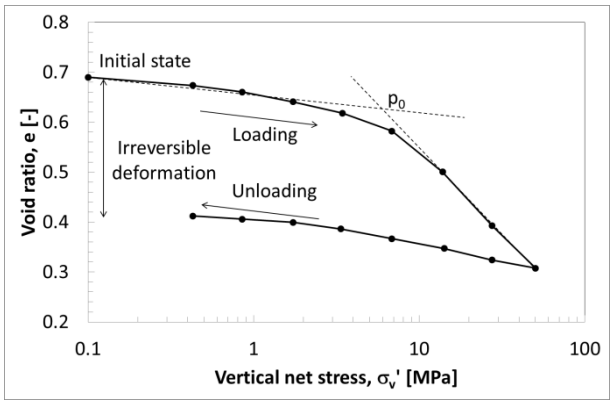

Fig. 4.1: Controlled-suction oedometer test (s = 38 MPa) on a mixture of MX-80 bentonite and sand compacted at a dry density ρ_d = 1.67 Mg/m^3 (Wang, Tang, et al. 2013)

Oedometer compaction tests at different suction (i.e. water content) levels are performed in order to evaluate the influence of the hydraulic state on the mechanic parameters. Swelling-consolidation tests are conducted for this purpose. Fig. 4.2 presents the oedometer compression curves obtained by (Lloret et al. 2003) for Febex bentonite compacted at initial dry density equal to ρ_d=1.70 Mg/m^3. It is possible to observe that the apparent preconsolidation stress p_0 (marked by arrows in Fig. 4.2) decreases with decreasing suction (Fig. 4.3). At the same time, the slope of the virgin compression line λ decreases with increasing suction, namely the material becomes stiffer when dried.

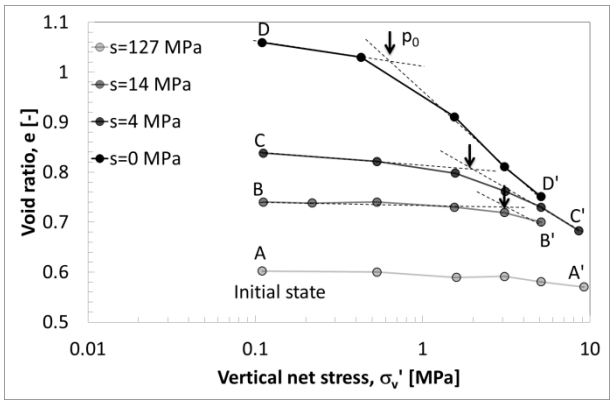

Fig. 4.2: Void ratio evolution as function of vertical net stress during controlled-suction oedometer tests on Febex bentonite compacted at an initial dry density ρ_d=1.70 Mg/m^3 (Lloret et al. 2003).

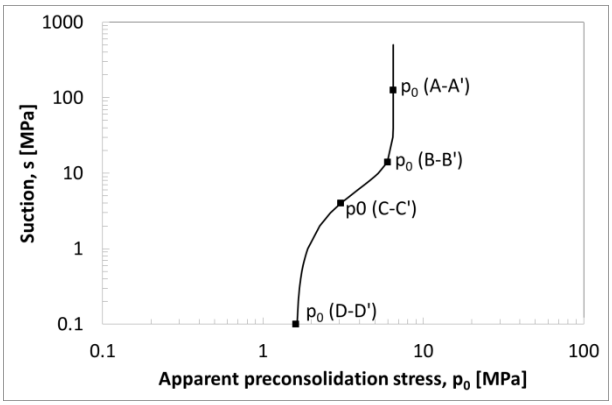

Fig. 4.3: Preconsolidation stress evolution with suction obtained via controlled-suction oedometer tests on Febex bentonite compacted at an initial dry density ρ_d=1.70 Mg/m^3 (Lloret et al. 2003).

Preconsolidation pressure and compressibility plastic coefficient for change in net stress are consequentially mostly considered monotonically increasing with increasing suction. However, this trend is not always observed. (Wang, Tang, et al. 2013) and (Marcial 2003) highlight the opposite tendency for MX80 and sand mixture and pure MX80 respectively (Fig. 4.4). It can be easily observed that the materials compressibility initially decreases for decreasing suction level and increases again up to saturation. In Fig. 4.4, the void ratio evolution is also reported. It can be observed that for high suction level, low void ratio increase is obtained, whereas the largest part of the deformation is experienced at low suction. It is possible to see that the compression coefficient clearly increases when the largest void ratio increase takes place (at s<12 MPa for MX80/sand mixture and s<26 MPa for pure MX80 bentonite). On the other hand, Fig. 4.5 shows the void ratio evolution upon mechanical loading for granular MX80 bentonite (Baryla et al. 2018). The compaction

tests follow different stress paths. Namely compaction after swelling at constant vertical stress and compaction after wetting at constant volume are reported, both paths are conducted until full saturation. For the compaction after swelling at constant vertical stress, the slope of the virgin consolidation line is not constant. The slope of the virgin line evolves from $\lambda(0)$=0.600 (high compressibility) to $\lambda(0)$=0.200 (low compressibility, high stiffness), corresponding to the compressibility coefficient evaluated for the compaction after wetting in isochoric conditions. These experimental evidences allow suspecting that for low saturation levels the compressibility is controlled by suction, whereas for high saturation, the compressibility depends on the material void ratio (i.e. dry density). It is necessary to remind that the multi-structural levels (see Chapter 2) of bentonite-based materials evolve upon hydration with dry density and followed stress paths. Thus, they could also be responsible for the observed macroscopic compressibility features.

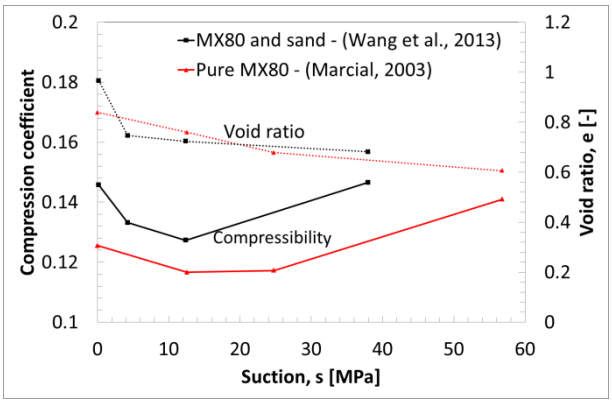

Fig. 4.4: Void ratio and compression coefficient evolution with suction for MX80 and sand mixture (Wang, Tang, et al. 2013) and pure MX80 bentonite (Marcial 2003)

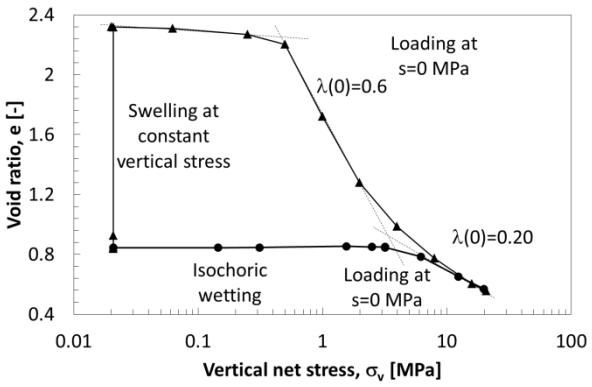

Fig. 4.5: Void ratio evolution as function of vertical net stress for MX80 granular bentonite (Baryla et al. 2018). Compaction after wetting at constant vertical stress and wetting at constant volume.

4.2.2. Hydraulic loading under constant stress

Volume increase upon wetting from unsaturated state is one of the most relevant properties of bentonite based materials in the context of nuclear waste disposals. Fig. 4.6 shows the void ratio evolution of three bentonite samples subjected to suction decrease (i.e. wetting) at constant stress of 0.1 MPa. The bentonite based materials analysed in the follows are pure MX80 compacted at initial dry density ρ_d=1.79 Mg/m^3 (Tang, Cui, and Barnel 2008) and MX80 and sand mixture in 70/30 respective proportion compacted at ρ_d=2.04 Mg/m^3 (Gatabin et al. 2016) (bentonite density equal to ρ_d=1.79 Mg/m^3) and ρ_d=1.67 Mg/m^3 (Wang, Tang, et al. 2013) (bentonite density equal to ρ_d=1.39 Mg/m^3). It is easy to distinguish a linear response in the semi-logarithmic plane suction versus void ratio ($ln\ s - e$). It may be relevant to underline that the higher the bentonite dry density, the higher the volume increase rate with suction, regardless the initial dry density of the overall mixture (i.e. sand percentage). In general, the slope of the reversible wetting-drying line is denoted κ_s and it is function of the bentonite component initial dry density.

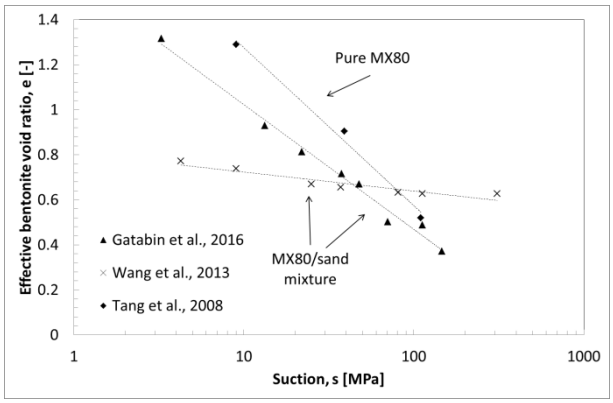

Fig. 4.6: Bentonite void ratio evolution with suction for MX80 and sand mixture (Gatabin et al. 2016; Wang, Tang, et al. 2013) and pure MX80 bentonite (Tang, Cui, and Barnel 2008)

(Lloret, Romero, and Villar 2004) investigated the swelling capabilities of Febex bentonite compacted at several initial dry densities for different vertical net stress. The samples were firstly compacted with their hygroscopic water content and then wetted. Fig. 4.7 shows that for increasing dry density increasing swelling deformation is obtained. For increasing vertical net stress, smaller volume increase is observed with also volume decrease (collapse) for high stress level inversely correlated with dry density, underlining a certain dependency of the bentonite swelling potential on the applied stress level. The structural levels evolutions and interaction during saturation account for this phenomenon. Several authors (Marcial 2003; Imbert and Villar 2006; Lloret et al. 2003) consider that volume decrease takes place when the micro-pores (i.e. particles) swelling potential is not sufficient to compensate for macro-pores collapse deformation upon hydration.

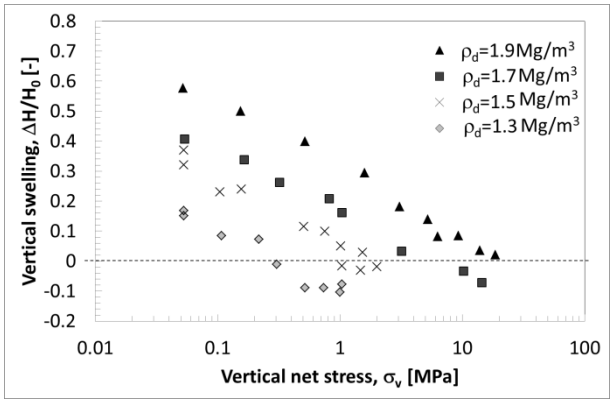

Fig. 4.7: Final swelling deformation obtained during wetting at different constant vertical stresses for Febex bentonite compacted at several initial dry densities (Lloret, Romero, and Villar 2004).

4.2.3. Hydraulic loading under constant volume

After the filling of the in-situ underground galleries' technological gaps, the bentonite-based materials plugs would establish full contact with the surrounding host-rock. The geological formation, which is the main water source in most repository designs, would prevent the volume increase of the bentonite material, resulting in the development of confined bentonite swelling pressure. This occurrence reflects two major sealing properties of bentonite structures for nuclear waste engineering barriers: first, potential radionuclide leakage pathways between the bentonite structures and the host-rock interfaces are closed. Secondly, the swelling pressure exerted by the bentonite on the host-rock would minimize the gallery convergence and likely close rock fractures caused by excavation. On the other hand, excessive swelling pressure would enhance host-rock damage. Thus, it is central to precisely determine the magnitude of bentonite swelling pressure development upon hydration in constant volume conditions. This is generally obtained performing simple laboratory tests taking advantage of constant volume oedometric cells. The sample hydration is

applied via water saturation (most common) or controlling relative humidity (suction) via salts solutions. The resulting swelling pressure is generally measured via axial force transducers.

Using a large number of experimental campaigns results (Bernachy-Barbe et al. 2020; Börgesson, Karnland, and Johannesson 1996; Dueck and Nilsson 2010; Gatabin et al. 2016; Karnland et al. 2008; Komine, Yasuhara, and Murakami 2009; Lloret et al. 2003; Villar, Gómez-Espina, and Gutiérrez-Nebot 2012; Wang, Tang, et al. 2013), A semi-log linear relation between bentonite dry density and swelling pressure can be evidenced (Fig. 4.8), regardless the macro-structure size and position inside the assembly (i.e. pellets mixture or compacted bentonite forms) or the initial water content of the sample (Hoffmann, Alonso, and Romero 2007).

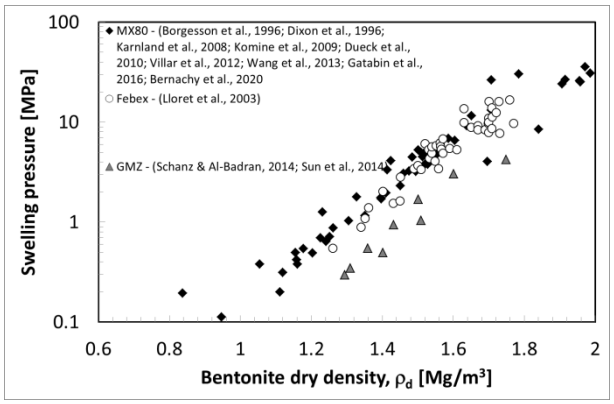

Fig. 4.8: Evolution of the swelling pressure of three reference bentonites with dry density. Synthesis of 10 papers results.

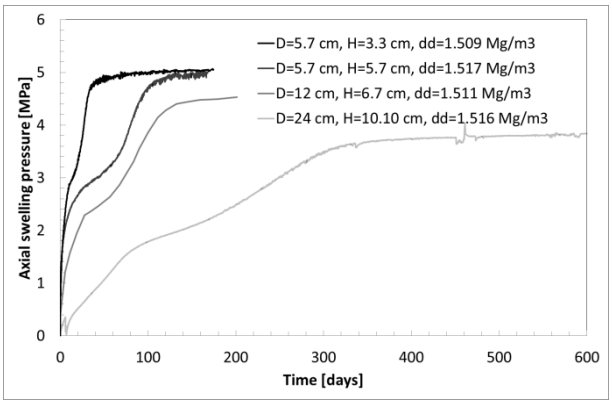

Fig. 4.9: Decreasing trend in swelling pressure curves for four sample geometries (tested at approximately 1.51 g/cm3 dry density: the legend indicates cell diameter (D), sample height (H) and final dry density (dd) (Bernachy-Barbe et al. 2020).

However, as it is possible to observe in Fig. 4.8, experimental measurements are affected by a relevant dispersion, which can span up to the 200% of discrepancy. Apart from laboratory uncertainties, possible causes are likely linked to the diameter/height ratio of the testing cells (Bernachy-Barbe et al. 2020; Imbert and Villar 2006).

Swelling pressure time evolution on MX80 35 mm-pellets/powder mixture at initial dry density equal to ρ_d=1.50 Mg/m^3 are tested by (Bernachy-Barbe et al. 2020) (Fig. 4.9) for different diameter/height samples ratios. A decreasing trend is recorded for the different samples geometries. Together with the geometric sample properties, the development of friction at the interface between the material and the cell wall may also account for the data scattering (Molinero et al. 2019; Saba et al. 2014). Friction influence on swelling pressure measurements will be extensively investigated in the following.

Swelling pressure evolution upon hydration is also relevant given the important time for in-situ bentonite plug saturation. (Imbert and Villar 2006) determined the development of three distinct phases in which it is possible to see a first quick swelling pressure increase, a second phase with a slower increase or decrease and a last increase with respect to FoCa bentonite granular mixture prepared at different dry densities (i.e. 1.30, 1.40 and 1.60 Mg/m^3). It could be observed that the higher dry density, the higher swelling pressure drop and final swelling pressure values are obtained. (Lloret et al. 2003) found similar stress paths analysing the behaviour of compacted Febex bentonite subjected to constant volume hydration (Fig. 4.10). The author relates the first swelling pressure increase corresponding to the stage of high suction level and elastic state. The stress path can be assumed to be determined by the increase in load needed to compensate for the small swelling strains caused by suction reduction. The stress paths encounter a drastic change of slope in the second phase after reaching the preconsolidation pressure (yield locus). According to (Lloret et al. 2003), the micro-structure may present sufficiently high load to cause the macro-structure to collapse, with the subsequent vertical stress decrease due to compensation for the collapse compressive strains. The

microstructural swelling strains contribute to the compensation for collapse deformation, and if it is large enough it can compensate the swelling pressure decrease. The third phase corresponds to the region of low suction and high saturation. In this range, the microstructural swelling strains exhibit their largest magnitude (Wang, Cui, et al. 2013) and overcome any possible collapse strains. The stress increases again to compensate for the large swelling strains. These experimental evidences highlight that the micro-macro structures evolutions depend obviously on the material dry density. However, as this thesis aims to underline and especially reproduce, not only the initial dry density accounts for this pattern but also the initial macro-micro porosities distributions (i.e. pellets mixtures or compacted bentonite forms, see Chapter 2). Fig. 4.11 presents the stress paths in the (p – s) plane of two identical geometry MX80 bentonite samples of initial dry density equal to ρ_d=1.50 Mg/m^3 presenting different initial macro-micro structures distributions (namely pellets and compacted blocks samples). Although toward low suction levels the two stress paths seem to correspond, at the beginning of the hydration, the swelling pressure concerning the compacted block sample develops very quickly at almost constant suction and undergoes suction decrease at constant stress, differently from the pellets mixture one, which experiences bi-univocal suction decrease-swelling pressure increase. Chapter 5 evidences that macro pores structures affect water transport mechanism and mechanic phenomena only at the beginning. After reorganisation they behave similarly.

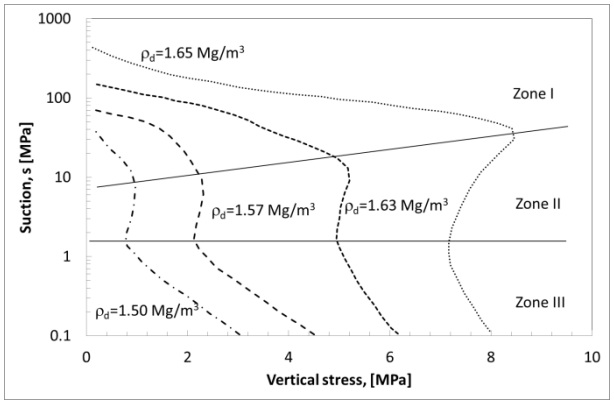

Fig. 4.10: Evolution of the swelling pressure in tests performed with compacted Febex bentonite at different dry density (Lloret et al. 2003).

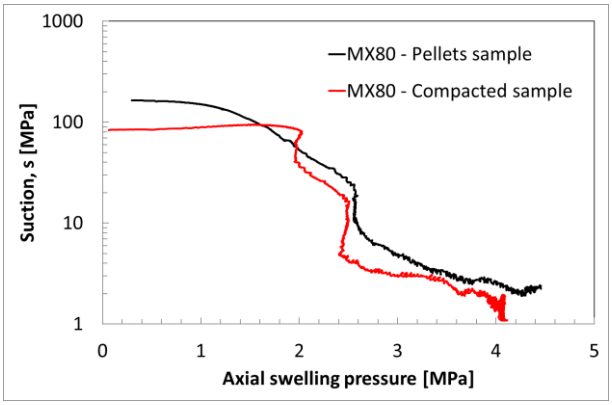

Fig. 4.11: Stress path in the (p – s) of MX80 pellets mixture and compacted samples at dry density ρd=1.50 Mg/m^3 (Gramegna et al., 2020).

4.2.4. Shear properties

Triaxial and direct shear tests are adopted for the determination of soils cohesion and friction angle. However, shear properties characterisation on unsaturated bentonites has been poorly performed during years. Thus, very few experimental data are available. Nevertheless, it is generally accepted that apparent shear strength increases with increasing suction. This assumption follows experimental observations obtained for other soils type (Blight 1966; Cui 1993; Escario and Sáez 1986). In particular, with respect to cohesion, (Romero 2012) tested Kunigel V1 bentonite in triaxial apparatus evidencing a linear dependency between suction and apparent cohesion *c(s)* via:

$$c(s) = c(0) + ks \qquad \text{Eq. 4.1}$$

Where *c(0)* is the cohesion in saturated conditions, *k* a constant value and *s* the suction. Such experimental evidence confirmed indeed (Fredlund, Morgenstern, and Widger 1978) postulation on the shear strength behaviour of unsaturated soils.

With respect to friction, the very few available experimental observations are contradictory into considering the friction angle constant or evolving. Studies have been done on MX80 bentonite by (Börgesson, Broc, and Plas 1990), which evidenced a decreasing friction angle tendency with increasing dry density (namely *c(0)*=50 - 150 kPa and φ=5 - 10° for high dry density). Recent experimental tests were performed by EPFL team in the framework of BEACON project on different MX80 granulations. Friction angle values between φ=22 and 38° were determined together with decreasing cohesion with increasing water content for dry density approximately equal to ρ_d=1.5 Mg/m^3.

4.2.5. Additional properties determination

In the framework of the European project BEACON, the teams involved in the numerical modelling of experimental tests (as the ULG team) often highlighted the difficulty to find in scientific literature parameters such as Poisson ratio or/and cohesion for example. Back analyses and strategies choices provided by the different teams often resulted in heterogeneous values selection. These parameters are very difficult to determine during classical experimental tests on bentonite, but, nevertheless, are essential for the reproduction of several physical phenomena. Hence, the ULG team took advantage of a collaboration with CEA LECBA laboratory (involved in the experimental part of BEACON) to design simple but robust uniaxial compression tests. The practical know-how and utilities of CEA together with the theoretical and analytical capabilities of ULG resulted in the production of the following analysis, thanks to a 3 months visit of the thesis author in CEA LECBA (autumn 2019) and a number of meetings.

The uniaxial compression test is a laboratory test generally used to determine the maximum axial compressive stress (UCS) that a rock specimen can bear under zero confining stress. UCS parameter is widely used in rock geomechanics. However, in the context of unsaturated soils, attention is especially given to the axial load and axial and lateral deformations, which are commonly measured to derive the material's elastic modulus and Poisson's ratio (ASTM 2004) and to evaluate the UCS, which allows an estimation of the cohesion.

In the framework of ULG-CEA partnership, a number of uniaxial compression tests have been performed on bentonite samples. The apparatus used to perform the uniaxial compression test consists in a loading device (which can be stress or strain controlled), the steel plates, used to transfer the axial force from the loading device to the material sample, and strain measurements devices. The axial strain measurements consisted of a LVDT integrated in the press, whereas the radial deformation measurements were obtained thanks to high speed camera and post-processed image analyses (Fig. 4.12).

Fig. 4.12: Uniaxial compression device employed in LECBA (CEA) during the partnership ULG-CEA.

Fig. 4.13 and Fig. 4.14 show the typical results of uniaxial compression tests. Axial Young's modulus, E (defined as the ratio of the axial stress change to axial strain produced by the stress change) of the specimen may be evaluated using any one of several methods employed in accepted engineering practice (ISRM 1977). Among others, in this campaign, average Young's modulus is determined on linear elastic paths between 0 and 2.5 MPa axial stress from the average slopes of the more-or-less straight line portion of the axial stress-axial strain curve (Fig. 4.13). Poisson's ratio, ν, may be calculated from the ratio between the Young's modulus E and the slope of the more-or-less straight line portion of the radial strain – axial stress curve, in the same Young's modulus computation procedure (Fig. 4.14).

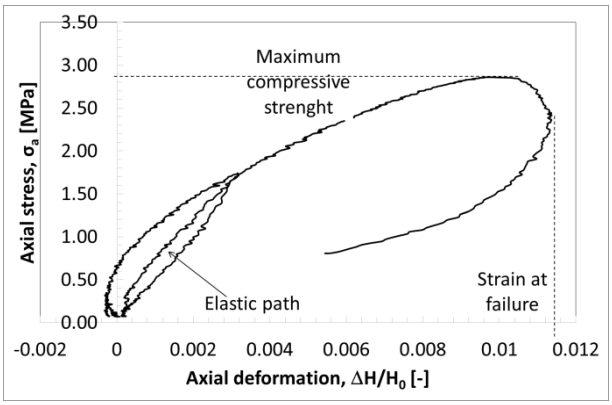

Fig. 4.13: Axial stress-axial strain curve for a MX80 bentonite specimen.

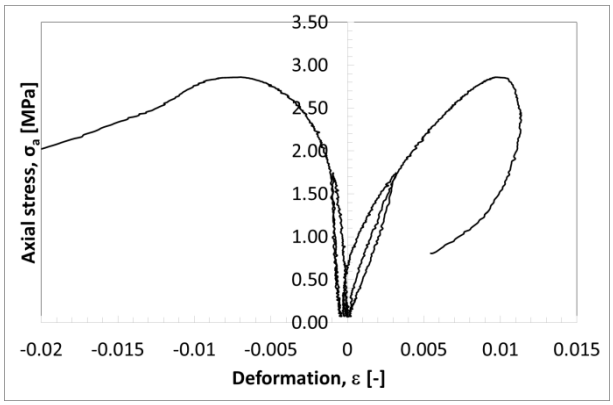

Fig. 4.14: Axial stress-axial strain and axial stress-radial strain curves for a MX80 bentonite specimen

The presented experimental campaign considers MX80 samples isotropically compacted at dry density between ρ_d=1.73÷1.85 Mg/m^3 and water content w=11.34% and 13.54%. After compaction, the samples were machined presenting diameter between 6 and 7 cm and sample height between 12 and 14 cm. Axial compression stress and deformation are presented in Fig. 4.15. Elastic paths, on which Young's modulus E and Poisson ratio ν are determined, are given in Fig. 4.16.

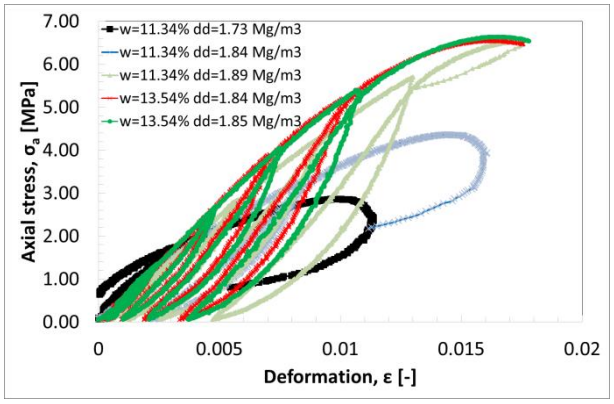

Fig. 4.15: Axial stress-axial strain curve for five MX80 bentonite specimen compacted at different water content and dry density.

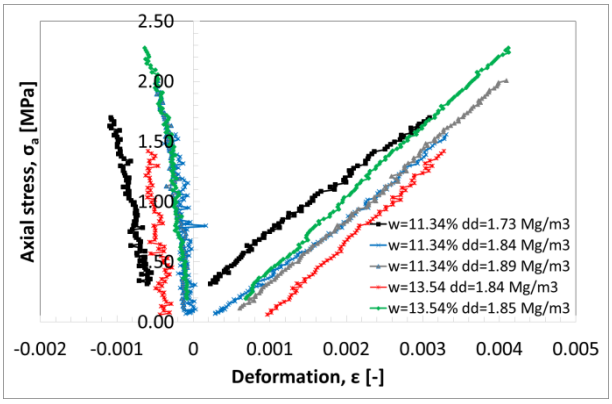

Fig. 4.16: Vertical axial pressure as function of axial and radial deformation.

ULG-CEA calculated Young's moduli present an increasing tendency with increasing dry density and water content (Fig. 4.17), with values ranging between 450 and 600 MPa. The obtained Young's moduli are compared to literature data (Dueck and Nilsson 2010; Kiviranta et al. 2018) (Fig. 4.17). Kiviranta and Dueck performed uniaxial compression tests on MX80 bentonite samples presenting dry density between ρ_d=1.6÷1.75 Mg/m^3 and respective water content w ~17% and w ~21%, on samples with diameter equal to D=2.5 cm and height H=5 cm. The Young's moduli trend remains increasing with dry density but for lower water contents, higher values are obtained. However, it is worth mentioning that the obtained Young's moduli are influenced by how and in which intervals they are evaluated and that a more general formulation

of the evaluation could be based on the inflection point of the obtained stress-strain curve (Kiviranta et al. 2018).

Fig. 4.18 shows the Poisson's ratio values obtained in the framework of ULG-CEA partnership. Higher Poisson's ratio values are in general obtained for the higher water content (i.e. w=13.54%). This observation was reported by (Som and Simons 1969) for London clay, which determined Poisson ratios in saturated (ν=0.40÷0.50) and unsaturated state (ν=0.10÷0.30). Decreasing rate for increasing dry density between ν=0.12÷0.17 is also observed.

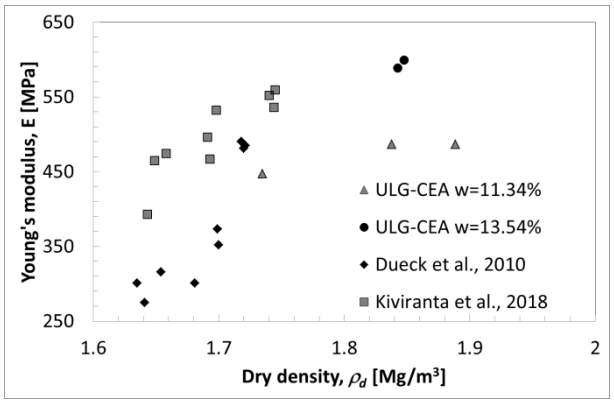

Fig. 4.17: Computed Young's modulus as dry density function. ULG-CEA experimental study compared to literature (Dueck and Nilsson 2010; Kiviranta et al. 2018).

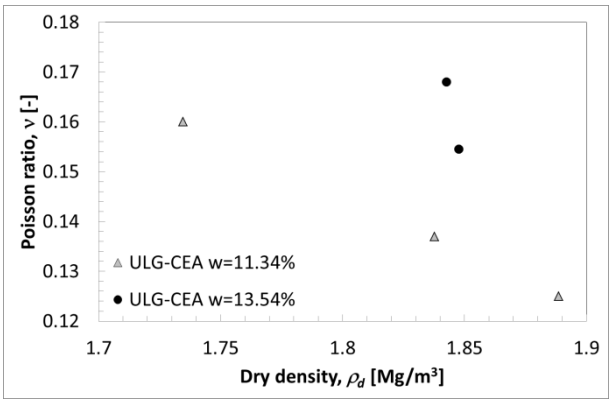

Fig. 4.18: Computed Poisson ratio as dry density function. ULG-CEA experimental study.

Uniaxial compression stress (UCS) is also compared. Fig. 4.19 shows the UCS as function of dry density. Increasing UCS tendency for increasing dry density is observed for each water content value. Fig. 4.19 is normalised in terms of saturation by considering constant water density equal to ρ_w=1 Mg/m^3 and solid density of MX80 equal to ρ_s=2.78 Mg/m^3 accordingly to Eq. 3.3of Chapter 3. Experimental outcomes underline a clear increase of UCS with saturation. Experimental data obtained by ULG-CEA and (Kiviranta et al. 2018) are noticeably aligned.

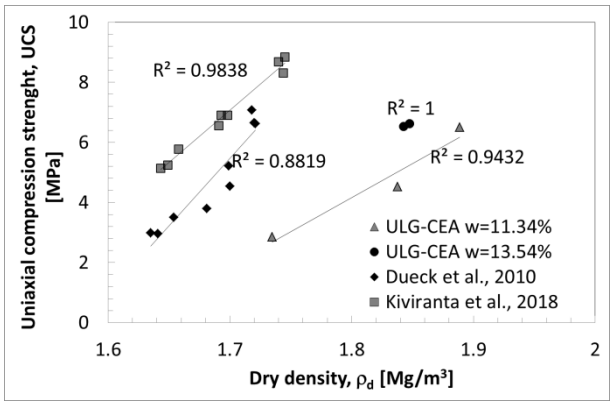

Fig. 4.19: Measured UCS as dry density function. ULG-CEA experimental study compared to literature (Dueck and Nilsson 2010; Kiviranta et al. 2018).

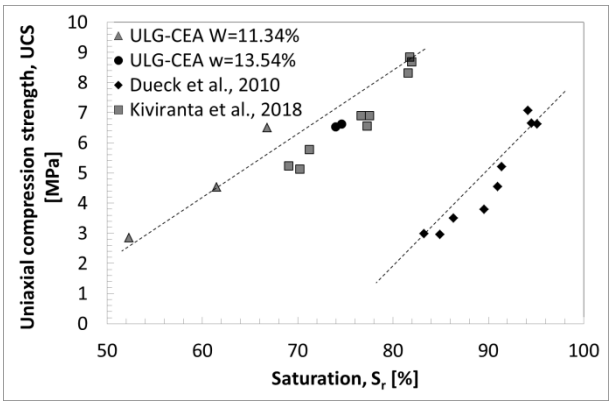

Fig. 4.20: Measured UCS as saturation function. ULG-CEA experimental study compared to literature (Dueck and Nilsson 2010; Kiviranta et al. 2018).

A Mohr-Coulomb criterion is selected in order to evaluate the cohesion from the UCS. The evaluation results are reported in Fig. 4.21 This analytical evaluation is performed by considering null and constant friction angle, thus the computed cohesion is the maximum, which can be obtained in a Mohr-Coulomb circle. Surprisingly, the cohesion increases with saturation (i.e. decreasing suction), contradicting the experimental observations presented in the previous paragraph. Possibly, dry density plays an important role with respect to cohesion estimation, together with friction angle precise definition. Hence, further experimental campaigns are needed.

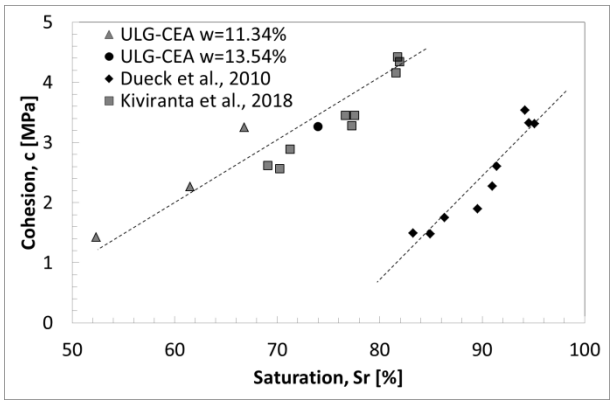

Fig. 4.21: Evaluated maximum cohesion as saturation function. ULG-CEA experimental study compared to literature (Dueck and Nilsson 2010; Kiviranta et al. 2018).

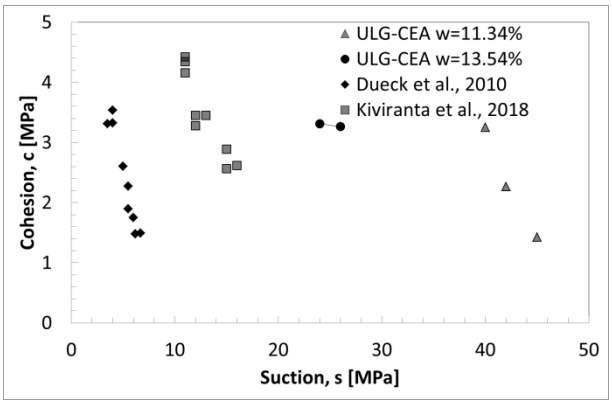

Fig. 4.22: Evaluated maximum cohesion as computed suction function. ULG-CEA experimental study compared to literature (Dueck and Nilsson 2010; Kiviranta et al. 2018).

Finally, it is necessary to highlight an important point: the nature of the analysed bentonite sample evolves with its dry density. Namely, the sample compactness (and consequentially the possibility to test it) is very poor for dry density lower than 1.65 Mg/m^3. For dry density lower than 1.65 Mg/m^3, bentonite samples easily crumble with the development of discontinuity regions, or, for even lower dry density values, those have the consistency of granular soils. Whereas, for dry density higher than 1.65 Mg/m^3, bentonite compacted samples resemble rock drilled cores (Fig. 4.23). Thus, the bentonite dry density range that can be tested via uniaxial compression experiments is quite limited.

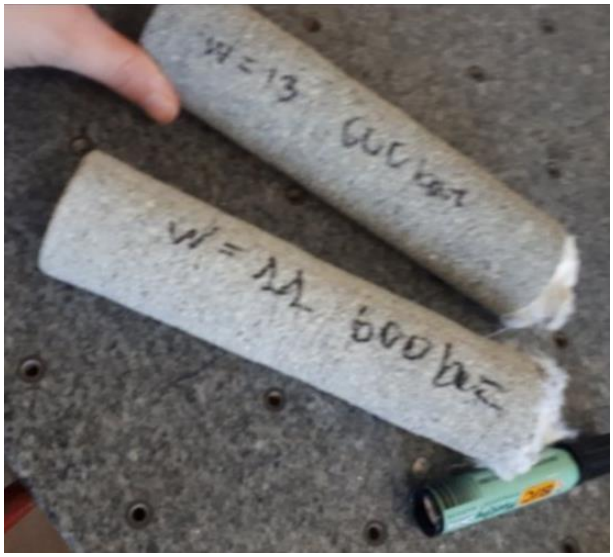

Fig. 4.23: MX80 compacted samples appearance for ρ_d>1.65 Mg/m^3. ULG-CEA experimental study.

4.3. Existing modelling frameworks

In the framework of European project BEACON, numerous university and institutions propose different mechanical models, which will be employed for the safeness assessment and behaviour prediction of nuclear waste disposals bentonite sealing structures. Some of them are listed in the following:

- BGR (Bundesanstalt für Geowissenschaften und Rohstoffe, DE) linear elastic model formulated in terms of effective stress. BGR focuses on the description of the coupled THM formulation implemented in Open Geo Sys (OSG) code.

- The CU (Charles University, CZ) model is a double structure formulation developed within the framework of hypoplasticity. The complete development of this model can be found in (Mašín 2005, 2017).

  Clay Technology (Clay Tech, SE) is developing a model that accounts for clay potential (Dueck et al. 2019). The model developed is called the Hysteresis Based Material (HBM) model and, at the present state, it is applicable to the saturated state only.

- The Imperial College (EN) – Double Structure model (IC DSM) is a development of an existing and tried IC SSM (Imperial College Single Structure Model). They are defined in the framework of elasto-plasticity similarly to BExM and BBM (Ghiadistri et al. 2019; Potts and Zdravkovic 1999).

- The model developed by Quintessa (EN) is called the Internal Limit Model (ILM). It alludes to a rather different process of constitutive model formulation based on an interesting empirical observation (Thatcher 2017).

As it could have been noticed, there are several methodologies and complexity levels for describing unsaturated swelling clays mechanic behaviour. However, within these models, attention is paid to the elasto-plasticity framework, which allows associating a number of simple features with a strong consistency. Hence, this section is devoted to the brief description of elasto-plasticity models such as BBM, ACMEG-T and BExM summarised and compared in the hypothesis of isotropic conditions. Emphasis is put on the following characteristics:

- number of structural levels considered in the mechanic, hydraulic or hydro-mechanical coupled behaviours (single or multi-porosity theories);

- dry density dependent bentonite features (i.e. mechanic and/or hydraulic properties);

- the adopted stress formulation (i.e. one variable or two independent variables formulations).

With respect to this last point, further specifications are required. (Nuth and Laloui 2008) provide a detailed framework with respect to stress definition. In the following, net stress (BBM and BExM, macro-void) and effective stress (EPFL and BExM micro-void ratio) are mentioned.

One variable formulation approach extends for instance the definition of Terzaghi's effective stress to the partial saturation domains. One relevant definition is proposed by (Bishop 1959):

$$\boldsymbol{\sigma}' = (\boldsymbol{\sigma_t} - u_g\boldsymbol{I}) + \chi(u_g - u_w)\boldsymbol{I} \qquad \text{Eq. 4.2}$$

In which $\boldsymbol{\sigma}_T$ is the total stress tensor, u_g is the gas pressure, u_w is the pore water pressure and $\boldsymbol{I}$ represent the identity tensor. χ is a material parameter that depends on the saturation degree. For full saturated state Sr=1 and $u_g=0$, so that the traditional Terzaghi's effective stress formulation is recovered. This stress definition

assures a smooth transition from the unsaturated to saturated state but its parameters calibration for unsaturated materials can become particularly complex.

On the other hand, numerous constitutive models take advantage of two independent state variables formulation, in particular net stress $\boldsymbol{\sigma}$ and suction s are often used to describe the unsaturated behaviour of soils. Net stress is therefore written as follows:

$$\boldsymbol{\sigma} = \boldsymbol{\sigma}_T - u_a \boldsymbol{I} \qquad \text{Eq. 4.3}$$

With $\boldsymbol{\sigma}_T$ representing the total stress tensor, u_a representing the air pressure for $s>0$, and $\boldsymbol{I}$ representing the identity tensor.

4.3.1. Barcelona Basic Model

The Barcelona Basic Model (BBM) (Alonso, Gens, and Josa 1990) will be exhaustively presented in the following but for sake of completeness it is briefly summarised. The BBM was developed in the framework of the elasto-plastic theory, being an extension of the Cam clay model to unsaturated conditions. Net stress $\boldsymbol{\sigma}$ (Eq. 4.3) and suction *s*[4] are used as stress variables in the model.

According to the BBM, the variation of volumetric elastic strain is related to changes in mean net stress *p* and suction *s* under isotropic stress conditions (Eq. 4.4).

$$d\varepsilon_v^e = \frac{de}{1+e} = \frac{\kappa}{1+e}\frac{dp}{p} + \frac{\kappa_s}{1+e}\frac{ds}{s+u_{atm}} \quad \text{Eq. 4.4}$$

With κ elastic compressibility coefficient for changes in mean net stress and κ_s elastic compressibility coefficient for changes in suction at null stress level. As it can be observed in Eq. 4.4, the model considers one single total structural level, identified by the total void ratio e.

The evolution of the preconsolidation pressure $p_0(s)$ is modelled using the principle of increasing elastic domain with increasing suction (Eq. 4.5) as well as the rate of increase of the soil stiffness with suction (Eq. 4.6).

$$p_0(s) = p_c\left(\frac{p_0^*}{p_c}\right)^{\frac{\lambda(0)-\kappa}{\lambda(s)-\kappa}} \quad \text{Eq. 4.5}$$

$$\lambda(s) = \lambda(0)[(1-r)\,exp(-\omega s) + r] \quad \text{Eq. 4.6}$$

with p_0^* preconsolidation pressure for saturated state, p_c reference pressure controlling the shape of the LC curve, $\lambda(0)$ slope of the saturated virgin consolidation line, r and ω parameters that respectively define the minimum soil compressibility and the soil stiffness.

4.3.2. EPFL effective stress model

The EPFL constitutive model (J. A. Bosch, Ferrari, and Laloui 2020; Jose A. Bosch, Ferrari, and Laloui 2021; Di Donna and Laloui 2015; Laloui and Cekerevac 2003; Laloui and François 2009) allows the analysis of thermo-hydro-mechanical processes in porous media. The model is formulated in the framework of elasto-plasticity and generalised effective stress $\boldsymbol{\sigma'}$ (single state variable) (Nuth and Laloui 2008), that is linked to the degree of saturation (Eq. 4.7),

$$\boldsymbol{\sigma'} = \boldsymbol{\sigma}_T - (u_a - sS_r)\boldsymbol{I} \quad \text{Eq. 4.7}$$

With $\boldsymbol{\sigma}_T$ representing the total stress tensor, u_a representing the air pressure for $s>0$, S_r the degree of saturation and $\boldsymbol{I}$ representing the identity tensor. Eq. 4.7 is a particular form of the expression suggested by (Bishop 1959).

According to this model, the variation of volumetric elastic strain is related to changes in mean effective stress *p'* under isotropic stress and isothermal conditions (Eq. 4.8):

$$d\varepsilon_v^e = \frac{de}{1+e} = \frac{dp'}{K} \quad \text{Eq. 4.8}$$

4 It is worth reminding that suction s can be defined as gas pressure in excess of the water pressure ($s=u_g-u_w$)

With K a material parameter defining the soil elastic compressibility. As it can be observed in Eq. 4.8, also the EPFL model considers one single total structural level, identified by the total void ratio e.

The evolution of the preconsolidation pressure $p_0(S_r)$ evolves with saturation similarly to (A. N. Zhou et al. 2012) (Eq. 4.9) as well as the rate of increase of the soil stiffness with decreasing saturation (Eq. 4.10).

$$p'_0(S_r) = p'_c \left(\frac{p'^*_0}{p'_c}\right)^{\frac{\lambda(1)-\kappa}{\lambda(S_r)-\kappa}} \quad \text{Eq. 4.9}$$

$$\lambda(S_r) = \lambda(1) - r'(\lambda(1)-\kappa)(1-S_r{}^{\zeta})^{\xi} \quad \text{Eq. 4.10}$$

with p_0^* preconsolidation pressure for saturated state at a given temperature, p_c reference pressure controlling the shape of the LC curve, $\lambda(1)$ slope of the saturated virgin consolidation line, where parameter $r'(0 < r' < 1)$ expresses the decrease of elastoplastic compressibility from saturated to dry state ($S_r = 0$); and ζ and ξ are material parameters.

4.3.3. Barcelona Expansive Model

The Barcelona Expansive Model (BExM) (Alonso, Vaunat, and Gens 1999) was developed in the framework of the elasto-plasticity considering specifically the double-structure unsaturated swelling clays nature accordingly to (Gens et al. 2011; Gens and Alonso 1992; Sanchez et al. 2005). The macrostructural volumetric elastic strain $d\varepsilon^e_{vM}$ is expressed as a function of mean net stress $\boldsymbol{\sigma}$ (Eq. 4.3) and suction s, similarly to Eq. 4.4:

$$d\varepsilon^e_{vM} = \frac{de_M}{1+e_M} = \frac{\kappa}{1+e_M}\frac{dp}{p} + \frac{\kappa_s}{1+e_M}\frac{ds}{s+u_{atm}} \quad \text{Eq. 4.11}$$

The evolution of the preconsolidation pressure $p_0(s)$ is modelled using the principle of increasing elastic domain with increasing suction (Eq. 4.5) as well as the rate of increase of the soil stiffness with suction (Eq. 4.6) exactly corresponding to the classic BBM.

In addition, the behaviour of the microstructure is formalised by means of an e$/\!/\!/$ective stress $\boldsymbol{\sigma'}$ concept (Eq. 4.7) generalised for unsaturated conditions. Thus, the microstructural volumetric strain $d\varepsilon^e_{vm}$ (Eq. 4.12) looks similar to Eq. 4.8:

$$d\varepsilon^e_{vm} = \frac{de_m}{1+e_m} = \frac{dp'}{K_m} \quad \text{Eq. 4.12}$$

With K_m elastic micro structure compressibility coefficient, which can be written as:

$$K_m = \frac{exp\,\{\alpha_m(p+s)]}{\beta_m} \quad \text{Eq. 4.13}$$

With α_m and β_m parameters controlling the microstructural Bulk Modulus.

The BExM considers the microstructure mainly saturated (i.e. Bishop coefficient equal to S_r=1), with elastic and volumetric behaviour, at hydraulic and mechanical equilibrium with macrostructure (i.e. the total stress $\boldsymbol{\sigma}_T$and the suction s exerted on the micro and macrostructures are the same) and mainly responsible for the development of macrostructure elastoplastic strain. This latter feature is formalized by the introduction of Eq. 4.14 and Eq. 4.15:

$$d\varepsilon^p_{vM} = f_D\, d\varepsilon^e_{vm} \quad \text{Eq. 4.14}$$

$$d\varepsilon_{vM}^{p} = f_I d\varepsilon_{vm}^{e} \quad \text{Eq. 4.15}$$

f_D and f_I are coupling function activated when respectively the suction increase or decrease mechanism is activated. Thus, the mechanical response of the expansive soils is accomplished by the consideration of several plastic mechanisms (Eq. 4.16) that can act jointly or not at different stages of the analysis depending on the direction of the stress/strain path (Fig. 4.24).

$$d\varepsilon = d\varepsilon^{e} + d\varepsilon_{M}^{p} + d\varepsilon_{m}^{p} \quad \text{Eq. 4.16}$$

where $d\varepsilon_{M}^{p}$ is the plastic strain induced by the macro-structural yielding and $d\varepsilon_{m}^{p}$ is the plastic strain induced by the micro-structural yielding, i.e. the interaction mechanism.

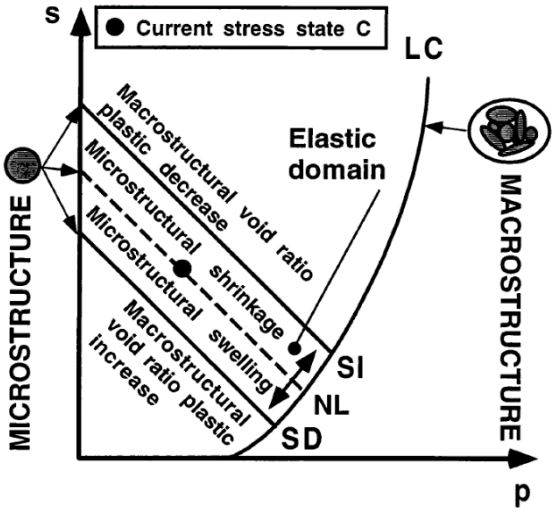

Fig. 4.24: BExM yield loci in p-s plane (Alonso, Vaunat, and Gens 1999).

4.3.4. Discussion

The presented mechanic constitutive models present a number of similarities and discrepancies, which are summarised in the following. First of all, the three models (BBM, EPFL model and BExM) are developed on the elasto-plasticity framework (an example of non elasto-plastic model is the hypoplastic double porosity model can be found in (Mašín 2005)). In addition, some of the most evident correspondences are related to the strongly hydro-mechanical coupling characterising the models. Namely, it is clear that the mechanic behaviour is controlled by suction and/or saturation (Eq. 4.4, Eq. 4.8, Eq. 4.11 and Eq. 4.12), together with the compressibility properties evolution (Eq. 4.6, Eq. 4.10 and Eq. 4.13) and the shape of the yielding surface (Eq. 4.6, Eq. 4.9 and Eq. 4.16). Apart from other dissimilarities, the adopted stress variable formulation represents one of the most relevant differences. BBM and BExM rely on net stress (Eq. 4.3) and suction s, whereas EPFL model adopts an effective stress formulation (Eq. 4.7). Differently from BBM and BExM, the EPFL model assures a smooth transition from the unsaturated to saturated state due to its effective stress formulation. On the other hand, it predicts an excessive stress collapse during wetting under isochoric conditions when the yield surface is reached (Fig. 4.25) (Talandier 2019). Moreover, between these three constitutive models, the BExM explicitly considers two interacting structural levels (micro and macro), differently from the BBM and EPFL model that account only for one (total void ratio). Nevertheless, in LAGAMINE, the BBM is accompanied by a double porosity dry density dependent hydraulic constitutive model (Dieudonné, Della Vecchia, and Charlier 2017), which permits to consider the micro-macro interacting structures (Chapter 3) and to model the important structural changes occurring during hydration.

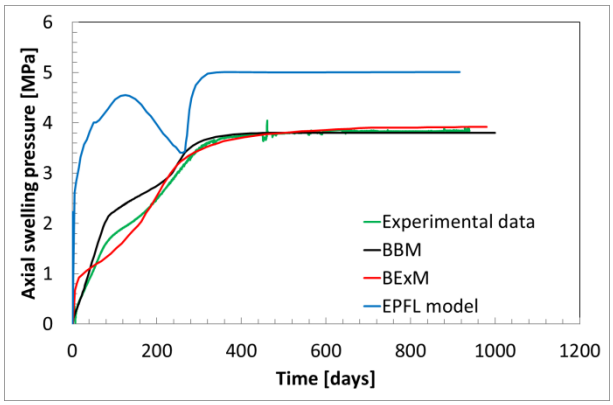

Fig. 4.25: Axial swelling pressure time evolution for isochoric wetting tests on MX80 pellets mixture (Bernachy-Barbe et al. 2020). Comparison between experimental and numerical results obtained via LAGAMINE BBM, BExM and EPFL model (Talandier 2019).

4.4. LAGAMINE mechanic constitutive modelling

4.4.1. The Barcelona Basic Model

The Barcelona Basic Model (BBM) was selected in order to describe the mechanical behaviour of low to moderate activity unsaturated soils such as bentonite based materials. This mechanic constitutive model will be adopted in all the numerical analyses presented in this thesis.

It was proposed by Alonso (Alonso, Gens, and Josa 1990), who pioneered the development of mechanical constitutive models for partially saturated soils. Most of the existing models for unsaturated soils rely indeed on the concepts developed in the BBM. The idea behind the model is the extension of the existing model for saturated soils to unsaturated conditions.

Accordingly, the behaviour of unsaturated soils should be modelled consistently and full saturation has to be considered as a limiting case. Therefore, the Barcelona Basic Model consists in the extension of the Modified Cam-Clay Model (Roscoe and Burland 1968) to unsaturated conditions, by using suction as an additional stress variable. It is formulated adopting net stress σ and suction s as stress variables.

It is worth reminding the definition of net stress $\boldsymbol{\sigma}$:

$$\boldsymbol{\sigma} = \boldsymbol{\sigma}_T - u_a \boldsymbol{I} \qquad \text{Eq. 4.17}$$

With $\boldsymbol{\sigma}_T$ the total stress tensor, u_a the air pressure for $s > 0$ and $\boldsymbol{I}$ the identity tensor.

The model is first formulated for isotropic stress states and then it is progressively extended to triaxial and three-dimensional stress states.

Isotropic stress states

Volumetric behaviour

Mean net stress $p = \sigma_i$ and suction s are used to describe the mechanical state under isotropic stress conditions ($\sigma_1 = \sigma_2 = \sigma_3$).

As the Barcelona Basic Model corresponds to the Modified Cam-Clay Model (Roscoe and Burland 1968) in full saturated state, it belongs to the family of elastoplastic strain-hardening models. Accordingly, the total volumetric strain increment of the soil $d\varepsilon_v$ is written as the sum of the elastic $d\varepsilon_v^e$ and plastic $d\varepsilon_v^p$ incremental volumetric strain components:

$$d\varepsilon_v = d\varepsilon_v^e + d\varepsilon_v^p \qquad \text{Eq. 4.18}$$

In the elastic domain, the increment of volumetric strain associated to changes in mean net stress dp and suction ds is calculated as:

$$d\varepsilon_v^e = d\varepsilon_{vp}^e + d\varepsilon_{vs}^e = \frac{\kappa}{1+e}\frac{dp}{p} + \frac{\kappa_s}{1+e}\frac{ds}{s+u_{atm}} = \frac{dp}{K} + \frac{ds}{K_s} \qquad \text{Eq. 4.19}$$

Where $d\varepsilon_{vp}^e$ and $d\varepsilon_{vs}^e$ represent respectively the elastic volumetric strain associated to the change in net stress and the one related to the change in suction, e is the void ratio, u_{atm} is the atmospheric pressure and κ and κ_s are the elastic coefficients for change in net stress and suction, defining the slope of the elastic loading-unloading line in the $(p-e)$ space and of the wetting drying line in the $(s-e)$ space. In LAGAMINE BBM implementation and in the following numerical analyses, the elastic coefficient for change in net stress κ is considered constant, whereas a number of relations have been proposed to define the elastic coefficient for change in suction κ_s, as it will be discussed in Section 4.4.5.

The Modified Cam-Clay Model considers non-linear elasticity. Namely, the bulk moduli K and K_s are respectively written as functions of the void ratio e and the mean net stress p and of the void ratio e and suction s summed to the atmospheric pressure u_{atm} according to:

$$K = \frac{(1+e)p}{\kappa} \qquad K_s = \frac{(1+e)(s+u_{atm})}{\kappa_s} \qquad \text{Eq. 4.20}$$

The plastic volumetric strain increment $d\varepsilon_v^p$ develops when the preconsolidation pressure $p_0(s)$ or/and the suction yield locus s_0 are reached, according to the increments dp and ds. The corresponding hardening law reads:

$$d\varepsilon_v^p = \frac{\lambda(s)-\kappa}{1+e}\frac{dp_0(s)}{p_0(s)} + \frac{\lambda_s-\kappa_s}{1+e}\frac{ds_0}{s_0+u_{atm}} \qquad \text{Eq. 4.21}$$

Where $\lambda(s)$ and λ_s are the plastic coefficients respectively for change in net stress and suction, defining the slope of the virgin compression line in the $(p-e)$ space and of the drying line in the $(s-e)$ space.

The slope $\lambda(s)$ of the virgin compression line and the yield stress $p_0(s)$ are functions of suction (Fig. 4.26 and Fig. 4.27). The plastic coefficient $\lambda(s)$ is calculated as:

$$\lambda(s) = \lambda(0)[(1-r)\,exp(-\omega s) + r] \qquad \text{Eq. 4.22}$$

with r and ω material parameter respectively related to the maximum stiffness of the soil ($\lambda(s) = r \times \lambda(0)$ when $s \to \infty$) and to the rate of the soil stiffness increase with suction.

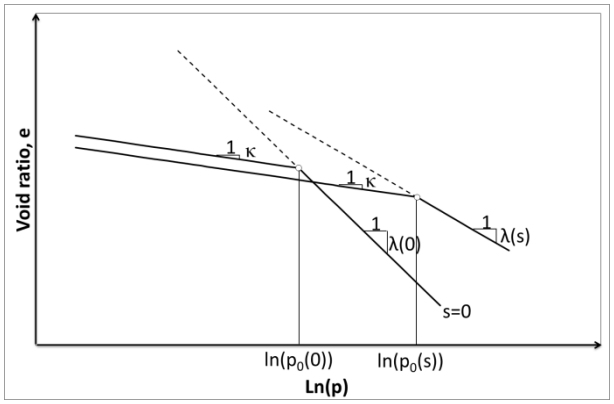

Fig. 4.26: Compression curves for saturated and unsaturated states (Alonso, Gens, and Josa 1990).

Yield surfaces and hardening laws

The BBM considers two yield loci in the plane $(s - p)$, for increase in suction (i.e. drying) and increase in net stress (i.e. loading). These latter are denoted SI (suction increase) and LC (loading collapse) curves (Fig. 4.27).

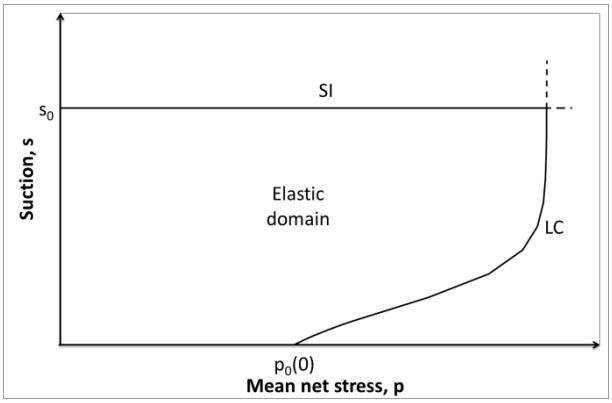

Fig. 4.27: Yield curves of the Barcelona Basic Model for isotropic stress states: Loading-Collapse (LC) and Suction Increase (SI) curves.

The evolution of the LC curve, in other terms "preconsolidation pressure $p_0(s)$" suction dependence, is modelled consistently with the concept of increasing the elastic domain with increasing suction, whereas the SI does not depend on net stress.

$$p_0(s) = p_c \left(\frac{p_0(0)}{p_c}\right)^{\frac{\lambda(0)-\kappa}{\lambda(s)-\kappa}} \qquad f_{SI} \equiv s = s_0 \qquad \text{Eq. 4.23}$$

where p_c is a reference net pressure and s_0 defines a threshold value of suction after which irreversible plastic strain develops for a given drying path.

Irreversible plastic strains control the position of the LC and SI yield surfaces as follows:

$$\frac{dp_0(0)}{p_0(0)} = \frac{1+e}{\lambda(0)-\kappa} d\varepsilon_V^p \qquad \frac{ds_0}{s_0 + u_{atm}} = \frac{1+e}{\lambda_s - \kappa_s} d\varepsilon_V^p \qquad \text{Eq. 4.24}$$

Accordingly, the hardening of both yield surfaces is coupled because the total increment of plastic volumetric strain ε_V^p appears in both equations. Depending on the sign of the volumetric plastic strain, hardening or softening of the yield surface will take place.

Loading collapse curve

Two samples presenting initial state s_1 and p_1 in the $(p - s)$ plane are considered (Fig. 4.28). The stress states lay on the yielding curve LC_1. The first sample is loaded from p_1 to p_2 at constant suction, following the path denoted L. Volumetric plastic strain is developed and the material undergoes hardening according to Eq. 4.24. The second sample is subjected to suction decrease at constant mean net stress. The material stress state evolves following the stress path denoted C. On the path C, elastic swelling and plastic collapse are computed. If the plastic collapse overcomes the elastic swelling, hardening occurs according to Eq. 4.24. In this latter case, the LC curve evolves similarly to the first case and irreversible volumetric plastic strain is obtained. As a result, the Loading-Collapse curve principle enables consistent modelling of compressive strains due to loading and collapse strains due to wetting.

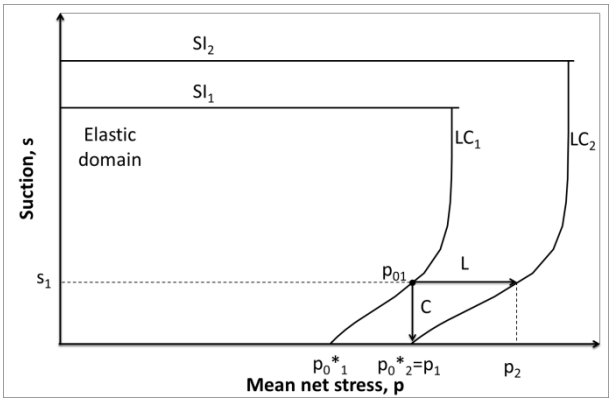

Fig. 4.28: Effects of loading at constant suction (L) and wetting at constant mean net stress (C) on the LC curve

Triaxial test stress states

Under triaxial test conditions ($\sigma_1 \neq \sigma_2 = \sigma_3$), the mechanical stress state can be described by the mean net stress p, suction s and the deviatoric stress $q = \sigma_1 - \sigma_3$ (see Fig. 4.29).

Deviatoric behaviour

The deviatoric strain ε_d can be generally defined as:

$$\varepsilon_d = \frac{\sqrt{2}}{3}\sqrt{(\varepsilon_1 - \varepsilon_2)^2 + (\varepsilon_1 - \varepsilon_3)^2 + (\varepsilon_2 - \varepsilon_3)^2} \qquad \text{Eq. 4.25}$$

In the elastic domain, the deviatoric deformation due to the deviatoric stress is given:

$$d\varepsilon_d^e = \frac{1}{3G}dq \qquad \text{Eq. 4.26}$$

where $d\varepsilon_d^e$ is the deviatoric strain elastic increment and G is the shear modulus.

This modulus can be set as a constant value or as a function of the bulk modulus K, as shown below:

$$G = \frac{3(1-2\nu)K}{2(1+\nu)} \qquad \text{Eq. 4.27}$$

Yield surfaces and hardening laws

In the $(p-q)$ plane, the yield surface is expressed (see Fig. 4.29):

$$f_{LC} \equiv q^2 - M_\theta^2(p + p_s)(p_0 - p) = 0 \qquad \text{Eq. 4.28}$$

M_θ is the critical state line slope, p_s is the yield surface left intercept and p_0 is the apparent preconsolidation pressure at a suction s.

The friction angle φ is related to the slope of the critical state line M_θ via:

$$M_\theta = \frac{6sin\varphi}{3 - sin\varphi} \qquad \varphi = arcsin\frac{3M_\theta}{6 + M_\theta} \qquad \text{Eq. 4.29}$$

The left intercept of yield surface p_s increases with increasing cohesion. It can be given as a function of suction:

$$p_s(s) = \frac{c(s)}{tan\varphi} = \frac{c(0) + ks}{tan\varphi} \qquad \text{Eq. 4.30}$$

with $c(0)$ the cohesion under saturated conditions and k a parameter controlling the increase of cohesion with suction.

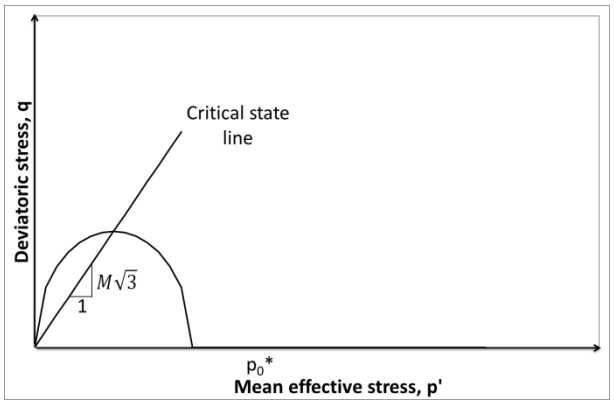

Fig. 4.29: Modified Cam-Clay Model.

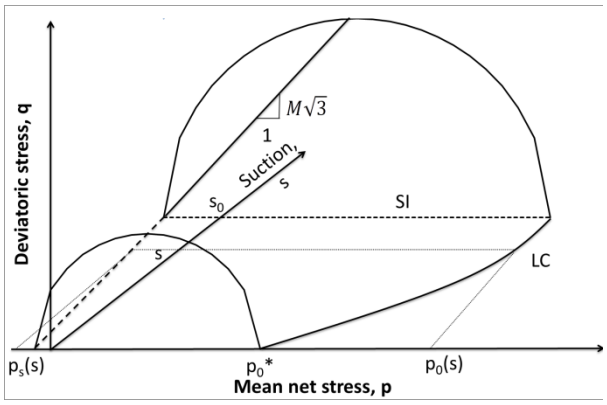

Fig. 4.30: Barcelona Basic Model.

A non-associated flow rule completes the Barcelona Basic Model's triaxial formulation. The following non-associated flow rule reads:

$$\frac{d\varepsilon_d^p}{d\varepsilon_v^p} = \frac{2q\alpha}{M_\theta^2(2p + p_s - p_0)} \qquad \text{Eq. 4.31}$$

where α is set so that Eq. 4.31 predicts zero lateral strain for stress states corresponding to Jacky's K_0 values, i.e.:

$$\alpha = \frac{M_\theta(M_\theta - 9)(M_\theta - 3)}{9(6 - M_\theta)} \frac{1}{1 - \frac{\kappa}{\lambda(0)}} \qquad \text{Eq. 4.32}$$

As a result, the flow surface is equal to:

$$g_{LC} \equiv \alpha q^2 - M_\theta^2(p + p_s)(p_0 - p) = 0 \qquad \text{Eq. 4.33}$$

Three dimensional stress states

The mechanical stress state is represented under three-dimensional conditions the mean net stress p, suction s, the second invariant of the deviatoric stress tensor J_2 and the Lode's angle θ, which are given by:

$$J_2 = \sqrt{\frac{1}{2}\boldsymbol{s} : \boldsymbol{s}} \qquad \theta = -\frac{1}{3}sin^{-1}\left(\frac{3\sqrt{3}}{2}\frac{J_3}{J_2^2}\right) \qquad J_3 = \frac{1}{3}\sigma_{ij}\sigma_{jk}\sigma_{ki} \qquad \text{Eq. 4.34}$$

where $\boldsymbol{s}$ is the deviatoric stress tensor given by $\boldsymbol{s} = \boldsymbol{\sigma_T} - p\boldsymbol{I}$, the Lode's angle θ gives the direction of the stress path in the deviatoric plane and J_3 the third invariant of the deviatoric stress tensor.

The stress increment is connected to the strain and suction increments in the elastic domain via:

$$d\boldsymbol{\sigma} = \boldsymbol{D}^e : d\boldsymbol{\varepsilon}^e + \boldsymbol{\alpha}_s ds \qquad \text{Eq. 4.35}$$

where $\boldsymbol{D}^e$ is the global elastic tensor and $\boldsymbol{\alpha}_s$ is the elastic tensor for suction changes, and they are calculated as follows:

$$D^e_{ijkl} = 2G\delta_{ik}\delta_{jl} + \left(K + \frac{2}{3}G\right)\delta_{ij}\delta_{kl} \qquad \boldsymbol{\alpha}_s = \frac{1}{K_s}\boldsymbol{D}^e : \boldsymbol{I} \qquad \text{Eq. 4.36}$$

Where K, G and K_s have already been discussed in the previous section.

Yield surfaces and hardening laws

The yield surface that limits the elastic domain is represented as shown in:

$$f_{LC} \equiv 3J_2^2 - M_\theta^2(p + p_s)(p_0 - p) = 0 \qquad \text{Eq. 4.37}$$

where M_θ is the slope of the critical state line, p_s considers the dependence of shear strength on suction and p_0 is the apparent preconsolidation pressure at a suction s.

The slope of the critical state line M_θ in three-dimensional stress states is a function of the Lode angle θ and defines the shape of the failure surface in the deviatoric plane. The van Eekelen (van Eekelen 1980) model is used to approximate the Mohr-Coulomb failure criterion. As a result, the critical state line slope M_θ is equal to:

$$M_\theta = a(1 + bsin3\theta)^n \qquad \text{Eq. 4.38}$$

where the parameter n is a constant that determines the convexity of the failure surface in the deviatoric plane and it is set to -0.229 to ensure the convexity of the surface ((van Eekelen 1980), (Barnichon 1998)) and a and b are proportional to the triaxial compression and extension friction angles φ_C and φ_E

$$a = \frac{r_C}{(1+b)^n} \qquad b = \frac{\left(\frac{r_C}{r_E}\right)^{1/n} - 1}{\left(\frac{r_C}{r_E}\right)^{1/n} + 1} \qquad \text{Eq. 4.39}$$

$$r_C = \frac{2sin\varphi_C}{\sqrt{3}(3 - sin\varphi_C)} \qquad r_E = \frac{2sin\varphi_E}{\sqrt{3}(3 + sin\varphi_E)}$$

where r_C and r_E are the reduced radii for axisymmetric triaxial stress paths of compression and extension.

The expression of the SI yield surface remains:

$$f_{SI} \equiv s = s_0 \qquad \text{Eq. 4.40}$$

With flow surface corresponding to the LC surface as:

$$g_{LC} \equiv \alpha 3J_2^2 - M_\theta^2(p + p_s)(p_0 - p) = 0 \qquad \text{Eq. 4.41}$$

4.4.2. Parameters calibration on oedometer test results

Oedometer swelling consolidation tests are often preferred to triaxial (i.e. isotropic) ones due to their more simple feasibility in laboratory conditions (Gens and Alonso 1992). However, one major disadvantage of this type of test is that radial pressure is not generally measured and is thus ignored in the studies. In this paragraph, taking advantage of BBM framework, some experimental observations are analysed and compared accounting for the possible influence of this latter feature.

(Dueck and Nilsson 2010) performed numerous swelling at constant vertical stress in oedometer conditions on compacted MX80 samples. Test labelled 02_0705 is accounted as example (Fig. 4.31, Fig. 4.32 and Fig. 4.34). The sample is compacted presenting initial diameter D=34.64 mm, void ratio equal to e=0.58, water content equal to w=9.55% and saturation equal to S_r=46.18%. It is successively placed in an oedometer ring and let it stabilise in order to obtain diameter D=35 mm, void ratio equal to e=0.61, water content equal to w=9.55% and saturation equal to S_r=43.7%. Hydration at constant vertical stress path is analysed. Axial and radial stresses, together with axial deformation (i.e. void ratio) and relative humidity and temperature (i.e. suction) are continuously measured. Radial stress and void ratio time and suction evolutions are reported respectively in Fig. 4.31 and Fig. 4.32. While full contact with the cell wall is established, radial stress quickly increases upon suction decrease up to s=70 MPa, then it reaches a peak value and starts to decrease. The void ratio continuously increases upon hydration. Axial stress remains constant at about 0.10 MPa.

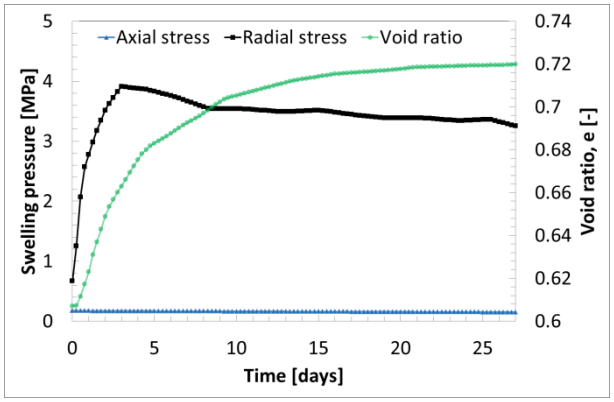

Fig. 4.31: Axial and radial stress and void ratio time evolution. Experimental results on compacted MX80 (Dueck and Nilsson 2010).

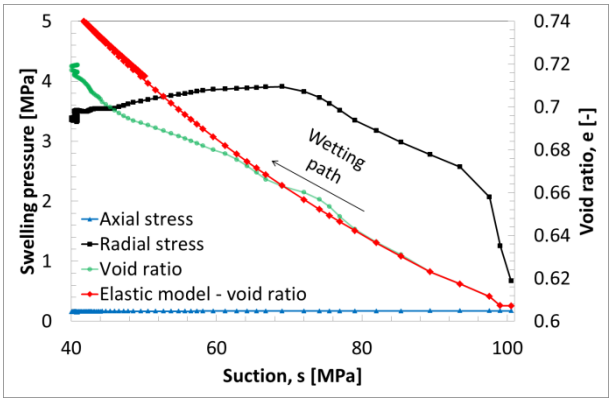

Fig. 4.32: Axial and radial stress and void ratio suction evolution. Experimental results on compacted MX80 modified after (Dueck and Nilsson 2010) and elastic model.

Taking advantage of the elasto-plastic framework formulated in the BBM, further observations can be done in the (p – s) (Fig. 4.33) and in the (p – q) plane (Fig. 4.34). Mean stress increases from 0.5 MPa to 1.6 MPa at about constant suction until full contact between the bentonite sample and the cell ring takes place (Fig. 4.33). After that, the mean (radial) stress increase becomes more evident for suction decrease. The mean (radial) stress development is increasing until the elastic limit (i.e. yielding surface), then it decreases, possibly following the yielding surface, while remaining almost constant. The radial swelling pressure at suction s=40 MPa is equal to 3.5 MPa, whereas the void ratio e=0.70. The resulting water content is equal to w=16.18% (and saturation S_r=64.19%). The test conditions (i.e. oedometric swelling at constant and low axial stress) result in the development of high stress deviator (Fig. 4.34). Due to the radial stress development at constant axial stress, the deviatoric stress q reaches 4 MPa with slope equal to 1.5 in the p – q plane. The stress deviator successively decreases until 3 MPa with slope equal to 1.5 (but always related to oedometer conditions).

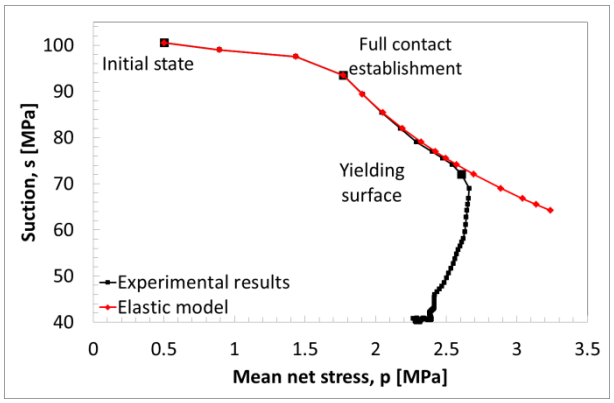

Fig. 4.33: Stress path in the (p – s) plane. Comparison between experimental data and elastic model results modified after (Dueck and Nilsson 2010)

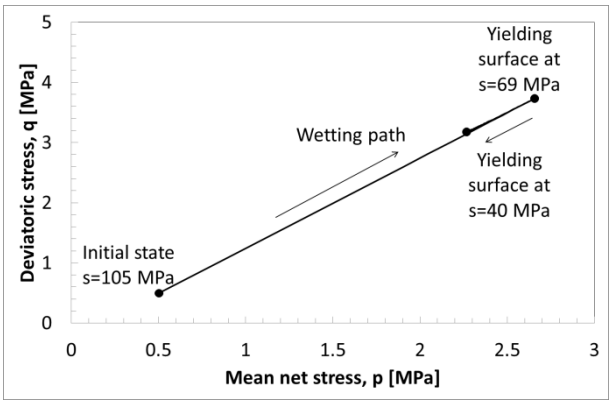

Fig. 4.34: Stress path in the (p – q) plane. Experimental data modified after (Dueck and Nilsson 2010).

The elastic radial stress development resulting from BBM (see APPENDIX A for complete analytical development) during wetting at constant vertical stress reads as follows:

$$\sigma_{rB} = \frac{1}{2}\left[\left(\sigma_{a,0} + 2\sigma_{rA}\right)\left(\frac{s_A + u_{atm}}{s_B + u_{atm}}\right)^{\frac{\kappa_s}{\kappa}\frac{2(1-2\nu)}{3(1-\nu)}} - \sigma_{a,0}\right] \qquad \text{Eq. 4.42}$$

It can be seen that it is function of the elastic compressibility coefficient of change in net stress κ, of the elastic compressibility coefficient of change in suction κ_s and of the Poisson's ratio ν.

On the other hand, the void ratio evolution in elastic domain is obtained via:

$$e_B = -\kappa_s \frac{(1+\nu)}{3(1-\nu)} \ln\left(\frac{s_A + u_{atm}}{s_B + u_{atm}}\right) + e_A \qquad \text{Eq. 4.43}$$

Being function of κ_s and ν only.

Eq. 4.43 is similar to Eq. 4.44, which would be obtained by the integration of Eq. 4.19 in the case of wetting at constant isotropic stress.

$$e_B = -\kappa_s \ln\left(\frac{s_A + u_{atm}}{s_B + u_{atm}}\right) + e_A \qquad \text{Eq. 4.44}$$

It follows that the elastic volume increase upon wetting obtained in oedometer conditions (i.e. constant vertical stress) is smaller with respect to the one which would result under wetting at constant isotropic stress (Fig. 4.35).

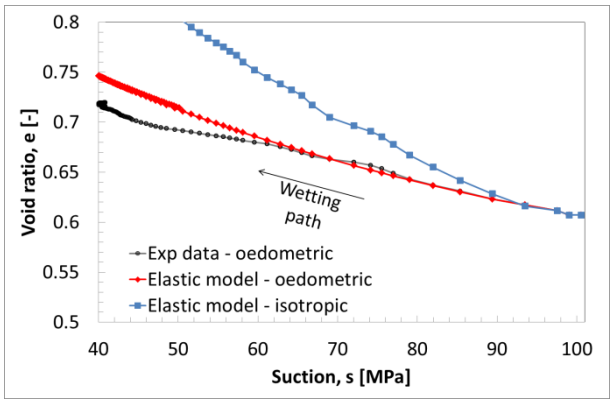

Fig. 4.35: Void ratio suction evolution. Comparison between experimental data modified after (Dueck and Nilsson 2010) and elastic model responses in oedometer and isotropic conditions.

It can be seen that for increasing Poisson coefficient, increasing deformation and decreasing radial swelling pressure development are obtained. For $\nu = 0.2$ the exponents of Eq. 4.42 and Eq. 4.43 are both divided by a factor 2 (i.e. multiplied by 0.5). It means that the developed elastic radial swelling stress is half with respect to the one that would be computed during hydration in constant volume conditions and the swelling deformation is half with respect to the one that would be obtained during hydration at constant isotropic stress.

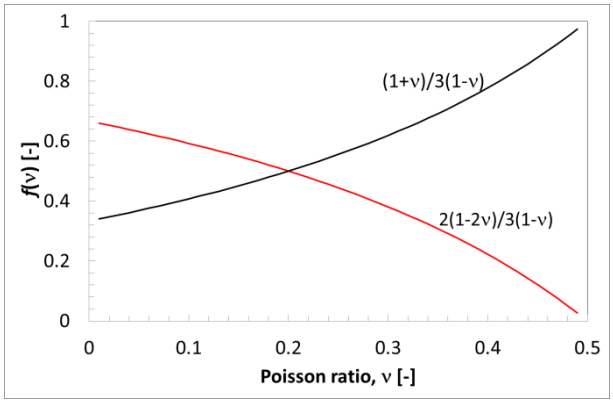

Fig. 4.36: Eq. 4.42 and Eq. 4.43 function dependency on Poisson ratio ν (for constant κ and κ_{s0}).

Finally, it can be assumed that the simultaneous analyses of radial stress, suction and deformation measurements upon wetting at constant stress allow evaluating the parameters triplet of κ, κ_s and ν that can be used in the BBM.

The analysis of the presented experimental test conducted on MX80 bentonite compacted at initial dry density equal to ρ_d=1.70 Mg/m^3 permits determining the following triplet: $\kappa = 0.085$, $\kappa_s = 0.300$ and $\nu = 0.23$.

Let us now consider the second phase of the classic oedometer swelling consolidation tests: the vertical compaction phase. For this purpose, the axial stress is increased from 0.1 MPa to 8 MPa at constant suction s=40 MPa. At the same time, radial stress and axial deformation are measured (Fig. 4.37).

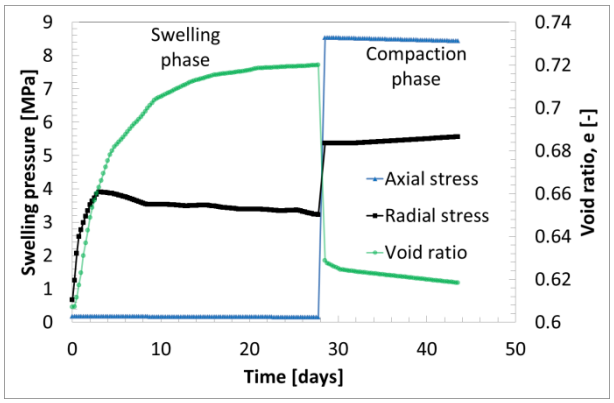

Fig. 4.37: Axial and radial stress and void ratio time evolution. Experimental results on compacted MX80

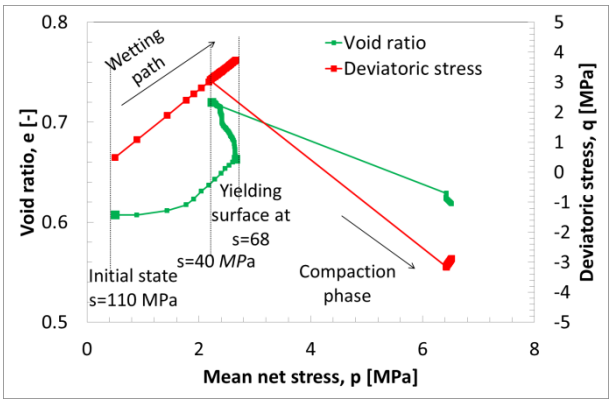

Fig. 4.38: Void ratio and deviatoric stress as function mean net stress. Experimental results on compacted MX80 modified after (Dueck and Nilsson 2010).

The deviatoric stress q evolution with respect to mean net stress p follows the slope of -1.5 for axial stress increase accordingly to oedometer compaction conditions (Fig. 4.38).

It is possible to obtain from the *(p – e)* plane (Fig. 4.38) the slope of the compaction curve, which corresponds to $\kappa = 0.085$, namely the value computed via the elastic model.

Moreover, if oedometric compaction path is considered, the ratio between the horizontal and vertical stresses depends on the Poisson ratio only via Eq. 4.45.

$$\frac{\sigma_h}{\sigma_v} = \frac{\nu}{1-\nu} \qquad \frac{\Delta\sigma_h}{\Delta\sigma_v} = \frac{\nu}{1-\nu} \qquad \text{Eq. 4.45}$$

By analysing the axial and radial stress measurements, it is possible to validate the Poisson's ratio value $\nu = 0.23$ determined in the swelling at constant vertical stress phase.

The stress values accounted in these test are relatively low with respect to the suction level, thus it is not possible to determine an additional point of the yielding surface in the *(p – q)* and *(p – e)* planes, which would help to define the size of the elastic domain.

For sake of completeness, void ratio evolution as function of vertical net stress is presented in Fig. 4.39. The slope of the elastic path results much lower with respect to the results obtained by considering the mean net stress (i.e. the material looks stiffer). Hence, it is worth reminding that when radial stress measurements are not available, oedometer compaction tests need to be read carefully and the elastic compressibility coefficient has to be modified consistently. However, the proportionality coefficient between the strain and stress increments K=10 MPa is very low if compared with Young moduli determined in section 4.2.5 (E=250 – 600 MPa). This could be related to the different hydro-mechanical state of the material, but unluckily very few experimental characterisations are available and further research would be needed.

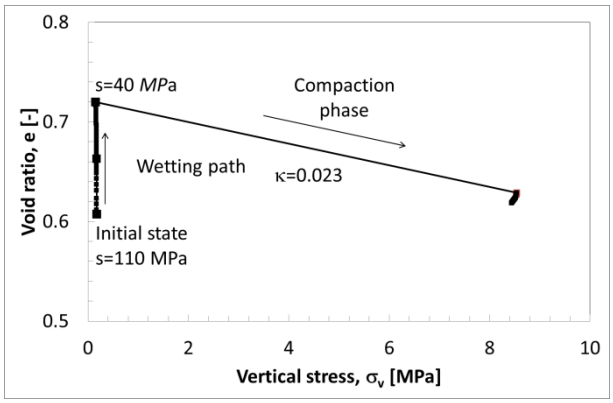

Fig. 4.39: Void ratio as function vertical net stress. Experimental results on compacted MX80 (Dueck and Nilsson 2010).

The above computed triplet of elastic parameters is applied to predict the elastic behaviour of MX80 bentonite investigated by (Villar 2005). This further comparison is given in order to assess the reliability of the above presented parameters determination procedure.

(Villar 2005) performed suction controlled oedometer tests to study one-dimensional compressibility of compacted MX80 bentonite. The specimens were obtained by uniaxial compaction of the clay directly in the oedometer ring. The clay was previously mixed with deionised water to reach water content equal to w=17%. The initial height of the specimen was H=1.20 cm with diameter D=4.95 cm and dry density ρ_d=1.69 g/cm^3. The compaction pressure required to achieve this dry density was 32 MPa. The tests were performed at a constant temperature of T=20°C. The samples have been subjected to hydration under a low vertical load and, once saturated, they have been loaded.

Fig. 4.40 shows the void ratio evolution as function of suction and the elastic model response with the parameters $\kappa_s = 0.300$ and $\nu = 0.23$. Information with respect to radial stress development is not provided, thus no further validation on the proposed procedure can be given.

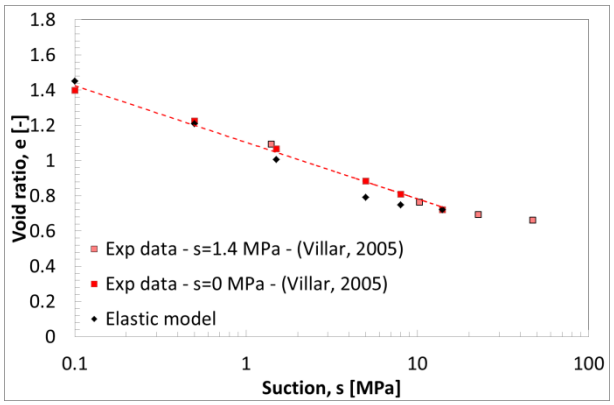

Fig. 4.40: Void ratio suction evolution. Experimental results on compacted MX80 (Villar 2005) and elastic model.

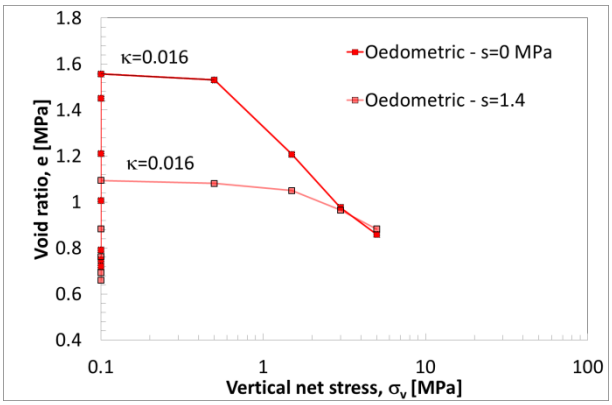

Fig. 4.41: Void ratio as function vertical net stress. Experimental results on compacted MX80 (Villar 2005)

For sake of completeness, the compaction phase results are given in Fig. 4.41. The elastic compressibility coefficient for change in stress can be computed considering the slope of the elastic loading path. The obtained value is equal to 0.016, which is much lower with respect to $\kappa = 0.085$ (i.e. the slope in the space (p – e)), but much closer to 0.023 (given in the *(σ_v – e)* of Fig. 4.39).

Information on the elastic domain size is provided in this case (Fig. 4.41). The change of slope allows determining the limit of the space in which the material elastic-reversible behaviour is shown (i.e. yielding surface) and the plastic compressibility coefficient for change in net stress λ at the analysed suction levels.

The one-dimensional compressibility behaviour of the compacted MX80 is compared to the isotropic one in Fig. 4.42. For this purpose, experimental swelling-isotropic consolidation tests by (Tang and Cui 2010) are presented. The sample was obtained via static compaction under an isotropic pressure of 40 MPa and suction s=110 MPa. After compaction, the soil specimen was placed in a chamber at a relative humidity of 44% and a temperature of 20 °C. This procedure allowed obtaining compacted soil specimens with a dry density ρ_d=1.78±0.3 Mg/m^3 and a void ratio e = 0.55±0.3.

Fig. 4.42 shows the above-mentioned discrepancies on the elastic paths of the analysed specimens (i.e. different slope). On the other hand, with respect to the elasto-plastic behaviour, it is possible to see that at saturation the compressibility is nicely comparable. Hence, oedometric plastic compressibility can be adopted for isotropic models. One final remark on the yield loci determined in oedometer conditions is necessary. It may appear that the elastic limit is larger with respect to the isotropic one (Fig. 4.42). However, as Eq. 4.45 reports, the radial stress and consequentially the mean net stress are always smaller than the vertical one.

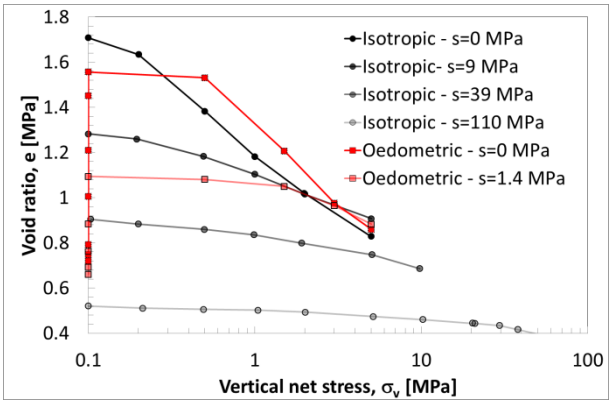

Fig. 4.42: Void ratio as function vertical net stress. Experimental results for oedometer compaction (Villar 2005) and isotropic compaction ((Tang and Cui 2010) on compacted MX80.

4.4.3. Validation of the BBM constitutive model

The Barcelona Basic Model is validated against experimental data on bentonite-based materials from the literature. Three types of bentonites are considered, namely Febex (compacted and pellets mixtures), MX80 and sand mixture and pure MX80 (compacted and pellets mixture). In addition, based on experimental observations, the mechanic parameters for pure MX80 at a different dry density are also determined. The BBM mechanical parameters can be found in Table 4.1.

Febex bentonite

Compacted Febex

(Lloret et al. 2003) performed suction-controlled oedometer tests on compacted Febex bentonite. The samples were compacted at an initial dry density of ρ_d=1.70±0.02 Mg/m^3 and water content equal to w=13.55±.65%. Suction levels equal to 127 MPa, 14 MPa, 4 MPa and 0 MPa were taken into account in order to consider the compressibility properties evolution. With respect to the experimental procedure: each sample reaches the given level of suction under a vertical load of 0.1 MPa, it is successively compacted. The experimental data and the model response correspond remarkably well (Fig. 4.43). Swelling strain increases and plastic compressibility and preconsolidation pressure decrease as the suction reduces, both in experimental and numerical cases. Calibrated parameters for the BBM are reported in Table 4.1.

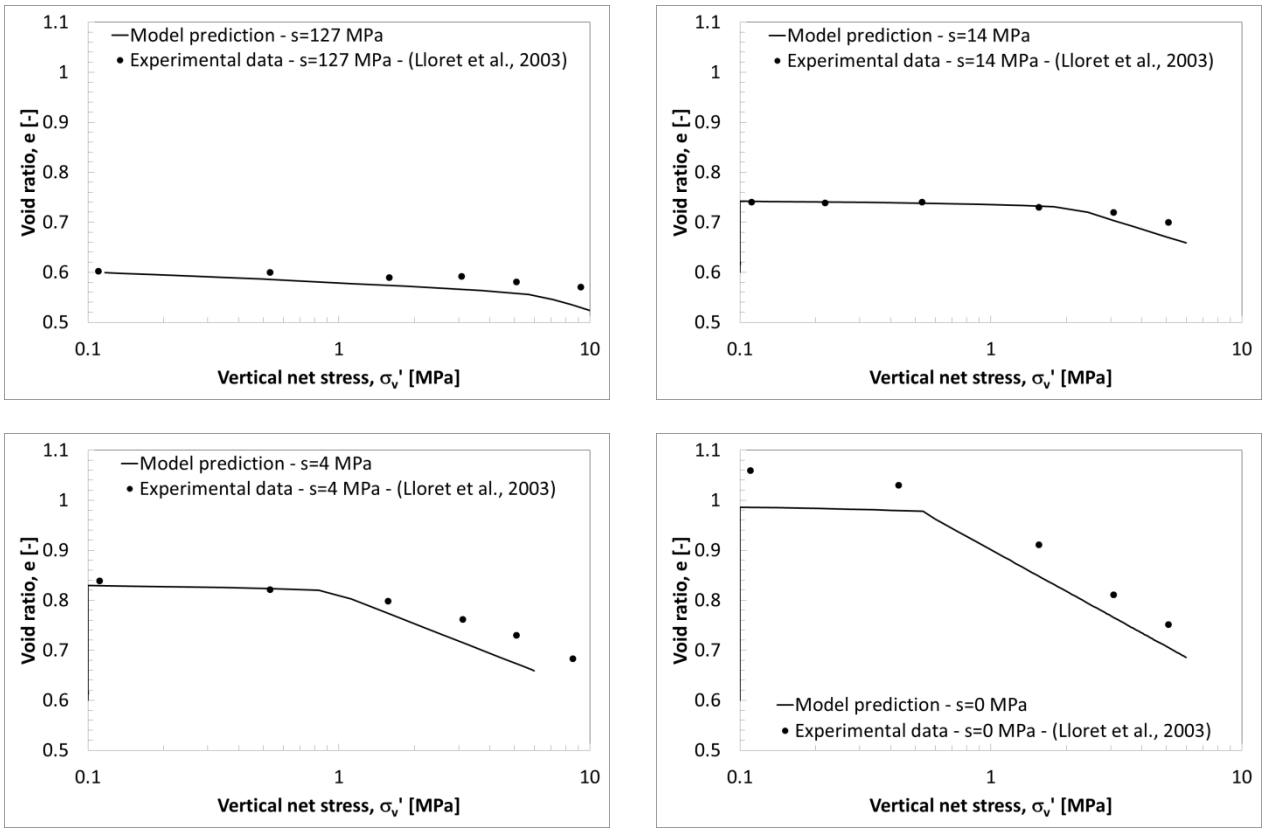

Fig. 4.43: Controlled-suction oedometer tests on compacted Febex bentonite. Comparison between experimental data (Lloret et al. 2003) and model responses on loading paths.

Table 4.1: Parameters for Barcelona Basic Model for commercial bentonites.

			Compacted Febex	Pellet Febex	MX80/Sand	Pellet MX80	Compacted MX80	Compacted MX80
ρ_d	[Mg/m^3]	Dry density	1.60	1.28	1.69	1.50	1.69	1.50
κ	[-]	Elastic compressibility coefficient for changes in mean net stress	0.012	0.074	0.025	0.06	0.007	0.03
κ_s	[-]	Elastic compressibility coefficient for changes in suction	0.12	0.075	0.073	0.08	0.340	0.220
α_p	[Pa^{-1}]	Parameter controlling the stress dependency of the swelling strain for change in suction	4.4×10^{-8}	3×10^{-6}	2.6×10^{-7}	2.6×10^{-7}	1.5×10^{-7}	3.5×10^{-7}
p_0*	[MPa]	Pre-consolidation pressure for saturated state	1.6	0.65	1.4	1.86	0.15	0.3
p_c	[MPa]	Reference pressure controlling the shape of the LC curve	0.395	0.325	0.01	0.93	0.02	0.086
$\lambda(0)$	[-]	Slope of the saturated virgin consolidation line	0.12	0.20	0.12	0.20	0.25	0.25
r	[-]	Parameter defining the minimum soil compressibility	0.55	0.70	0.80	0.75	0.32	0.32
ω	[MPa^{-1}]	Parameter controlling the soil stiffness	0.25	0.008	0.09	0.10	0.051	0.051
φ	[°]	Friction angle	20	26	25	25	10	20
v	[-]	Poisson ratio	0.25	0.35	0.35	0.40	0.17	0.17
$c(0)$	[MPa]	Cohesion in saturated conditions	0	0	0.1	0.1	0.1	0.10
k	[-]	Parameter controlling the increase of cohesion of increase of suction	0.0046	0.0046	0.046	0	0	0.0046

Febex Pellets

Febex pelletized material was exhaustively investigated by (Alonso, Hoffmann, and Romero 2010) in the context the EB test (Chapter 7). Suction controlled oedometer tests were performed on the typical bentonite dry densities obtained via pneumatic injection techniques equal to ρ_d=1.30 Mg/m^3 and ρ_d=1.50 Mg/m^3. In this thesis, Febex pellets material at ρ_d=1.30 Mg/m^3 will be considered in the framework of the EB test analysis, thus attention is focused on this one. Fig. 4.44 presents oedometer compression at suction s=60 MPa. The numerical response well reproduces the experimental data. Compressibility and swelling properties are calibrated in order to reproduce reference work experimental results (Hoffmann, Alonso, and Romero 2007). The calibrated data can be found in Table 4.1.

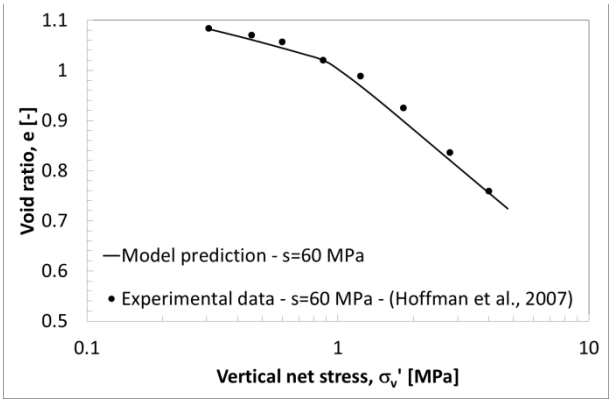

Fig. 4.44: Controlled-suction oedometer tests on Febex pellets bentonite. Comparison between experimental data (Hoffmann, Alonso, and Romero 2007) and model responses on loading paths.

Compacted MX80 and sand mixture

(Wang, Tang, et al. 2013) performed suction-controlled oedometer tests on MX80 bentonite-sand mixture with respective proportion of 70/30 in dry mass. The samples were compacted at an initial dry density of ρ_d=1.67 Mg/m^3 and water content equal to w=11%. The suction values taken into account are 4.2 MPa, 12.6 MPa and 38 MPa. With respect to the experimental procedure: each sample reaches the given level of suction under a vertical load of 0.1 MPa, it is successively compacted to a vertical stress of 50 MPa and finally unloaded.

The experimental data and the model response are represented in Fig. 4.45. The model is able to well reproduce the swelling deformation during the hydration together with the compaction strain obtained upon loading. It is possible to tackle the increase of stiffness with increasing suction as well as the increase of preconsolidation pressure with increasing suction. The calibrated mechanical parameters obtained for the numerical modelling of this test are given in Table 4.1.

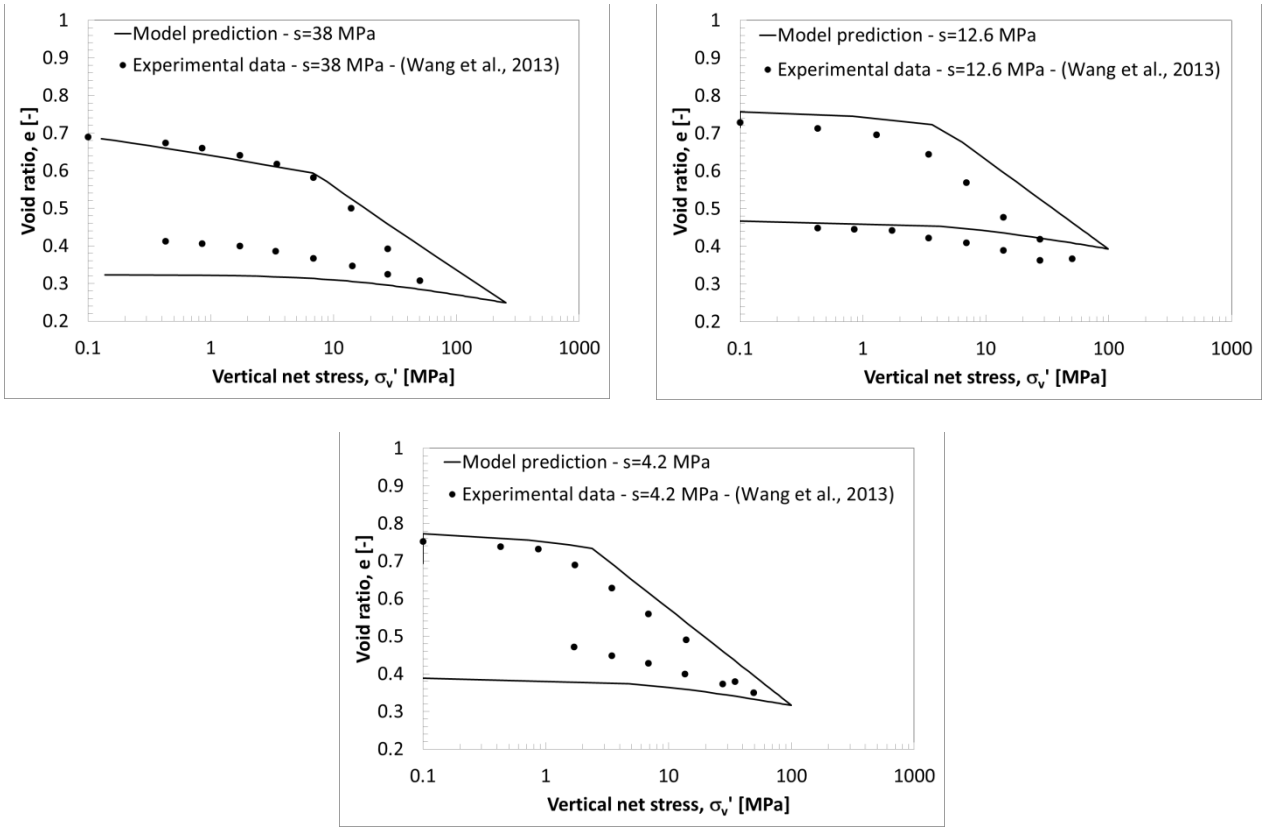

Fig. 4.45: Controlled-suction oedometer tests on MX80/sand mixture bentonite (proportion 70/30). Comparison between experimental data (Wang, Tang, et al. 2013) and model responses on loading and unloading paths.

Pure MX80

MX80 Pellets

(Molinero et al. 2019) investigated the hydro-mechanical behaviour of MX80 bentonite pellet/powder mixture at a proportion of 80/20 in dry mass via swelling-consolidation tests. Pellets were produced in the Laviosa-MPC company by instantaneously compacting MX80 bentonite in a mould of 7mm in diameter and 7 mm in height. The fabrication water content was w=6.0 ± 1.0% and the dry density was ρ_d=2.06 ± 0.06 Mg/m^3 with initial suction (s=135 ± 3 MPa). The MX80 bentonite powder was produced by crushing pellets just after their fabrication. The maximum size of grains was 2 mm and the portion of the grains smaller than 80 μm was 5%. An initial water content of w=3.2 ± 1.0% was found in the laboratory by oven-drying at 105 °C for 24 h, corresponding to an initial suction s=191 MPa.

The mixture was prepared by filling the cell by packets corresponding to one layer of pellets spread over the base of the cylinder, with the corresponding amount of powder, respecting the proportion of 80-pellets/20-powder. The global dry initial density of the mixture thus prepared was 1.49 Mg/m^3. The analysed compressibility properties are related to suction values equal to 0, 9 and 138 MPa, applying the selected value of relative humidity with vapour. Swelling strains upon wetting were recorded as well as the compressive strain due to the applied loading.

Fig. 4.46 depicts the experimental data and the model response. The model reproduces the swelling deformation that appears during hydration, as well as the compaction strain that develops during loading. Increasing stiffness and preconsolidation pressure are both well addressed for increasing suction also in this case of initial heterogeneous macrostructure and dry density distribution. Table 4.1 summarizes the calibrated mechanical parameters obtained for the numerical modelling of this test.

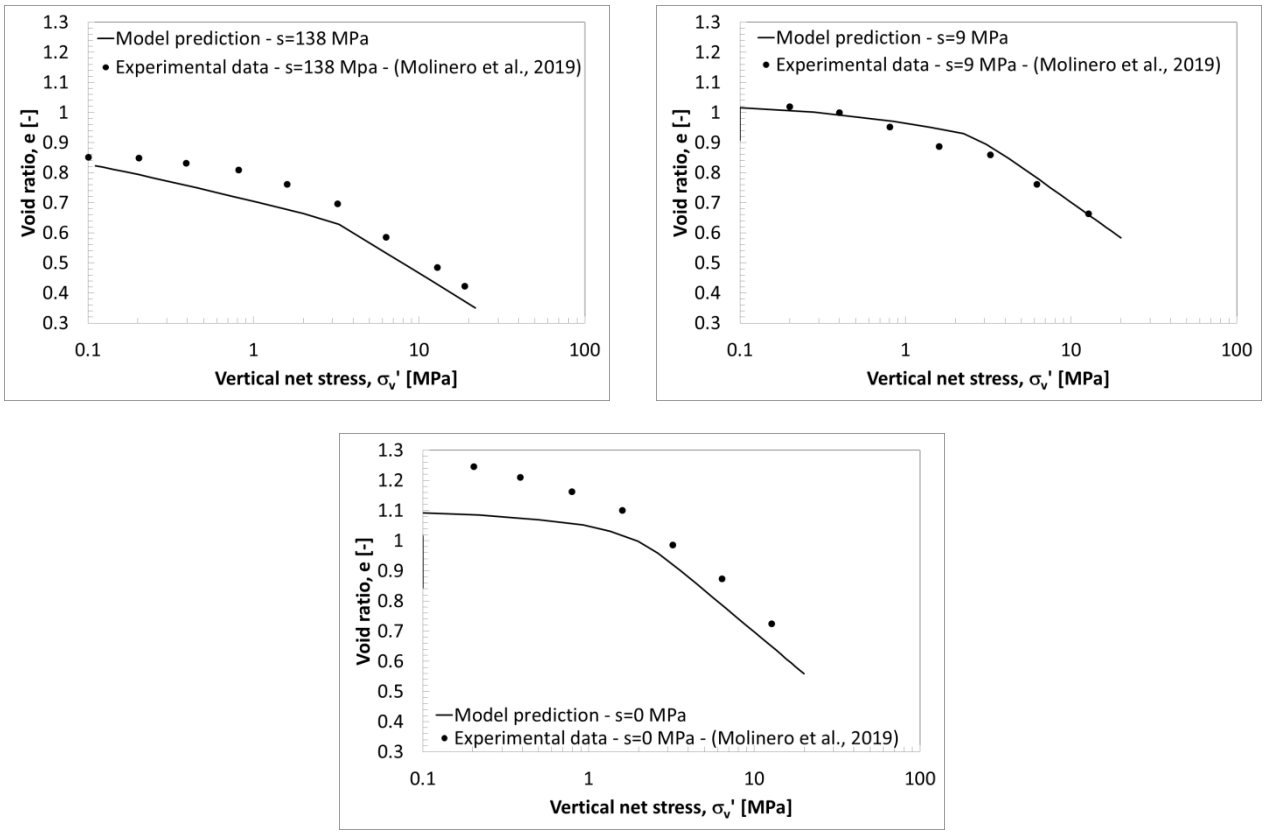

Fig. 4.46: Controlled-suction oedometer tests on MX80 pellets bentonite. Comparison between experimental data (Molinero et al. 2019) and model responses on loading paths.

Compacted MX80

(Tang, Cui, and Barnel 2008) performed suction-controlled isotropic compression tests on pure MX80 compacted bentonite. Prior to utilization, the clay was sieved at 2 mm and dried at 44% of relative humidity, which corresponded to a suction s=110 MPa at temperature T=20 °C. After reaching equilibrium, the soil water content was w=10%±2%. Then the soil was statically compacted under an isotropic pressure of 40 MPa. After compaction, the soil specimen was placed in a chamber at a relative humidity of RH=44% and a temperature of T=20 °C. This procedure allowed obtaining compacted soil specimens with a dry density ρ_d=1.78±0.3 Mg/m^3 and void ratio e=0.55±0.3. The considered suction levels were 110 MPa, 39 MPa and 9 MPa. The comparison between the experimental data and the model predictions is shown in Fig. 4.47. The numerical predictions are in good agreement with experimental data.

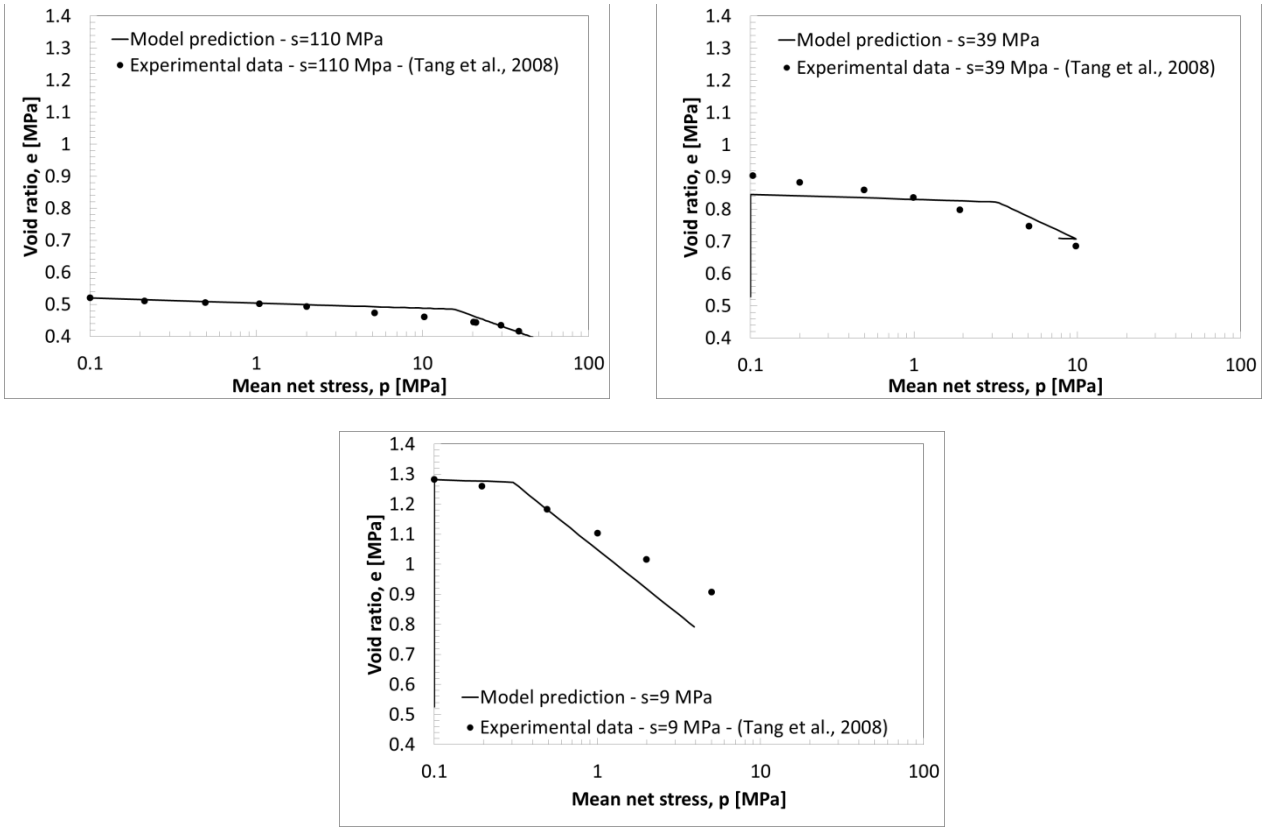

Fig. 4.47: Controlled-suction isotropic tests on pure MX80 compacted bentonite. Comparison between experimental data (Tang, Cui, and Barnel 2008) and model responses on loading paths.

Data extrapolation for a different dry density

The widespread use of bentonite in nuclear waste disposals facilities requires the evaluation of specific swelling capacities, which have to be sufficiently high to enable the sealing of technological gaps, while remaining low enough not to exceed the host-rock strength resistance. These characteristics are inextricably related to the dry density of the bentonite material (Fig. 4.48 and Fig. 4.49). However, given the difficulty and the important time required to perform laboratory tests, experimental characterisations on compacted bentonite are limited and not always available for any dry density and type. Thus, collecting data from available experimental campaigns (and dry densities) and adapting them for the particular purpose becomes important for numerical modelling. In this paragraph, parameters for the BBM are extrapolated from experimental results presented by (Tang, Cui, and Barnel 2008) for pure MX80 compacted at dry density equal to ρ_d=1.69 Mg/m^3 for the same material compacted at the lower dry density equal to ρ_d=1.50 Mg/m^3.

Among other parameters, the swelling capacity upon suction decrease for BBM is mostly defined by the elastic compressibility coefficient for change in suction κ_s. The κ_s coefficient controls the slope of the stress paths in free swelling conditions in the $(s-e)$ (Fig. 4.48) and respectively in $(p-s)$ planes for constant stress and constant volume conditions, where it affects the final swelling pressure. Consequentially, it is selected in order to fit the experimental evidences concerning swelling capacity dry density dependence. Namely, upon hydration (i.e. suction decrease) numerical results have to show lower swelling deformation with respect to an initially more compacted bentonite (red line Fig. 4.48). At the same time, the swelling pressure developed during hydration at constant volume conditions must to be lower than the one presented by a denser material and higher with respect to the one of a looser one (red square Fig. 4.49). The value at zero stress that fits these requirements is equal to $\kappa_{s0} = 0.220$ for MX80 at ρ_d=1.50 Mg/m^3 (instead of $\kappa_{s0} = 0.310$ for MX80 ρ_d=1.69 Mg/m^3) and the parameters controlling its dependency on the stress value equal to $a_p = 0.035\ MPa^{-1}$.(instead of $a_p = 0.015\ MPa^{-1}$) (as it will be discussed in the following).

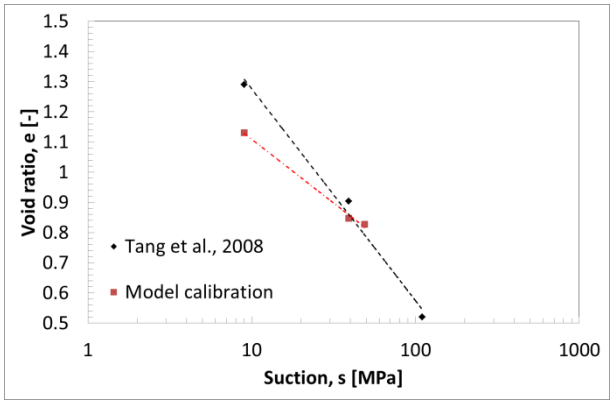

Fig. 4.48: Influence of suction changes and initial bentonite dry density on the volumetric behaviour of compacted bentonite-based materials, under free swelling conditions. Comparison between experimental data (Tang, Cui, and Barnel 2008) and model response.

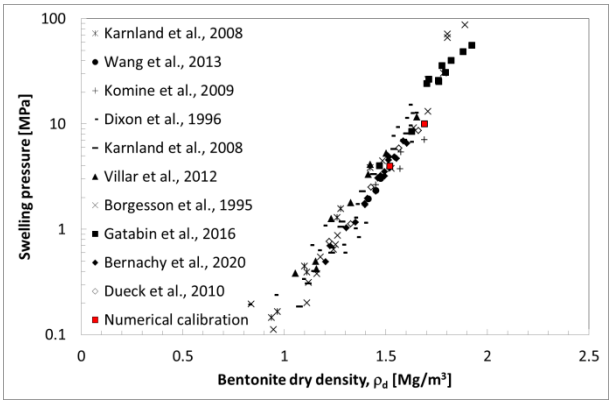

Fig. 4.49: Evolution of the swelling pressure with effective bentonite dry density. Comparison between experimental data (isochoric swelling) and model responses.

Accordingly, the compressibility properties (and coefficients) for change in net stress have to be reasonably similar to the ones of the same material. It is necessary to remind that the elastic and plastic compressibility coefficients for change in net stress κ and λ do not affect remarkably the swelling deformation upon wetting under constant stress conditions. On the other hand, in the BBM framework, these control both the stress path and the shape of the yielding surface with its evolution. In general, these parameters are not considered being dry density dependent. Nevertheless, it can be observed in Fig. 4.47 (but also Fig. 4.45 and Fig. 4.46), especially with respect to the elastic coefficient κ, that for higher void ratio (i.e. lower dry density), the elastic compressibility of the material slightly increases. Thus, according to this evidence the elastic

compressibility coefficient for change in net stress concerning MX80 at ρ_d=1.50 Mg/m^3 is selected equal to $\kappa = 0.030$ (instead of $\kappa = 0.007$ for MX80 compacted at ρ_d=1.69 Mg/m^3). The plastic compressibility coefficient for change in net stress λ, that is assumed suction dependent, corresponds to the one of MX80 bentonite compacted at dry density ρ_d=1.69 Mg/m^3. The calibrated data for MX80 at ρ_d=1.50 Mg/m^3 are compared to the ones related to the experimental suction-controlled isotropic compression performed by (Tang, Cui, and Barnel 2008) (Fig. 4.50). At suction s=38 MPa, the void ratios (i.e. dry densities) and the compressibility of the experimental and numerical responses correspond quite well. The void ratios are strikingly different at s=9 MPa due to the different swelling capabilities related to the initial dry density difference, but the compressibility are comparable for the numerical and experimental cases.

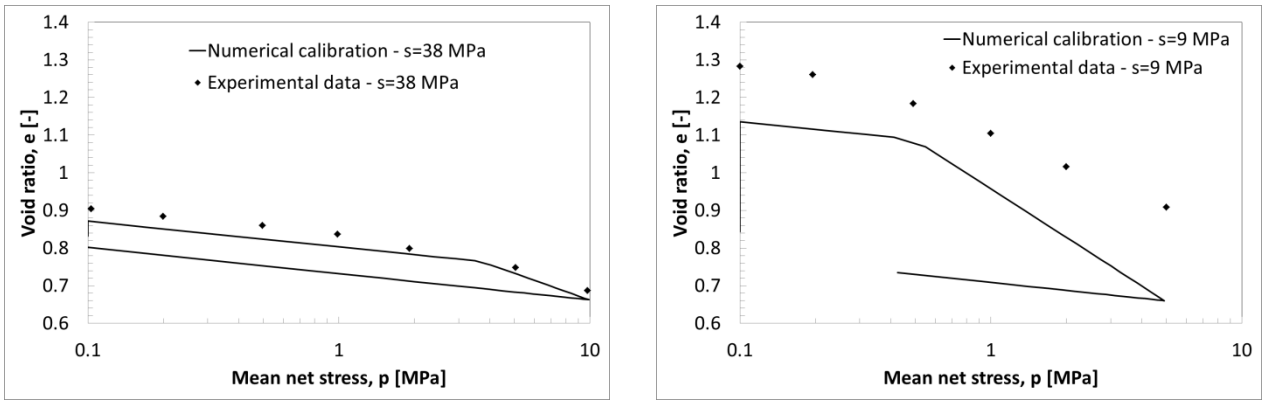

Fig. 4.50: Controlled-suction isotropic tests on pure MX80 compacted bentonite. Comparison between experimental data for initial dry density ρ_d=1.70 Mg/m^3 (Tang, Cui, and Barnel 2008) and model responses for initial dry density ρ_d=1.50 Mg/m^3 on loading paths.

It was not possible to extrapolate the shape of the yielding surface from experimental data. Hence, the parameters defining the LC curve were determined in order to fit the swelling pressure development in constant volume conditions.

4.4.4. Parameters dependency on density

BBM parameters of the five different materials presented in the previous section are summarized in the follow. Table 4.2 recalls symbols (square and circle respectively for compacted and pellet mixtures) and colours (black, white and grey respectively for Febex, pure MX80 and MX80 and sand) adopted for each type of considered bentonite. For sake of completeness, the "extrapolated" parameters calibrated for a different dry density of MX80 are also reported (red triangle).

Table 4.2: Distinction adopted in the following plots with dry density.

	Compacted		Pellets	
Febex	■	ρ_d=1.60 Mg/m^3	●	ρ_d=1.28 Mg/m^3
Pure MX80	□	ρ_d=1.69 Mg/m^3	○	ρ_d=1.50 Mg/m^3
MX80 and sand	■	ρ_d=1.69 Mg/m^3		
Pure MX80 (Extrapolated)	▲	ρ_d=1.50 Mg/m^3		

The following representations are given in terms of "effective bentonite dry density" (obtained via *Eq. 4.46* (Gatabin et al. 2006)).

$$\varrho_{d\ clay} = \frac{p_{clay}}{\varrho_{d\ mixture} - \frac{p_{component}}{\varrho_{d\ component}}} \qquad \text{Eq. 4.46}$$

p_{clay} and $p_{component}$ are respectively the bentonite and the second component proportions in the mixture, $\varrho_{d\ mixture}$ and $\varrho_{d\ component}$ are respectively the dry densities of the mixture and of the second component.

This distinction is done in order to consider the clay dry density in materials such as MX80 and sand mixtures, which is the responsible for the swelling capabilities of the overall assembly. In addition, even though the following analyses are given in terms of "initial/dry" bentonite dry density, it becomes necessary to distinguish the "final/saturated" bentonite dry density, due to the important volume changes occurring upon hydration.

Fig. 4.51 and Fig. 4.52 show the evolution of the elastic compressibility coefficients κ (for change in net stress) and κ_{s0} (for change in suction) with initial effective bentonite dry density. The parameter κ is considered constant for a given dry density, whereas a pressure dependence relation is adopted for κ_{s0} (section 4.4.5), whose value is considered at null stress. The elastic parameter κ seems to be in general inversely proportional to the bentonite dry density (Fig. 4.51). The lowest value (related to higher material stiffness) equal to κ=0.003 is found for dry density equal to ρ_d=1.69 Mg/m^3 and the higher one (higher compressibility) equal to κ=0.074 is found for dry density equal to ρ_d=1.28 Mg/m^3. Compacted bentonite materials show in general lower compressibility for change in net stress (between 0.003 and 0.012), whereas pellets mixture look more compressible (values between 0.06 and 0.074). This tendency can also be observed in the calibration of the experimental data from Fig. 4.43 to Fig. 4.47. The elastic constant parameter κ fits remarkably well the initial dry densities (i.e. lower void ratios) and less precisely the lower ones.

The evolution of the elastic compressibility coefficient for change in suction at null stress κ_{s0} as function of dry density is given in Fig. 4.52. Data calibrated on experimental tests clearly present proportionality with the dry density. For the higher dry density ρ_d=1.69 Mg/m^3, κ_{s0}=0.330 is observed and for the lowest ρ_d=1.28

Mg/m^3, κ_{s0}=0.075 is given. The minimum κ_{s0}=0.072 is found for MX80 and sand mixture at ρ_d=1.44 Mg/m^3, but the discrepancy is very low.

These observations allow concluding that bentonite-based materials elastic compressibility coefficients for change in stress, κ, and in suction, κ_s, are respectively inversely and directly proportional with dry density. Namely, the denser material corresponds to the stiffer behaviour for change in stress, as well as, the denser material corresponds to the more swelling behaviour for suction increase. These conclusions are confirmed by numerous experimental observations. However, further experimental campaigns would allow determining a more precise tendency for a wider dry density range.

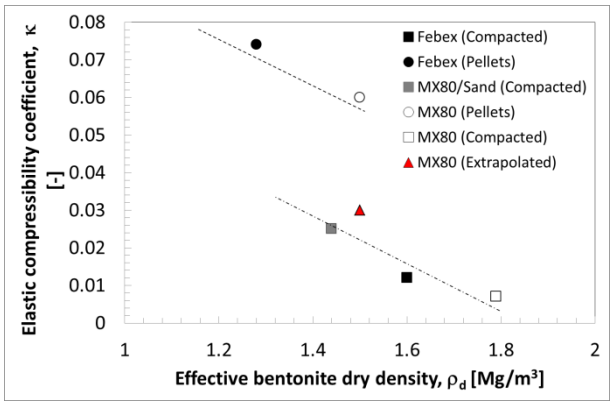

Fig. 4.51: Evolution of elastic compressibility coefficient for change in net stress κ of five bentonites with dry density.

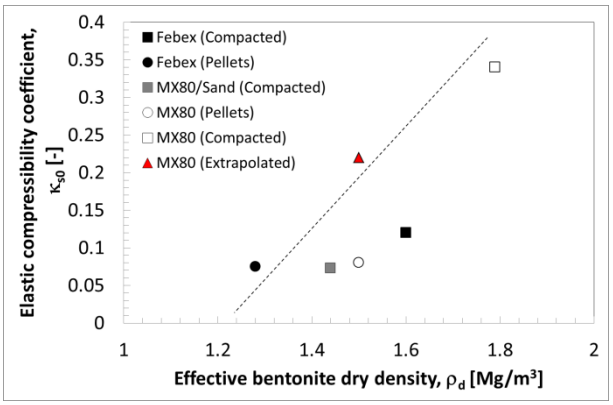

Fig. 4.52: Evolution of elastic compressibility coefficient for change in suction κ_{s0} at zero stress of five bentonites with dry density.

Fig. 4.53 and Fig. 4.54 show the plastic compressibility coefficient λ for change in stress as function of initial dry density. As Eq. 4.22 suggests, this parameter decreases for increasing suction (i.e. the material becomes stiffer when dried), thus the values as dry density function are given for the saturated state (Fig. 4.53) and for the dry state (s=1000 MPa, Fig. 4.54). The plastic compressibility coefficient in the dry state is in general inversely proportional to the dry density of the material. Compacted assemblies look stiffer than pellets bentonite mixtures (Fig. 4.54). It does not seem possible to extrapolate a clear tendency with dry density of the plastic compressibility coefficient at the saturated state (Fig. 4.53). However, it is relevant to point out that at saturation, the final dry density is completely different from the initial one at the dry state (accounted in the plot), due to the important volumetric change occurring during hydration.

Similarly to the elastic compressibility coefficient for change in stress, also the plastic compressibility coefficient evidently evolves with dry density underlining increasing stiffness for increasing compactness as Fig. 4.5 suggests.

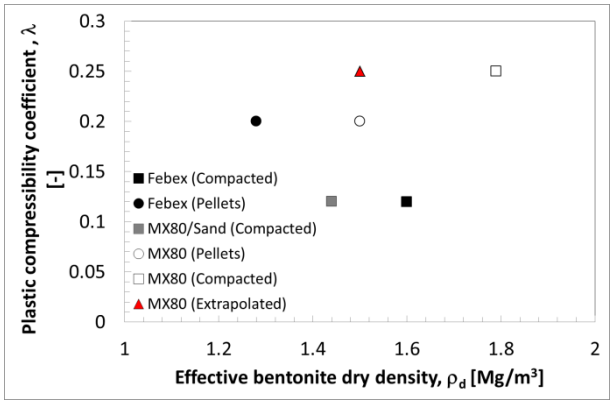

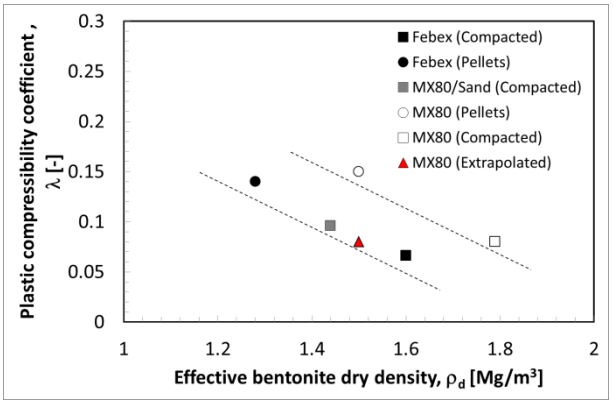

Fig. 4.53: Evolution of plastic compressibility coefficient for change in net stress λ at suction s=0 (i.e. saturated state) of five bentonites with initial dry density.

Fig. 4.54: Evolution of plastic compressibility coefficient for change in net stress λ at suction s=∞ (i.e. dry state) of five bentonites with initial dry density.

Similarly to Fig. 4.53 and Fig. 4.54, Fig. 4.55 and Fig. 4.56 show the preconsolidation pressure p_c as function of initial dry density. The preconsolidation pressure, i.e. the elasticity threshold, increases for increasing suction (Eq. 4.23), namely calibrated values are reported for saturated state (i.e. s=0, Fig. 4.55) and the dry state (i.e. s=1000 MPa, Fig. 4.56). Remarkable proportionality can be observed between the preconsolidation pressure at the dry state and the dry density, with compacted assemblies generally stiffer than pellet mixtures. The sand component may increase the stiffness of the mixture. For the saturated state (Fig. 4.55), it is not possible to extrapolate a clear tendency. Also in this case, it is relevant to point out that at saturation, the final dry density is completely different from the initial one at the dry state (accounted in the plot), due to the important volumetric change occurring during hydration. This occurrence was also considered in Darde et al numerical model (Dardé 2019) and may allow a more reasonable analysis of the experimental data.

It was not possible to present similar analyses on experimental data characterising the deviatoric behaviour (such as friction angle and cohesion) due to the scarcity of experimental evidences at the present state.

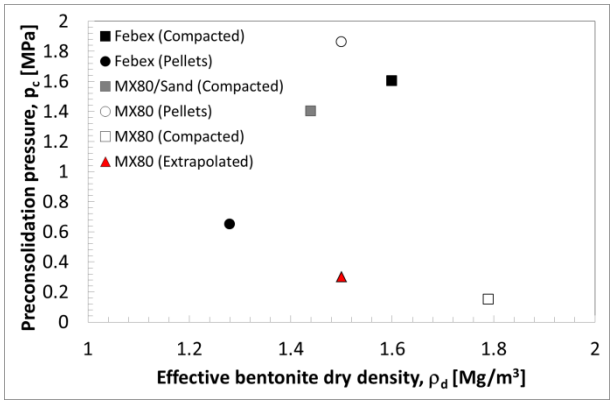

Fig. 4.55: Evolution of preconsolidation pressure at suction s=0 (i.e. saturated state) of five bentonites with initial dry density.

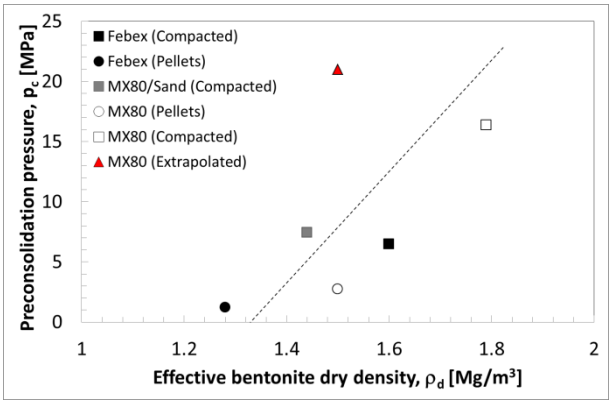

Fig. 4.56: Evolution of preconsolidation pressure suction s=∞ (i.e. dry state) of five bentonites with initial dry density.

4.4.5. Alternative formulation for compressibility coefficient for change in suction

Even though, the Barcelona Basic Model is able to reproduce a wide range of phenomena taking place during bentonite hydration, an important drawback is represented by the significant swelling pressure overestimation when isochoric wetting tests are modelled (Gens and Sanchez 2014).

When the BBM is selected to model swelling clays during saturation in constant volume conditions, the swelling stress can be obtained by integrating equation Eq. 4.19. Thus, under isotropic and elastic conditions, the resulting stress increment reads as follows:

$$p(s) = p_A \left(\frac{s_A + u_{atm}}{s_B + u_{atm}}\right)^{\frac{\kappa_s}{\kappa}} \quad \text{(Elastic state)} \qquad \text{Eq. 4.47}$$

The stress increment is an exponential function of the ratio between the elastic compressibility parameters for change in suction (κ_s) and change in net stress (κ). In the hypothesis of isothermal conditions and stress paths mainly based on suction decrease (as reported in the analyses of this work), the elastic parameter κ accounts for the evolution of the yielding surface (Eq. 4.23) and irreversible plastic deformation development (Eq. 4.21), apart from the elastic volumetric evolution upon loading (Eq. 4.19). On the other hand, the parameter κ_s controls only volumetric changes upon hydration (Eq. 4.19). Thus, in order to limit the swelling pressure overestimation and to keep the following analysis straightforward, it is decided to evaluate only the effect of the parameter κ_s . Three strategies are presented:

1. Original constant elastic compressibility coefficient for change in suction κ_s (Alonso, Gens, and Josa 1990) (Eq. 4.48).

$$\kappa_s = constant \qquad \text{Eq. 4.48}$$

Even though the classic BBM formulation results into an overestimation of swelling pressure while modelling isochoric wetting tests, (Alonso, Gens, and Josa 1990) already introduced u_{atm} in Eq. 4.19 to avoid the infinitive swelling that occurs when null suction value is approached.

2. Constant elastic compressibility coefficient for change in suction κ_s for saturation values below a given threshold (Dieudonné 2016) (Eq. 4.49);

$$\kappa_s = \kappa_{s0}\ if\ S_r < S_r^* \ \&\ \kappa_s = 0\ if\ S_r \geq S_r^* \qquad \text{Eq. 4.49}$$

(Dieudonné 2016) proposes Eq. 4.49 considering the experimental tests performed by (Agus et al. 2013) on Calcigel bentonite and quartz mixtures. This model is formulated assuming that swelling pressure maintains a steady value when saturation is reached. Considering the high air entry values that bentonite based materials present (i.e. suction levels the material is able to sustain without desaturating), it is obvious that saturation is reached when suction is still high (Seiphoori, Ferrari, and Laloui 2014). Thus a threshold saturation value S_r^* is introduced beyond which the swelling capacity of the material (i.e. κ_s coefficient) is null. This assumption provides remarkable results when isochoric conditions are modelled, however it contradicts other experimental observations stating that most of the swelling deformation takes place when incredibly low suction values are approached (Seiphoori et al. 2016).

3. Elastic compressibility coefficient for change in suction κ_s pressure dependence (Eq. 4.50) (employed after discussion with Dieudonne' and various strategies assessment);

$$\kappa_s(p) = \kappa_{s0} * exp\ (-\alpha_p * p) \qquad \text{Eq. 4.50}$$

Where κ_{s0} is the elastic compressibility parameter for change in suction at null stress and α_p is a parameter controlling its dependency on the stress level. As it was observed in section 4.2.2, the swelling upon wetting at constant stress is strongly linked to the applied stress level (Fig. 4.7). (Dueck and Nilsson 2010) also observe this behaviour on compacted MX80 bentonite samples hydrated at constant vertical load (Fig. 4.57). It is clear that for increasing applied stress, decreasing swelling capacity is obtained, with possible wetting collapse according to (Lloret, Romero, and Villar 2004) and as the BBM modelling suggests. Differently from the other two formulations, this modelling strategy allows reducing the influence of initial stress conditions on the development of swelling pressure upon hydration as it will be clearly explained in the following. Moreover, Eq. 4.50 does not present abrupt coefficient variations such as Dieudonne' strategy. Thus, swelling pressure evolution evolves smoothly, without pressure drops that could affect numerical stability.

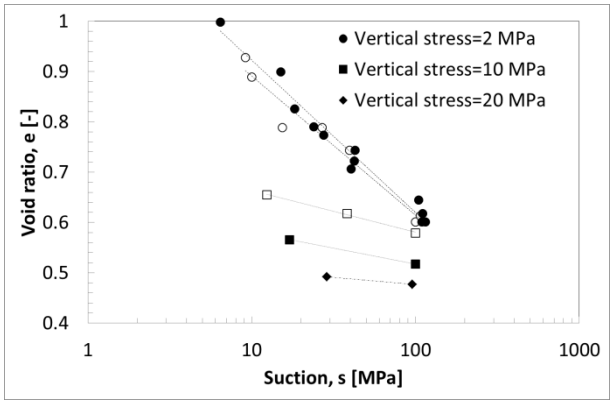

Fig. 4.57: Void ratio evolution with suction at constant vertical stress on MX80 compacted bentonite samples (Dueck and Nilsson 2010). White and black points differ for loading paths conditions before swelling.

The performances comparison between the three strategies is conducted on the experimental test adopted to calibrate the MX80 and sand mixture of paragraph 0. The model parameters are given in Table 4.1 and coincide for the three strategies, which evolves only for the κ_s formulation. For Eq. 4.49 the saturation threshold value is selected equal to $S_r^* = 0.98$.

Initial state is equal to suction s=38 MPa and confining net stress equal to p=0.10 MPa.

Fig. 4.58 shows the stress paths and the unique LC curve in the (p – s) plane for wetting under isochoric conditions for the three numerical strategies. Eq. 4.49 and Eq. 4.48 result into completely overlapping stress paths up to $S_r^* = 0.98$. Indeed Eq. 4.48 can be read as Eq. 4.49 with $S_r^* = 1$. In the elastic domain, the stress increment is related to the constant ratio $\frac{\kappa_s}{\kappa}$ (Eq. 4.47) and it results into a straight line into the log-log (p – s) plane. Consequentially, among other factors, the initial conditions (i.e. initial suction and confining stress) affect remarkably the point in which the yielding surface is touched and the computed final swelling pressure value. On the other hand, with respect to Eq. 4.50 strategy, it can be observed that the stress path slope is decreasing, as a result of the κ_s decrease for increasing net stress (Fig. 4.59). For this modelling strategy, the stress increase and the κ_s evolution are coupled according to Eq. 4.47 and Eq. 4.50. This significantly reduces the impact of the initial conditions on the stress path and computed swelling pressure development and final value.

The elasto-plastic swelling pressure development does not depend only on the κ_s parameter, but also on the yielding surface evolution. However, as Fig. 4.58 shows, the stress paths given by Eq. 4.49 and Eq. 4.48 diverge when $S_r \geq S_r^*$, resulting in final swelling pressure values respectively equal to ~10 MPa (Eq. 4.49) and ~110 MPa (Eq. 4.48). With respect to Eq. 4.49 strategy, a stress drop takes place. This is obtained in order to maintain the constant volume conditions without violating the yield criterion. Indeed, further suction decrease does not cause any elastic deformation, but, the preconsolidation pressure is still decreasing with

suction. Thus, a decrease in mean net stress is observed. The elasto-plastic stress path related to Eq. 4.50 is somehow similar to the one of Eq. 4.49. However, the excessive swelling pressure development is limited by the decreasing tendency of κ_s (Fig. 4.59). The final swelling pressure value is equal to 4 MPa and it is much more reasonable with respect to experimental observations (Fig. 4.49 section 4.2.3).

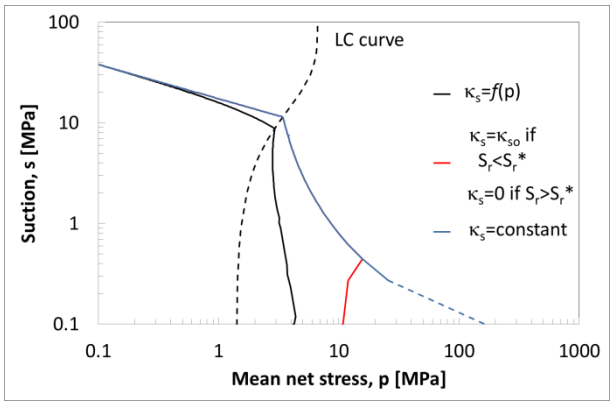

Fig. 4.58: Stress paths and LC curves in the (p – s) plane for wetting under isochoric conditions. Comparison between numerical strategies.

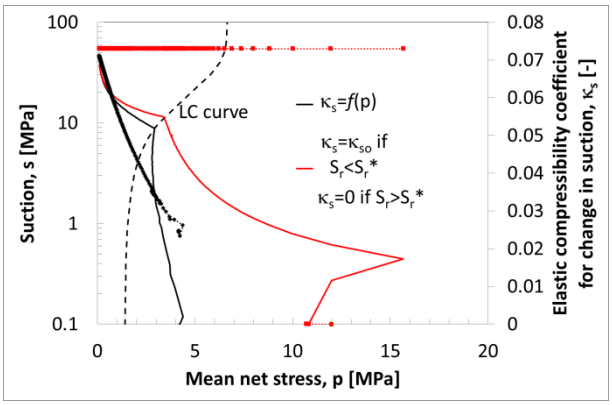

Fig. 4.59: Stress paths and LC curves in the (p – s) plane for wetting under isochoric conditions and κ_s evolution with mean net stress. Comparison between numerical strategies (Eq. 4.50 and Eq. 4.49).

Fig. 4.60 presents the comparison between for the proposed numerical strategies with respect to the void ratio evolution with suction at constant vertical stress. Also in this case, Eq. 4.49 and Eq. 4.48 present overlapping stress paths up to the selected threshold value. The slope of the strategy accounting for Eq. 4.50 is again lower. Fig. 4.61 shows that κ_s decreases for decreasing suction. This phenomenon is mostly related to the development of radial swelling pressure upon hydration at constant stress conditions. However, when the yielding surface is touched, the radial swelling pressure decreases Hence, κ_s increases again. Due to the fact that the radial stress development is limited, the κ_s value does not decrease dramatically. The final void ratio values are quite similar for the three strategies. They range between e=0.95 (for Eq. 4.50) and e=1.05 (Eq. 4.48). The final swelling deformation difference is negligible with respect to the one related to the swelling pressure development (which ranges between 4 MPa and 105 MPa). This allows concluding that even though Eq. 4.50 requires back analysis calibration for the determination of κ_{s0} and α_p parameters, it provides more accurate results for a larger range of phenomena and stress paths conditions.

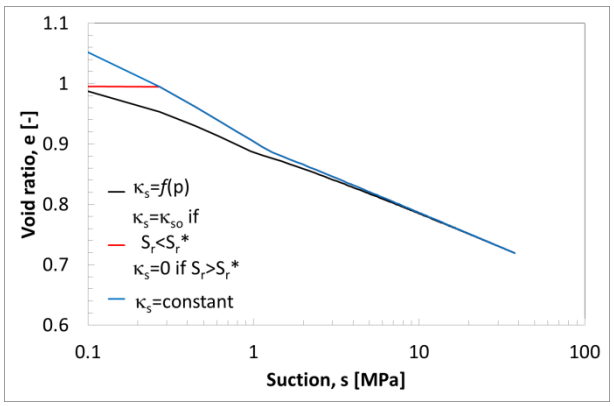

Fig. 4.60: Void ratio evolution at constant vertical stress as function of suction. Comparison between numerical strategies.

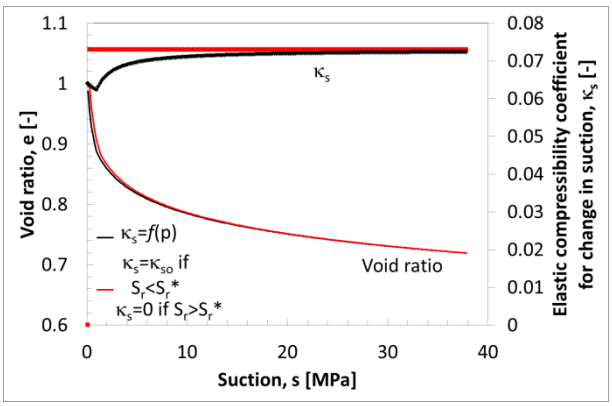

Fig. 4.61: Void ratio at constant vertical stress and κ_s evolutions as function of suction. Comparison between numerical strategies (Eq. 4.50 and Eq. 4.49).

4.5. Conclusions

This chapter aimed to present the most significant mechanical properties of bentonite-based materials and their reproducibility in the framework of constitutive models.

Classical experimental observations were firstly presented. Compressibility, swelling capacities and deviatoric responses were investigated via simple and robust laboratory tests. Regardless the unavoidable laboratory uncertainties and limitations, the strong suction (i.e. water content or/and saturation) and dry density dependences were highlighted for all the swelling clays mechanic characteristics and responses.

Successively, a number of existing constitutive mechanical models were recalled. Emphasis was put on models implemented in the elasto-plasticity framework.

Among those, the Barcelona Basic Model was exhaustively described. Given its well-known capacity to reproduce a wide range of phenomena taking place during bentonite hydration, it was selected to describe the numerical analyses presented in this thesis.

Calibration procedures were therefore proposed to underline some advantages of the BBM, while remarking its suitability also for the interpretation and homogenisation of laboratory tests results.

The section was continued with the introduction of the BBM parameters calibration of a number of bentonites, which will be deeply investigated in the following chapters, and it was enriched with comparison and discussions. An alternative procedure to overcome BBM limitations was also presented and compared to other recent strategies.

CHAPTER 5: MULTI-STRUCTURE ASSEMBLIES AT THE LABORATORY SCALE

CHAPTER 5: MULTI-STRUCTURE ASSEMBLIES AT THE LABORATORY SCALE

5.1.Introduction

The analysis of the hydro-mechanical features evolution of bentonite materials upon hydration is challenging.

The goal of this chapter is to take advantage of a combined experimental and numerical approach to study the effect of different pore structure distributions on mechanic and water transfer mechanisms for similar average dry density assemblies of bentonite.

The analysed experimental tests have been performed by CEA on MX80 pellet mixtures (7 mm and 32 mm pellets diameters are considered) and compacted block in multi-sensors equipped cells in the context of the BEACON project (Baryla et al. 2018; Bernachy-Barbe 2020; Sellin et al. 2020).

These tests provide quantitative information on granular materials, which is not as exhaustive as the one available for bentonite compacted blocks.

Then, the numerical strategy takes advantage on the Barcelona Basic Model (Alonso, Gens, and Josa 1990), which is considered for the bentonite mechanical behaviour, on pressure dependence, adopted for some mechanical parameters, and on the double porosity model proposed by Dieudonné, selected for the water retention behaviour and water permeability evolution (Dieudonné, Della Vecchia, and Charlier 2017).

Despite the heterogeneous initial pores structure distributions of the analysed samples are well-recognized, in the adopted numerical strategy the overall assemblies are described in the framework of continuum mechanic. The selected numerical approaches compare remarkably well with experimental measurements.

Especially, the non-monotonic evolution of the swelling pressure during the hydration phase is in good agreement with the experimental outcomes.

With reference to experimental results and numerical simulations comparisons at dismantling (i.e. dry density and water content distributions), this work allows determining the limits of numerical modelling simplifications with respect to real laboratory conditions and vice versa.

The detailed hydro-mechanical experimental and numerical studies provided in this chapter help to better understand the homogenisation processes that occur during the hydration of bentonite.

5.2.Materials

MX-80 bentonite in different forms is analysed (Fig. 5.1).

Isochoric wetting tests are performed on MX-80 bentonite. Tests WP5_1B, C_1 and C_2 consider pellets and crushed pellets mixtures (MX-80 bentonite: Laviosa-MPC Expangel SP32) with respective proportion between 70/30 and 67/33 in dry mass, differently from test C_6 that concerns a compacted block specimen. During the pellets samples preparation, the components are arranged to minimize macroscopic gradients by building layer by layer dense arrangements of pellets with a fraction of powder (obtained from crushed pellets) filling the inter-pellets gaps, not exceeding the prescribed target dry density.

The dry density for one pellet 32 mm pellet (a. Fig. 5.1) is between 2.01 and 2.05 Mg/m^3 and initial water content w≈4.04%, whereas crushed pellets present a particle size between 0 and 2.5 mm and w≈4.55% (Talandier 2018) (Fig. 5.2). Further information concerning this pellet size can be found in (Bernachy-Barbe et al. 2020). The dry density for one 7 mm-pellet (b. Fig. 5.1) is approximately 2.10 Mg/m^3 with initial water content equal to 5.07%. Further details concerning the 7 mm pellets features can be found in (Molinero et al. 2017). The crushed pellets present the same granulometry curve as the one of test WP5_1B.and initial water content w≈10.33%. Test C_6 concerns MX-80 compacted bentonite powder (c. Fig. 5.1) that is placed in the cell with a radial gap partially filled with loose powder.

Differences between the complex initial pores structure distributions of the three assemblies are easily detectable. They consist in small diameter pores structures, given by the pellets and compacted block (high dry density) and large diameter pores structures composing crushed pellets and gaps space filled with loose powder (low dry density). With respect to tests WP5_1B, C_1 and C_2, those structures and dry densities are randomly positioned inside the samples due to the casting technique, whereas in test C_6 the largest pores structures are mainly placed between the highly compacted bentonite sample and the cell wall in the radial direction.

a. b. c.

Fig. 5.1: MX-80 bentonite assemblies analysed in the experimental tests.

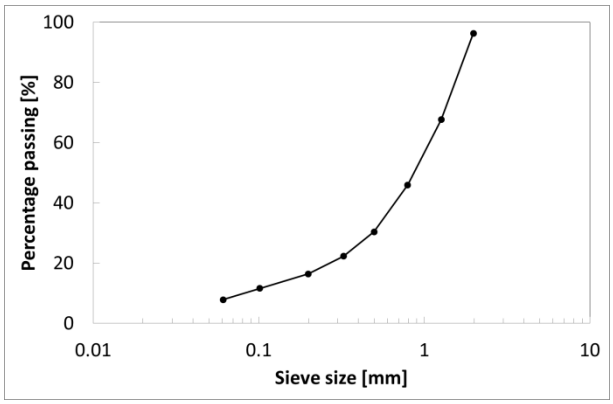

Fig. 5.2: Grain size distribution of the crushed pellets powder for test WP5_1B, C_1, C_2 and C_6.

5.2.1. Water retention behaviour

The selected double porosity dry density dependent water retention model does not distinguish the initial pore structure distributions of the considered assemblies, thus a unique set of parameters corresponding to the calibration proposed by (Dieudonné, Della Vecchia, and Charlier 2017) for compacted MX-80 bentonite is selected (Fig. 5.3 and Table 5.1: Parameters of the water retention curve model.)

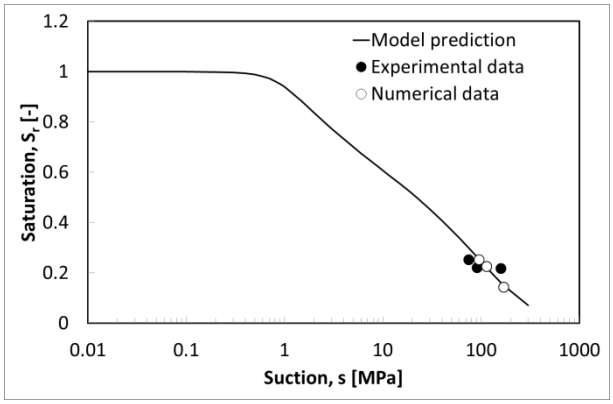

Fig. 5.3: Model simulation for the water retention curve. Initial experimental data and initial numerical data for tests WP5_1B, C_1, C_2 and C_6.

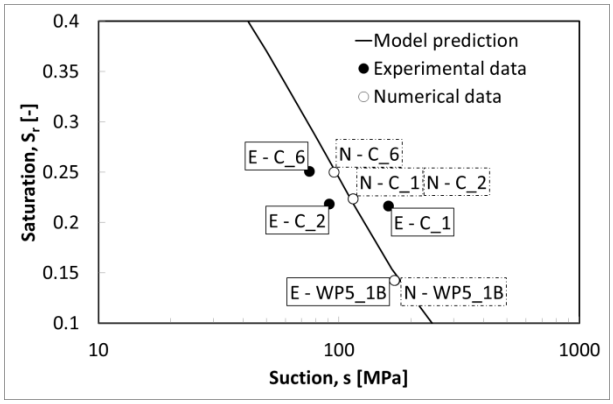

Fig. 5.4: Model simulation for the water retention curve. Initial experimental data and initial numerical data for tests WP5_1B, C_1, C_2 and C_6. Suction s between 10 and 1000 MPa and Saturation degree between 0.10 and 0.40.

Table 5.1: Parameters of the water retention curve model.

EXPERIMENTAL TESTS		WP5_1B	C_1 - C_2	C_6
e_{m0}	[-]		0.31	
β_0	[-]		0.1	
β_1	[-]		0.48	
C_{ads}	[MPa^{-1}]		0.0075	
n_{ads}	[-]		0.2	
n	[-]		3	
m	[-]		0.45	
A	[MPa]		0.2	

One single retention curve is used for the four tests and three different materials. Then the initial suction is deduced from the retention curve. It is considered that the water ratio measurement is more accurate than the suction one. With respect to this modelling choice, the initial relative humidity (i.e. suction) of the numerical samples is different from the one measured at the initial stage of the corresponding test (Fig. 5.3). It is worth noting also that the initial saturation values differ between the model and the experiments due to the slightly different initial dry density taken in consideration (Fig. 5.4).

5.2.2. Flow properties

The parameters for the water permeability evolution (Table 5.2 and Fig. 5.5) were calibrated by best-fitting the responses of the water intake time evolution for the three different assembly types, thus the initial values differ being the water intake kinetics non-identical. Consequentially, the model is validated by comparing the swelling pressure kinetics and final dry density and water content distributions.

Table 5.2: Parameters of the permeability evolution model.

EXPERIMENTAL TESTS		WP5_1B	C_1 - C_2	C_6
C_k	[m^2]	1.8×10^{-20}	1.8×10^{-20}	1.8×10^{-20}
m	[-]	1.5	1.5	0.4
n	[-]	0.2	0.4	0.4
γ	[-]	4	3	2

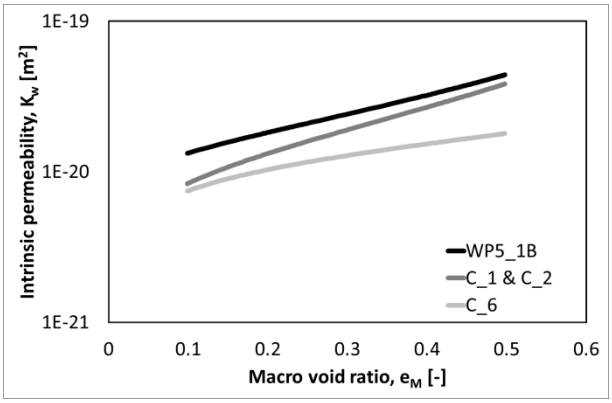

Fig. 5.5: Intrinsic permeability evolution with macro-void ratio accordingly to **Eq. 3.29** and Table 5.2.

5.2.3. Mechanical behaviour

The mechanical parameters (Table 5.3) for test WP5_1B, C_1 and C_2 were derived from the experimental campaign performed by (Molinero et al. 2019) on a similar assembly of MX-80 pellets mixture and for test C_6 from the experimental campaign performed by (Tang, Cui, and Barnel 2008) on MX-80 bentonite sample compacted with the same procedure. Mechanical parameters such as the friction angle, Poisson ratio and cohesion are in general very difficult to measure during experimental campaigns on swelling unsaturated bentonites (especially with respect to pellets mixtures) and very few data are available. Due to this, a trial and error procedure was adopted to reproduce the target results in terms of the swelling pressure measurements presented in this work.

Table 5.3: Parameters of the mechanical model.

EXPERIMENTAL TESTS		WP5_1B	C_1 - C_2	C_6
κ	[-]	0.06	0.06	0.03
κ_s	[-]	0.07	0.08	0.220
α_p	[-]	2.6×10^{-7}	2.6×10^{-7}	3.5×10^{-7}
p_0*	[MPa]	1.86	1.86	0.3
p_c	[MPa]	0.93	0.93	0.086
$\lambda(0)$	[-]	0.20	0.20	0.25
r	[-]	0.75	0.75	0.32
ω	[Pa^{-1}]	1.00×10^{-7}	1.00×10^{-7}	0.51×10^{-7}
φ	[°]	25	25	20
ν	[-]	0.35	0.40	0.17
$c(0)$	[MPa]	0.10	0.10	0.10
k	[-]	0	0	0.0046

5.3.Multistructural samples at laboratory scale analysis

5.3.1. Description of the test

The objective of this series of tests is to investigate the re-saturation in isochoric conditions of four MX-80 bentonite samples presenting different initial pore-size structure distributions and hydration lengths but similar samples dry density.

The tests were performed by French Atomic Energy Commission (CEA) in the context of BEACON project (Sellin et al. 2020).

These tests are performed in controlled conditions, presenting extensive instrumentation, making possible the complete monitoring of the hydromechanical state of the samples.

Indeed, the swelling pressure field development upon saturation (and heterogeneities) is assessed using an array of sensors at various spatial locations, as well as the relative humidity field and the water intake time evolution.

Physical state in terms of dry density and water content are characterized only in a post-mortem way (in the final state of the experiment), together with Mercury Intrusion Porosimetry (MIP) measurements performed on freeze-dried samples after dismantling.

Test WP5_1B sample is composed of 32 mm-pellets and crushed pellets, thus of three layers of intact pellets (38÷39 pellets) and a fourth layer with lower number of split pellets (≈8 pellets) with a final sample height equal to 105.15 mm and diameter equal to 240 mm. The sample to pellet diameter ratio (D/d) and sample height to pellet diameter ratio (H/d) are respectively equal to 7.5 and 3.3. The initial water content of the total assembly is equal to 4.23%.

Tests C_1 and C_2 are carried out on 7 mm-pellets/powder mixes. The initial dry densities of tests C_1 and C_2 are respectively equal to 1.50 mg/m^3 and 1.49 Mg/m^3, with initial water content equal to w≈6.65% and w≈6.81% and samples heights equal to 45.02 mm and 45.23 mm and diameter equal to 57 mm. The sample to pellet diameter ratio (D/d) and sample height to pellet diameter ratio (H/d) are respectively equal to 8.1 and 6.4 (twice as WP5_1B H/d ratio).

Test C_6 concerns MX-80 bentonite sample isotropically compacted at initial dry density equal to ρ_d=1.75 g/m^3 and water content w=7.44%. In order to perform the isotropic compaction, the clay was first compacted in a neoprene tube (90 mm in diameter, 120 mm in length and 1.2 mm in thickness) with a closed end. The sample within the tube was then compressed in an isotropic cell under a static pressure of 40 MPa and finally machined in order to fit the cell dimensions to a height equal to 45.82 mm and diameter equal to 52.8 (versus a cell diameter equal to 57 mm). The sample is placed in the cell with a radial gap partially filled with 3.35 g of loose powder (w=7.44%) in order to obtain an overall final dry density equal to ρ_d=1.52 Mg/m^3. The powder selected for the compaction of the sample and to fill the gap is the same as the one adopted for tests WP5_1B, C_1 and C_2. The addition of loose powder in the gap was used to adjust density and to avoid as much as possible instantaneous flooding of the gap by water.

Test WP5_1B was stopped at 1214 days after the beginning of hydration, C_1 after 68 days, C_2 after 45 days and C_6 after 182 days.

Experimental samples specifications can be found in Fig. 5.6 and Table 5.4.

Table 5.4: Initial state and characteristics of the experimental samples.

EXPERIMENTAL TESTS	WP5_1B	C_1	C_2	C_6
Type of assembly	32 mm pellets/crushed pellets	7 mm pellets/crushed pellets	7 mm pellets/crushed pellets	Compacted block/loose powder
Diameter [mm]	240	57	57	57
Height [mm]	105.15	45	45.2	45.8
Pellets/Crushed pellets [% mass]	69.9/30.1	66.9/33.1	66.9/33.1	[-]
Dry density [Mg/m^3]	1.52	1.50	1.49	1.52
Water content [%]	4.23	6.65	6.81	7.44
Sample to pellet diameters ratio (D/d) [-]	7.5	8.1	8.1	[-]
Sample height to pellet diameter ratio (H/d) [-]	3.3	6.4	6.4	[-]

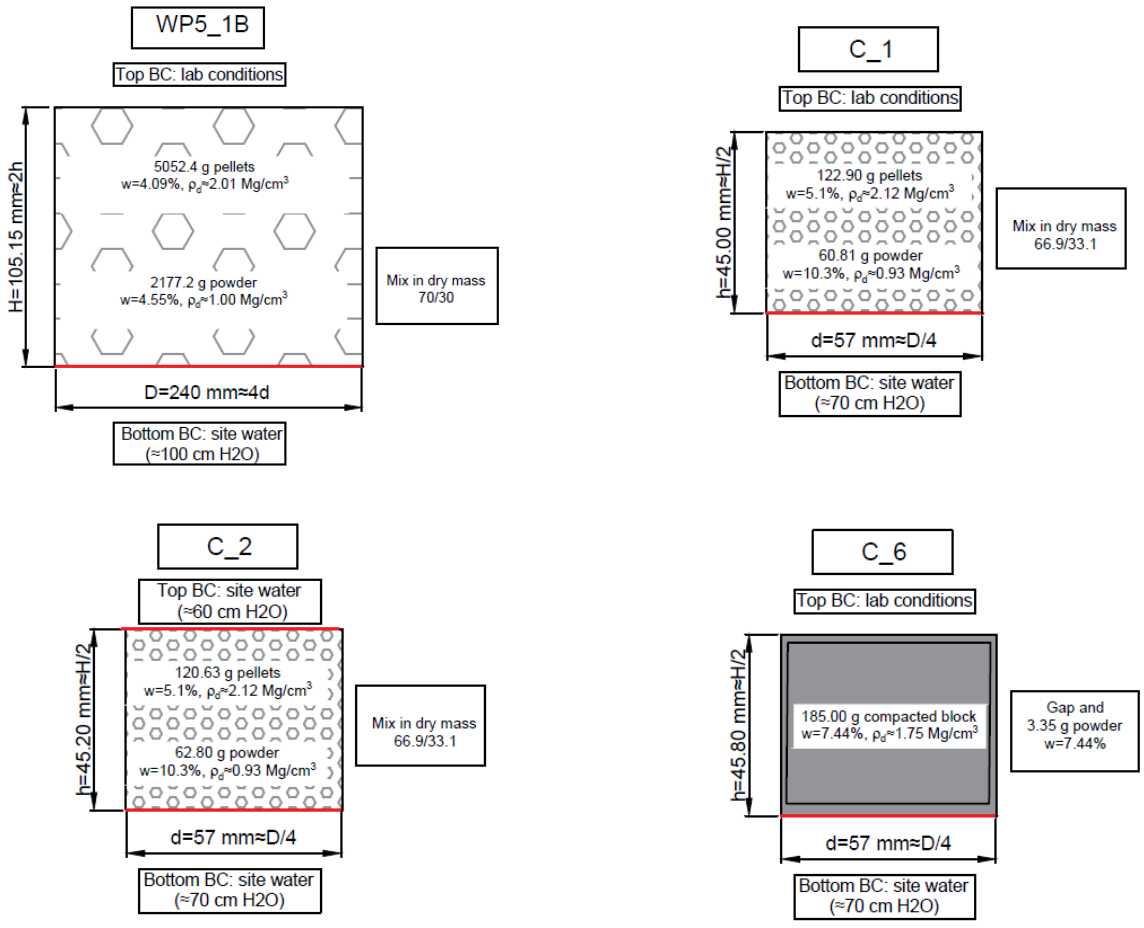

Fig. 5.6: Characteristics of the considered samples.

The experimental devices consist in constant volume cells described in details in (Imbert and Villar 2006).

Sensors measure axial force and displacements, radial total pressure and relative humidity at several levels. Water columns and tanks are placed on a continuous weighing device. Hydration is allowed with a slight differential pressure. Synthetic site water is injected with a very small hydraulic head (100 cm for test WP5_1B and 60-70 cm for tests C_1, C_2 and C_6) through porous plates on the bottom side (and/or the upper side) of the chamber, blocked at approximately zero displacement. In the case of unilateral hydration, the other side is placed at laboratory conditions to ensure evacuation of entrapped air.

Two different diameters multi-equipped-sensors cells are used. The device selected for test WP5_1B presents a cell diameter equal to 240 mm and it is equipped with four radial pressure sensors and five relative humidity/temperature sensors at 20, 40, 60, 80 and 100 mm from the bottom face (Fig. 5.7).

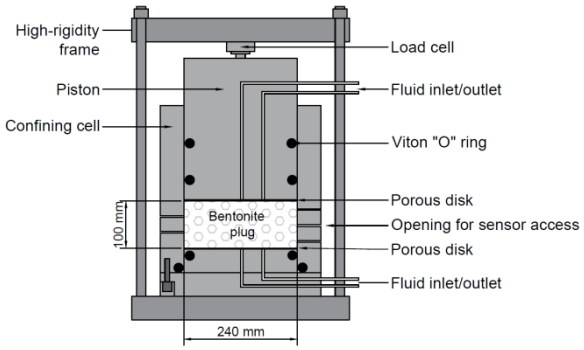

Fig. 5.7: Schematic representation of the experimental set-up of test WP5_1B.

Tests C_1, C_2 and C_6 are carried in a smaller multi-sensor oedometric cell of diameter 57 mm equipped with 9 pressure sensors (total pressure or interstitial pressure) at three vertical positions (6.6 mm, 23.3 mm and 40 mm) and angular positions (0°, 90° and 180°) (Fig. 5.8). These sensitive elements are 7.6 mm in diameter. Three thermo-hygrometers are positioned at 270° at the same vertical positions as the pressure sensors.

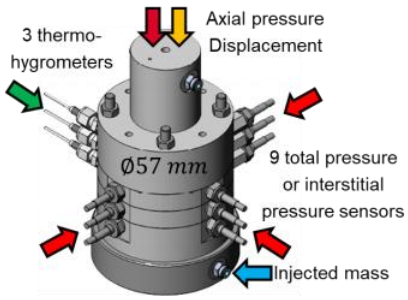

Fig. 5.8 Schematic representation of the experimental set-up of tests C_1, C_2 and C_6.

5.3.2. Features of the analysis

The numerical bentonite samples are modelled with 25 eight-noded isoparametric elements. The problem is assumed mono-dimensional and oedometer conditions are considered (Fig. 5.9). The above-mentioned differences between the complex initial pores structure distributions of the three assemblies are well-recognized. Nevertheless, in these modelling strategies, these distinctions are not taken in consideration. Thus, initial uniform dry density equal to ρ_d=1.52 Mg/m^3 is assumed for all the four tests (considering the similar initial dry density in the experimental tests). Same hydro-mechanical properties and hydro-mechanical state are set in the entire domain with initial uniform suction s related to the saturation degree S_r, (obtained by the corresponding water content w and ρ_d=1.52 Mg/m^3) via the adopted dry density dependent water retention model (Table 5.5). Initial water contents w in the numerical model are equal to the ones experimentally measured at the initial state (Table 5.4).

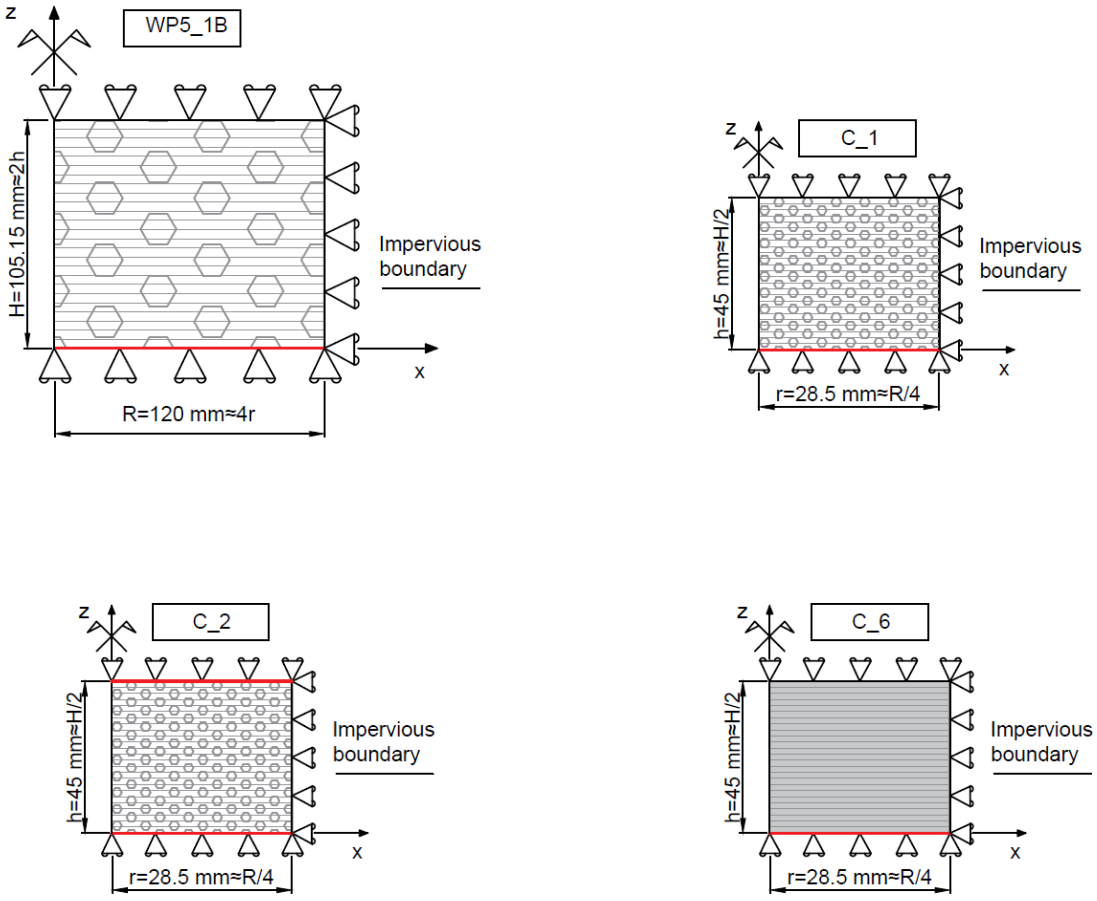

Fig. 5.9: Boundary conditions of the model.

Table 5.5: Initial state and characteristics of the numerical samples.

NUMERICAL SIMULATIONs	WP5_1B	C_1	C_2	C_6
Type of assembly	Homogeneous porosity	Homogeneous porosity	Homogeneous porosity	Homogeneous porosity
Diameter [mm]	240	57	57	57
Height [mm]	105.15	45	45	45
Pellets/Crushed pellets [% mass]	[-]	[-]	[-]	[-]
Dry density [Mg/m3]	1.52	1.52	1.52	1.52
Water content [%]	4.23	6.65	6.65	7.44
Initial suction [MPa]	171.00	115.00	115.00	100.00

The hydration of the sample is provided from the bottom face for tests WP5_1B, C_1 and C_6 (red line, Fig. 5.9) and additionally from the top for test C_2, assuming a suction decrease from the initial value to the experimental boundary conditions (Fig. 5.6) occurring in 1000 seconds.

The sample of test WP5_1B is subjected to an initial confining stress value of 0.02 MPa in the axial direction and 0.2 MPa in the radial one similarly to experimental records. On the other hand tests C_1, C_2 and C_6 are subjected to 0.02 MPa of confining stress in both axial and radial directions, considering an average isotropic stress state computed on all the experimental measurements. Such low initial stress values help stabilising numerical convergence at the beginning of the computation, but thanks to the adopted strategy of elastic compressibility coefficient for change in suction κ_s pressure dependence, they do not affect final swelling pressure results.

5.3.3. Experimental and numerical results

Water intake

Fig. 5.10 shows the water inflow time evolution normalized with respect to the cell volume together with semi-logarithmic scale for time. This normalisation helps to compare different cell sizes (and stabilisation times) and to avoid uncertainties related to the initial water content of the samples. It represents a good alternative with respect to the sample average saturation degree time evolution (Fig. 5.11), to which is linearly proportional. For instance test WP5_1B presents a final water mass injection value equal to 1849 g, 30 times larger with respect to the final water quantity measured in test C_6. Tests WP5_1B, C_1 and C_2 present a final water inflow/cell volume ratio equal to 0.40, with an unexpected increase and decrease of water inflow for test C_2 possibly related to the establishment of water flux between the bottom and top wetting surfaces. Test C_6 shows a water inflow/cell volume ratio equal to 0.60, larger with respect to the other experimental tests and unexpected with respect to the initial saturation degree. Water intake stabilisation time scale is proportional with the square of the hydration length (after Terzaghi consolidation theory for saturated soil). Namely, test WP5_1B presents a hydration length equal to 105.15 mm, tests C_1 and C_6 approximately equal to 45 mm and test C_2 equal to 22 mm, due to the fact that it is hydrated from the top and bottom surfaces simultaneously.

These experimental results show that the 57 mm diameter cell (tests C_1, C_2 and C_6) outcomes in water injections evolution, which are not as smooth and monotonic as the one related to the 240 mm diameter cell (Fig. 5.10 and Fig. 5.12). This can be related to the shorter experimental time scale, characterized by evident oscillations, but also to the difficulty to measure such small water quantities, which can undergo evaporation.

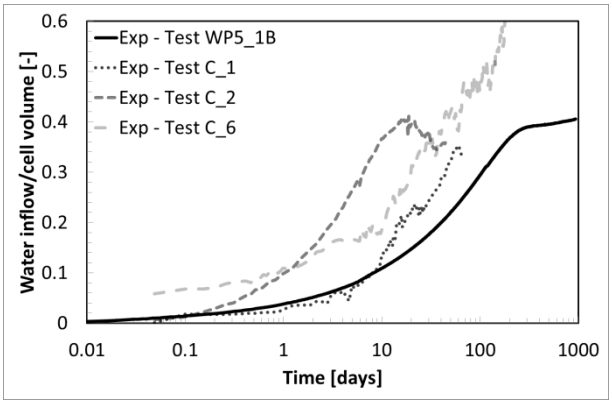

Fig. 5.10: Water mass injection time evolution divided by cell volume for tests WP5_1B, C_1, C_2 and C_6. Comparisons between experimental data.

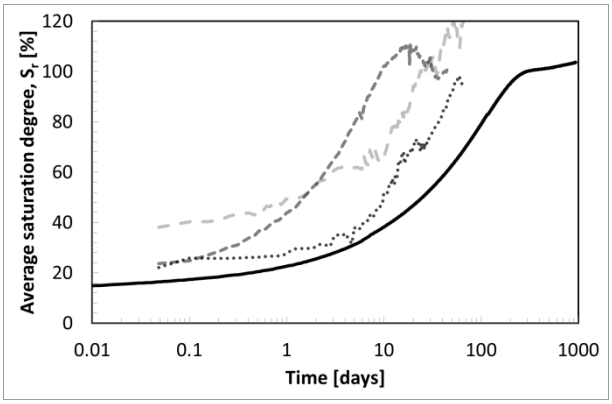

Fig. 5.11: Average water saturation time evolution divided by cell volume for tests WP5_1B, C_1, C_2 and C_6. Comparisons between experimental data.

The permeability law evolution is calibrated on the experimental water intake time records for each type of assembly. Due to this, the numerical simulations for water intake evolution (Fig. 5.12) reproduce well the experimental results especially for test WP5_1B (32 mm-pellets mixture). With respect to 7 mm-pellets mixtures, it is interesting to note that for test C_1 (one side hydration) the numerical and experimental results do not coincide during the initial hydration phase. Namely, the experimental results underline a hydration process which is slower than the numerical one. On the other hand, numerical and experimental results for test C_2 (double side hydration) coincide well in the initial and final phases. Nevertheless, the numerical simulation of test C_2 does not reproduce the experimental increase and decrease of water inflow occurring between the 8^{th} and the 30^{th} days of the test.

For test C_6, the numerical and experimental water intake time evolution correspond completely, especially at the initial phase, with respect to the variation rate with an evident discrepancy in final values. The numerical simulations are consistent with the initial experimental and numerical water contents, therefore, an experimental uncertainty is assumed.

For tests WP5_1B, C_1 and C_2, the numerical and experimental final water injection quantities are comparable as a consequence of similar initial saturation degrees. This result allows concluding that in terms of hydraulic properties the selected dry densities for tests C_1 and C_2 and sample dimensions for tests C_2 and C_6, which are slightly different between the experimental and numerical tests, do not affect remarkably the results.

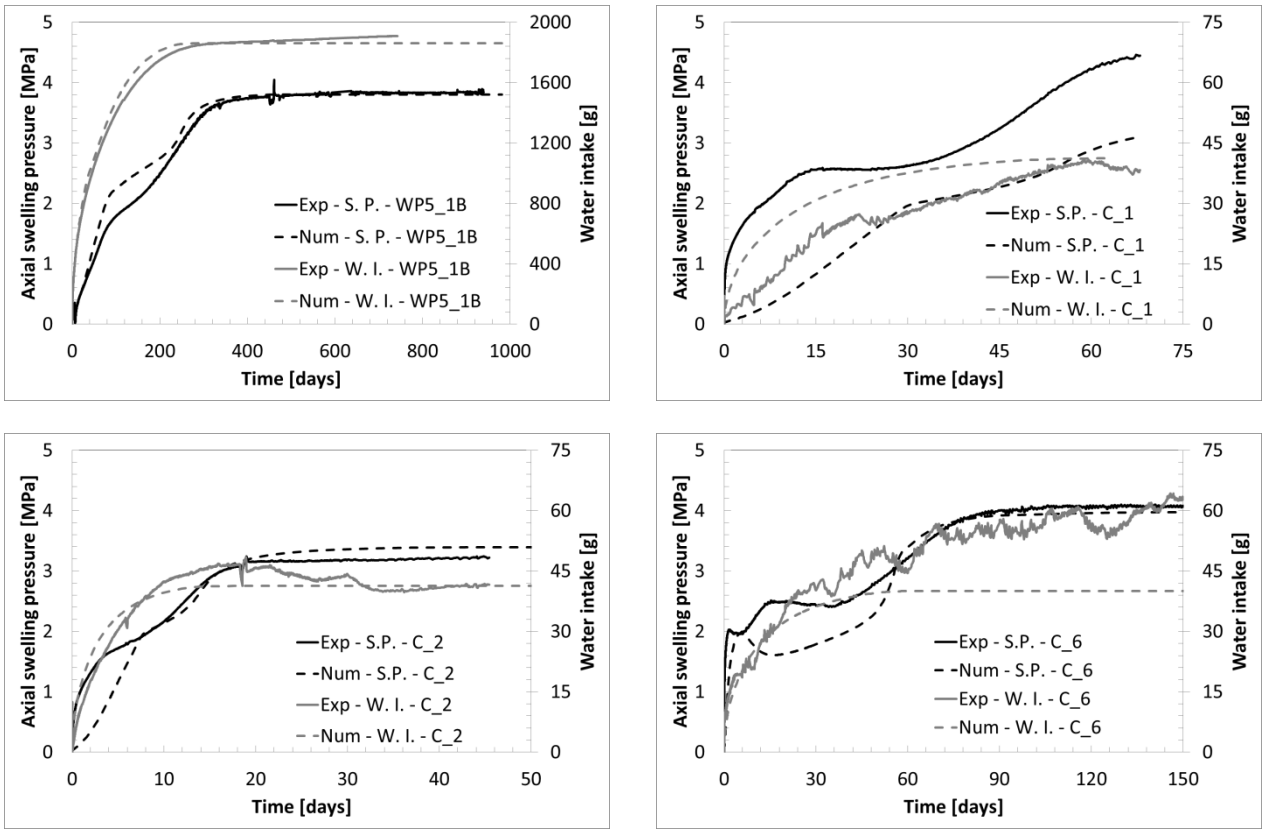

Fig. 5.12: Swelling pressure in axial direction and water mass injection time evolution for tests WP5_1B, C_1, C_2 and C_6. Comparisons between experimental data and numerical simulations.

Swelling pressure

Swelling pressures are measured axially. The axial total stress is considered uniform on each sample. The final axial swelling pressure values range between 3 MPa and 4 MPa, with the maximum value equal to 4.45 MPa recorded in test C_1 and the minimum equal to 3.27 MPa recorded for test C_2 (Table 5.6). While each sample presents about the same initial density and same initial water content, the final axial pressures differ highly, which is unexpected and not predictable by most constitutive mechanical models. Tests C_1 and C_2 are the same type of assembly (i.e. 7 mm pellets mixture) with dry density ρ_d=1.50 Mg/m^3 and ρ_d=1.49 Mg/m^3 respectively. The dry density discrepancy between the two tests is equal to 0.67%, which does not justify a final axial swelling pressure discrepancy equal to 26%.

Table 5.6: Final axial swelling pressure values. Comparisons between experimental data and model simulations for tests WP5_1B, C_1, C_2 and C_6.

Test Reference	Final Axial Swelling Pressure [MPa]	
	Experimental	Numerical
WP5_1B	3.80	3.80
C_1	4.45	3.25
C_2	3.27	3.27
C_6	4.08	3.98

Axial swelling pressure experimental results of the four tests (Fig. 5.12 and Fig. 5.13) show similar pressure evolution with time. Three phases can be distinguished: an initial quick swelling pressure increase, a second phase with a slower increase, a change of curvature, and the last one with a new increase of the swelling pressure. Such features have already been described by (Imbert and Villar 2006) with respect to FoCa bentonite granular mixtures. (Lloret et al. 2003) describes similar stress paths analysing the behaviour of compacted Febex bentonite subjected to constant volume hydration with a special focus on the interaction between micro and macrostructure.

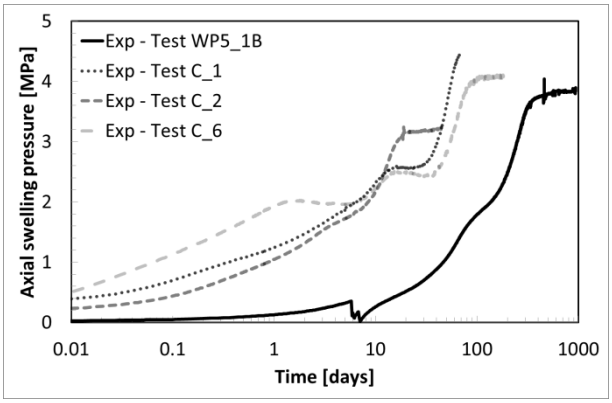

Fig. 5.13: Swelling pressure in axial direction time evolution for tests WP5_1B, C_1, C_2 and C_6. Comparisons between experimental data.

The first swelling pressure increase corresponds to the stage of high suction and low swelling pressure. In the framework of elasto-plasticity, the stress state has not reached the yielding surface. It can be assumed that the stress path is defined by the increase of load required to compensate the small swelling strains due to suction reduction (Fig. 5.12). The elastic swelling pressure in the axial direction develops with higher rate in test

C_6 (compacted bentonite sample) with respect to tests WP5_1B, C_1 and C_2. The second phase occurs after reaching the preconsolidation pressure (yield locus), in which the stress paths encounter a drastic change of slope. According to (Lloret et al. 2003), the micro-structure can present a load sufficiently high that can cause the collapse of the macro-structure, where the successive vertical stress decrease is due to the compensation for the collapse compressive strains. The microstructural swelling strains contribute to the compensation for collapse deformation, and if it is large enough it can compensate the swelling pressure decrease. The third phase corresponds to the region of low suction and high saturation. In this range, the microstructural swelling strains exhibit their largest magnitude (Wang, Cui, et al. 2013) and overcome any possible collapse strains. The stress increases again to compensate for the large swelling strains.

Fig. 5.14 and Fig. 5.15 propose an alternative procedure to analyse the bentonite samples stress-path. The average saturation degree and the water inflow are global quantity of a given specimen. Contrarily, suction, which characterises the classical mean stress – suction plane (p – s), depends on the position inside the sample of the analysed point at a given time. Fig. 5.14 and Fig. 5.15 show respectively the experimental and numerical axial swelling pressure as function of the average degree of saturation of the sample results and simulations. The average saturation degree is computed via the water intake time evolution records considering a constant water density equal to ρ_w=1Mg/m^3. This representation allows avoiding the use of the semi-logarithmic scale during the comparison of different sample sizes

Especially with respect to experimental data, it is possible to observe an evident axial swelling pressure rate increase for high saturation degree (i.e. ~80%). This zone corresponds to low suction level. The three material assemblies' present different trends in this plane, with similar curves shape for tests C_1 and C_2. This is due to the fact that they consist in the same material type (i.e. 7 mm pellet mixtures). The experimental results are more disperse with respect to the numerical ones. Discrepancies are due to several factors:

- A number of experimental investigations (Bernachy-Barbe et al. 2020; Imbert and Villar 2006) indicate that the final swelling pressure value depends on the sample size (here different sample sizes are accounted);

- The hydro-mechanical response of a given assembly is also due to its composition. For instance the percentage of powder-pellets (Dardé 2019) plays a relevant role;

- Undeniably, the pores structure distribution in the sample is the main reason of such dispersion, as this work assesses.

From a numerical point of view, tests C_1 and C_2 are superposed, due to the fact that the same hydro-mechanical parameters are set and the test conditions are fully controlled and determined. Differences between the numerical simulations are related to the different calibrated mechanical parameters and to the water transfer mechanism.

This can be easily proved by considering the same stress path in the (s – p) plane (Fig. 5.16). Average suction is obtained by corresponding average saturation via the adopted WRCs in the hypothesis of constant dry density. During saturation at constant volume conditions, in the elastic domain, the stress path slope is controlled by the ratio κ_s/κ (via eq 3.31 chapter n "on the mechanical behaviour…"). Accordingly, increasing swelling pressure is obtained for increasing ratio κ_s/κ for the same suction change. The elasto-plastic response is controlled by the yield loci and their evolution. Tests C_1 and C_2 do present the same response due to the fact that the same mechanical parameters are set. Test WP5_1B is similar to tests C_1 and C_2 in the post-yielding phase because the same yielding surface is selected for the similar assemblies. Test C_6 path is completely different in agreement with the selection of the elastic parameters and with the shape of the yielding surface. The calibrated mechanic parameters are recalled in Table 5.3.

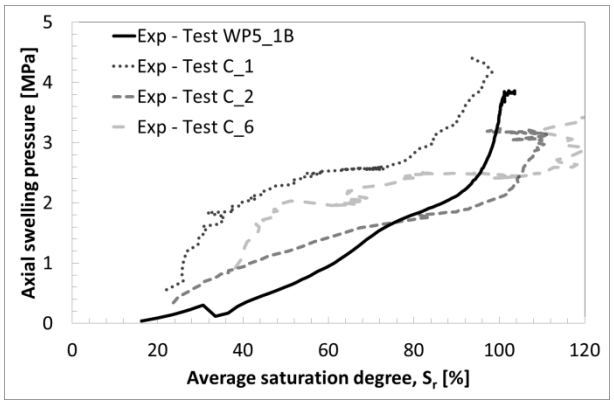

Fig. 5.14: Swelling pressure in axial direction as average saturation degree of the sample function for tests WP5_1B, C_1, C_2 and C_6. Experimental data.

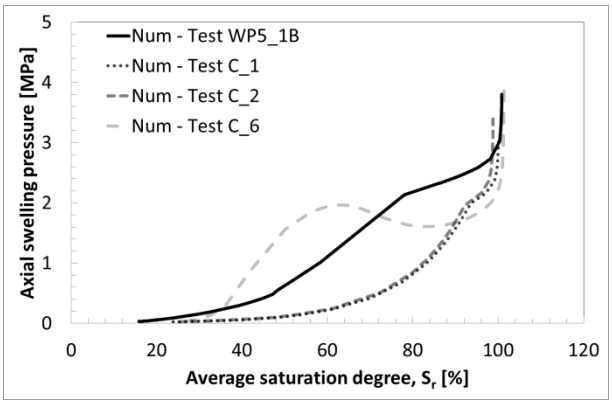

Fig. 5.15: Swelling pressure in axial direction as average saturation degree of the sample function for tests WP5_1B, C_1, C_2 and C_6. Numerical simulation.

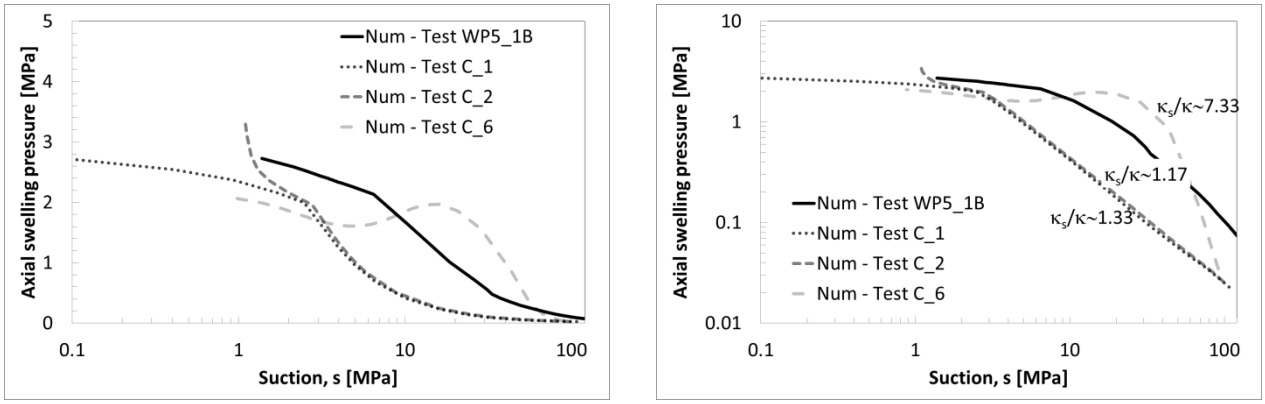

Fig. 5.16: Swelling pressure in axial direction as average suction level of the sample function for tests WP5_1B, C_1, C_2 and C_6. Numerical simulation.

The radial total pressure measurements (Fig. 5.17, Fig. 5.19 and Fig. 5.18) show variations with respect to the sensors position. It is important to mention that, during an experimental test, the radial pressure is more difficult to measure with respect to the axial ones due to the fact that it is strongly affected by the test conditions and representative only of a limited portion of the sample. Also the presence of a possible radial pressure gradient has to be taken into account (particularly evident in test C_6). Consequentially, those values have to be treated and interpreted with caution. Those measurements are averaged. The experimental records differ in general from the average value of the $\pm$5%. More dispersed measurements with respect to the average ($\pm$20%) for test C_1 and z=40 mm are found.

The final average values range between 2.8 MPa and 4.8 MPa (Table 5.7 and Table 5.8), much more than the axial pressure values. The time evolution of the radial pressures is mostly similar to the axial pressure evolution. It can be observed the similarity of pressure values between the top radial sensors measurements and the upper axial sensor, especially close to saturation. This suggests an isotropic stress state near the top sensor.

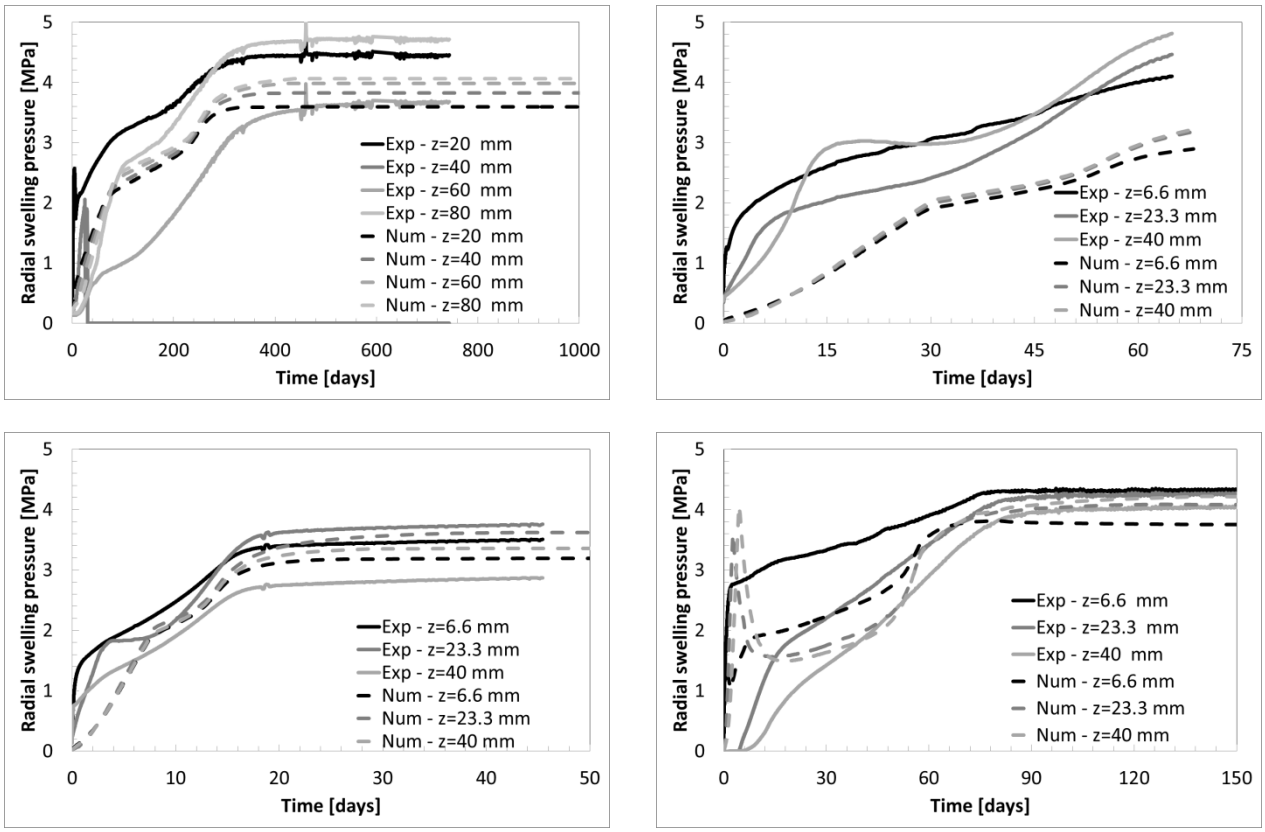

Fig. 5.17: Swelling pressure in radial direction at several locations time evolution for tests WP5_1B, C_1, C_2 and C_6. Comparisons between experimental average data and model simulations.

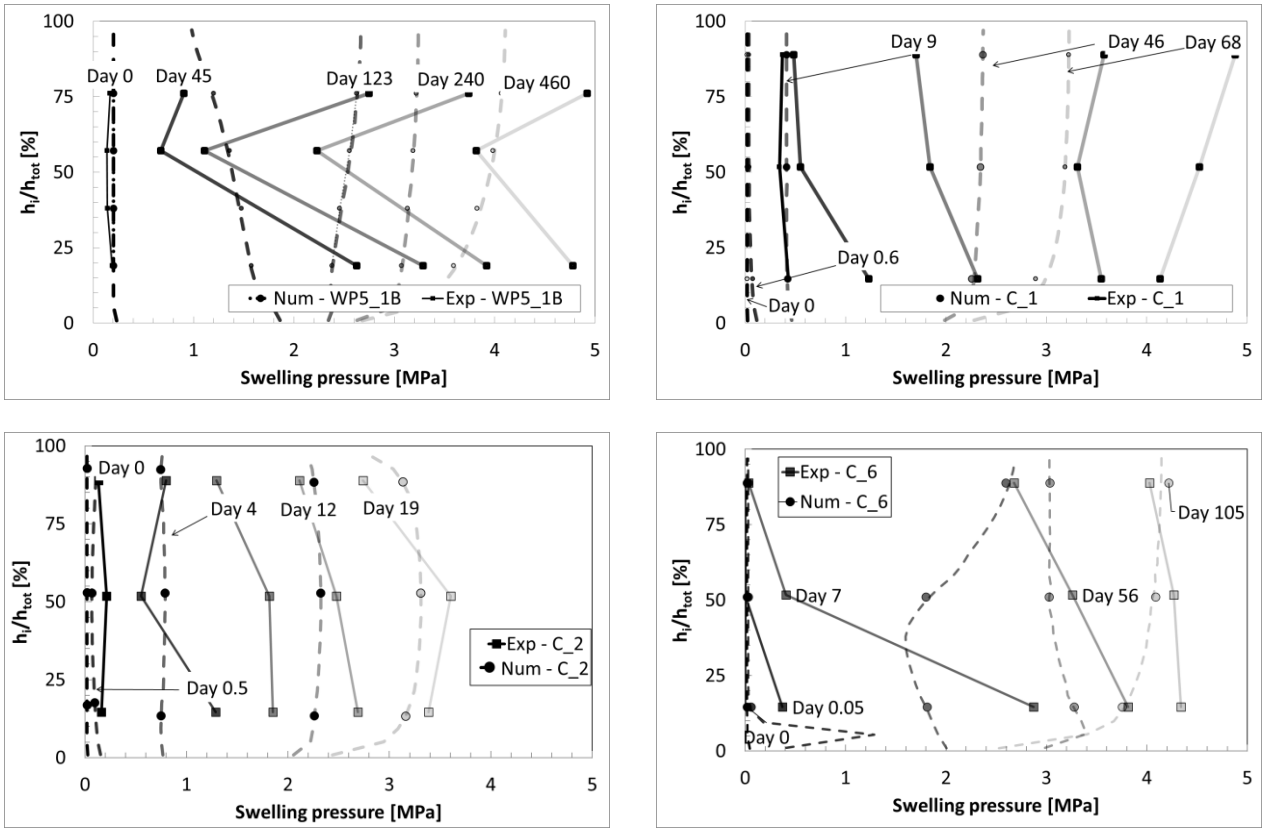

Fig. 5.18: Radial swelling pressure profiles for tests WP5_1B, C_1, C_2 and C_6. Comparison between experimental average measurements and numerical simulations. Time steps are selected considering the initial conditions, 25%, 50%, 75% and 100% of the final experimental axial swelling pressure of each test.

High stress gradient can be observed at early stages of hydration for compacted block test C_6, where the effect of the gap appears important. Indeed, it can be observed in Fig. 3.13, that the sensors located at z=40 mm from the bottom detects a null radial swelling pressure at the 7th day of the test time. At the same moment, the sensor at z=6.6 mm presents a radial swelling pressure equal to 3 MPa. Thus, when the 60% of the total axial swelling pressure has already developed, the radial contact has not been reached yet at the upper location. This means that hydration has highly developed at the bottom but not at the top of the sample.

The pellet/powder arrangements (tests WP5_1B, C_1 and C_2) do not show such high stress gradients. Surprisingly, there not a high difference in the radial pressure gradient between C_1, which is only hydrated by the bottom, and C_2, which is hydrated by the top and the bottom.

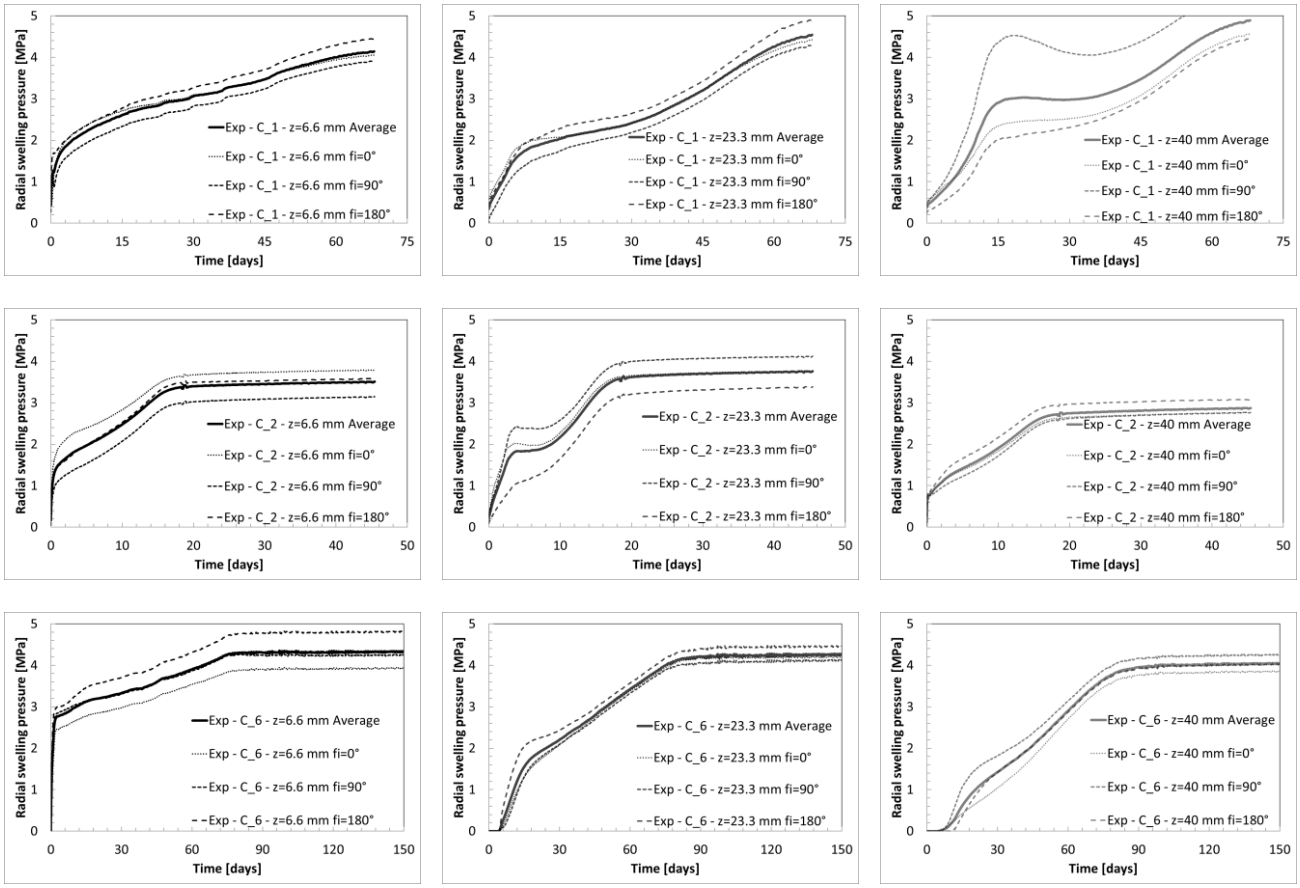

Fig. 5.19: Swelling pressure in radial direction at several locations time evolution for tests C_1, C_2 and C_6. Comparisons between experimental average data and measurements at angular position 0°, 90° and 180°.

Table 5.7: Final radial swelling pressure values. Comparisons between experimental data and model simulations for test WP5_1B.

	Final Radial Swelling Pressure [MPa]					
	Experimental			Numerical		
z [mm]	20	60	80	20	60	80
WP5_1B	4.43	3.74	4.69	3.59	4.00	4.07

Table 5.8: Final radial swelling pressure values. Comparisons between experimental average data and model simulations for tests C_1, C_2 and C_6.

Test Reference	Final Radial Swelling Pressure [MPa]											
	Experimental									Numerical		
Angular position [°]	0			90			180			[-]		
z [mm]	6.6	23.3	40	6.6	23.3	40	6.6	23.3	40	6.6	23.3	40
C_1	4.05	4.42	4.57	3.91	4.29	5.65	4.45	4.91	4.45	2.89	3.19	3.22
C_2	3.79	3.77	2.77	3.15	4.12	2.77	3.58	3.38	3.08	3.19	3.62	3.37
C_6	3.95	4.22	3.87	4.26	4.14	4.27	4.83	4.47	4.04	3.75	4.08	4.21

The hydration duration can be observed on Fig. 5.10 and Fig. 5.12. Test WP5_1B was stopped at 1214 days after the beginning of hydration, C_1 after 68 days, C_2 after 45 days and C_6 after 182 days, with pressure measurements for test WP5_1B, C_2 and C_6 stable respectively since approximately the age of 600 days, 20 days and 80 days (test C_1 does not seem to reach stabilisation). It can be observed that the stabilisation times scale with the square of hydration length as observed for the water intake.

It is worth noting that the swelling pressure stabilizations are not consistent with the suction measurements, which reach the 0 value far earlier (Fig. 5.21). The first and fast increase of the pressures seems to follow the suction decrease. The second swelling pressure increase arrives for low suctions, when relative humidity is near 100%. Alternatively, the swelling pressure developments are more coherent with the water intake evolutions (Fig. 5.10 and Fig. 5.12).

Fig. 5.12 and Fig. 5.17 show the time evolution through of the swelling pressure measured in the axial direction on the top and in the radial one at different height of the samples. The numerical results are compared to the experimental ones. The trend of the transient phase is well reproduced as well as the stabilization time.

As the comparisons in Fig. 5.12 show, the agreement between the experimental and the numerical results for the axial pressure is remarkably good for test WP5_1B, C_2 and C_6. Discrepancies between model simulations and experimental results are found in test C_1, as the last increase is not reproduced. Given the same initial conditions in terms of confining stress and saturation, the same final swelling pressure is obtained in numerical simulations for tests C_1 and C_2. If the numerical axial swelling pressure as function of the average degree of saturation is considered (Fig. 5.15), test C_1 and C_2 are completely overlapping as a consequence of the complete numerical correspondence in hydromechanical parameters and test initial conditions.

Indeed, apart from different stabilisation times proportional to the square of the hydration length equal to 45 mm for test C_1 (one side hydration) and 22.5 mm for test C_2 (double-sided hydration), the two numerical tests present the same final swelling pressure values equal to 3.2 MPa. This value is evidently lower with respect to the one observed during the experimental test C_1.

Moreover, differently from test WP5_1B, in which the initial elastic experimental swelling is remarkably well reproduced, test C_1 and C_2 present an elastic swelling pressure development delayed with respect to the experimental records. This occurrence can be related to the selection of the mechanical elastic parameters for change in pressure κ (constant) and for change in suction κ_s (pressure dependent). Hydraulic mechanisms dependence causes are excluded as it was explained in the previous paragraph.

On the other hand, the numerical post-yielding path for test C_2 is perfectly corresponding to the experimental measurements. The numerical simulation of axial swelling pressure for test C_6 is able to reproduce the path described by (Lloret et al. 2003) without explicitly taking into account the small-large pores diameter interaction but considering mono-modal pore distribution in the mechanical model (i.e. BBM).

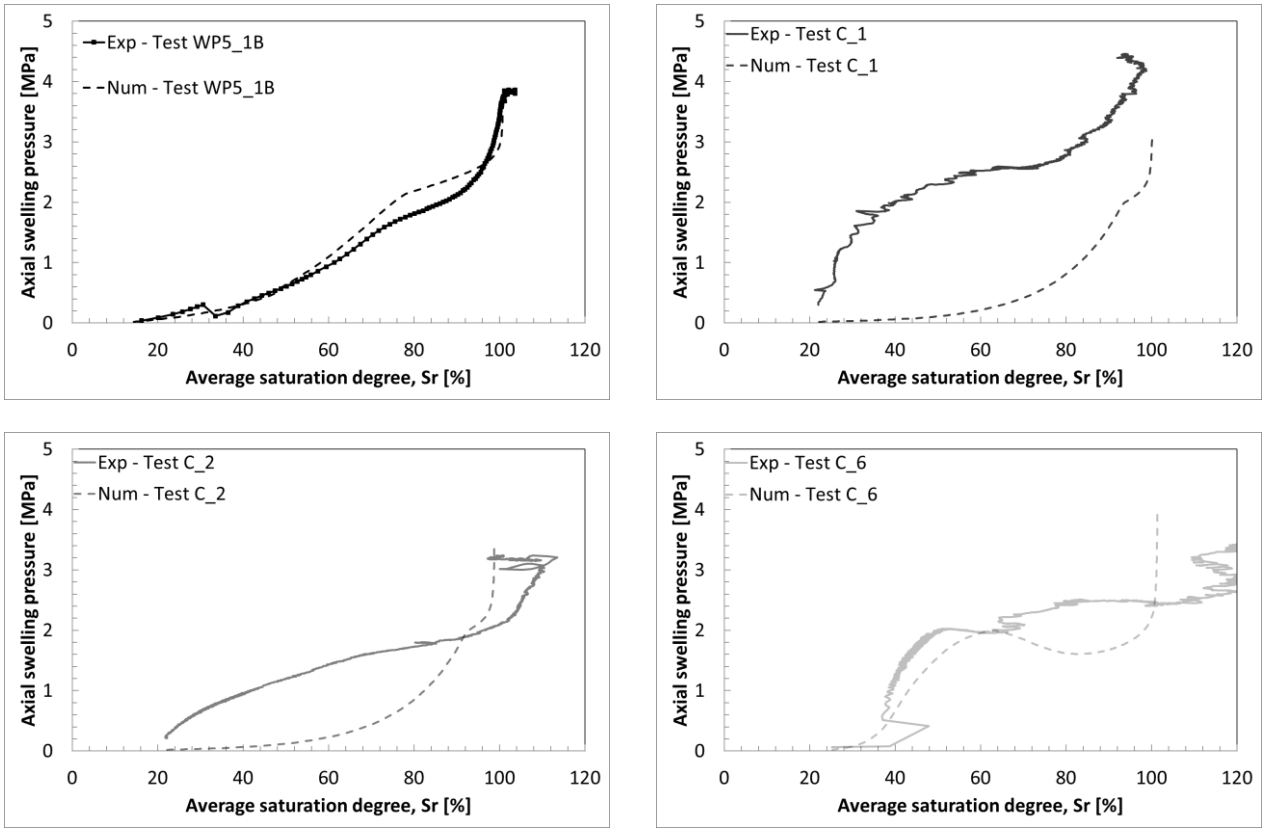

Fig. 5.20: Swelling pressure in axial direction as average saturation degree of the sample function for tests WP5_1B, C_1, C_2 and C_6. Comparisons between experimental data and model simulations.

Fig. 5.20 presents the comparisons between the experimental data and the model simulations of the axial swelling pressure as function of the average saturation degree of the sample for tests WP5_1B, C_1, C_2 and C_6. As for test WP5_1B there is a complete correspondence in terms of water inflow and axial swelling pressure, the experimental and numerical results are overlapped. Also for test C_6, a very good correspondence is found despite the experimental uncertainties related to the excessive water inflow at the end of the test. The discrepancies between experimental and numerical outputs at the beginning of tests C_1 and C_2 are observed also in this plane. In particular, the experimental and numerical concavities (i.e. axial swelling pressure development with respect to water intake rates) are opposite.

Radial stress measurements comparisons are shown in Fig. 5.17 and Fig. 5.18. Numerical simulations present a pressure gradient in the hydration direction, with a maximum value for the sections further from the wetting surfaces. The non-monotonic evolution of the swelling pressure during the hydration phase is well

captured by this model. However, numerical radial pressure simulations are in general lower than the averaged experimental ones and are not affected by local uncertainties. Indeed, the numerical radial stress distributions at the end of the tests (Fig. 5.18) preserve the developed pressure gradient, differently from experimental records. With respect to tests C_1 and C_2, numerical initial radial confining pressure is selected equal to 0.02 MPa, lower with respect to the measured quantities, which have to be treated with caution considering also the sensors precision and dimension (Dardé 2019). The numerical simulations for the radial pressure evolution of test C_6 are similar to the axial ones (i.e. increase of pressure up to a peak followed by a decreasing and a final increase up to stabilisation), in contrast to what is observed in the experimental outcomes where the role of the initial gap is dominant. Since the numerical strategy considers mono-dimensional conditions, initial mono-modal pore structure distribution and no gap with the cell wall, this experimental evidence is not well-captured in this study. The very high initial radial pressure peak gradient observed during experimental results of test C_6 is due to the different stress path to which the material portions placed on the bottom and on the top are subjected.

Namely, the material placed close to the wetting surface undergoes a kind-of swelling in the axial direction upon saturation at constant stress, whereas the material placed far from the bottom is subjected to compaction at constant suction. This is due to the boundary conditions and the very low permeability of the medium. Logically, close to the wetting surface, the suction immediately decreases and, far from the hydration source, it remains constant due to the very low permeability.

Suction

As soon as the water injection begins, the suction decreases for all the heights in all the tests (Fig. 5.21 and Fig. 5.22). The rate of decrease is inversely proportional to the distance from the water source, with the maximum rate recorded at the sensors closest to the wetting surface. With respect to experimental tests WP5_1B, C_1 and C_2, at the beginning of the injection, water mostly flows into the bigger diameter pores composing the crushed pellets powder (Fig. 5.27) in which the sensors are immersed. Because of this, the suction immediately decreases. When the water front proceeds through the sample, the pellets hydrate and swell, compacting the surrounding powder. From a multi-structural point of view, pellets' dominating small diameter pore structure invades the crushed pellets large diameter one, preventing the local water transfer mechanism and consequentially slowing down the suction decrease. For test WP5_1B, the zero experimental suction values at all the sensors are reached at the age of day 200, when the swelling pressure reaches 65% of its total swelling pressure. Thus it can be concluded that at that time, the crushed pellets component is fully saturated, as sensors indicate, whereas the pellets component continues to hydrate, as the water intake evolution shows, still causing swelling pressure development until the age of day 400 when full saturation is assumed.

This latter occurrence is also found in tests C_1 and C_2 in which the zero suction values are obtained at the time of 50 and 10 days respectively, whereas the swelling pressures and water intake stabilise at the time of 70 and 20 days. However, the immediate water invasion of crushed pellets component is not as evident as the one observed in test WP5_1B. Indeed, the numerical results show faster suction decrease rates with respect to the experimental ones, possibly suggesting a different pore structure evolution kinetic due to the different pellets size (7 mm-pellets instead of 32 mm).

Due to this it can be assumed that the suction measurements are not representative of the overall bentonite sample but mainly of the pore space corresponding to the crushed inter-layer pellets for tests WP5_1B, C_1 and C_2 and to the powder gap space for test C_6, i.e. to the larger pores. These measurements are local, in the same way as the radial pressure measurements, whereas the axial pressure and the water intake are global values. Fig. 5.22 presents the evolution with time of the vertical gradient of suction. WP5_1B and C_1 tests

presents similar tendency, consistently with powder material and only bottom hydration. A clear about uniform gradient appears for intermediate state of hydration (45 days for WP5_1B, 9 days for C_1). Test C_6 presents also the same trend. Test C_2 is hydrated from the top and bottom, and this is clearly reflected in the “chevron” shape of the suction profile. All these profiles at intermediate state of hydration are a signature of the permeability evolution of the materials at early stages.

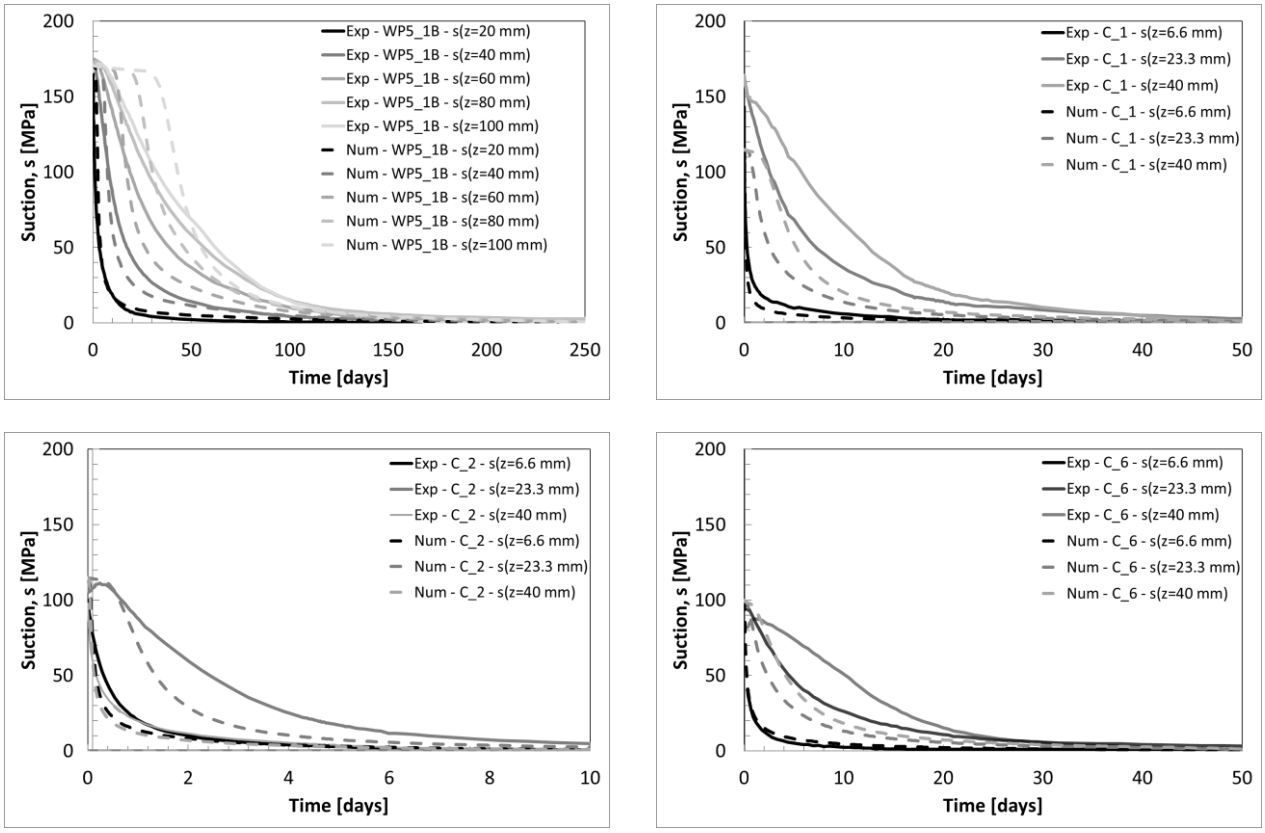

Fig. 5.21: Suction at several locations time evolution for tests WP5_1B, C_1, C_2 and C_6. Comparisons between experimental data and model simulations.

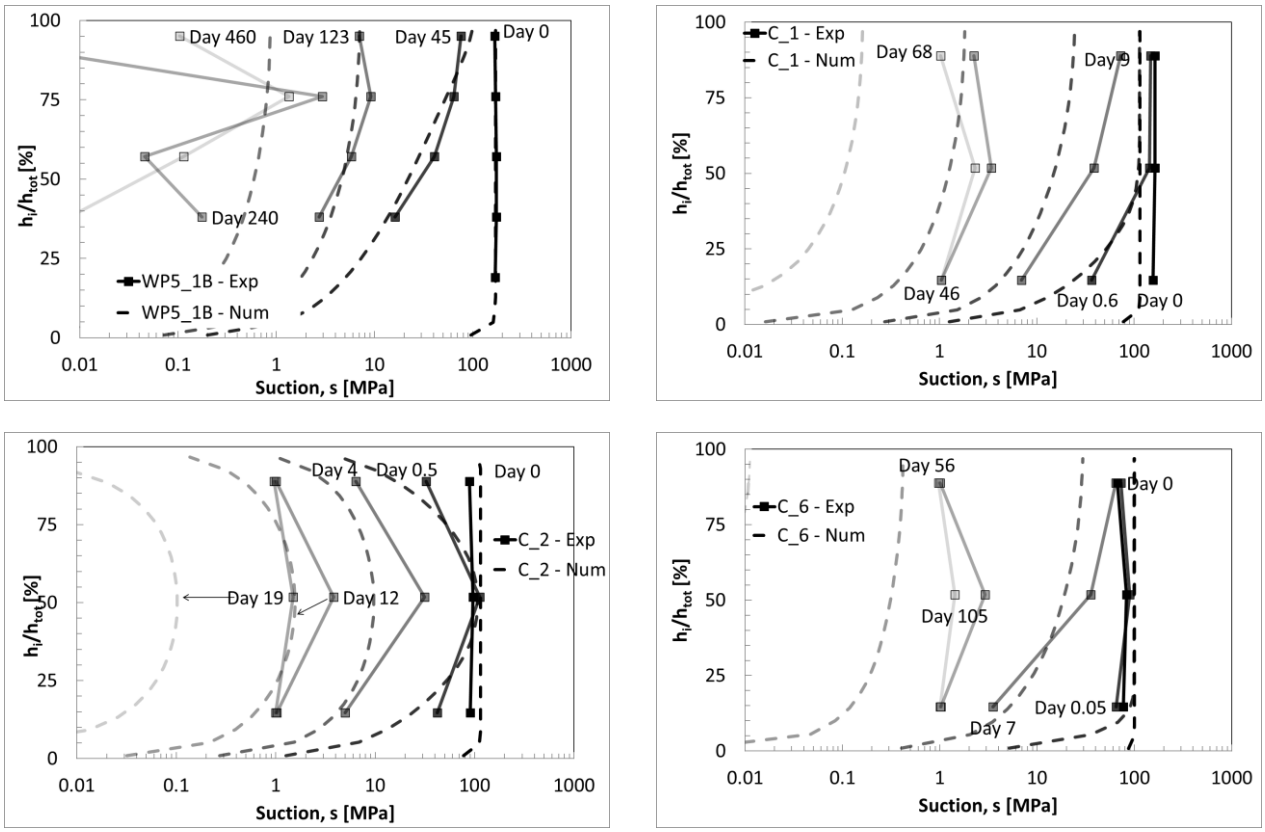

Fig. 5.22: Suction profiles for tests WP5_1B, C_1, C_2 and C_6. Comparison between experimental measurements and numerical simulations. Time steps are selected considering the initial conditions, the 25%, 50%, 75% and 100% of the final experimental axial swelling pressure of each test.

The numerical model captures very well the progressive decrease in suction experimental measurements (Fig. 5.22 and Fig. 5.21). Moreover, the numerical results reproduce nicely the experimental profile at intermediate times (Fig. 5.22), when the suction is far from being uniform on the sample (at day 45, 9 and 0.5 for tests WP5_1B, C_1 and C_2 respectively). This shows that the model reproduces well the suction evolution. The best agreement between numerical and experimental is found for measurements placed the closest to the wetting faces. The very fast reaction of these sensors is well reproduced numerically. Discrepancies are found for the sensors further from the injection fronts.

With respect to test WP5_1B, a quick experimental suction decrease for all the sensors is observed, which is not reproduced by the numerical model. Indeed, for the further sensors, at the beginning of the hydration, the numerical simulations display quasi-constant suction values, which start to evolve at a time proportional to the distance from the wetting surface. As the hydration process continues, the numerical suction decrease rates overcome the experimental one up to full saturation.

Also for tests C_1 and C_2 the numerical model reproduces well the decrease of suction for the sensors located closer to the wetting surfaces, with slightly higher numerical values with respect to the experimental ones (as observed for water intake comparisons). As the distance from the wetting surfaces increases, the rate of suction decrease is higher for the numerical model with respect to the experimental measurements. These discrepancies can be explained by analysing the important pores structure changes occurring during hydration described in the experimental analyses.

Finally test C_6 suction comparison shows that also in this case the suction evolution is very well reproduced for the sensor at z=6.6 mm, where the contact between the sample and the cell immediately occurs. For the further sections, it needs to point out that during the experimental test, the suction starts to decrease due to

the water hydration only after the establishment of the contact between the material and the sensors. In the numerical modelling, the suction evolution for the further sensors locations is not very well reproduced at the very beginning because initial contact is assumed and for the initial suction value, which is different from the experimental one.

The proposed numerical strategy does not consider such a complex pore structure distribution, its dramatic evolution upon hydration and the different saturation processes between small diameter pores structures (pellets and compacted blocks) and large diameter pores structures (crushed pellets and gaps components), but it gives interesting hints in terms of pore structure evolution homogenisation and kinetics.

Permeability evolution

According to (Cui 2017) the unsaturated permeability in bentonite based materials is undeniably linked to the multi-structures evolution upon hydration. Hence, in the specific cases of tests WP5_1B, C_1 and C_2, it can be assumed that the crushed pellets component, thanks to its large pores diameter dominating structure in the initial unsaturated state, represents a preferential pathway for the water transfer mechanism during the first phases of hydration. This feature results in a quite high initial permeability, which immediately decreases as the pellets swell and the small diameter structure expansion proceeds on wetting. This topic was also faced by (Navarro et al. 2020) with respect to test WP5_1B. In the same fashion, it can be considered that in test C_6 (i.e. compacted bentonite block), the water transfer mechanism takes mainly place in the largest diameter pores during the first phases of hydration with a permeability, which decreases as the larger diameter pores structure is invaded by the expansion of the small diameter pore structure upon saturation. Differently from pellets mixtures, it can be assumed that the compacted bentonite sample composing test C_6 does not present an initial permeability as high as the one postulated for test WP5_1B, C_1 and C_2 pellet mixtures. This is related to the fact that the very large pores size diameter characterising the crushed pellets medium is not likely in the compacted materials structure.

Moreover, it seems evident with respect to the water intake evolution, swelling pressure stabilisation and suction (Fig. 5.10, Fig. 5.12, Fig. 5.12, Fig. 5.17 and Fig. 5.21,), that test C_6 (compacted bentonite block, which stabilises after more than 80 days) presents an average permeability slightly lower than the one related to tests C_1 (7-mm pellets mixture), despite the comparable initial hydraulic state and dry density.

Let us remind that in media presenting heterogeneous pores size structures distributions, such as the ones here analysed, large pores diameter structures (i.e. the crushed pellets medium or gaps) are preferential (and possibly unique) hydration paths, especially at the beginning of the hydration process. Here, the water is free and behaves exactly as a Darcean fluid (contrarily to what occurs in the small pores diameter structures). Fig. 5.23 shows the numerical permeability simulations profiles through the height of the samples.

The selected numerical model for the permeability evolution allows reproducing the permeability decrease due to the micro-structure evolution upon water saturation (Fig. 5.24). In all the studied cases (i.e. isochoric hydrations), the micro-porosity becomes dominant with respect to the macro-porosity (i.e. inter aggregates and inter pellets pore space) upon water saturation according to Eq. 2.11. Due to this, starting from uniform values of intrinsic permeability (Table 5.2), obtained thanks to **Eq. 3.29** (Fig. 5.5) and depending on the saturation degree via e_M and k_r (Eq. 3.17 and Eq. 3.35), as the water front proceeds from the wetting faces, the intrinsic permeability of the material decreases reaching a-quasi-uniform value when fully saturated along the height of the samples (i.e. , s=0 MPa, Fig. 5.22 and Fig. 5.21 dashed lines).

As the hydration begins, the permeability of the material placed closest to the wetting faces immediately decreases as the large pores structures are invaded by the small pore one. Despite these portions of the samples being subjected to a generalised swelling (Fig. 5.25), which should correspond to a permeability increase, the large pores structures are instantly invaded by the micro pores structures causing the observed

permeability decrease. This phenomenon is predominant with respect to other mechanisms and occurs in pellets mixtures, in which the powder/crushed pellets inter-pellets place (preferential path way of hydration) is compacted due to the pellets swelling, but also in the compacted block, in which the radial gap is invaded by the compacted sample swelling upon hydration in isochoric conditions (Seiphoori, Ferrari, and Laloui 2014).

The initial and slower permeability decrease observed in the samples portions further from the wetting surfaces are initially related to the compaction caused by the bentonite swelling and successively by the multi-structural evolution, occurring in both experimental observations and numerical simulations. All these phenomena are linked between them and testify the strong hydro-mechanical and multi-porosity coupled processes characterising unsaturated swelling clays.

These causes explain the observed suction rate decrease after the first and quicker hydration phase, confirming the hypothesis of water transfer mechanism mainly occurring in large pores diameter structures during the first phases of hydration.

The calibration performed for the three different assemblies shows the highest initial uniform permeability equal to $K_w=4\times10^{-20}$ m^2 for 32-mm pellets mixture (test WP5_1B) and the lowest equal to $K_w=8\times10^{-21}$ m^2 for the compacted sample (test C_6). Intermediate value equal to $K_w=2\times10^{-20}$ m^2 for 7-mm pellets mixture (tests C_1 and C_2).

The final permeability values corresponding to the full saturated state are equal to $K_w\approx6.5\times10^{-21}$ m^2 for 32-mm pellets mixture (test WP5_1B), $K_w\approx5.5\times10^{-21}$ m^2 for the compacted sample (test C_6). And the 7-mm pellets mixtures (tests C_1 and C_2).

The permeability rate decrease upon saturation can be also observed in Fig. 5.5. Despite several simplifications adopted to model these experimental tests (i.e. unique water retention curve, different initial suction and macro void ratio e_M depending only on the saturation degree and not on effective pore structure distribution), the numerical model and its calibration are able to well reproduce the transient phase of swelling pressure development, suction evolution and dry density and water content final states (as it will be observed in the following) and give realistic results in terms of permeability evolutions.

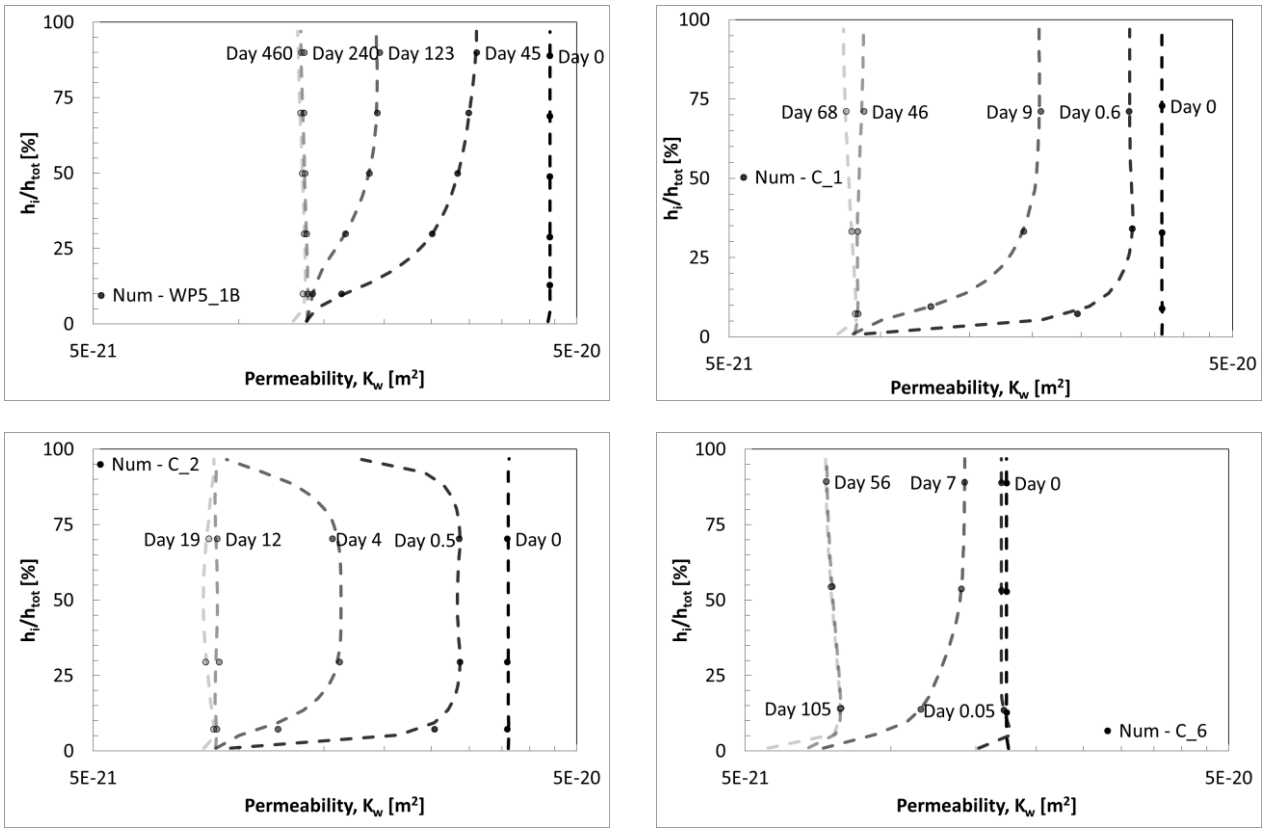

Fig. 5.23: Permeability profiles for several time steps. Numerical simulations for tests WP5_1B, C_1, C_2 and C_6.

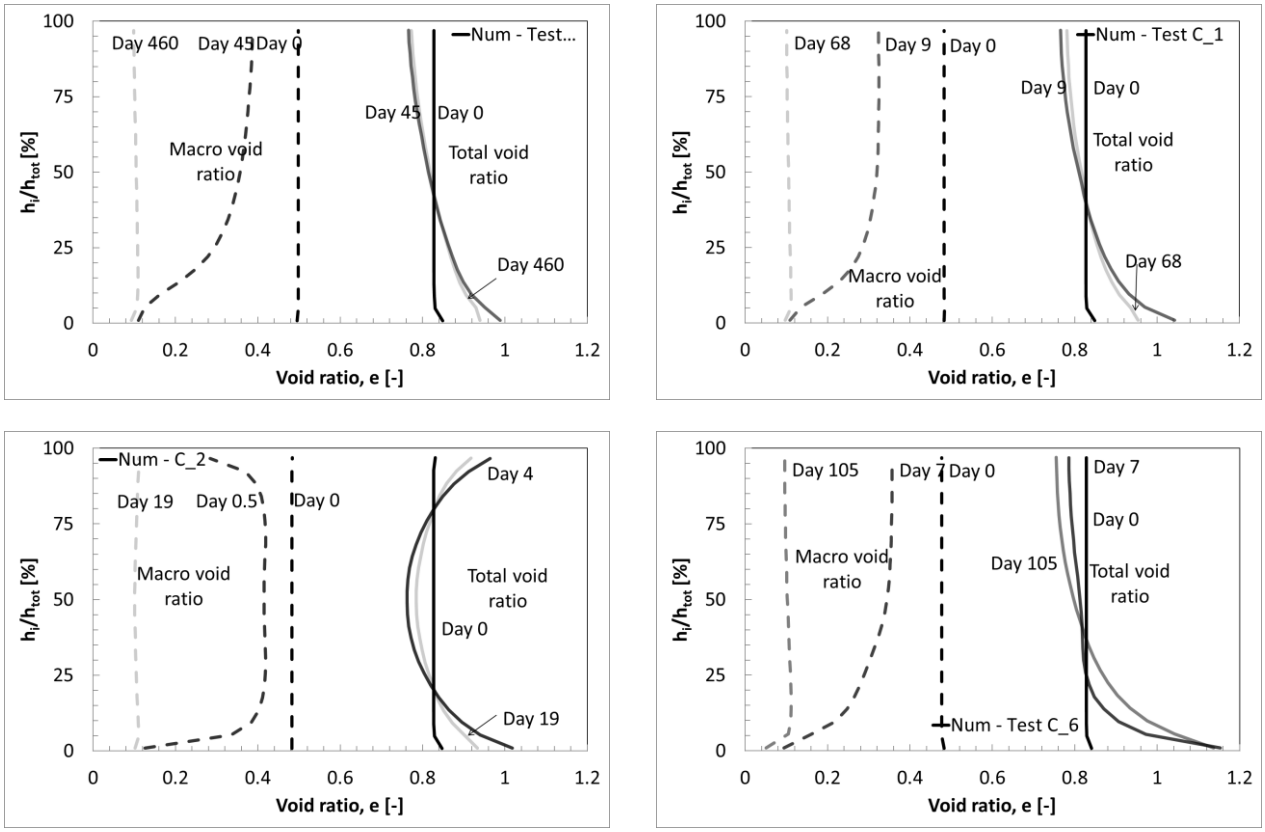

Fig. 5.24: Total and macro void ratios profiles for several time steps. Numerical simulations for tests WP5_1B, C_1, C_2 and C_6.

Dry density and water content

Dry density and water content were evaluated thanks to post mortem analyses. Water content was measured using 105°C oven drying for 24 h and the apparent density from hydrostatic weighing in oil. Consequentially, dry density is computed for each sub-sample. For test WP5_1B, six dry density measurements at four heights are taken. Dry density and water content results consider the mean and standard deviations, which underline a certain level of results dispersion (between ρ_d=1.47 and 1.58 Mg/m^3) (Bernachy-Barbe et al. 2020). For tests C_1, C_2 and C_6, apparent density measurements (three for tests C_1 and C_2 and one for test C_6) and one water content measurement are taken at three locations through the vertical axis of the samples. The dry density measurements dispersion of tests C_1, C_2 and C_6 is much smaller with respect to test WP5_1B.

A vertical density gradient is observed in the direction of hydration, inversely correlated with water content (Fig. 5.25 and Fig. 5.26) for tests WP5_1B, C_1 and C_2. The minimum dry density values (maximum water content values) are found in the locations close to the wetting surfaces. When water is injected, the material placed close to the wetting surfaces undergoes an important volume increase. Accordingly to the prescribed isochoric conditions, this volume increase should be counterbalanced by a volume decrease far from hydration front. Thus, this latter zone is compressed by the swollen of the wetted material. As the saturation front penetrated within the sample, the transition between the swollen and compressed zone recedes from the injection sides and stops before the first half of the hydration length (~45% h_i/h_{tot} from the wetting surface).

With respect to the experimental results related to test C_2 (Fig. 5.25), experimental outcomes underline a generalized volume increase, which contradicts the hypothesis of constant volume hydration.

On the other hand, the detected experimental dry density general decrease can also be due to post dismantling and sampling swelling. Indeed, as observed for the numerical simulation of test C_2 final state, the central part presents a higher dry density with respect to the top and bottom parts (i.e. a gradient in the hydration direction).

Test C_6 show a final homogeneous dry density (and water content) distribution between ρ_d=1.45 and 1.50 Mg/m^3. (and w=30%). It is interesting to note that the initial dry density of the compacted block was equal to ρ_d=1.75 Mg/m^3, with a swelling deformation, possibly occurred in the radial direction (i.e. the gap). Also in this case post dismantling and sampling swelling is assumed due to the fact that the overall final dry density is slightly lower with respect to the total sample one (ρ_d=1.52 Mg/m^3).

Samples composed of pellets mixtures present a larger density variation: 0.10 Mg/m^3 for WP5_1B, 0.12 Mg/m^3 for C_1 and for C_2.

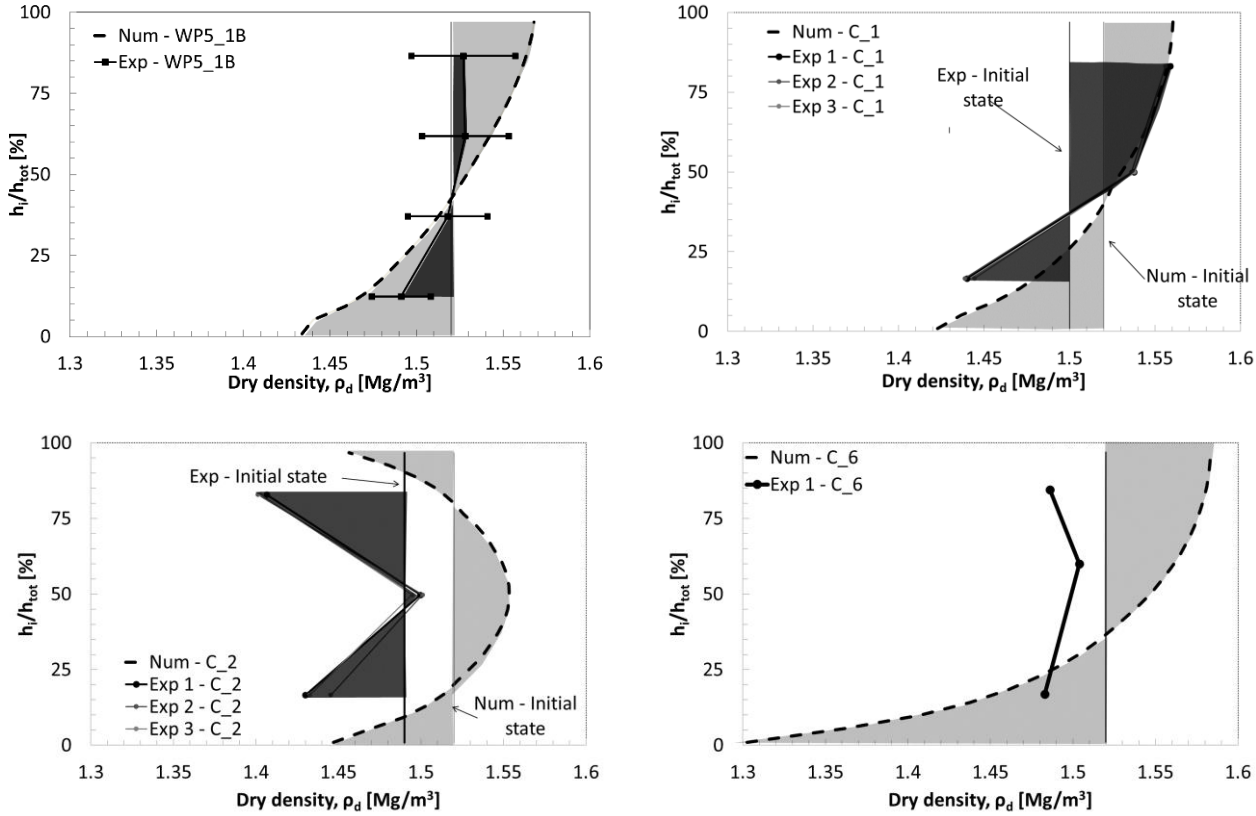

Fig. 5.25: Dry density distribution over the height of the sample (in percentage) at the beginning and the end of the test for tests WP5_1B, C_1, C_2 and C_6. Comparisons between experimental data and model simulations.

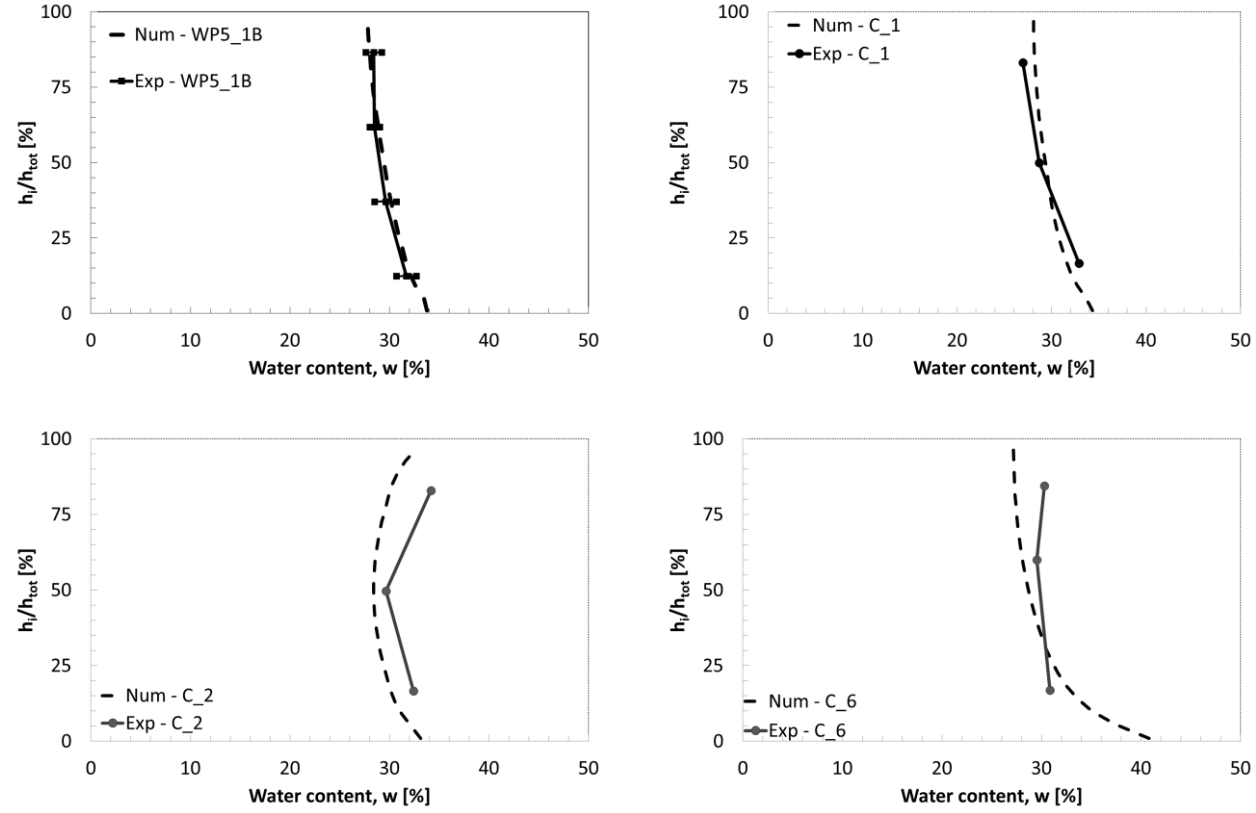

Fig. 5.26: Water content distribution over the height of the sample at the end of the test for tests WP5_1B, C_1, C_2 and C_6. Comparisons between experimental data and model simulations.

Dry density and water content comparisons of experimental measurements at dismantling and numerical results are presented (Fig. 5.25 and Fig. 5.26). For tests WP5_1B, C_1 and C_2, the final experimental and numerical states show similar qualitative features: a vertical density gradient is observed in the direction of hydration, inversely correlated with water content. The resulting vertical gradient is related to the progressive hydration of the samples. The numerical simulations for tests WP5_1B, C_1, C_2 and C_6 present this behaviour with a good agreement between experimental and numerical results for tests WP5_1B and C_1 (despite the difference in initial dry density for this latter one). However, discrepancies between experimental results and numerical simulation are found in tests C_2 and C_6.

As already mentioned, with respect to test C_2 (Fig. 5.25), experimental outcomes underline a generalized volume increase, which contradicts the hypothesis of constant volume hydration. On the contrary, numerical simulations highlight an expected swelling in proximity of the wetting surfaces (top and bottom here) and the consequential compaction of the central part. The variation of density with the axial position is well reproduced by the numerical simulation.

For test C_6, the dry density and water content gradient simulated by the numerical simulations do not correspond to the experimental results, which are strongly affected by the experimental radial gap. Indeed, it can be observed a homogeneous dry density distribution for the experimental test, which suggests that the swelling upon hydration has mainly occurred in the radial direction.

The experimental compacted bentonite volume increase occurs in the radial gap rather than compacting the sample portion located in the opposite hydration location, as the numerical model reproduces, generating a quasi-homogeneous dry density distribution. The water content profiles (Fig. 5.26) are precisely related to the dry density distributions and full saturated states.

Mercury intrusion porosimetry

The experimental campaign included Mercury Intrusion Porosimetry (MIP) measurements performed on freeze-dried samples taken from tests WP5_1B, C_1 and C_2 after dismantling (Fig. 5.27) and also measurements on the initial state of the material, i.e. pellets and powder (Bernachy-Barbe 2020). At the initial state, the single pellet presents a predominant pore family with a very small pore entry diameter (between 10 and 20 nm), whereas the crushed pellets-powder mixture is characterised by a similar fine porosity plus a predominant pore entry diameter which is 5 orders of magnitude larger.

After saturation all the analysed tests present a first peak value in proximity of a pore entry diameter equal to d=20 nm (close to the pellet pore size value), which has a contribution to the total porosity similar to the pellets in initial state. A second peak value is observed at d=50 µm (remarkably smaller with respect to the initial pore size dominating the crushed pellets pore structure). This occurrence denotes that the very large initial volume occupied by the large pore families structure has evidently reduced upon saturation. Consequentially, the very high initial permeability has simultaneously reduced. Conversely from test WP5_1B, tests C_1 and C_2 presents an additional pore family with a peak corresponding to the pore entry diameter equal to d=200 nm, just in between the above-mentioned pore families. Those additional pore families are detected close to the wetting surfaces (bottom for test C_1 and top and bottom for test C_2), where the lowest dry density is observed during the post mortem analysis (Fig. 5.25). The initial very large pores observed in the initial crushed powder have disappeared and are transformed in pores of diameter around 200 nm and around 50 µm.

MIP experimental results on pellets mixtures present comparable features as the ones found by (Seiphoori, Ferrari, and Laloui 2014) on compacted MX-80 pure bentonite and (Wang et al. 2014) on MX-80 and sand compacted mixture after saturation.

Despite several authors (Wang, Cui, et al. 2013), (Zhang, Cui, and Ye 2018), (Seiphoori, Ferrari, and Laloui 2014) propose possible quantitative distinctions and thresholds between the *larger pore diameter families* and *smaller pore diameter families* with respect to different criteria, it is evident that the strongly coupled multi-structural and multi-physics phenomena modifying these distributions do not allow a unique and abrupt separation between structures.

Indeed, the presented experimental results show how in tests C_1 and C_2, an additional pore family arise just in between the larger and smaller diameter structures at the end of the test. Moreover, different authors refer indiscriminately to different pores diameter structures with the same definition and with different definitions to the same pores diameter structure, leading incontrovertibly to misunderstandings. Consequentially, in this work, the definition of micro and macro porosity has not been used when commenting experimental results, but the wordings “large pore diameter structures” and “small pore diameter structures” was preferred. In contrast to other distinctions, this separation is straightforward thanks to the fact that the dominating pores families diameters span several orders of magnitude. Nevertheless, a unique distinction between large pores diameter structures and small pores diameter structures was necessary and unavoidable when dealing with the numerical modelling, as it is showed with reference to numerical results of water retention behaviour (Fig. 5.22) and permeability evolution (Fig. 5.23).

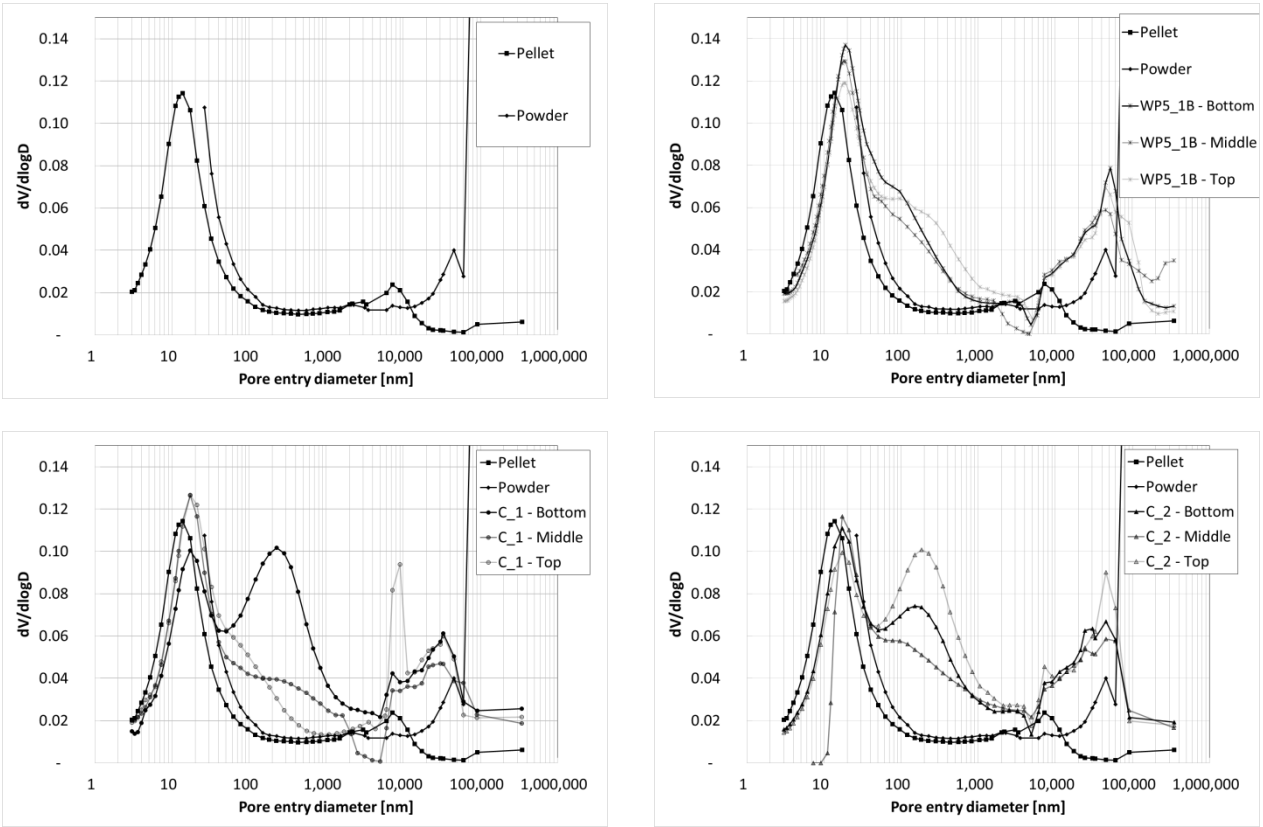

Fig. 5.27: MIP characterisation of single pellets and powder at initial state and for tests WP5_1B, C_1 and C_2 at several locations through the height of the sample at the end of the tests.

Conclusions

This paragraph presented isochoric-wetting tests performed on a MX80 bentonite in the form of different assemblies (i.e. 32-mm pellets mixture, 7 mm-pellets mixtures and isotropic compacted block surrounded by radial gap) with similar dry densities and different hydration lengths. The considered experimental tests present an initial very heterogeneous pore structures and dry density distributions, which evolves toward a homogenised structure. This feature affects undeniably the swelling pressure development and water transfer mechanisms.

Firstly, it is possible to see that the elastic swelling pressure develops with a higher rate in compacted bentonite samples (test C_6) with respect to pellets mixtures samples (tests WP5_1B, C_1 and C_2).

Secondly, after reaching the pre-consolidation pressure (yield locus), it is observed that the pores structure distribution of a compacted bentonite sample does not present enough microstructural swelling strains to compensate for collapse deformation. Differently from pellets mixtures, test C_6 presents a load sufficiently high that causes the collapse of the macro-structure. The successive vertical stress decrease is due to the compensation for the collapse compressive strains.

Although the proposed numerical approach does not take into account the distinctions between pores diameter structures and their distributions, the numerical results underline a good agreement with experimental measurements. Especially, the non-monotonic evolution of the axial swelling pressure is well captured for all the tests.

Discrepancies between numerical simulations and experimental results are found for the radial pressure developments of test C_6. Those are related to the experimental radial gap partially filled with bentonite powder, which is not considered in the numerical modelling. The post mortem analyses comparisons between experimental results and numerical simulations also show similar features. These comparisons allow detecting experimental uncertainties (i.e. dry density experimental evaluation for test C_2) and the limits of numerical simplifications (i.e. numerical dry density vertical gradient vs homogeneous dry density vertical experimental profile for test C_6). With respect to test C_6, it is possible to underline how the position of the large pores diameter structure (i.e. gap partially filled with loose powder in the radial direction) with respect to the small pores diameter structure (i.e. central compacted bentonite sample) plays an essential role concerning swelling pressure development and final state performances assessments (i.e. dry density and permeability distributions). With respect to this, numerical modelling simplifications should always be taken with caution especially dealing with in situ real scale sealing structures.

Finally, a numerical approach is presented and adopted in order to evaluate the permeability evolution of large pores diameter structures. The results of this experimental evaluation are compared to other experimental records (i.e. swelling pressure, water intake and RH) underlining and confirming a strongly coupled hydro-mechanic and multi-porosity processes characterising the unsaturated swelling clays.

5.4.Numerical modelling of experimental radial gap

5.4.1. Description of the test

The sample preparation of test C_6 has already been discussed in section 5.3.1, as well as its experimental results. Nevertheless, for sake of clarity, some relevant information is repeated. This test concerns MX-80 bentonite sample isotropically compacted at initial dry density equal to ρ_d=1.75 g/m^3 and water content w=7.44%. In order to perform the isotropic compaction, the clay was first compacted in a neoprene tube (90 mm in diameter, 120 mm in length and 1.2 mm in thickness) with a closed end. The sample within the tube was then compressed in an isotropic cell under a static pressure of 40 MPa and finally machined in order to fit the cell dimensions to a height equal to 45.82 mm and diameter equal to 52.8 (versus a cell diameter equal to 57 mm). The sample is placed in the cell with a radial gap partially filled with 3.35 g of loose powder (w=7.44%) in order to obtain an overall final dry density equal to ρd=1.52 Mg/m^3. The addition of loose powder in the gap was used to adjust density and to avoid as much as possible instantaneous flooding of the gap by water. The initial radial technological gap between the bentonite sample and the cell wall is about 362 mm^3, which represents 15% of the total volume of the cell. An important decrease in the bentonite sample dry density associated to the progressive filling of this radial gap is expected.

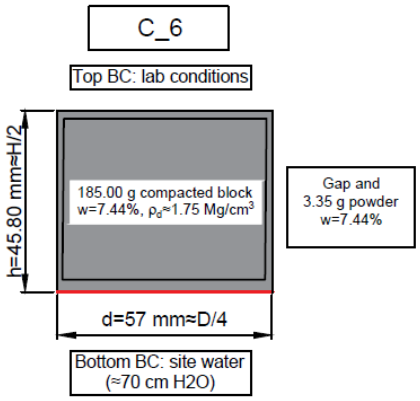

Fig. 5.28: Characteristics of the test C_6.

5.4.2. Features of the analysis

The analysis considers two numerical bentonite samples modelled in different fashions.

A monodimensional sample is modelled with 25 eight-noded isoparametric elements. In this strategy, the problem is assumed monodimensional and oedometer conditions are considered neglecting the experimental radial gap (Fig. 5.29). Initial uniform dry density equal to ρ_d=1.52 Mg/m^3 is assumed (considering the similar initial dry density in the experimental test). However, a 1D model neglects the radial gap. Due to this, a bidimensional axisymmetric bentonite sample is modelled with 800 eight-noded isoparametric elements with initial material dry density equal to ρ_d=1.75 Mg/m^3 (considering the actual experimental test) and a radial empty gap (i.e. the experimental bentonite powder is not considered). The experimental radial gap representing the large pore structure component and the radial cell wall are modelled via 40 3-noded iso-parametric interface elements (Cerfontaine et al. 2015) (green line Fig. 5.30), neglecting the friction. The cell wall can be considered as a very rigid element, representing a mechanical constraint for the bentonite materials. In this way, the cell wall represents only a normal constraint and the material sample is free to slide in the axial direction. The interface mechanical parameters are presented in Table 5.9

For sake of simplicity, the longitudinal and transversal transmittivity of the interface is supposed to be null. (i.e. there is no water exchange between the interface and the bentonite nor longitudinal flux into the interface itself and, consequentially, in the gap).

Same hydro-mechanical properties and hydro-mechanical state are set in the entire bentonite domains with initial uniform suction s related to the saturation degree S_r, (obtained via the corresponding water content w=7.44% and dry density) via the adopted dry density dependent water retention model (Table 5.5).

Initial water contents w in the numerical models are equal to the ones experimentally measured at the initial state (Table 5.4).

Table 5.9: Interface mechanical properties.

Penalty coefficient in the normal direction	K_t	[N/m^3]	108
Penalty coefficient in the longitudinal direction	K_l	[N/m^3]	108
Friction angle	φ	[°]	0
Friction coefficient	μ	[-]	0
Cohesion	c'	[MPa]	0

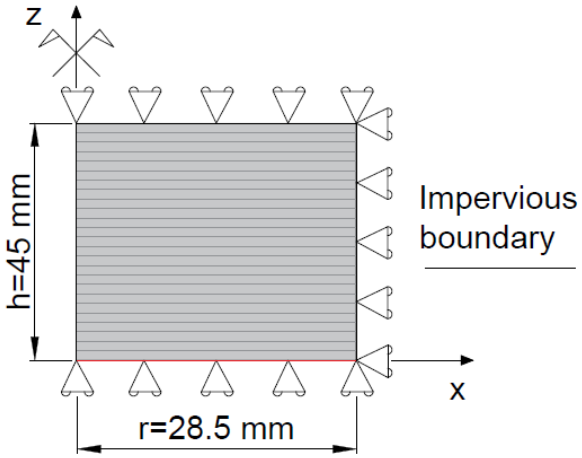

Fig. 5.29: Boundary conditions of the monodimesional model.

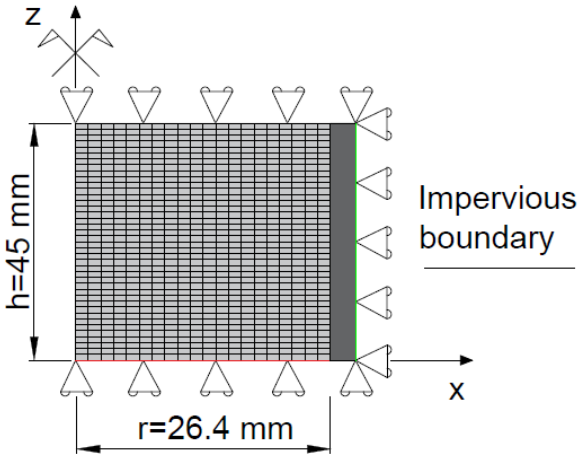

Fig. 5.30: Boundary conditions of the bidimesional model.

The hydration of the sample is provided from the bottom face (red line, Fig. 5.29 and Fig. 5.30) and assuming a suction decrease from the initial value to the experimental boundary conditions (Fig. 5.28) occurring in 1000 seconds. The monodimensional sample of test C_6 is subjected to isotropic confining stress of 0.02 MPa. On the other hand, axial confining stress equal to 0.06 MPa and null radial stress are applied to the bidimensional sample. The computed mean net pressure is equal to p^{net} =0.02 MPa for both cases.

Table 5.10: Initial state and characteristics of the numerical samples.

NUMERICAL SIMULATION	Monodimensional	Bidimensional
Type of assembly	Isochoric	Radial gap
Diameter [mm]	57	52.8
Height [mm]	45	45
Dry density [Mg/m3]	1.52	1.75
Water content [%]	7.44	7.44
Initial suction [MPa]	100.00	91.00

5.4.3. Experimental and numerical results

The presented numerical strategies and analyses are characterised by different initial bentonite specimens' dry densities. Given the well-known and strongly coupled dry density dependent bentonite mechanical behaviour (put citations) the material mechanical characterisation should correspond to different mechanical parameters set. However, the goal of this chapter is to analyse the influence of the radial gap on the numerical analyses of the same sample. Thus, considering a second parameters set would make the following comparisons more complex.

Water intake

Fig. 5.31 presents the evolution of the injected water mass through time. The experimental and numerical curves are characterized by a rapid increase of the injected water volume.

As water injection proceeds, the injection rate becomes lower and lower, mainly as a result of the smaller pressure gradient. The experimental injected water mass reaches 60 g at the end of the injection, whereas the numerical values are both equal to 42 g.

The numerical models compare remarkably well with the experimental curve especially at the initial phase, with respect to the variation rate with an evident discrepancy in final values. The numerical simulations are consistent with the initial experimental and numerical water contents, therefore, an experimental uncertainty is assumed.

The small numerical differences are due to the fact that the very small experimental bentonite powder amount in the radial gap (Fig. 5.28) was not taken into consideration in the bidimensional model.

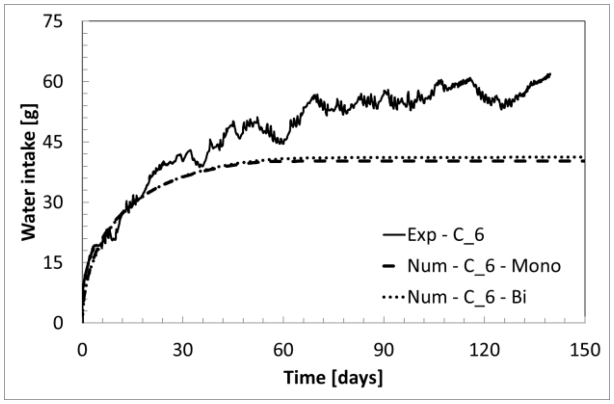

Fig. 5.31: Water mass injection time evolution for test C_6. Comparisons between experimental data and model simulations.

Swelling pressure

Fig. 5.32 shows the time evolution through of the swelling pressure measured in the axial direction on the top for the experimental test and the monodimensional model and on the top and the bottom for the bidimensional model. The numerical results are compared to the experimental ones.

As the experimental records, the two numerical results are able to distinguish the three phases described in the previous paragraph: the initial quick elastic swelling pressure increase, a second phase starting from the yield locus characterized by a change of curvature with a slower increase or also a decrease, and the last one with a new increase of the swelling pressure.

The first elastic swelling pressure increase in the axial direction develops with higher rate for the monodimensional strategy with respect to the bidimensional one. This is mostly related to the different stress paths that the two models encounter.

The second phase occurs after reaching the preconsolidation pressure (yield locus), in which the stress paths encounter a drastic change of slope. The numerical simulations of the bidimensional model reproduce very nicely the very smooth decrease of the experimental outcomes.

The third phase corresponds to the region of low suction, high saturation and last swelling pressure increase and it is similar for the three cases.

As the comparisons in Fig. 5.32 show, the agreement between the experimental and the numerical results for the axial pressure is remarkably good. The trend of the transient phase is well reproduced as well as the stabilization time.

Discrepancies between the model simulations of the bidimensional model and experimental results are reported in the very first swelling pressure development. The numerical swelling pressure increase rate is lower with respect to the experimental one and results in a lower final stabilised value, which is equal to 3.38 MPa instead of the experimental 4.08 MPa (Table 5.11). This occurrence is related to the choice of using the same set of mechanical parameter for the two numerical simulations, calibrated for the dry density ρ_d=1.52 Mg/m^3.

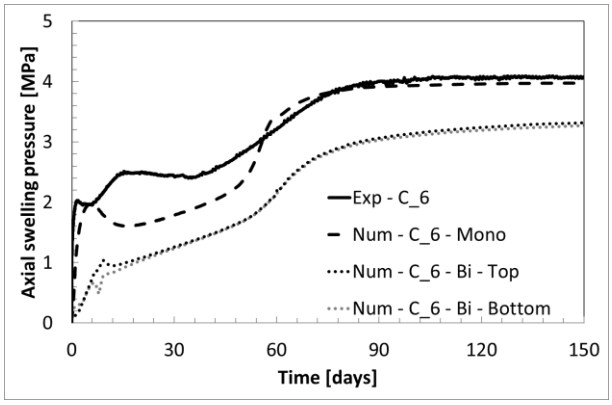

Fig. 5.32: Swelling pressure in axial direction time evolution for test C_6. Comparisons between experimental data and model simulations.

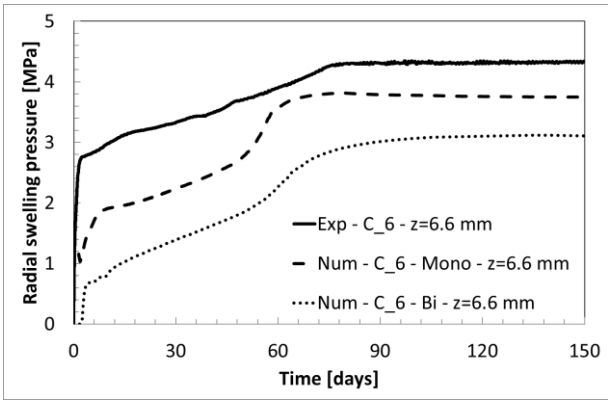

Fig. 5.33: Swelling pressure in radial direction at z=6.6 mm time evolution for test C_6. Comparisons between experimental data and model simulations.

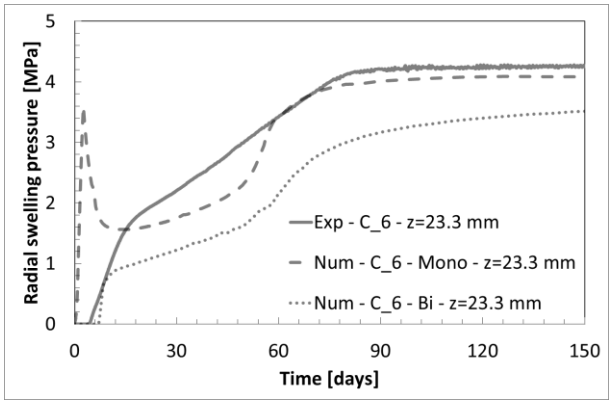

Fig. 5.34: Swelling pressure in radial direction at z=23.3 mm time evolution for test C_6. Comparisons between experimental data and model simulations.

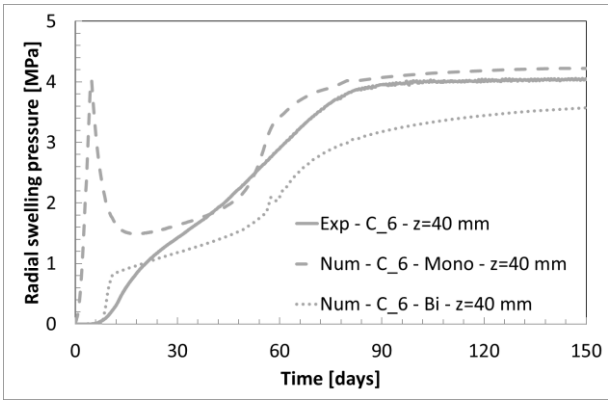

Fig. 5.35: Swelling pressure in radial direction at z=40 mm time evolution for test C_6. Comparisons between experimental data and model simulations.

The time evolution of the radial pressures is mostly similar to the axial pressure evolution.

Radial stress measurements comparisons are shown in Fig. 5.33, Fig. 5.34 and Fig. 5.35. Experimental results and numerical simulations present a prominent pressure gradient in the hydration direction, with a maximum value for the sections further from the wetting surfaces. The non-monotonic evolution of the swelling pressure during the hydration phase is well captured by these models. However, numerical radial pressure simulations are in general lower than the averaged experimental ones and are not affected by local uncertainties.

The stress gradient observed at early stages of hydration in the experimental results are very well reproduced especially by the numerical simulations of the bidimensional model. Indeed it can be observed in Fig. 5.33 and Fig. 5.35, that when the experimental the sensor at z=6.6 mm presents a radial swelling pressure equal to 3 MPa, the sensor located at z=40 mm from the bottom detects a null radial swelling pressure (7^{th} day of the test time).

The proposed bidimensional numerical model considering the radial gap reproduces the same phenomenon and time scale. Thus, when the 60% of the total swelling pressure has already been developed, the radial contact has not been reached yet at the upper location, highlighting the importance of the effect of the gap.

The numerical simulations for the radial pressure evolution of the monodimensional model are similar to the axial ones (i.e. increase of pressure up to a peak followed by a decreasing and a final increase up to stabilisation), in contrast to what is observed in the experimental outcomes where the role of the initial gap is dominant.

Since the numerical strategy considers monodimensional conditions, initial mono-modal pore structure distribution and isochoric conditions since the very beginning (i.e. no radial gap with the cell wall), this experimental evidence is not captured as well as the bidimensional model does. The very high initial radial pressure peak observed is due to the different stress path to which the material portions placed on the bottom and on the top are subjected. Major details can be found in the paragraph “Stress paths analysis”.

Table 5.11: Final swelling pressure values. Comparisons between experimental data and model simulations for test C_6.

Final Swelling Pressure [MPa]										
	Radial									Axial
z [mm]	6.6			23.3			40			40
Angular position [°]	0	90	180	0	90	180	0	90	180	[-]
Exp	3.95	4.26	4.83	4.22	4.14	4.47	3.87	4.27	4.04	4.08
Num - Mono	3.75			4.08			4.21			3.98
Num - Bi	3.07			3.60			3.68			3.38

Suction and saturation degree

Fig. 5.36 and Fig. 5.37 show the evolution through time of the suction (experimental result and numerical simulations) and degree of saturation (numerical simulations) at several locations. Water injection yields a progressive decrease of suction and increase of degree of saturation in the samples. The suction decrease rate and saturation increase one are inversely proportional to the distance from the water source, with the maximum rate recorded at the sensors closest to the wetting surface.

Discrepancies between numerical simulations (Fig. 5.36) are very small despite the different initial suction values.

The saturation degree at several locations time evolution presents the comparisons between the proposed numerical strategies simulations (Fig. 5.37). The two strategies are characterised by different initial saturation values, namely S_r=25% for the monodimensional model and S_r=35% for the bidimensional one. It is important to mention that this is related to the different initial dry densities set for the material in the two cases (respectively equal to ρ_d=1.52 Mg/m^3 and ρ_d=1.75 Mg/m^3). Very small distance is found at the beginning of hydration at z=6.6 mm because of the immediate contact with the cell wall of the material placed the closest to the wetting surface for the bidimensional model, which initially and immediately reaches the dry density equal to ρ_d=1.52 Mg/m^3. Successively this sample portion undergoes further swelling and the two curves start to diverge. For z=23.3 mm and 40 mm, especially at the beginning of hydration the two strategies differ evidently. This occurrence is linked to the dry density dependence feature of the adopted water retention model. The full saturation of the sample is reached in both cases after the 80th day of the simulations time.

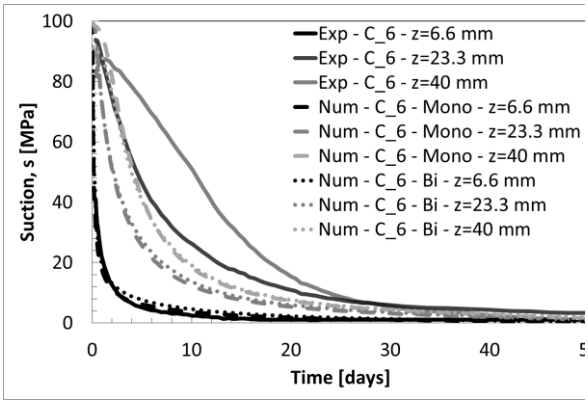

Fig. 5.36: Suction at several locations time evolution for test C_6. Comparisons between experimental data and model simulations

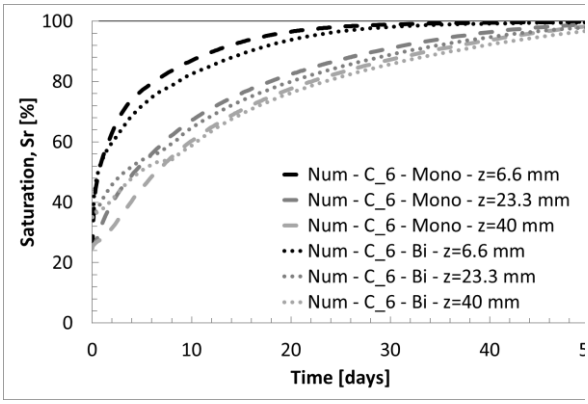

Fig. 5.37: Saturation at several locations time evolution for test C_6. Comparisons between model simulations.

Stress paths analysis

In order to better understand and explain the discrepancies in the two numerical models results, the stress-strain paths description of a point located at z=6.6 mm on the symmetry axis is presented. Such analysis will also be applied to the experimental data.

Monodimensional model

- From A' to B': the suction decrease imposed at the bottom face has caused an elastic volume increase resulting in void ratio e evolution from 0.82 to 0.89 with slope in the $(e - s)$ plane equal to 0.092 (Fig. 5.39, d). This value is slightly lower (-11%) with respect to the one corresponding to elastic axial swelling in oedometer conditions at constant stress (computed as $\kappa_s\,(1+\nu)/3(1-\nu) \approx 0.220(1+0.17)/3 * (1-0.17) \sim 0.10$) because of the axial swelling pressure increase and to the pressure dependence of the parameter κ_s. While locally the material can undergo to swelling deformation, the sample presents global isochoric conditions. Thus, due to the prominent hydration, the suction decrease also controls the swelling pressure increase in both axial and radial directions. The evolution rate in the radial direction is higher with respect to the axial one because of the imposed null radial deformation. This causes the increase of deviatoric stress q (Fig. 5.39, a) linearly proportional to the mean net stress p^{net} via the coefficient 1.31 (-12% with respect to the oedometric one 1.5). As it can be observed, the material behaviour up to the point B' is linear elastic.
- From B' to C': the pressure increase is such that the stress path has reached the LC curve (Fig. 5.39, a and b). The behaviour is now elastoplastic. Point B' is located exactly on the intercept between the LC curve with the critical state line. The point representing the material behaviour follows the evolution of the LC curve, whose size decreases as the suction decreases. Therefore, the mean net stress and deviatoric stress decrease (Fig. 5.39, a). Void ratio increase occurs as concomitant result of further suction decrease (Fig. 5.39, d).
- From C' to D': the evolution of the unsaturated cohesion c(s) and of the apparent preconsolidation pressure is that point C' is finally located at the right side of the critical state line. The suction decrease causes mean swelling pressure increase. This latter one causes the increase of the preconsolidation pressure. Deviatoric stress decreases causing a-kind-of axial unloading and consequentially void ratio increase.
- From D' to E': the mean net stress remains almost constant but the deviatoric stress becomes negative, namely the axial swelling pressure has become higher with respect to the radial one. In a small void ratio decrease is found.
- From E' to F': the wetting front has reached the further zones of the sample, which are now swelling. This swelling causes the compaction of this material portion and the consequentially increase of mean net stress, with an almost constant deviatoric stress.
- From F' to G': this further suction decrease is more important than swelling of the upper elements leading to compressive strain and it causes void ratio decrease. This generates deviatoric stress increases at constant mean net stress.
- From G' to H': hydration of the material proceeds with evident volume changes and mean net pressure increase at the considered point until the full saturation of the sample.

a) Stress path in the (p – q) plane.

b) Stress path in the (p – s) plane.

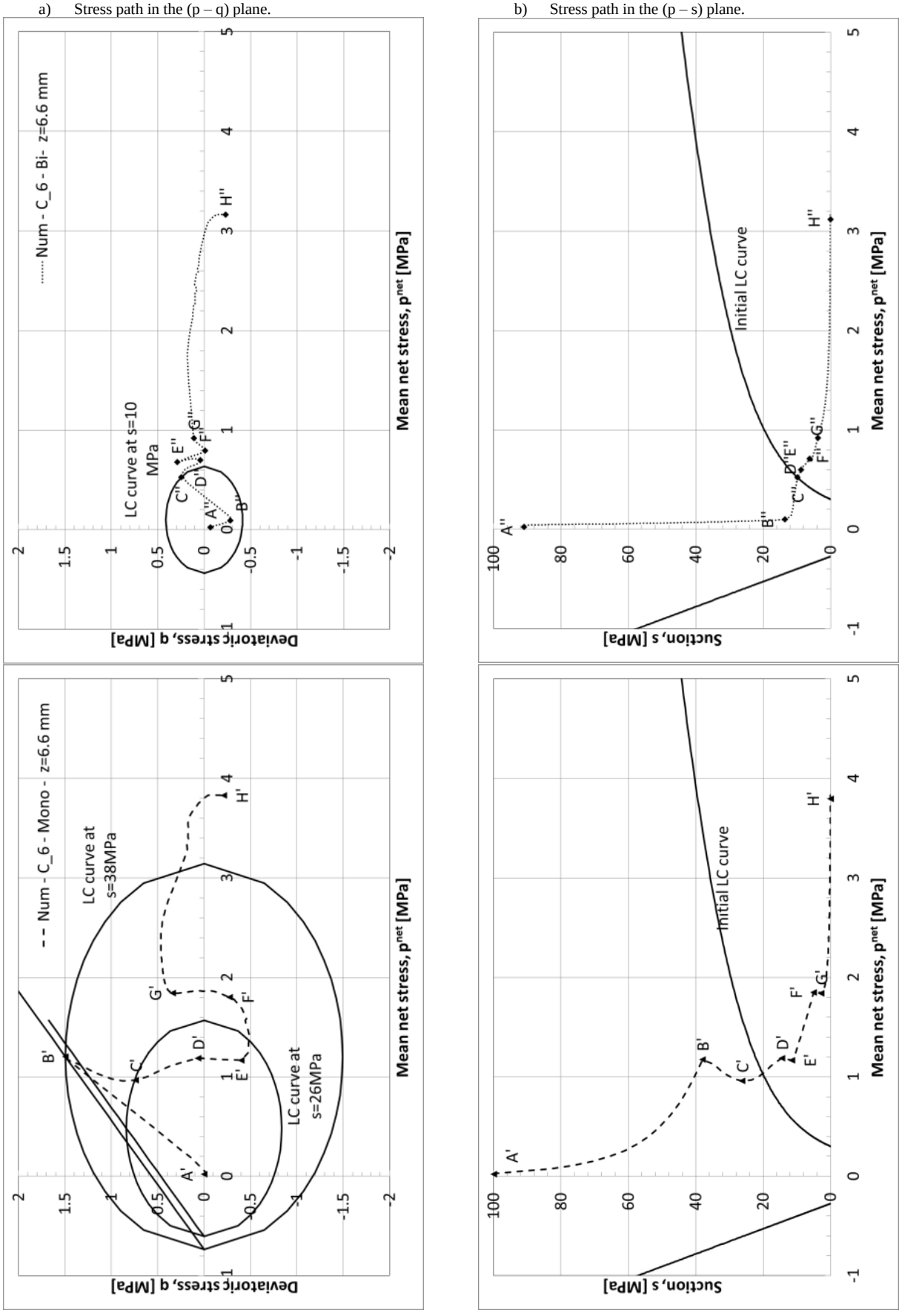

c) Evolution of the void ratio with the mean net stress.

d) Evolution of the void ratio with suction.

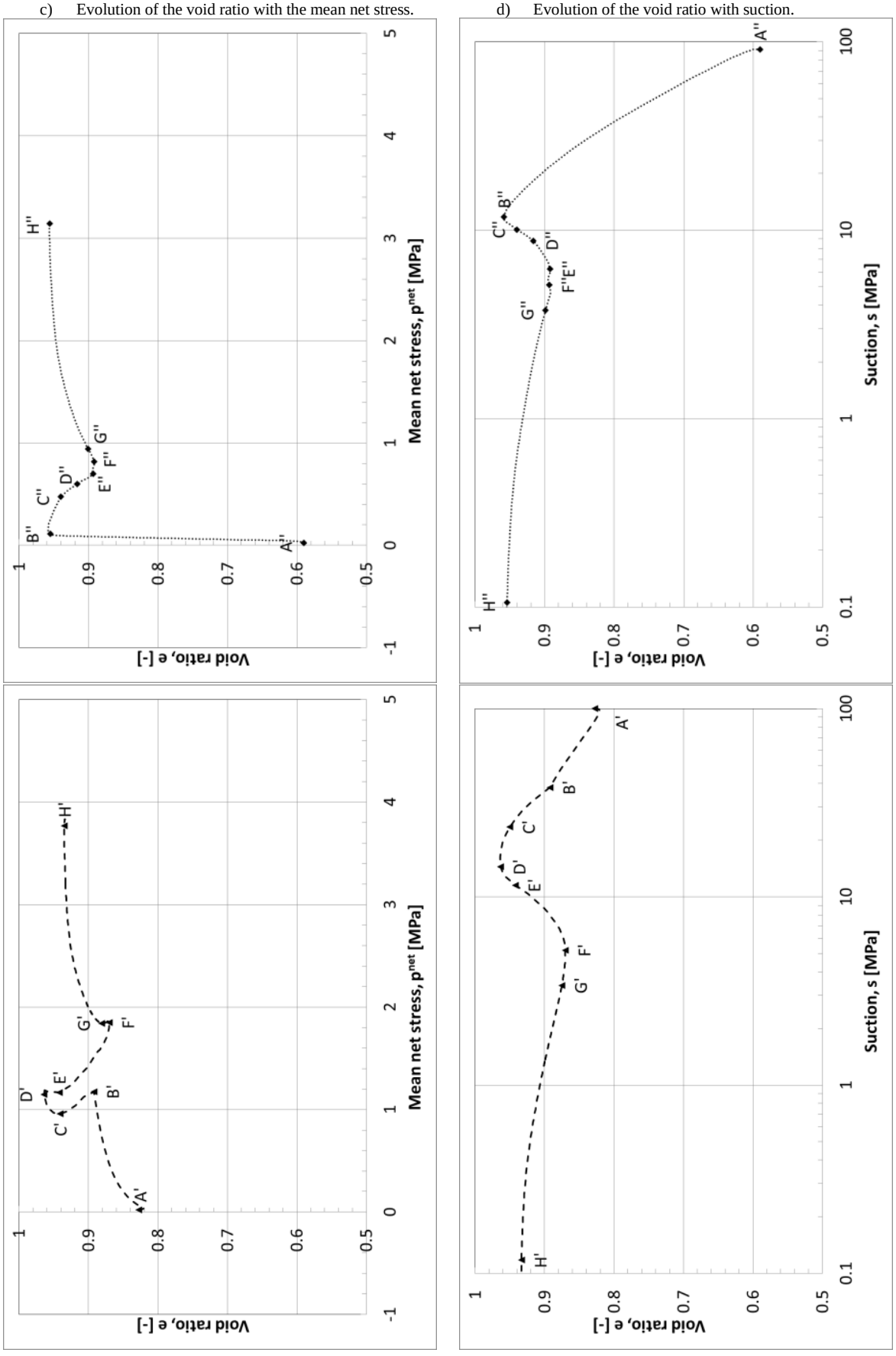

Fig. 5.39 Stress/strain paths followed by a point located at z=6.6 mm from the bottom face Fig. 5.38 Stress/strain paths followed by a point located at z=6.6 mm from the bottom face for the monodimensional numerical model. for the bidimensional numerical model.

Bidimensional model

- From A'' to B'': the suction decrease imposed at the bottom face has caused an elastic volume increase resulting in void ratio *e* evolution from 0.59 to 0.96 with slope in the $(e - s)$ plane equal to 0.188 (**Erreur ! Source du renvoi introuvable.**, d). This value is slightly lower (-15%) with respect to the one corresponding to elastic swelling at constant stress (selected as $\kappa_s \approx 0.220$) because of the axial swelling pressure increase and to the pressure dependence of the parameter κ_s. Differently from the monodimensional case, the material can swell in both axial and radial direction, even though, the axial deformation of the whole sample is prevented.
  Thus, due to the prominent hydration, the suction decrease also controls the swelling pressure increase in axial direction, whereas the radial stress is null since the material does not touch the radial cell wall and it is free to swell.
  The stress path in the $p - q$ plane presents a slope equal to -3.20, which is higher than -3, value corresponding to the axial compression path. However, the axial stress does not increase significantly at this stage showing a behaviour easily comparable to the one related to swelling at constant stress (i.e. vertical suction evolution in the $p - s$ plane)
- From B'' to C'': the material swelling has finally caused the contact with the radial cell wall. From this point, radial deformation is prevented and the development of radial stress begins. The deviatoric stress increases linearly with the mean net stress with a slope equal to 1.34 in the p – q plane, quite similarly to the oedometer compression conditions. Despite the suction decrease, the void ratio decreases (slope in the p - e plane ~0.057) due to the hydration and swelling of the upper zones. In the p – s plane, the increase of mean net stress becomes significant with respect to the suction decrease.
- From C'' to D'': the pressure increase is such that the stress path has reached the LC curve (**Erreur ! Source du renvoi introuvable.**, a and b). The behaviour is now elastoplastic. Plastic collapse is observed and the void ratio at this location decreases, despite the suction decrease. The vertical stress, hence mean stress, remains increasing as hydration and swelling of the sample proceeds. However, laterally, the stress increases at a lower rate due to collapse, so that the deviatoric stress decrease takes place. Finally, yielding comes along with hardening of the LC curve and increase of the preconsolidation pressure and elastic domain size.
- From D'' to E'': hydration continues and the behaviour is still elastoplastic. Radial stress increases as well as the deviatoric one. However, void ratio decrease is still observed despite the suction decrease.
- From E'' to F'': finally from point E'' on, elastic swelling due to suction decrease becomes more important than the plastic collapse and the void ratio increases again. The radial stress decreases and the deviatoric decreases to become equal to zero.
- From F'' to G'' and to H'': hydration of the material proceeds with evident volume changes and mean net pressure increases at the considered point until the full saturation of the sample, with constant deviatoric stress.

Fig. 5.40 and Fig. 5.41 show the stress paths in the p – q and p – s planes followed by two additional points located at distances of 23.3 mm and 40 mm from the bottom wetting surface, corresponding to the positions of the experimental radial pressure and suction sensors. The comparisons between the experimental results and the models simulations are presented. It is possible to note that stress paths do not vary much from one point of the sample to another for the same strategy. It is also interesting to note that the experimental stress paths are remarkably similar to the ones of the bidimensional model strategy. Differences can be observed in the size of the elastic domain (namely in the probable position of the LC curve), which evidently affects the results in terms of swelling pressure. In the framework of elasto-plasticity, the elastic limit is also determined

as the point after which, the slopes of the stress/strain paths change. This makes possible to assume some limits with respect to the experimental LC curve.

It is also important to note that the experimental stress path in the *p – s* plane for z=6.6 mm is mostly similar to the one related to constant volume hydration. It means that the contact with the cell wall has already occurred. Differently for z=23.3 mm and z=40 mm, the stress path is mostly similar the one of swelling at constant stress, with an increase of suction in the time when there is not contact between the sensor and the material and the following decrease related to the contact.

Finally, it can be easily concluded that discrepancies between the numerical model and experimental results are also due to the selected yielding surface, which differ from the experimental one.

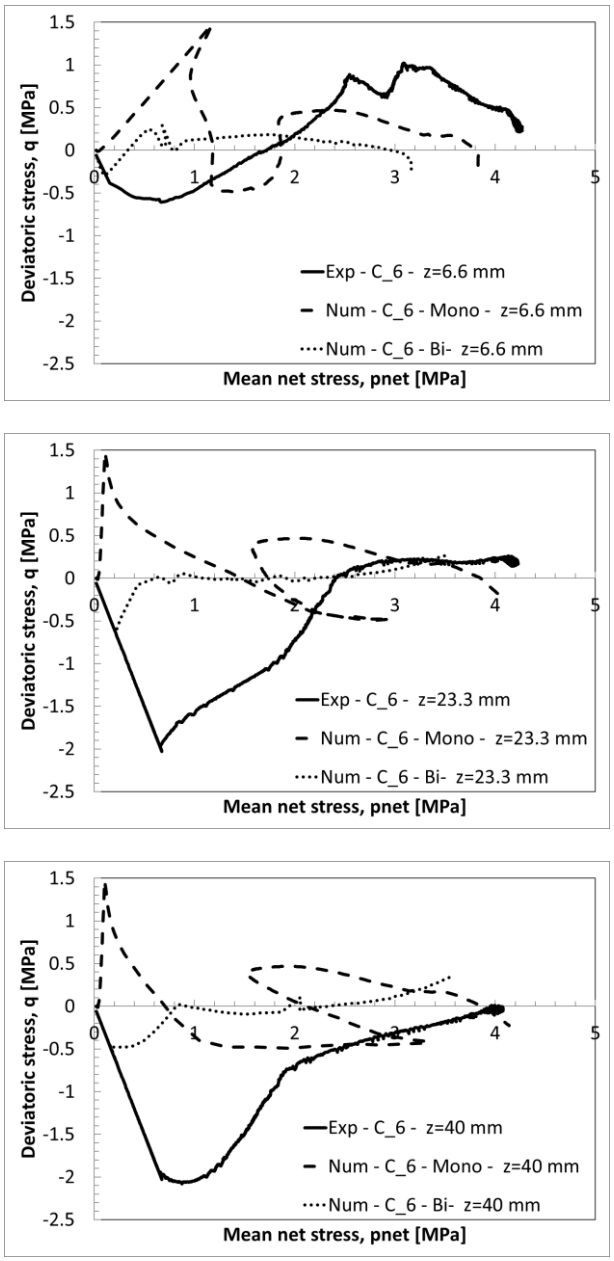

Fig. 5.40: Stress paths in the (p – q) plane followed by points located at different heights from the bottom face. Comparisons between experimental results and models simulations.

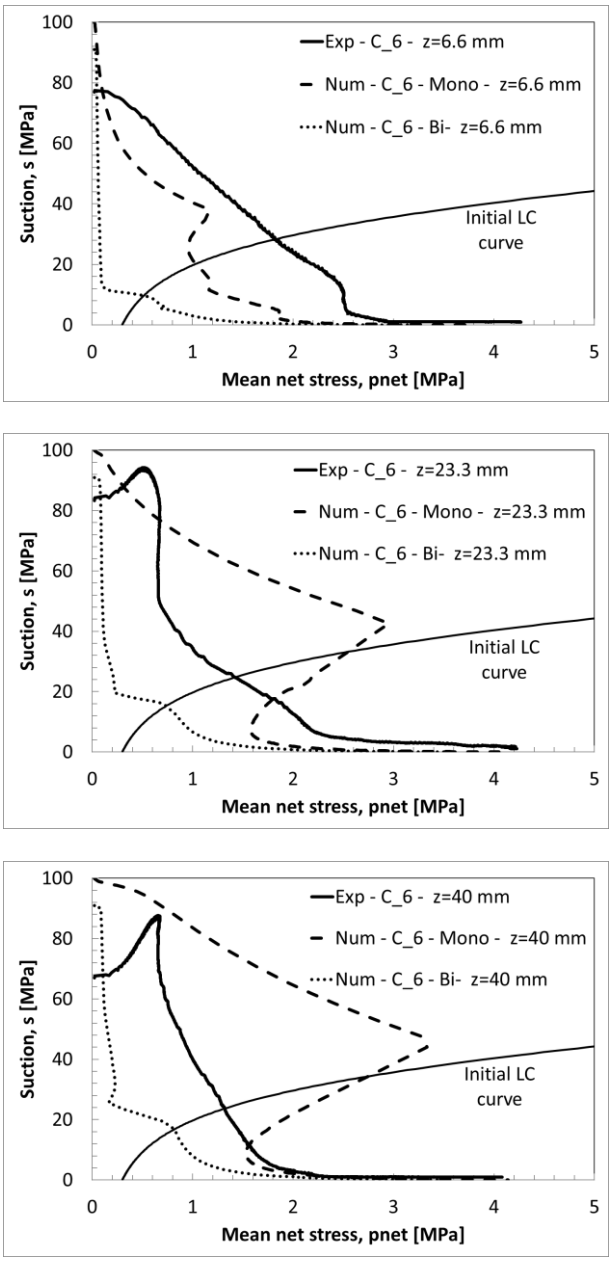

Fig. 5.41: Stress paths in the (p – s) plane followed by points located at different heights from the bottom face. Comparisons between experimental results and models simulations.

Permeability evolution

Fig. 5.42 shows the permeability time evolution at several locations for the two proposed numerical strategies.

The monodimensional model presents an initial permeability equal to $K_w=8\times10^{-21}$ m^2, whereas the bidimensional model shows an initial value equal to $K_w=6\times10^{-21}$ m^2.

This discrepancy is related to the different initial dry densities of the two models (namely $\rho_d=1.52$ Mg/m^3 for the monodimensional strategy and $\rho_d=1.75$ Mg/m^3 for the bidimensional one), which causes different initial macro-void ratio e_M.

In the first case, the micro-porosity becomes immediately dominant with respect to the macro-porosity (i.e. inter aggregates pore space) upon water saturation according to Eq. 2.11. Therefore, starting from uniform values of intrinsic permeability $K_w=8\times10^{-21}$ m^2, obtained thanks to Eq. 3.29 (Fig. 5.5) and depending on the saturation degree via e_M and k_r (Eq. 3.29 and Eq. 3.31), as the water front proceeds from the wetting face, the intrinsic permeability of the material decreases reaching a-quasi-uniform value when fully saturated along the height of the sample (Fig. 5.43).

As the hydration begins in the monodimensional model, the permeability of the material placed closest to the wetting faces immediately decreases as the large pores structures are invaded by the small pore one. Despite these portions of the samples being subjected to a certain generalised swelling (Fig. 5.44 and Fig. 5.47), which should correspond to a permeability increase, the large pores structures are instantly invaded by the micro pores structures causing the observed permeability decrease. This phenomenon is predominant with respect to other mechanisms for the monodimensional strategy model, which presents isochoric conditions since the beginning of the saturation process.

Contrarily, the bidimensional model presents at the beginning of the hydration the opposite trend, in which the permeability increases uniformly for all the considered points and only successively decreases. This phenomenon is related to the first swelling upon hydration in the radial direction toward the void space of the gap. Successively, as the contact with the cell wall occurs, the gap is closed and any further significant swelling deformation is prevented, the permeability decreases following the multi-structural evolution process described for the monodimensional model.

The initial and slower permeability decrease observed in the samples portions further from the wetting surfaces for the monodimensional model are initially related to the compaction caused by the bentonite swelling and successively by the multi-structural evolution, occurring in both experimental observations and numerical simulations. All these phenomena are linked between them and testify the strong hydro-mechanical and multi-porosity coupled processes characterising unsaturated swelling clays.

As already mentioned in the previous paragraph, the unsaturated permeability in bentonite based materials is undeniably linked to the multi-structures evolution upon hydration. Hence, in both cases, it is reasonable to consider that the water transfer mechanism takes mainly place in the largest diameter pores during the first phases of hydration with a permeability, which increases as the larger diameter pores enlarge upon a significant swelling (for the bidimensional model) and decreases as the larger diameter pores structure is invaded by the expansion of the small diameter pore structure upon saturation for isochoric conditions (monodimensional model and bidimensional model after radial gap filling).

The selected numerical model for the permeability evolution allows reproducing the permeability decrease due to the micro-structure evolution upon water saturation with the same parameters for the two different modelling strategies (Fig. 5.45).

The permeability evolutions explain the observed suction rate decrease after the first and quicker hydration phase, confirming the hypothesis of water transfer mechanism mainly occurring in large pores diameter structures during the first phases of hydration.

The final permeability values corresponding to the full saturated state are equal to $K_w \approx 5.5 \times 10^{-21}$ m^2 for the two numerical strategies.

The permeability rate evolution upon saturation can be also observed in Fig. 5.43. Despite several simplifications adopted to model this experimental test, the numerical models and its calibration are able to well reproduce the transient phase of swelling pressure development, suction evolution and dry density and water content final states (as it will be observed in the following) and give realistic results in terms of permeability evolutions.

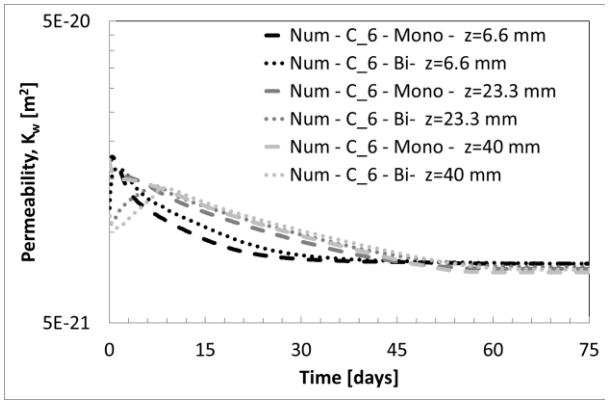

Fig. 5.42: Permeability at several locations time evolution for test C_6. Comparisons between model simulations.

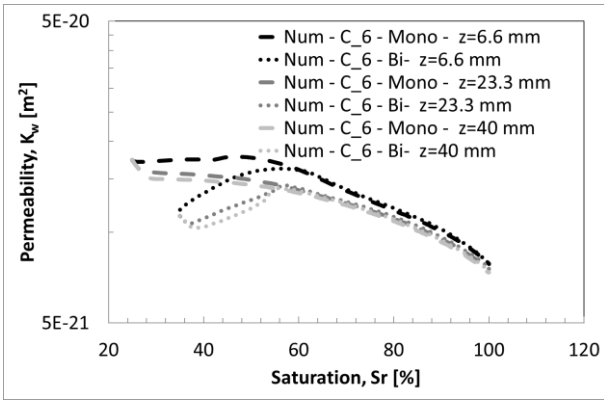

Fig. 5.43: Permeability at several locations as function of Saturation for test C_6. Comparisons between model simulations.

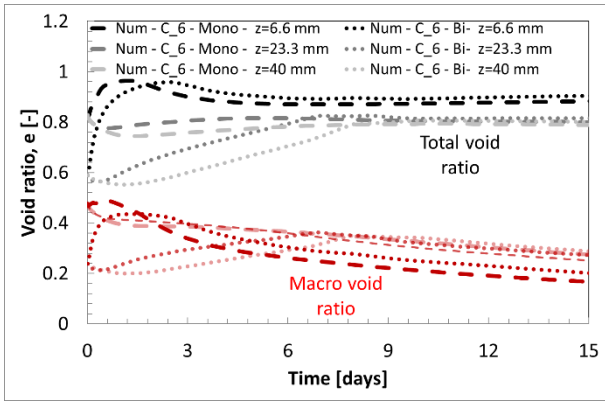

Fig. 5.44: Total and macro void ratio at several locations time evolution for test C_6. Comparisons between model simulations.

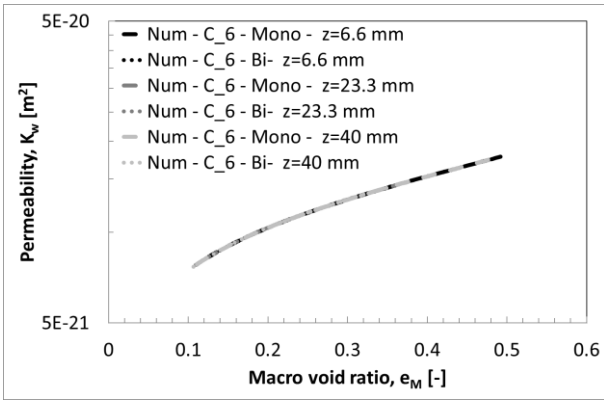

Fig. 5.45: Permeability at several locations as function of Macro void ratio for test C_6. Comparisons between model simulations.

Fig. 5.46 shows the radial gap thickness time evolution at several locations for the bidimensional model. The radial gap thickness is the distance between the bentonite sample and the cell wall. The time of the contact and the deformation kinetics can be determined. Namely it is possible to observe that at z=6.6 mm the contact with the cell wall occurs at the 3rd day of the simulation time, whereas it takes place at day 7 and 8 for z=23.3 and 40 mm respectively. Accordingly to the void ratio time evolution (Fig. 5.44), for the bidimensional model there is a first void ratio increase corresponding to the swelling in the radial direction. After the contact with the cell wall, the paths of the monodimensional and bidimensional models fully correspond.

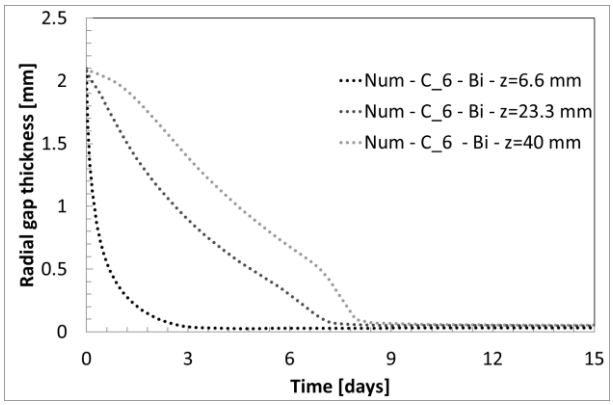

Fig. 5.46: Radial gap thickness at several locations as function of time for test C_6. Bidimensional model results.

Dry density and water content

Dry density and water content were evaluated thanks to post mortem analyses. Apparent density and water content measurement are taken at three locations through the vertical axis of the sample.

Experimental results show a final homogeneous dry density (and water content) distribution between ρ_d=1.45 and 1.50 Mg/m^3. (and w=30%) slightly lower with respect to the initial one (ρ_d=1.52 Mg/m^3) (Fig. 5.47 and Fig. 5.48). Experimental outcomes underline a small generalized volume increase, which contradicts the hypothesis of constant volume hydration. On the other hand, the detected experimental dry density general decrease can also be due to post dismantling and sampling swelling.

It is interesting to note that the initial dry density of the compacted block was equal to ρ_d=1.75 Mg/m^3, with a swelling deformation, possibly occurred in the radial direction (i.e. the gap), as the numerical bidimensional model predicts.

A vertical density gradient is observed in the direction of hydration, inversely correlated with water content for both numerical strategies.

The numerical minimum dry density values (maximum water content values) are found for both numerical strategies in the locations close to the wetting surfaces.

With respect to the monodimensional model, when water is injected, the material placed close to the wetting surfaces undergoes an important volume increase. Accordingly to the prescribed isochoric conditions, this volume increase should be counterbalanced by a volume decrease far from hydration front. Thus, this latter zone is compressed by the swollen of the wetted material. As the saturation front penetrated within the sample, the transition between the swollen and compressed zone recedes from the injection sides and stops before the first half of the hydration length (~45% h_i/h_{tot} from the wetting surface).

The above-mentioned process is similar for the two numerical strategies. Nevertheless, it is important to mention that for the bidimensional model the swelling upon hydration does not occur only in the vertical direction but also in the radial one. Thus, the compaction of the material related to the volume increase of the wetted portions of the sample is smaller with respect to the monodimensional case because the general volume increase in the radial direction is predominant.

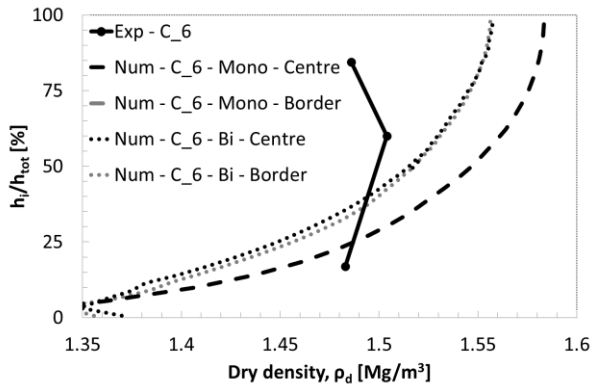

Fig. 5.47: Dry density distribution over the height of the sample (in percentage) at the end of the test for test C_6. Comparisons between experimental data and model simulations.

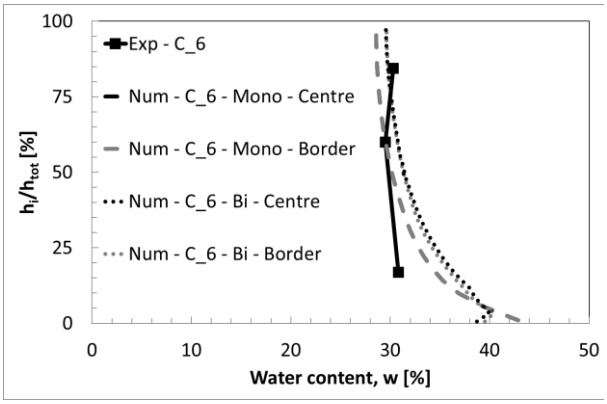

Fig. 5.48: Water content distribution over the height of the sample (in percentage) at the end of the test for test C_6. Comparisons between experimental data and model simulations.

Conclusions

This paragraph presented an alternative numerical bidimensional strategy for modelling an experimental isochoric-wetting test performed on a MX80 bentonite compacted block surrounded by radial gap.

Differently from the numerical monodimensional model presented in section 5.3, this advanced bidimensional analysis accounting for the real initial sample configuration provides further insights with respect to swelling pressure and deformation developments during the specimen hydration.

Firstly, the bidimensional model reproduces much better the experimental swelling pressure trends, which evidently depends on the stress paths undertaken by the material. As it could be observed, the material stress-paths depends on a number of factors, but, among others, especially on the constrain conditions (i.e. free swelling or isochoric hydration).

Moreover, the comparisons between the experimental and numerical stress paths in the p – s and p – q planes provide interesting information on the material characterisation in a complete innovative way (i.e. yielding surface position).

This numerical analysis allowed determining the influence of the experimental radial gap, which also affects undoubtedly the initial and transient hydration phases (i.e. void ratio and permeability increase), which could become particularly relevant when considering real in-situ structures.

5.5.Conclusions

This chapter presented a combined experimental and numerical analysis focused on the effect of different pore structure distributions on mechanic and water transfer mechanisms for similar average dry density assemblies of bentonite. Taking advantage of the finite element code LAGAMINE, the Barcelona Basic model is considered for the bentonite mechanical behaviour and the double porosity model is used for the water retention behaviour and permeability evolution. Given the already-known complexity of the multiphysical and multiscale coupled processes taking place during bentonite-hydration, the obtained numerical results are in good agreement with experimental measurements.

This study has identified a number of features regarding the role of multi-structures pores size distributions bentonite materials. Based on an elasto-plastic framework and multi-structures interaction, the swelling pressure developments of the different assemblies were described and compared. The introduction of an innovative representation concerning global features of the specimens such as the top axial swelling pressure and the average saturation degree allowed simplifying the comparison of different sample sizes. Indeed, differently from time dimension, which can span very large ranges going from few hours to several months, the average saturation degree of the sample has defined minimum and maximum values, for any sample size. The numerical analysis of the permeability evolution also gave relevant information with respect to the role of the large pores structure distributions and their evolution upon wetting, which progressively disappear leading a clear permeability decrease. The adopted numerical model and its calibration were able to well reproduce the transient phase of swelling pressure development, suction evolution and dry density and water content final states. The study of the dry density and water content distributions at dismantling permitted to better understand the local phenomena taking place in the overall constant volume cell accounting for the boundary conditions (i.e. one or double side hydration).

Moreover, the alternative and additional bidimensional strategy considering the existing radial gap of test C_6 overcame the limitations of the homogeneous monodimensional strategy adopted in the first general analysis. This latter study particularly underlined the importance of the volumetric deformation constraints on the stress path and material response, also providing information on the material characteristics in a possible elasto-plastic framework.

The current data highlighted the differences between hydro-mechanical responses of the available bentonite materials assemblies, which are mainly adopted for the sealing of nuclear waste disposals.

On the other hand, with respect to the sealing designs procedures and strategies, this study shows the relevance of the experimental radial gap for lab conditions, which becomes the larger existing technological void for real scale structures. This affects undoubtedly the initial and transient hydration phases (i.e. void ratio and permeability increase), which could become harmful and dangerous when considering real in-situ structures.

Notwithstanding the relatively limited samples and the evident simplifications, this work offers valuable insights into the knowledge and careful selection of bentonite based materials in several forms.

CHAPTER 6: MULTI-STRUCTURE ASSEMBLIES COMBINATIONS AT LABORATORY SCALE

CHAPTER 6: MULTI-STRUCTURE ASSEMBLIES COMBINATIONS AT LABORATORY SCALE

6.1. Introduction

The hydro-mechanical analysis of bentonite multi-structures assemblies combinations upon hydration is quite complex.

The aim of this chapter is to combine experimental and numerical approaches to better understand the hydro-mechanical phenomena taking place during the interaction of the different assemblies between them and with the experimental tools upon hydration. All these interactions affect the development and the evolution of the experimental and numerical measurements but they were never deeply investigated before.

For this purpose, large-scale oedometer tests (MGR) performed by CIEMAT are analysed. These tests were performed in order to evaluate one of the possible sources of bentonite heterogeneity: the combination in the same barrier of pellets and blocks of compacted bentonite, whose initial dry densities and structures noticeably differ. Several materials configuration and hydration boundary conditions are considered in this experimental campaign, which also provides interesting hints with respect to intermediate saturation states.

The experimental data on the investigated Febex pellets and compacted block layers are presented. Successively, the adopted hydro-mechanical parameters for the bentonite materials and the interface properties are given.

MGR experimental tests are described and finally modelled numerically. Comparisons between experimental and numerical results especially focus on intermediate saturation phases of the bentonite-based materials from both hydraulic and mechanic points of view.

The numerical strategy employs the Barcelona Basic Model (Alonso, Gens, and Josa 1990) for bentonite mechanical behaviour, pressure dependence for some mechanical parameters, and Dieudonné double porosity model for the water retention behaviour and water permeability evolution (Dieudonné, Della Vecchia, and Charlier 2017).

Despite the fact that the heterogeneous initial pores structure distributions of the studied samples are well-known, all the samples layers are represented in the context of continuum mechanics in the numerical strategy. The chosen numerical methods match experimental measurements surprisingly well.

The non-monotonic evolution of swelling pressure during the hydration process, in particular, is consistent with the experimental results.

This work allows determining the validity of the adopted numerical model and some shortcomings of the experimental measurements by comparing experimental results and numerical simulations at dismantling (i.e. dry density and water content distributions, but also MIP).

Through the introduction of an interface element, the development of friction between the material samples and the cell wall is also considered and numerically studied. It turns out to be crucial in explaining unexpected experimental outcomes.

6.2. Materials

Febex bentonite multi-structure combinations assemblies are analysed (Lloret and Villar 2007a).

All the experimental tests consider the combination of pellets and blocks of compacted bentonite, whose initial dry densities and structures noticeably differ.

The block part of the sample was compacted from the granulate material with its hygroscopic water content, which is ~14%. The pellets were prepared in a factory for the EB project (Lloret, Romero, and Villar 2004). The bentonite was dried and milled in a three-step process to produce a fine grade powder with a water content of 3.3%. Later, a commercial plant with an in-line highly automated briquetting process produced coarse (>7 mm) and fine (0.4-2 mm) grained materials with dry densities of 2.11 and 2.13 Mg/m^3, respectively. These two grain size fractions were subsequently combined to fit a Fuller shape curve with a maximum diameter of 12.7 mm and a minimum diameter of 0.425 mm, in order to reduce segregation. The different grain sizes were kept separated and mixed in the right proportion just before every test. The lab run out of pellets larger than 9.5 mm, and the granulometric distribution of tests MGR23 and MGR24 was modified to keep the Fuller's curve (Fig. 6.1). Also, in these tests the pellets were softly dried to water content closer to the fabrication one, because the water content of the pellets increased during storage.

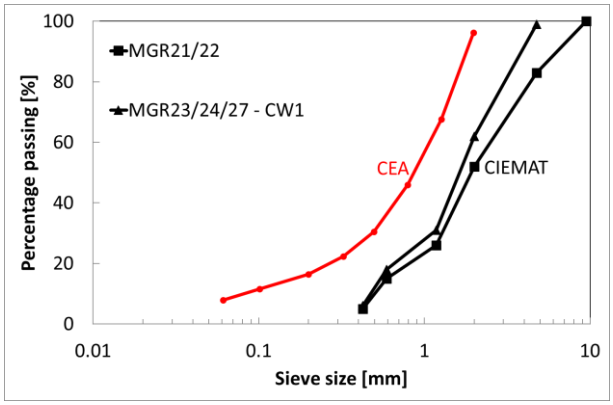

Fig. 6.1: Grain size distribution of the crushed pellets powder for CIEMAT tests serie and CEA tests serie (Chapter 5).

6.2.1. Water retention behaviour

The selected double porosity dry density dependent water retention model does not distinguish the initial pore structure distributions of the considered assemblies, thus a unique set of parameters corresponding to the calibration proposed by (Dieudonné, Della Vecchia, and Charlier 2017) for Febex bentonite is selected (Table 6.1 and Fig. 6.2)

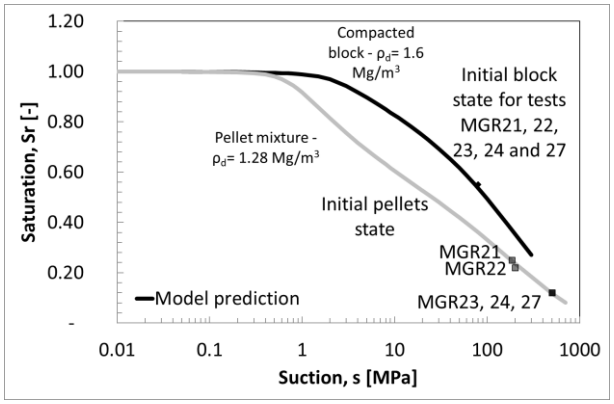

Fig. 6.2: Model prediction for the water retention curve. Initial experimental data and initial numerical data.

Table 6.1: Parameters of the water retention curve model.

		Compacted block	Pellets mixtures
ρ_d	[Mg/m^3]	1.60	1.28
e_{m0}	[-]	0.35	
β_0	[-]	0.15	
β_1	[-]	0.35	
C_{ads}	[MPa^{-1}]	0.0028	
n_{ads}	[-]	0.78	
n	[-]	3	
m	[-]	0.15	
A	[MPa]	0.24	

6.2.2. Flow properties

The parameters for the water permeability evolution (Table 6.2 and Fig. 6.3) were calibrated by best-fitting the responses of the water intake time evolution of test MGR23. Consequentially, the model is validated by comparing the swelling pressure kinetics and final dry density and water content distributions.

Table 6.2: Parameters of the permeability evolution model.

		Compacted block	Pellets mixtures
C_k	[m^2]	2.8 ×10-20	2.8 ×10-20
expm	**[-]**	1.2	0.9
expn	**[-]**	0.1	0.1
γ	**[-]**	3.4	3

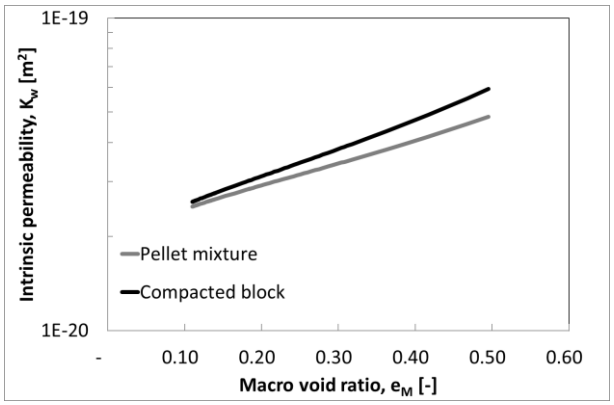

Fig. 6.3: Intrinsic permeability evolution with macro-void ratio accordingly to **Eq. 3.29** and Table 6.2.

6.2.3. Mechanical behaviour

The mechanical parameters were derived in Chapter 4 from the experimental campaign performed by (Lloret et al. 2003) on a similar dry density compacted Febex bentonite, whereas for the Pellets layer data from (Hoffmann, Alonso, and Romero 2007) were adapted (Furthermore, such values are selected similar to the ones adopted for MX80 pellets mixtures and compacted block of Chapter 5, in which radial pressure experimental records were available and could confirm their reliability.

Table 6.3). Mechanical parameters such as the friction angle, Poisson ratio and cohesion are in general very difficult to measure during experimental campaigns on swelling unsaturated bentonites (especially with respect to pellets mixtures) and very few data are available. Due to this, a trial and error procedure was adopted to reproduce the target results in terms of the swelling pressure measurements presented in this work. Furthermore, such values are selected similar to the ones adopted for MX80 pellets mixtures and compacted block of Chapter 5, in which radial pressure experimental records were available and could confirm their reliability.

Table 6.3: Parameters of the mechanical model.

		Compacted block	**Pellets mixture**
ρ_d	**[Mg/m^3]**	1.60	1.28
κ	**[-]**	0.012	0.074
κ_s	**[-]**	0.12	0.075
α_p	**[-]**	4.4×10^{-8}	3×10^{-6}
p_0*	**[MPa]**	1.6	0.65
p_c	**[MPa]**	0.395	0.325
$\lambda(0)$	**[-]**	0.12	0.20
r	**[-]**	0.55	0.70
ω	**[MPa^{-1}]**	0.25	0.008
φ	**[°]**	20	26
ν	**[-]**	0.25	0.35
$c(0)$	**[MPa]**	0	0
k	**[-]**	0.0046	0.0046

6.3. Binary mixtures large scale swelling pressure tests

6.3.1. Description of the tests

The objective of this series of tests is to investigate the re-saturation in isochoric conditions of a number of Febex bentonite samples composed of the layers' combination of pellets and blocks of compacted material, whose initial dry densities and pore-structures distributions significantly differ.

Precisely, the main goal of this experimental campaign is to evaluate both quantitatively and qualitatively the possible sources of bentonite heterogeneities.

The tests were performed by the Energetic, Environmental and Technological Investigations Centre (CIEMAT) in the context of BEACON project (Sellin et al. 2020).

All the MGR tests present two different Febex bentonite layers: a pellet layer 50.1±0.3 mm high, presenting initial dry density equal to ρ_d=1.28±0.02 Mg/m^3 and initial water content w=6.5±3% and a compacted bentonite block layer 49.8±0.3 mm high, with initial dry density equal to ρ_d=1.61±0.01 Mg/m^3 and initial water content w=13.8±0.4%. The overall samples are 99.9 mm high, with average dry density ρ_d=1.44±0.01 Mg/m^3 and average initial water content w=10.7±1.2%.

These tests, whose samples present almost identical initial states, hold a number of key originalities.

Additional information with respect to dry density and water content distributions during hydration is provided thanks to the fact that tests MGR21, 23 and 24 are stopped at different saturation times (i.e. average saturation degrees), respectively at the 34th, 210th and 14th day after the beginning of hydration.

Given the comparable initial states and the same hydration boundary conditions, it can be reasonable to assume the final states of tests MGR21 and 24 as intermediate states of test MGR23.

As a matter of fact, physical state in terms of dry density and water content can be characterized only in a post-mortem way (in the final state of the experiment), together with Mercury Intrusion Porosimetry (MIP) measurements performed on freeze-dried samples after dismantling.

Thus, very few data are available for intermediate states of dry density and water content distributions characterisation. This series of tests provides exhaustive complementary information with respect to this.

Experimental samples specifications can be found in Fig. 6.4 and Table 6.4.

Table 6.4: Initial state and characteristics of the experimental samples.

EXPERIMENTAL TESTS	**MGR21**	**MGR22**	**MGR23**	**MGR24**	**MGR27**
Position of the pellet layer	Bottom	Bottom	Bottom	Bottom	Top
Pellet height [mm]	49.7	50.4	50.0	50.2	50.0
Pellet dry density [Mg/m^3]	1.26	1.28	1.30	1.28	1.30
Pellet water content [%]	9.50	9.90	3.5	5.7	3.5
Position of the block layer	Top	Top	Top	Top	Bottom
Block height [mm]	50.1	49.4	49.8	49.7	49.8

Block dry density [Mg/m^3]	1.60	1.61	1.60	1.62	1.60
Block water content [%]	13.3	13.6	14.2	13.7	14.2
Diameter [mm]	100	100	100	100	100
Total height [mm]	99.8	99.8	99.8	99.9	99.8
Total dry density [Mg/m^3]	1.43	1.45	1.45	1.45	1.45
Total water content [%]	11.6	11.9	9.4	10.1	9.4
Test duration [days]	34	266	210	14	278

The experimental device consists in a constant volume large-scale oedometer cell. Constant volume conditions are assured by a rigid frame, which hinders the upper piston displacement of the samples.

Axial force and displacement are measured respectively by a 10-t load cell in the upper part of the frame and an external LVDT.

The device presents a cell internal diameter equal to 100 mm and the length of the sample inside is 100 mm. The top and bottom of the sample are in contact with filter papers and ceramic porous discs connected to outlets.

Hydration is allowed through different procedures. Namely, deionised water is injected with a very small hydraulic head (140 cm for tests MGR21, 23, 24 and 27) or under a constant low flow (0.05 cm^3/h for test MGR22), simulating a continuous contribution of water from an in-situ host-rock. In the first case the water intake is measured with an automatic volume change apparatus and in the second case with a pressure/volume controller and both are automatically recorded. Thanks to this, it becomes possible to define to which extent the hydraulic boundary conditions affect the heterogeneities distributions development of the material. Water is provided through porous plates on the bottom side of the chamber, blocked at approximately zero displacement and the other side of the sample is placed at laboratory conditions to ensure evacuation of entrapped air.

If on one hand the bottom part of the samples in direct contact with the water source is composed of the pellets layer (tests MGR21, 22, 23 and 24), the last test presents inverted configuration (i.e. bottom layer composed of compacted bentonite block, test MGR27).

A more detailed description of the experimental device can be found in (Talandier 2018; Villar et al. 2021).

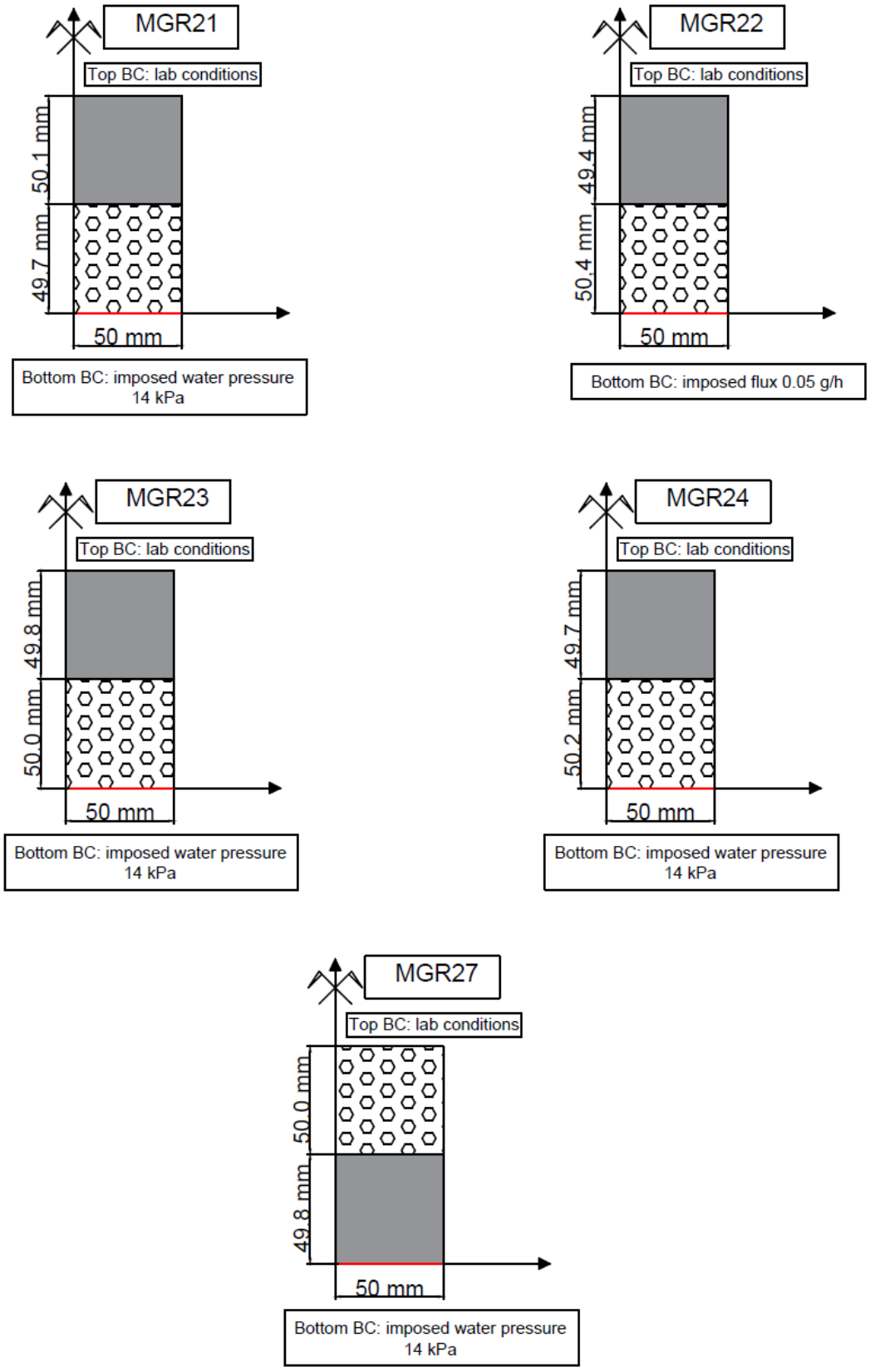

Fig. 6.4: Characteristics of the considered samples.

6.3.2. Features of the analysis

The numerical bentonite samples consist in 800 eight-noded isoparametric elements representing the bentonite materials (400 for the pellets and 400 for the compacted block). The problem is assumed bidimensional, axisymmetric and oedometer conditions are considered (Fig. 6.6).

The above-mentioned differences between the layers configurations of the five experimental tests are well-recognized. Consequentially for the tests MGR21, 22, 23 and 24 the pellet layer is positioned in direct contact with the hydration surface on the bottom part of the sample and compacted block in the upper one, whereas the opposite configuration is set for test MGR27.

The pellet and compacted block layers materials present the same dry density in all the five tests, namely equal to ρ_d=1.28 Mg/m^3 and ρ_d=1.60 Mg/m^3 respectively, considering the similar initial dry density in the experimental tests.

The water content slightly differ for the pellet layers in the analysed tests but it is the same for the block parts in all the tests (w=13.6%).

The strong heterogeneity of the pellets-mixture material is well-recognized, but in this modelling strategy, the pellets layer is considered homogeneous, presenting the same hydro-mechanical properties and state in the entire domain, as well as bentonite block layer.

Same hydro-mechanical properties and hydro-mechanical state are set with initial uniform suction s related to the saturation degree S_r, (obtained thanks to the corresponding water content w and dry density ρ_d) via the adopted dry density dependent water retention model. Initial water contents w in the numerical model are mostly similar to the ones experimentally measured at the initial state.

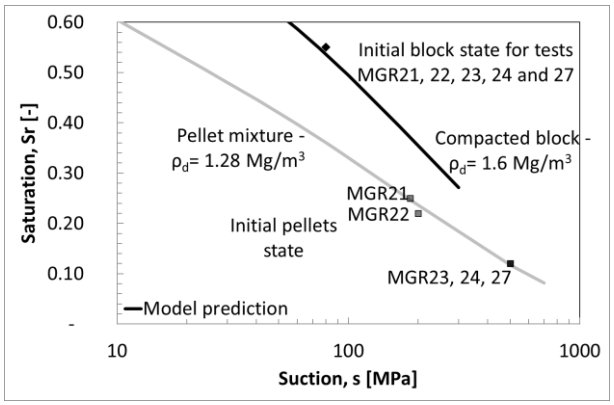

Fig. 6.5: Model prediction for the water retention curve. Initial experimental data and initial numerical data. Suction s between 10 and 1000 MPa and Saturation degree between 0.10 and 0.60.

Table 6.5: Initial state and characteristics of the numerical samples.

NUMERICAL SIMULATIONS	MGR21	MGR22	MGR23	MGR24	MGR27
Position of the pellet layer	Bottom	Bottom	Bottom	Bottom	Top
Pellet height [mm]	49.6	49.6	49.6	49.6	50.4
Pellet dry density [Mg/m^3]	1.28	1.28	1.28	1.28	1.28
Pellet water content [%]	9.80	10.0	4.90	4.90	4.90
Corresponding suction [MPa]	200	185	500	500	500
Position of the block layer	Top	Top	Top	Top	Bottom
Block height [mm]	50.4	50.4	50.4	50.4	49.6
Block dry density [Mg/m^3]	1.60	1.60	1.60	1.60	1.60
Block water content [%]	13.6	13.6	13.6	13.6	13.6
Corresponding suction [MPa]	80	80	80	80	80
Diameter [mm]	50	50	50	50	50
Total height [mm]	100	100	100	100	100
Total dry density [Mg/m^3]	1.44	1.44	1.44	1.44	1.44
Total water content [%]	11.9	12.0	9.76	9.76	9.76
Test duration [days]	34	266	210	14	278

The initial suction in the each layer of each test is estimated from the water retention model, considering initial water content and a dry density of the layer (Table 6.5).

The hydration of the sample is provided from the bottom face (red line, Fig. 6.6) assuming a suction decrease from the initial value to the experimental boundary conditions (Fig. 6.4) occurring in 1000 seconds (for tests MGR21, 23, 24 and 27) or 0.05 g/h of water injection during the 10th and the 220th of the simulation time (test MGR22).

All the samples are subjected to 0.1 MPa of confining stress in both axial and radial directions. This low initial confining stress is set in order to assure numerical stability at the beginning of the numerical simulation. However, thanks to the pressure dependence law adopted for the parameter κ_s, it does not affect the swelling pressure evolution and maximum values.

An interface element (Cerfontaine et al. 2015) is modelled with 40 3-noded iso-parametric elements in order to reproduce the interaction between the bentonite materials and wall of the cell (green line Fig. 6.6).

Friction is considered, so that, the cell wall at the same moment represents a normal constraint and prevents the bentonite samples to freely slide in the axial direction.

The longitudinal and transversal transmittivity of the interface is supposed to be null. (i.e. there is no water exchange between the interface and the bentonite nor longitudinal flux into the interface itself).

Hence, the total stress formulation is selected for the mechanical constitutive model of the interface element. The interface mechanical parameters are presented in Table 6.6. The choice of the friction angle is not an easy task. It will be discussed further in section 3.4 of this chapter.

Table 6.6: Interface mechanical properties.

Penalty coefficient in the normal direction	K_t	**[N/m^3]**	10^{11}
Penalty coefficient in the longitudinal direction	K_l	**[N/m^3]**	10^{11}
Friction angle	φ	**[°]**	7
Friction coefficient	μ	**[-]**	0.125
Cohesion	c'	**[MPa]**	0

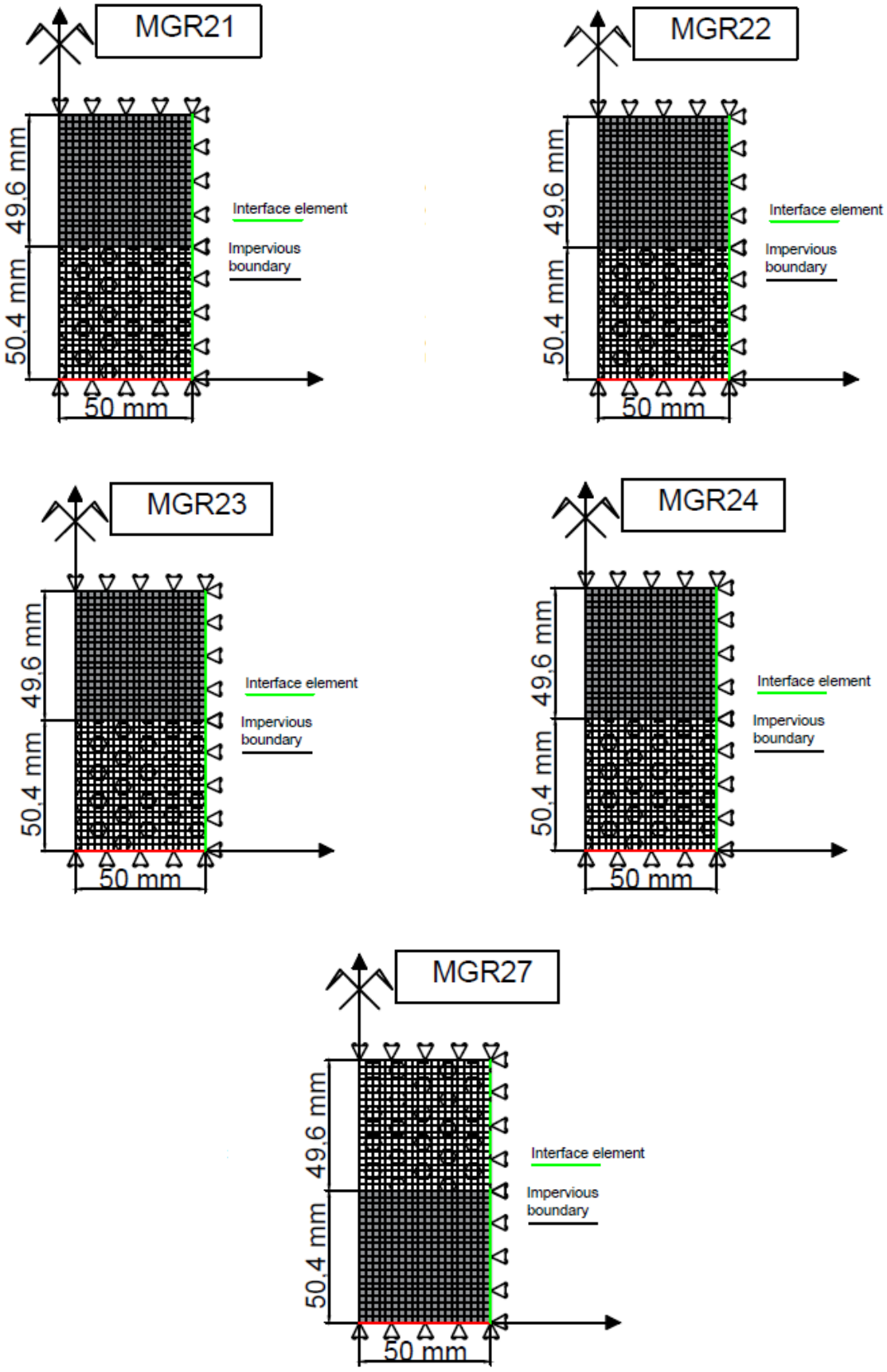

Fig. 6.6: Boundary conditions of the model

6.3.3. Experimental and numerical results

Water intake

From Fig. 6.7 to Fig. 6.10, experimental water intake and average saturation time evolutions are shown. The two different water supply strategies are easy to distinguish. Namely, it is possible to observe that for the constant injection pressure procedure adopted for tests MGR21, 23 and 24, the water intake is very quick and more than half of the water volume necessary for full saturation is taken in about 10 days (details in Fig. 6.9 and Fig. 6.10). This phenomenon is mostly linked to the very high permeability characterising the pellets layers. Accordingly the water transfer mechanism of test MGR27 appears much slower than the ones related to test MGR21, 23 and 24. This concerns the fact that the compacted bentonite block permeability is much lower than the pellets one. Furthermore, the water volume injected and, linearly proportional, the average saturation degree of the sample is fully controlled in test MGR22 and it is linear with time.

Tests MGR21, 23 and 24 experimental outcomes are very difficult to distinguish in the first phase of hydration and the water injection and average saturation curves nearly overlap. With respect to test MGR23, a plateau is observed between the 10th and the 28th days of the experimental test time, when 150 cm^3 of water have been injected. It is interesting to note that in the initial state of the pellet layers (i.e. dry density equal to ρ_d=1.28±0.02 Mg/m^3 and initial water content w=6.5±3%), assuming constant volume conditions and a closed system, the water volume needed to fully saturate the pellets material is very close to 150 cm^3. This quantity corresponds to the 70% of the average saturation degree of the samples. This phenomenon will be analysed in the following in a separated paragraph.

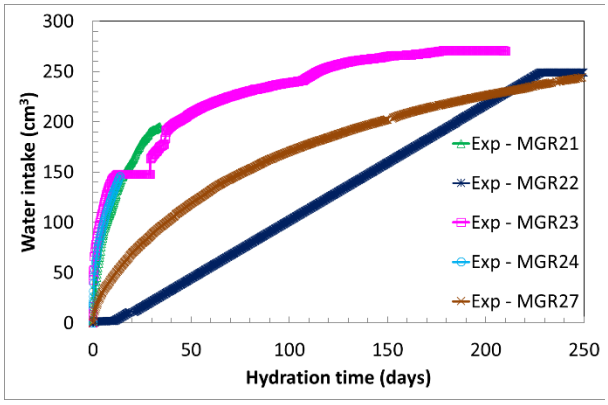

Fig. 6.7: Water mass injection time evolution for tests MGR21, MGR22, MGR23, MGR24 and MGR27. Comparisons between experimental data.

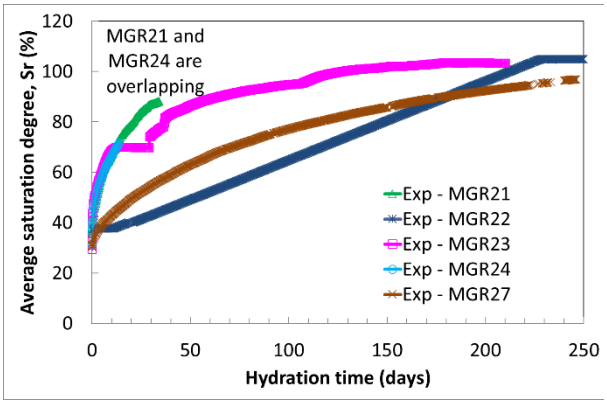

Fig. 6.8: Average sample saturation evolution for tests MGR21, MGR22, MGR23, MGR24 and MGR27. Comparisons between experimental data.

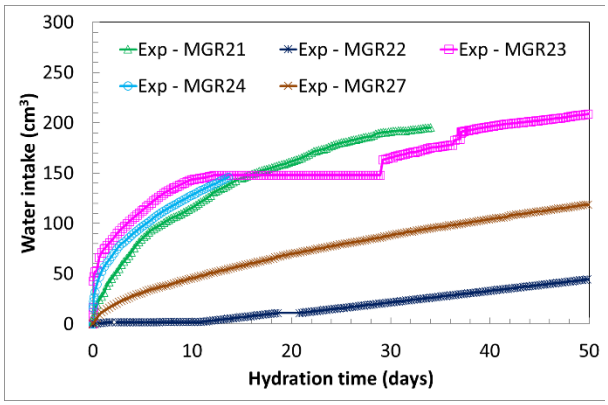

Fig. 6.9: Water mass injection time evolution for tests MGR21, MGR22, MGR23, MGR24 and MGR27. Comparisons between experimental data in the first 50 experimental test days.

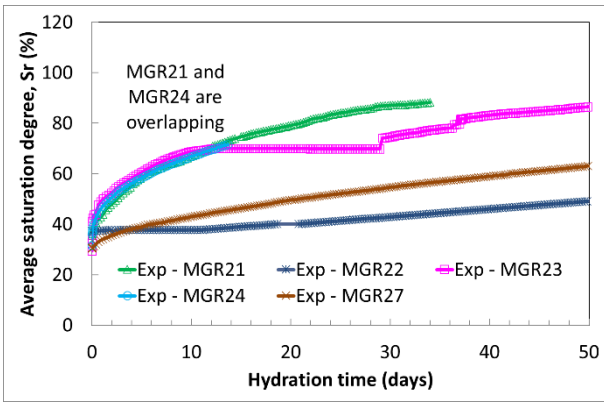

Fig. 6.10: Average sample saturation evolution for tests MGR21, MGR22, MGR23, MGR24 and MGR27. Comparisons between experimental data in the first 50 experimental test days.

Test MGR21 is stopped at the 34th day after the beginning of hydration with 195 cm^3 of injected water (W.I.) and 88% of average saturation (S_r), MGR22 at day 265, W.I.=249 cm^3 and S_r=105%, MGR23 at day 210, W.I.=270 cm^3 and S_r=103% and MGR24 at day 14, W.I.=146 cm^3 and S_r=72%.

The permeability law evolution for the pellets and compacted block materials is calibrated on the experimental water intake time records of test MGR23. Thus, the numerical simulations (Fig. 6.11) reproduce quite well the experimental results also for tests MGR21 and MGR24, which slightly differ from the MGR23 with respect to the initial water content.

Numerical and experimental results for test MGR23 coincide particularly well in the initial phase but diverge with respect to the above mentioned experimental plateau occurring between the 10th and 30th days of the test. Also the final values of injected water present discrepancies. This is mostly related to the very strong water density variation occurring in Febex bentonite during hydration (Villar 2000). With respect to test MGR22, the water inflow is imposed, thus the effect of permeability cannot be immediately observed. For MGR 22 there is a small bump on the stress curve at 220 days.

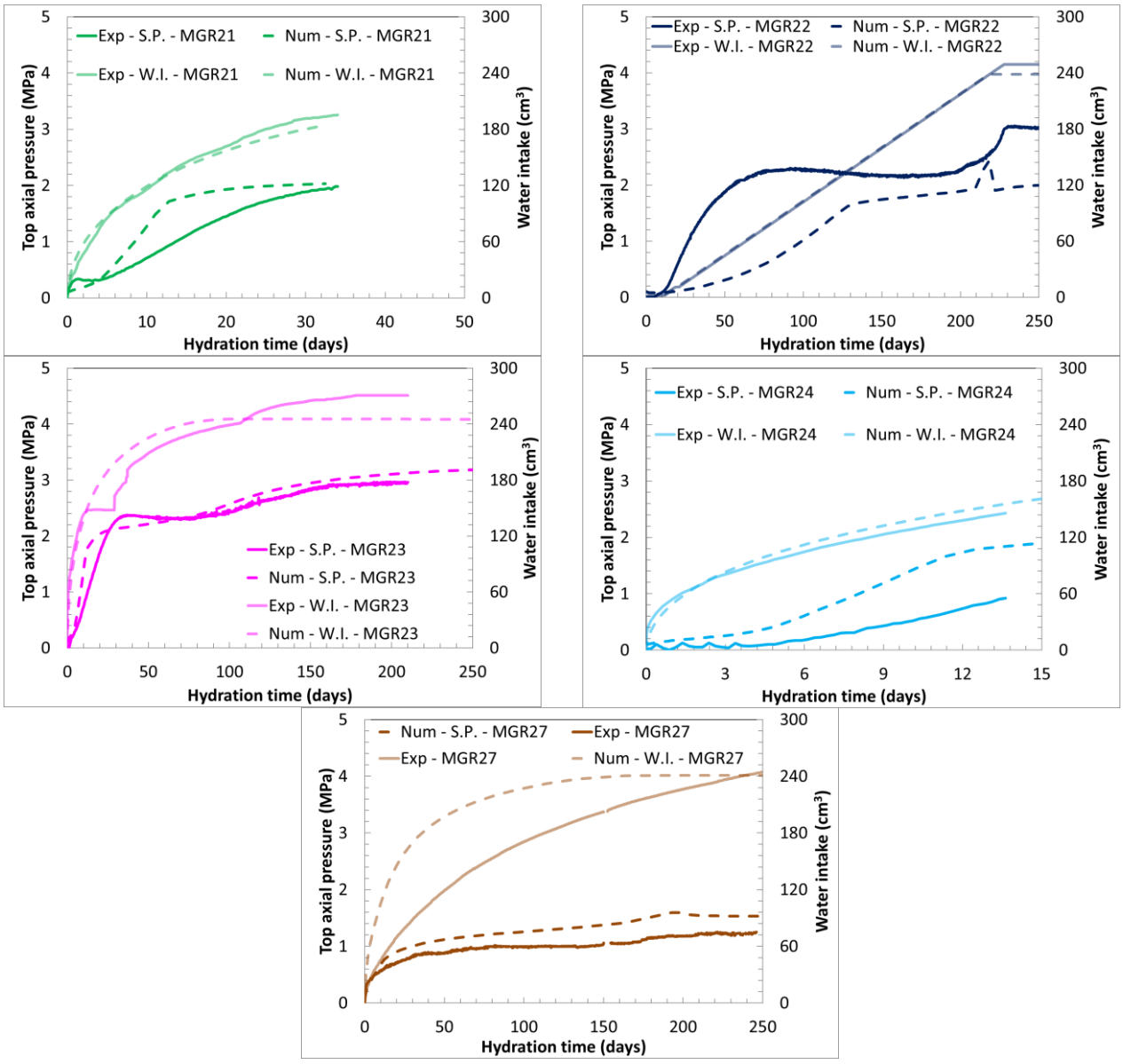

Fig. 6.11: Top swelling pressure in axial direction and water mass injection time evolution for tests MGR21, MGR22, MGR23, MGR24 and MGR27. Comparisons between experimental data and model predictions.

Fig. 6.7 and Fig. 6.9 show the comparison between the numerical and experimental water intake time evolutions of tests MGR23 and MGR27. It is worth to mention that the two experimental tests and the two simulations differ only for the configurations of the two layers, since the hydration boundary conditions and materials initial states are exactly the same. Namely, let us remind that for test MGR23 the pellets layer is placed on the bottom part of the sample in direct contact with the saturating surface, whereas for test MGR27 the bottom layer in direct contact with the water source is composed of the compacted bentonite block material.

In this latter case, the saturation process slows down accordingly to the lower permeability of the bentonite compacted block compared to the one of the pellets mixture layer, related to the much higher dry density and to the intrinsic pores structure nature. Hence, the MGR27 experimental results and numerical simulation show that the water intake process is initially slower than the one experimentally and numerically recorded for test MGR23. Successively, the injection rates decrease but less than the MGR23 case. With respect to these experimental conditions, it appears that the configuration with the denser material in contact with the water source causes a larger full saturation time, which can be particularly relevant in the case of real scale structure. If, according to the Terzaghi consolidation theory for saturated soil, water intake stabilisation time scale is proportional with the square of the hydration length, in this case, it appears clear that despite the hydration length is the same, the stabilisation times differ. Thus, the material configuration for in-situ structures has to be selected carefully. The water inflow numerical results of test MGR27 do not correspond precisely to the experimental outcomes in terms of value, but those are able to reproduce the above-mentioned circumstances.

Swelling pressure

Swelling pressures are measured axially on the top end of the samples. Top axial swelling pressure experimental results of the first four tests (Fig. 6.12 and Fig. 6.13) show similar pressure evolution with time. The phenomena related to the swelling pressure development upon constant volume hydration distinguished by (Imbert and Villar 2006) for FoCa bentonite granular mixtures and by (Lloret et al. 2003) with respect to compacted Febex bentonite can also be observed during these tests consisting in the combination of the two separated assemblies. Specifically, an initial quick swelling pressure increase characterises the four tests, with an evident delay in time with respect to test MGR22. Indeed, these first pressure peaks are reached after 80 days for test MGR22 and after 30 days for test MGR23.

The second phase, which consists in an intermediate phase of a small pressure decrease, is observed only in tests MGR22 and MGR23 because tests MGR21 and MGR24 are stopped far earlier. For test MGR22 this intermediate phase lasts until day 200th, whereas for test MGR23 this stage stops when the 70th day elapses.

The last phenomenon, occurring for high level of saturation (S_r>95%), includes a new increase of the swelling pressure. The experimental top final axial swelling pressure values range between 0.92 MPa and 3 MPa, depending on the hydration strategy for intermediates states of average saturation degrees (Fig. 6.14).

On the other hand, for test MGR27, the recorded behaviour appears quite different. The first pressure increase reaches a lower pressure value equal to 1 MPa and it is not followed by the above-mentioned pressure decrease. The recorded top axial swelling pressure is almost constant, very slowly increasing until the 200th day of the test time. It finally presents an almost imperceptible last increase of swelling pressure (much later with respect to MGR23) and a pressure stabilisation at 1.5 MPa (half of the final values of MGR22 and 23).

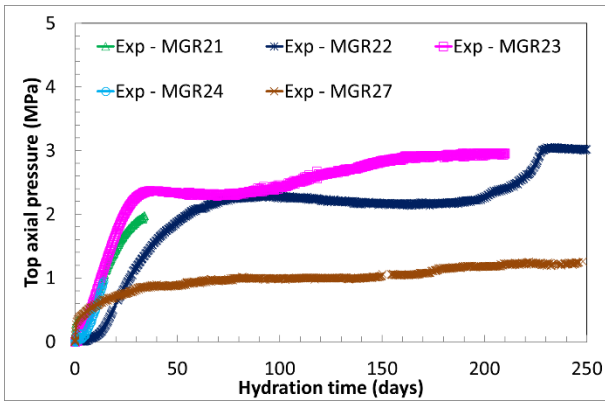

Fig. 6.12: Swelling pressure in axial direction time evolution for tests MGR21, MGR22, MGR23 and MGR24. Comparisons between experimental data.

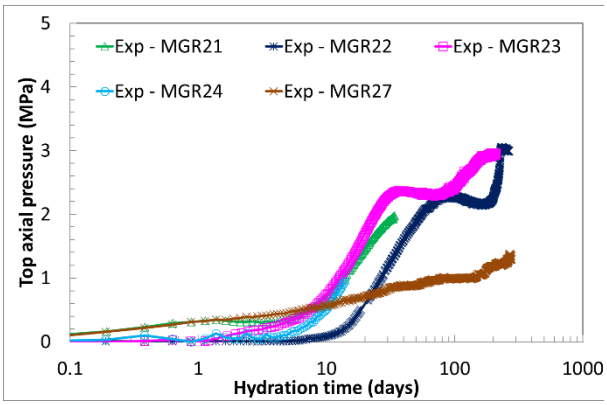

Fig. 6.13: Swelling pressure in axial direction time evolution for tests MGR21, MGR22, MGR23 and MGR24. Comparisons between experimental data (log scale).

Further information is provided by the analysis of the top axial swelling pressure development with respect to the average saturation degree (Fig. 6.14).

The average saturation degree is computed via the water intake time evolution records considering a constant water density equal to ρ_w=1Mg/m^3. This representation allows avoiding the use of the semi-logarithmic scale during the comparison of different tests durations.

Firstly, it is possible to notice that the top axial swelling pressure development is strongly affected by the water supply strategy. Tests MGR21, MGR23 and MGR24 present significant top axial swelling pressure development only for average saturation degrees higher than S_r=60%. On the other hand, test MGR22 shows top axial swelling pressure increase simultaneously to the average saturation degree increase. Test MGR27 presents a behaviour which is in between the one presented by test MGR22 and the one given by tests MGR21, 23 and 24. The top axial swelling pressure increases with saturation with a higher rate with respect to tests MGR21, 23 and 24, but lower with respect to test MGR22. The top axial swelling pressure increases up to 1 MPa for an average saturation level of S_r=60%. Then it remains almost constant until S_r=80% and it increases again until 1.5 MPa when full saturation occurs. Concerning test MGR23, a swelling pressure increase is observed at constant average saturation level equal to S_r=70%. This pressure increase takes place between the 10th and the 28th days of the experimental test time, when 150 cm^3 of water have been injected, concurrently with water inflow plateau recorded in Fig. 6.9 and Fig. 6.10.

Since tests MGR21 and MGR24 are stopped at earlier hydration phases, let us focus on the comparison between tests MGR22, MGR23 and MGR27. The top axial swelling pressure peak approximately equal to 2.3 MPa for MGR22 and MGR23, which delimitates the elastic domain in the framework of elasto-plasticity (Lloret et al. 2003), is observed for average saturation degrees S_r=56% for test MGR22 and S_r=76% for test MGR23. Those average saturation degrees correspond to water intake quantities respectively equal to ~80 g and ~150g (Fig. 6.7, Fig. 6.8 and Fig. 6.12). The boundary of the elastic domain is very difficult to determine for test MGR27, but a change of slope is observed after 1 MPa of top axial swelling pressure.

For test MGR22, top axial swelling pressure slightly decreases between average saturation Sr=50% and Sr=90%, then it increases again up to full saturation. A similar phenomenon is observed for test MGR23 for average saturation between approximately Sr=70% and Sr=90%. Test MGR27 does not show any axial swelling pressure decrease but an almost constant value between Sr=70% and Sr=90%, as observed for test MGR23. When high level of saturation is reached, the experimental top axial swelling pressure presents a last increase.

It is immediate to see that the pressure development kinetics of test MGR22 is very different to the other tests, due to the fact that the water supply is very low and controlled. Axial pressure started to develop slightly later than in the other tests (after 10 days), and when the degree of saturation was much lower than in the other tests (37%).

Moreover, the odd final shape of the curves for test MGR22 is explained by the fact that when full saturation is reached, the water injection equipment is not able to keep a constant low injection flow into a saturated sample without increasing the injection pressure, which inadvertently starts to increase (Fig. 6.12).

Also test MGR27 presents a very distinct behaviour with respect to tests MGR21, 23 and 24, despite the same hydration boundary conditions. Top axial pressure develops slightly before and when the degree of saturation is lower than in the other tests (30%). This is related to the fact that the block denser bentonite part, main responsible for the swelling pressure development, is immediately reached by the saturation front. Thus the pressure development process speeds up with respect to the average saturation degree.

Especially with respect to this, it is important to mention that during test MGR21, 23 and 24, the overall water inflow is firstly injected in the pellets layers, hence, it causes the modification of the pores-structure and the following permeability decrease. Consequentially, the swelling pressure development is delayed with respect to the case in which it occurs in the compacted block part directly.

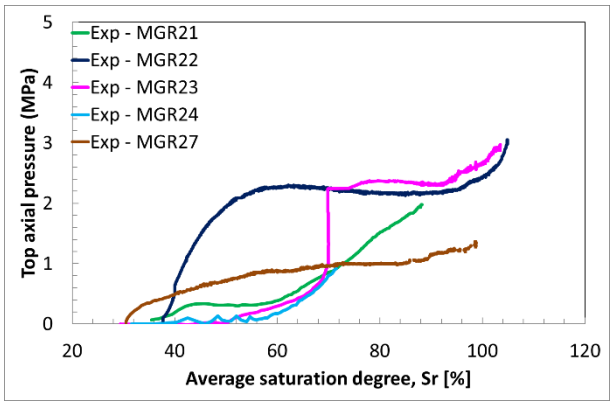

Fig. 6.14: Swelling pressure in axial direction as average saturation degree of the sample function for tests MGR21, MGR22, MGR23 and MGR24. Experimental data.

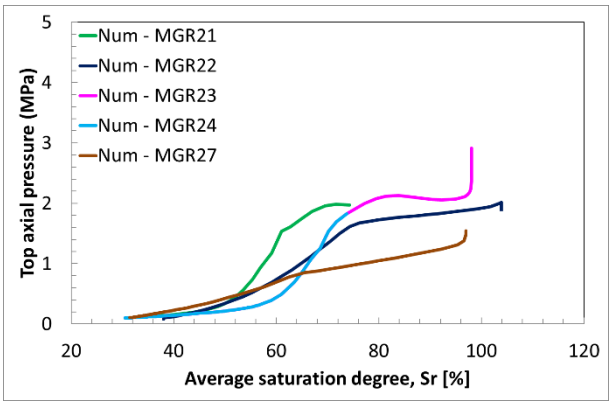

Fig. 6.15: Swelling pressure in axial direction as average saturation degree of the sample function for tests MGR21, MGR22, MGR23, MGR24 and MGR27. Numerical simulation.

Fig. 6.12 and Fig. 6.16 show the time evolution through of the swelling pressure measured in the axial direction on the top of the samples. The numerical results are compared to the experimental ones. Experimental measurements record only the axial swelling pressure on the top of the sample, but for sake of completeness numerical results with respect to axial swelling pressure on the bottom of the samples and radial swelling pressure at two different positions are presented. The trend of the transient phase is well reproduced as well as the stabilization time. The top axial swelling pressure of the numerical simulations for tests MGR21, 23, 24 and 27 compare impressively fine the experimental results, since the very beginning of hydration until the final stabilised value. The agreement between the experimental and numerical top axial swelling pressure measurements for test MGR22 is less precise at the initial hydration phase. The experimental pressure development appears faster than the numerical one.

Table 6.7: Final axial swelling pressure values. Comparisons between experimental data and model predictions for tests MGR21, MGR22 MGR23, MGR24 and MGR27.

Test Reference	Final Top Axial Swelling Pressure [MPa]	
	Experimental	Numerical
MGR21	1.95	1.97
MGR22	3.00	2.17
MGR23	2.92	3.10
MGR24	0.92	1.82
MGR27	1.23	1.53

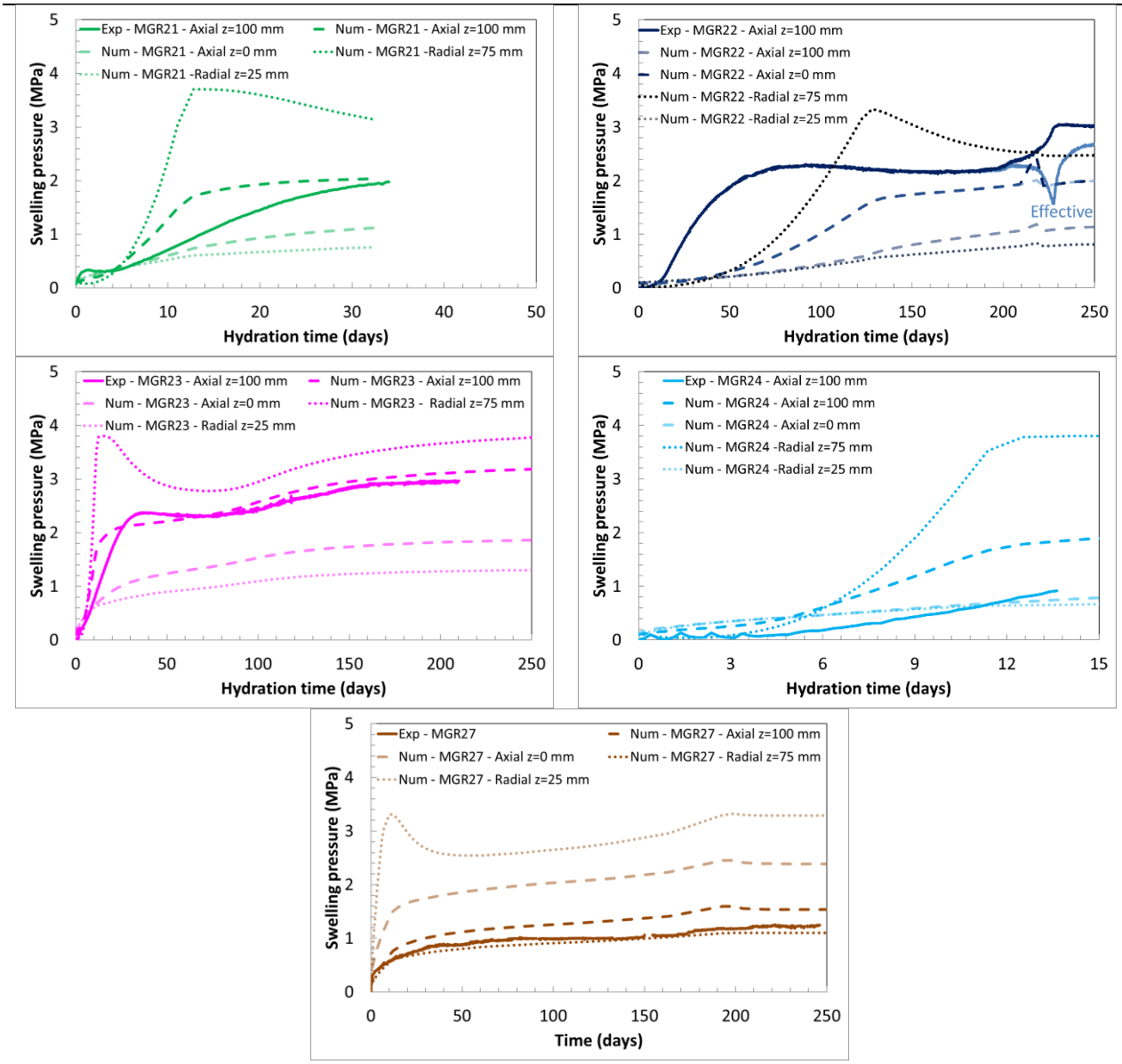

Fig. 6.16: Total swelling pressure evolution for tests MGR21, MGR22, MGR23, MGR24 and MGR27. Comparison between experimental results on the top axial measurement of the sample and numerical simulations at the axial top and bottom face of the sample and radial at the cell wall at z=25 mm and z=75 mm from the wetting surface.

It is essential to mention that the axial total stress is not considered uniform on each sample due to the friction development with the cell wall and it explains such a big discrepancy between the final top axial swelling pressure values of tests MGR22 and MGR23 with test MGR27, considering the same average dry density of the samples. The effect of friction on swelling pressure measurements was already met by a number of authors ((Molinero et al. 2018), (Talandier 2018), (Baryla et al. 2018)). Nevertheless, it has never been precisely determined and very few information are available. Thus, a numerical analysis helps to provide complementary information with respect to the much more variable and difficult to control experimental tests.

The numerical top axial and bottom swelling pressures of all the tests reasonably differ due to the friction phenomena modelled at the contact with the cell wall (Fig. 6.16). Friction develops since the very beginning of the hydration phase. The difference between the top and bottom pressure measurements increases up to a maximum value of approximately ~1 MPa, consistently with the radial pressure distribution (Fig. 6.17) and selected friction coefficient (μ=0.125). Successively it remains constant when the failure criterion is met (Eq. 6.1). At this moment, the resistance to the sliding exerted on the cell wall cannot increase any further. Thus, the axial pressure disparity remains constant for all the tests and the sliding of the material sample with respect to the cell wall occurs.

The axial and radial numerical swelling pressure measurements in the block layers do not differ significantly for the five cases, as well as the ones in the pellets layers. Namely, it can be observed that the axial swelling pressure measured in the block layers is typically much higher with respect to the one of the pellets material. The comparison between the experimental top axial swelling pressure measurement of test MGR23 and the numerical bottom one of test MGR27 appears of particular interest. The two values do not differ sensitively as well as the comparison between the experimental top axial swelling pressure measurement of test MGR27 and the numerical bottom one of test MGR23 shows. This observation helps to conclude that the friction clearly affects the experimental measurements, which have to be treated with full knowledge of the above mentioned circumstances.

For greater completeness, the numerical effective radial swelling pressure profiles for several average saturation degrees are given in (Fig. 6.17). The numerical radial swelling pressure becomes immediately larger in the block layers upon saturation with respect to the pellets ones, reaching a maximum quasi-uniform value equal to ~4 MPa instead of the value equal to 1 MPa of the pellets layers. This observation is confirmed in all the tests, thus, it can be concluded that the major sliding resistance is basically exerted by the block layer.

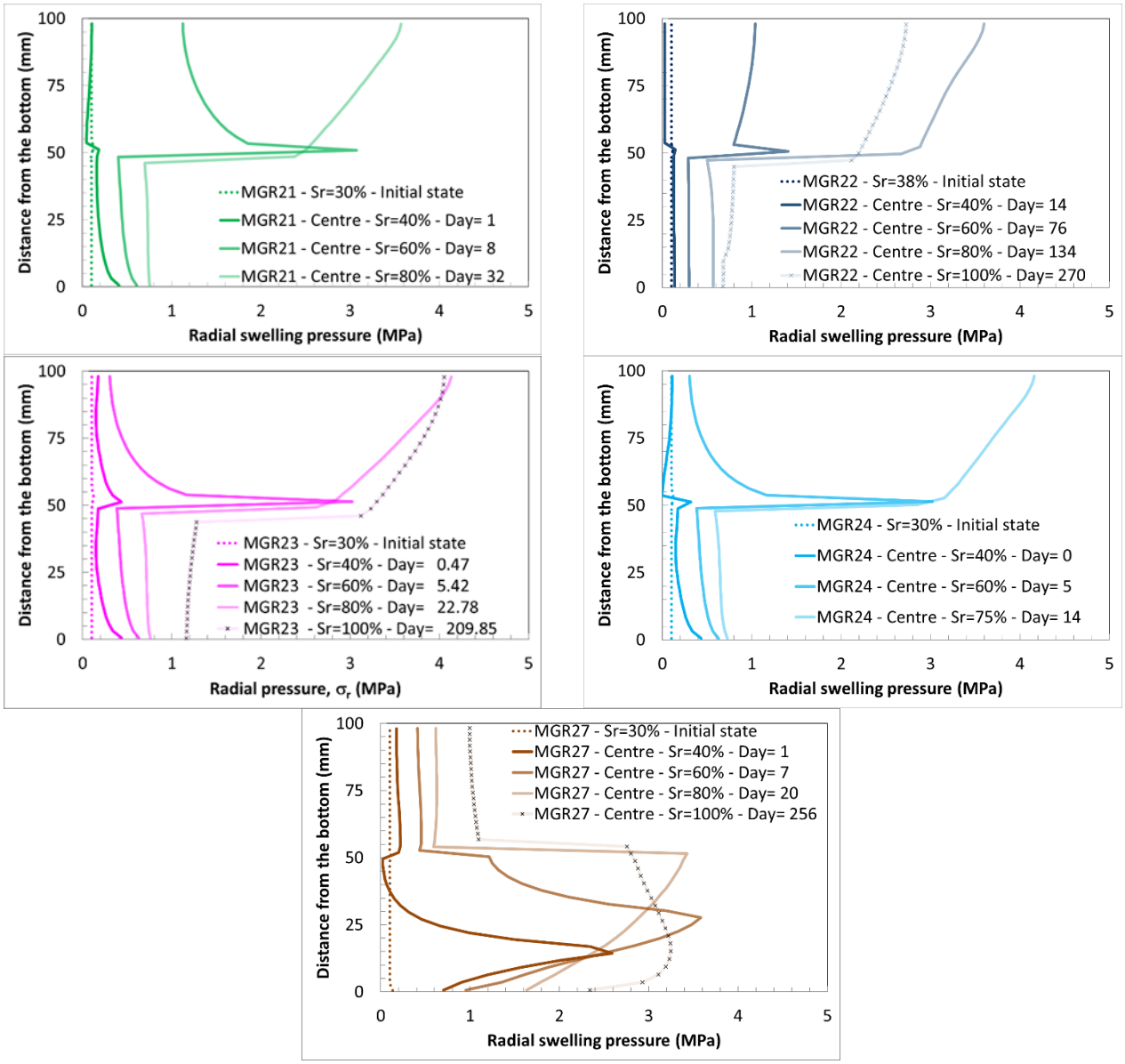

Fig. 6.17: Radial swelling pressure profiles for tests MGR21, MGR22, MGR23, MGR24 and MGR27. Comparison between numerical simulations. Time steps are selected considering the initial conditions, the 40%, 60%, 80% and the final value of each test with respect to the average saturation degree.

Suction and saturation degree

Fig. 6.18 presents the numerical results in terms of suction and saturation time evolution at z=25 mm and z=75 mm from the wetting surface. As soon as the water injection begins, the suction decreases for all the portions closest to the wetting surface (namely at z=25 mm), but it surprisingly increases for tests MGR21, 22, 23 and 24 at z=75 mm. This yields a respective saturation increase for z=25 mm and decrease for z=75 mm accordingly to the adopted water retention constitutive model. At z=75mm, the suction increase is less than 20 MPa, corresponding to a saturation decrease smaller than 10%, whereas the suction decrease at z=25 mm is much more significant (ranging from 80 MPa of tests MGR21 and 22 to 400 MPa of tests MGR23 and 24) and generates a saturation increase greater than the 40%. Successively, suction decreases and saturation jointly increases at all the height for all the tests until full saturation for tests MGR22, 23 and 27 (tests MGR21 and 24 are stopped far earlier).

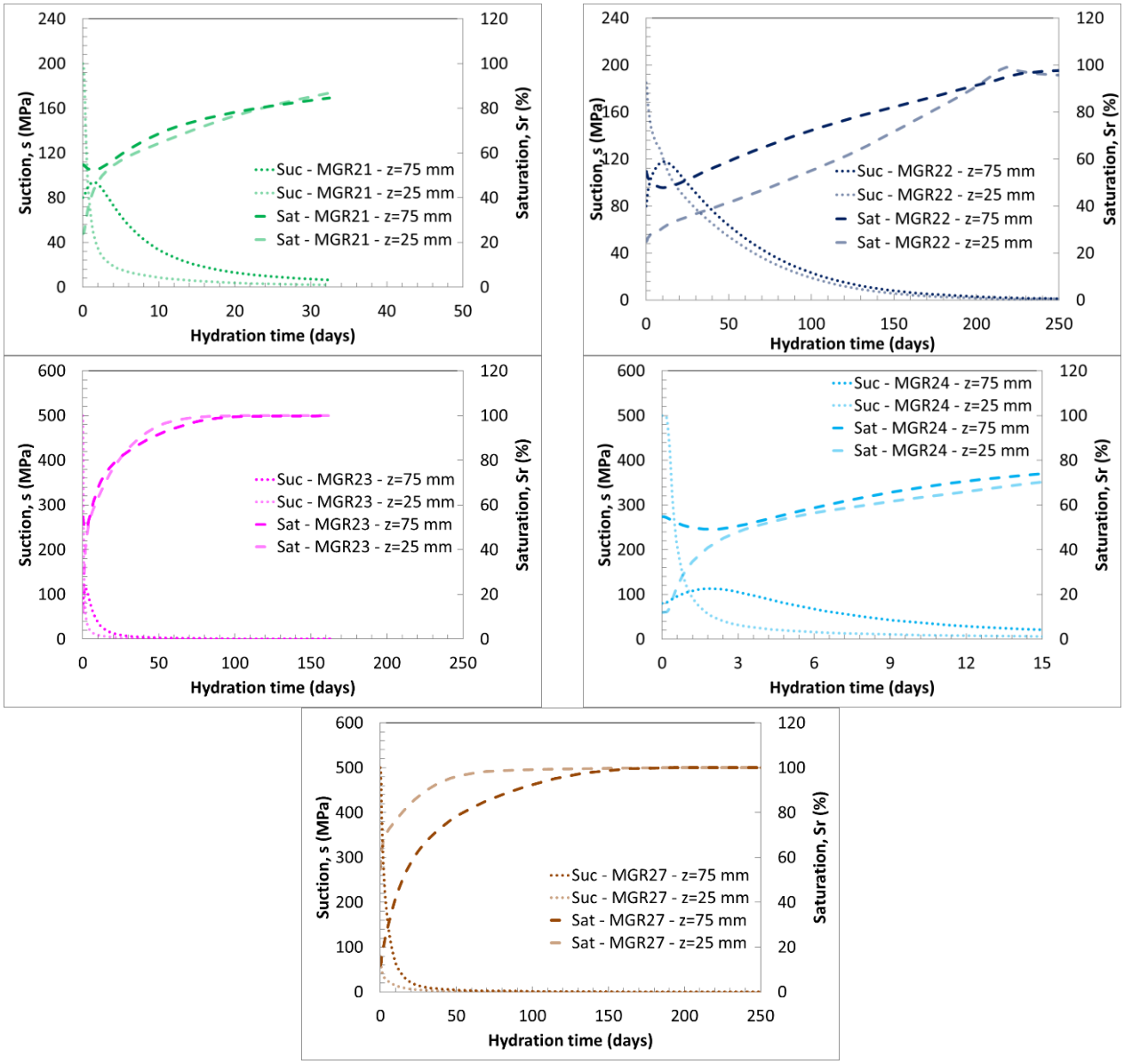

Fig. 6.18: Suction and saturation evolution for tests MGR21, MGR22, MGR23, MGR24 and MGR27. Comparison between numerical simulations at the cell wall at z=25 mm and z=75 mm from the wetting surface.

The above observed initial unexpected suction increase in the compacted block layers is linked to the very low initial saturation degree and very high initial suction level corresponding to the pellets layers. Despite it is well-recognized that the adopted initial suction level for the pellets parts is very high and unlikely (equal to 200 MPa for test MGR21, 180 MPa for test MGR22 and 500 MPa for tests MGR23, 24 and 27). But, in order to obtain realistic water intake volumes comparable to experimental outcomes, it was decided to take them in consideration. Nevertheless, assumed the strongly coupled hydro-mechanical interactions of the selected numerical constitutive models, a number of further simulations were performed in order to assess the influence of the initial suction level of the pellets layers. In the following, three simulations are performed modifying only the initial suction level of the pellets layer from 500 MPa to 200 and 100 MPa. Those resulted in negligible variations of final swelling pressure values and important final injected water quantity discrepancies (Fig. 6.19). With respect to post-mortem analysis, the initial numerical pellets layer suction consistently affects the initial water content and the final one, which becomes closer to the experimental results. No remarkable difference can be observed in the final dry density distribution profiles for different initial pellet suction (Fig. 6.20).

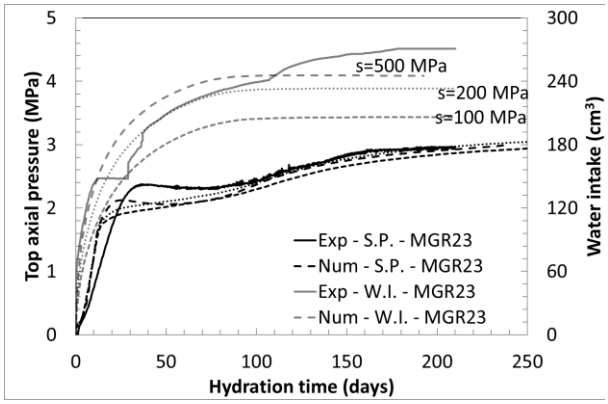

Fig. 6.19: Top swelling pressure in axial direction and water mass injection time evolution for test MGR23. Comparisons between experimental data and model predictions with different initial suction level in the pellets layer equal to 500, 200 and 100 MPa at the final state.

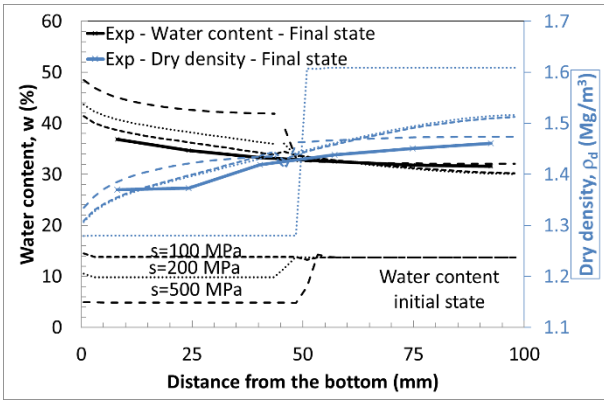

Fig. 6.20: Water content and dry density profiles for test MGR23. Comparison between experimental data and numerical simulations with different initial suction level in the pellets layer equal to 500, 200 and 100 MPa at the final state.

However, Fig. 6.21 and Fig. 6.22 show the numerical suction and saturation profiles for several average saturation degrees of all the analysed tests. It is evident that with respect to the pellets layers in tests MGR21, 22, 23 and 24, water is provided not only from the wetting face but also to the upper compacted block layer at the beginning. Successively, as the hydration process continues, suction decrease yielding saturation increase is distributed all over the height of the samples.

The ways in which suction and saturation evolve during water hydration seem depending on the hydration boundary conditions. Namely, if on one side a clear saturation gradient can be observed in the pellets part for the constant water pressure hydration conditions of tests MGR21, 23 and 24, test MGR22 is characterised by uniform saturation distributions in the pellets portion for all the average saturation degrees. For test MGR27, the block portion in direct contact with the upper pellet layer also undergoes desaturation in the very first hydration phases. Moreover, the saturation distribution of the compacted block layers evolves similarly and uniformly for test MGR21, 22, 23 and 24, in which water is injected in the pellets materials, while an evident saturation gradient develops upon hydration for test MGR27. This latter case differs also for the fact that the pellets saturation distribution firstly evolves showing a certain saturation gradient (as in tests MGR21, 23 and 24) and finally uniformly and similarly to the one on test MGR22, in the latest hydration phases. This is related to the very low compacted block permeability, which provides lower water quantities at the end.

Fig. 6.22 shows the comparisons between the experimental and numerical results in terms of saturation after dismantling. Test MGR21, stopped after 34 days after the beginning of hydration, presents a saturation gradient ranging between S_r=100% for the pellets material in direct contact with the hydration surface and Sr=60% for the uppermost height of the sample in the block layer. On the other hand, the numerical results for this test show the same saturation gradient in the pellets layers, but uniform saturation in the compacted block material. A similar trend is given in test MGR24. Indeed, it is possible to observe an evident saturation gradient in the pellets part between S_r=100% and S_r=60% at the 14th day after the beginning of hydration, and uniform saturation (S_r~60%) in the block part, similar for the experimental and numerical results but with 20% of difference (S_r~75% in the numerical simulation).

As the comparison in Fig. 6.11 shows, the global water volume injected in the samples for a given time is the same in terms of experimental and numerical results. Accordingly, the global saturation degree of the samples is also corresponding. Moreover, this value does not change abruptly during its evolution, which is quite monotonic.

Finally, the numerical results for tests MGR22, 23 and 24 show the complete saturation of the sample (with exception for test MGR22, in which due to the imposed boundary conditions, the pellets layer is not fully saturated). However, small differences with respect to experimental results are observed. Those differences may also be related to unavoidable desaturation post-dismantling.

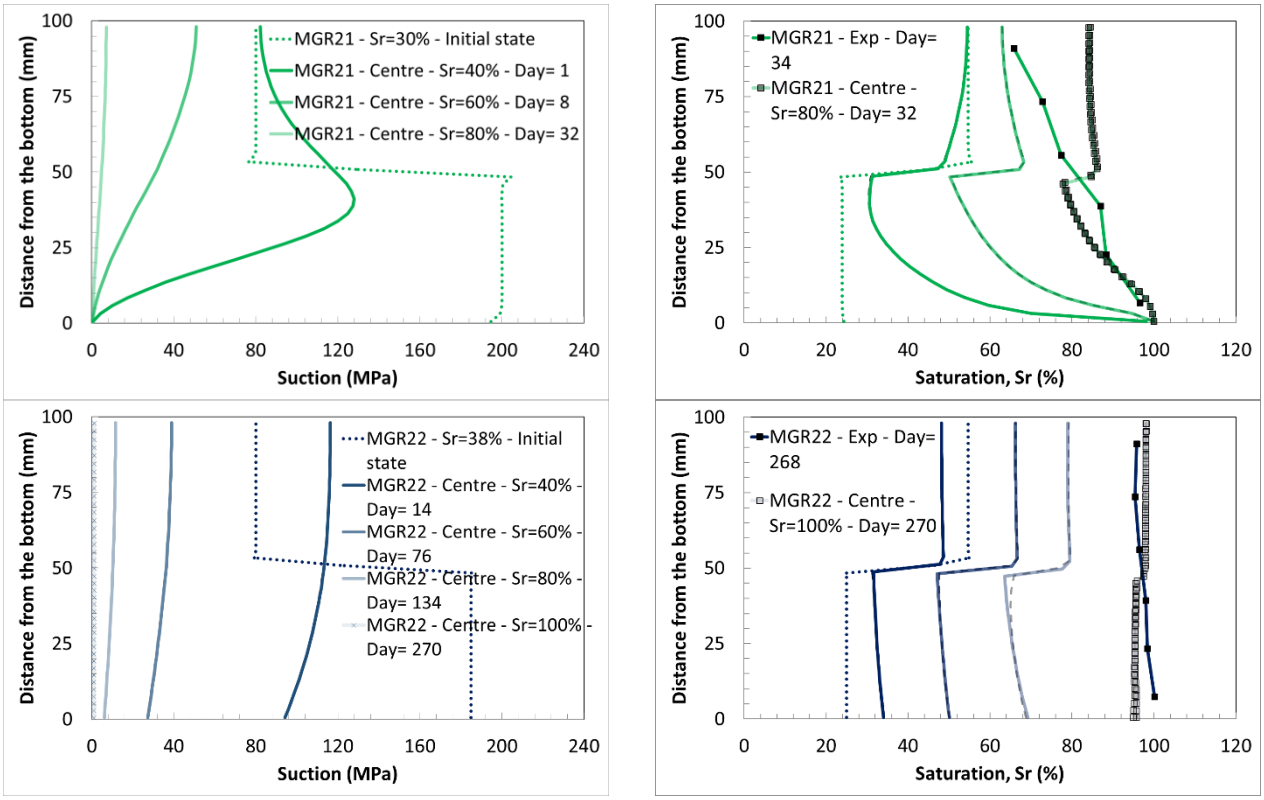

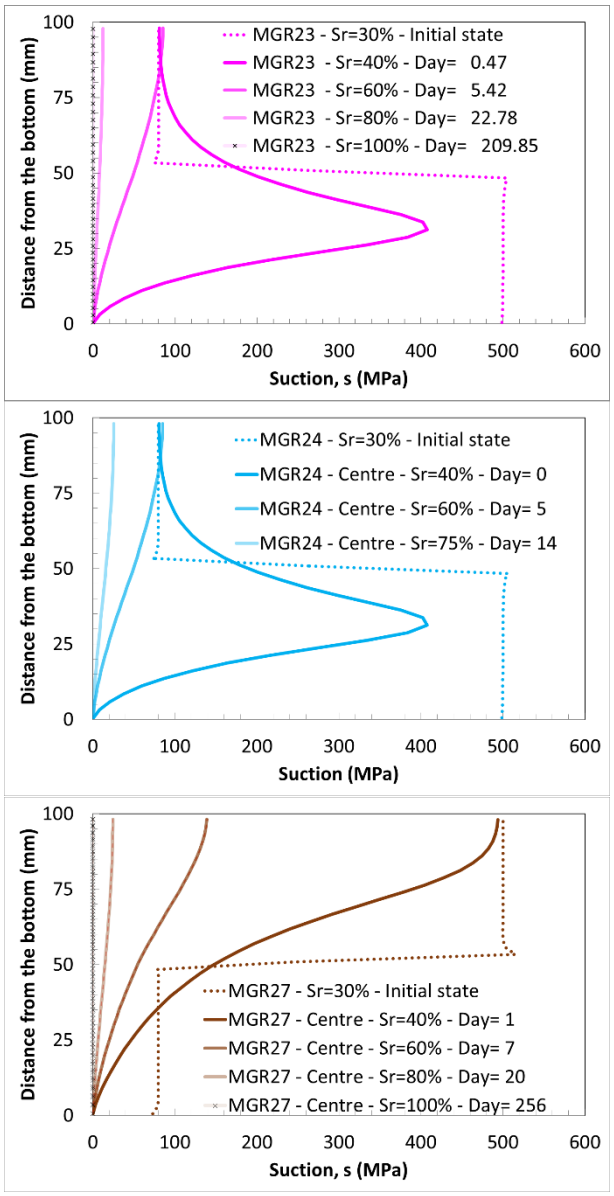

Fig. 6.21: Suction profiles for tests MGR21, MGR22, MGR23, MGR24 and MGR27. Comparison between numerical simulations. Time steps are selected considering the initial conditions, the 40%, 60%, 80% and the final value of each test with respect to the average saturation degree.

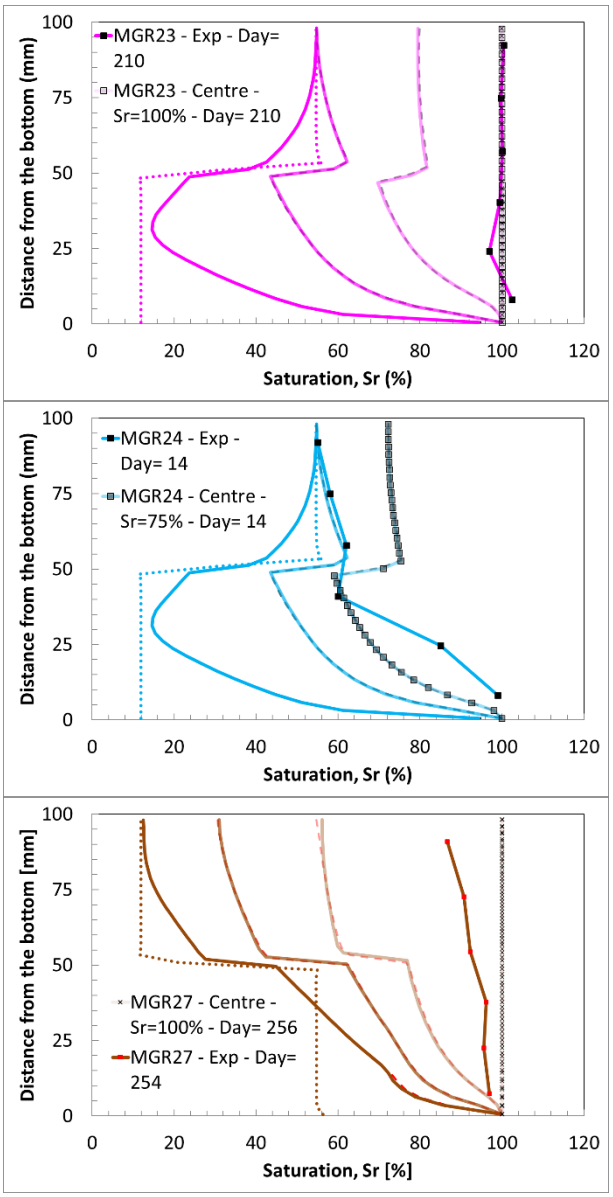

Fig. 6.22: Saturation profiles for tests MGR21, MGR22, MGR23, MGR24 and MGR27. Comparison between experimental data and numerical simulations at the final state. Time steps are selected considering the initial conditions, the 40%, 60%, 80% and the final value of each test with respect to the average saturation degree.

Permeability evolution

The link between the bentonite dry density, multi-pores structures distributions and their evolution upon hydration has been observed and studied by a number of authors ((Cui 2017), (Romero 2013), (Villar 2000b)). The adopted water transfer constitutive model allows tackling such a feature as presented in Fig. 6.23 and Fig. 6.24. The numerical permeability and the macro and total void ratios profiles for several average saturation degrees are shown indeed for all the five analysed tests.

The distinction between the compacted bentonite layer (ρ_d=1.60 Mg/m^3), presenting an initial permeability equal to K_w=3.20×10^{-20} m^2, and the pellet one (ρ_d=1.30 Mg/m^3), with permeability between K_w=7.5×10^{-20} m^2 (for tests MGR21 and 22) and K_w=8.6×10^{-20} m^2 (for tests MGR23, 24 and 27), is evident. Among other factors, the initial permeability also depends on the initial water content, which affects the initial macro-void ratio accordingly to the selected micro-void ratio law evolution (Eq. 2.11).

A general permeability decrease is observed for all the tests in all the material layers. This permeability decrease is mostly related to the reduction of macro-structures volume upon hydration.

More detailed observations allow distinguishing a number of phenomena occurring during the hydration of these multi-structural assemblies.

Tests MGR21, 23 and 24 show similar properties. As water is injected from the bottom face at constant water pressure, a permeability gradient establishes in the pellets layers. Even though, the material closest to the wetting face undergoes volume increase, the invasion of macro-porosity upon micro-porosity is dominant. As the saturation proceeds, the upper compacted bentonite block swells causing the compaction of the pellets layer and the following total and macro void ratios decrease. Also the permeability of the compacted block layer does not increase as the macro void ratio does, despite the material general volume increase. The compacted block swelling causes a lower permeability reduction in this layer with respect to the one observed in the pellets one because the micro-structure development process is less dominating. Hence, the final permeability of tests MGR23 for a full-saturated state appears constant all over the sample with a value equal to $K_w=3\times10^{-20}$ m^2 in both layers.

The permeability evolution through the sample for test MGR22 looks different from the ones observed during tests MGR21, 23 and 24. This test differs for the water supply boundary conditions, which consist of imposed water volume injection equal to 0.05 g/h. As observed for the saturation profiles evolution (Fig. 6.22), the permeability decrease is uniform.

With respect to test MGR27, it can be seen that as soon as water is injected in the compacted bentonite block swells causing a small permeability increase for the material portions in direct contact with the wetting surface. Successively, also in this case, despite the volume increase, the compacted block macro void ratio remains almost constant resulting in a small permeability decrease. In the pellets layer, the compaction due to the block swelling has caused a total void ratio uniform reduction, which, together with the micro-porosity expansion, is translated in strong permeability decrease. Also in this case, the total and macro void ratio evolutions do not present any gradient as observed for test MGR22.

The numerical model shows that for the final saturated states, all the different water supply boundary conditions and different layers configurations converge forward a unique almost-uniform permeability distribution, which depends only on the final dry density distribution.

With respect to frictional phenomena, it can be said that the influence on macro-void ratio and consequentially on permeability is less strong with respect to the one exerted on the total void ratio or swelling pressure development, but still present.

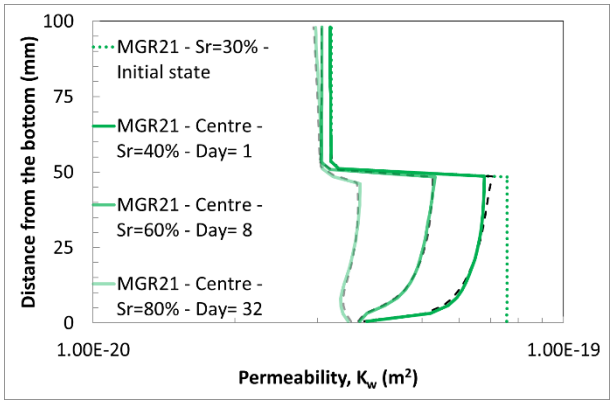

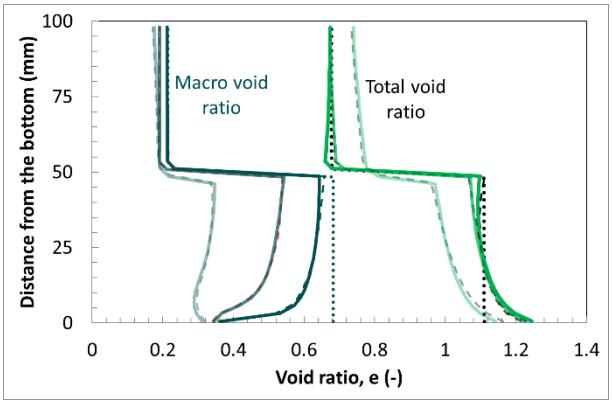

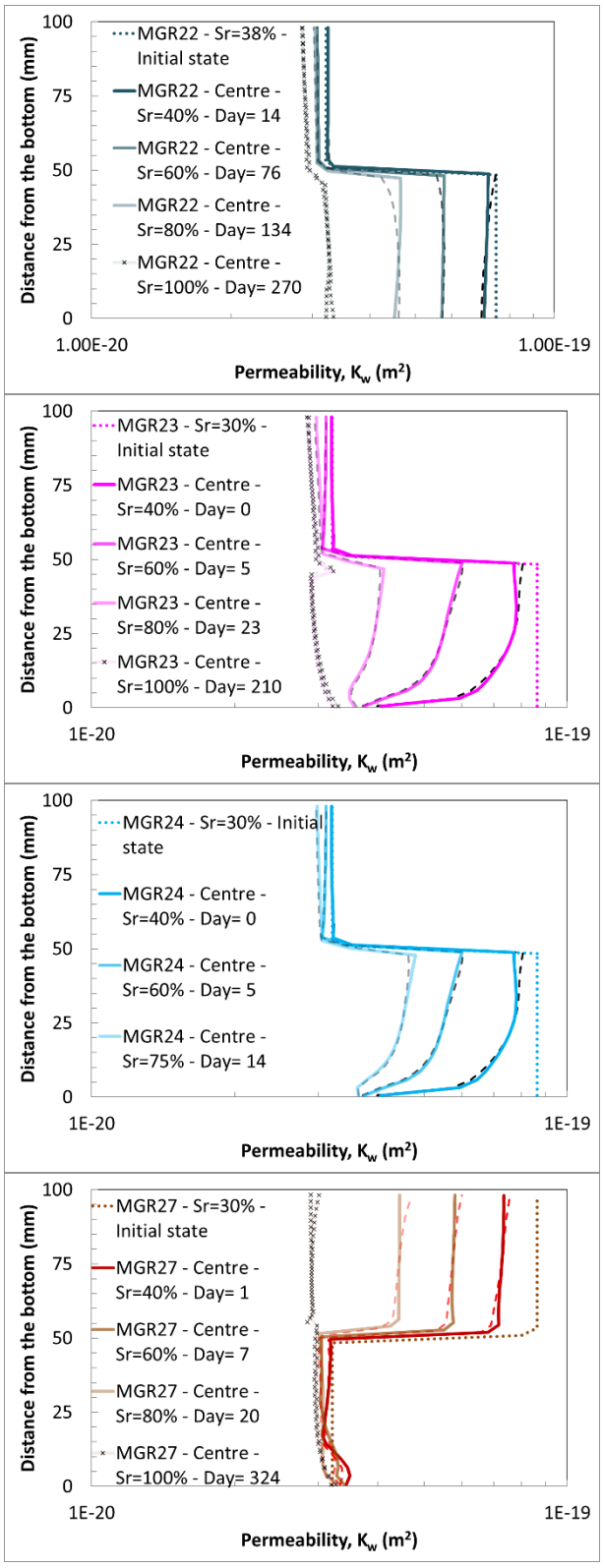

Fig. 6.23: Permeability profiles for tests MGR21, MGR22 MGR23, MGR24 and MGR27. Comparison between numerical simulations. Time steps are selected considering the initial conditions, the 40%, 60%, 80% and the final value of each test with respect to the average saturation degree.

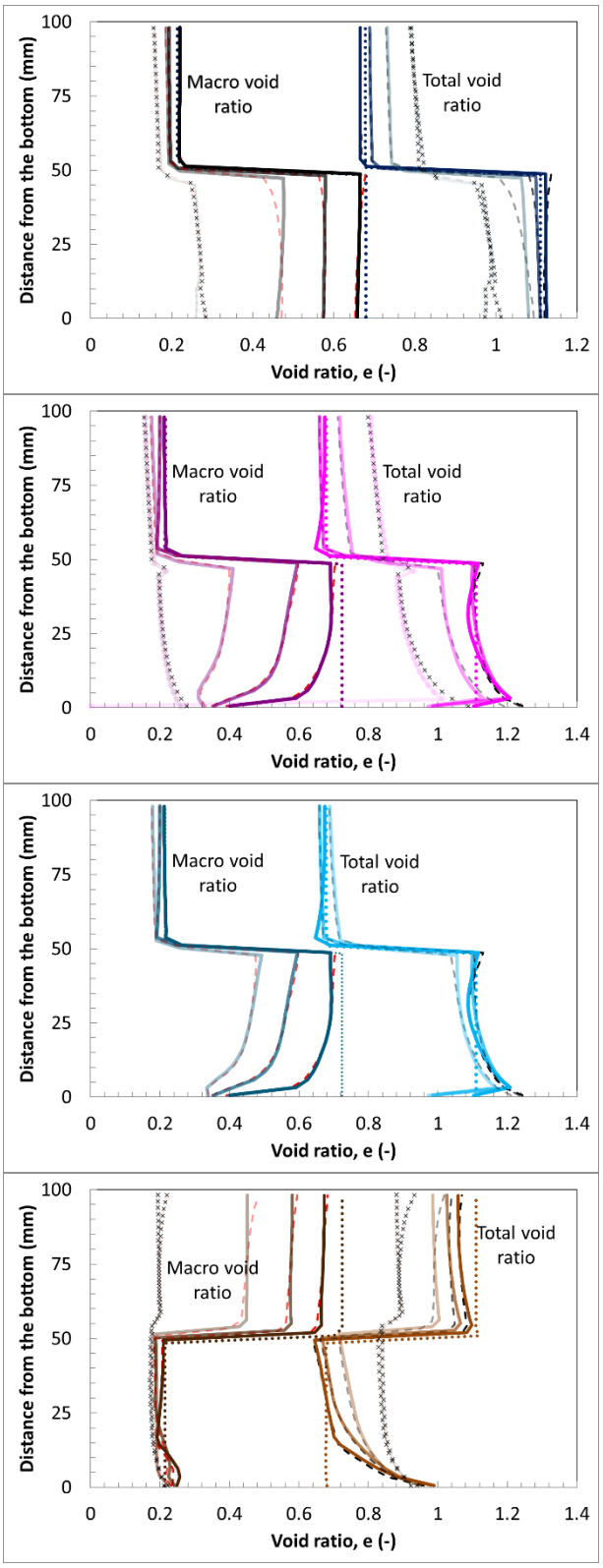

Fig. 6.24: Total and macro void ratios profiles for tests MGR21, MGR22 MGR23, MGR24 and MGR27. Comparison between experimental data and numerical simulations at the final state. Time steps are selected considering the initial conditions, the 40%, 60%, 80% and the final value of each test with respect to the average saturation degree.

Dry density and water content

Dry density and water content at different locations from the hydration surface were determined thanks to post-mortem analyses by cutting the overall assemblies in subsamples. Initial and final experimental dry density and water content values are indicated in Fig. 6.25 and Fig. 6.26.

The experimental tests MGR21, 23 and 24 present on the bottom part the loose pellets layer in contact with the wetting surface and the compacted block material in the top part. The hydration boundary conditions are the same for all the tests and consist of constant water pressure saturation procedure. Thus, it is possible to recreate the dry density and water content evolutions upon hydration.

This is possible due to the fact that those experimental tests present similar initial physical states and are stopped at different average saturations levels. Let us focus on the analysis of the dry density distribution of test MGR24. This test is stopped 14 days after the beginning of hydration at an experimental average saturation level of S_r=72%. The material pellets portion closest to the wetting surface experiences volume increase starting from an initial dry density equal to ρ_d=1.30 Mg/m^3 up to ρ_d=1.20 Mg/m^3, whereas the upper pellet material is subjected to compaction exerted by this pellet swelling and the one of the upper compacted block. Thus starting from ρ_d=1.30 Mg/m^3, it reaches ρ_d=1.35 Mg/m^3. The upper compacted block shows very low volume increase with a minimum dry density value equal to ρ_d=1.55 Mg/m^3 close to the pellets layer. It is suspected that this very low and almost uniform volume increase is not due to the saturation process but to post-dismantling swelling, given the high level of confinement of the block.

Test MGR21 is stopped and dismantled at the 34th day after the beginning of the hydration with an experimental average saturation degree equal to S_r=88%. In the bottom pellet layer a larger dry density gradient is observed. The material portion in direct contact with the wetting face did not increase any further its volume keeping the dry density value corresponding to ρ_d=1.20 Mg/m^3 (as in test MGR24). On the other hand, the compaction of the upper pellet layer part is more evident with respect to test MGR24. This material experiences a volume decrease up to a dry density value equal to ρ_d=1.40 Mg/m^3, mostly linked to the swelling of the top block layer. The compacted Febex bentonite at this stage shows a clear volume increase with dry density ranging from ρ_d=1.40 Mg/m^3 (in the upper and bottom layer borders) to ρ_d=1.50 Mg/m^3, in the central part.

Post-mortem analyses of test MGR23 represents the final state of the hydration process corresponding to the full saturation of the sample. The pellet layer reveals a general volume reduction with dry density spanning between ρ_d=1.38 Mg/m^3 in the lowest part and ρ_d=1.42 Mg/m^3 at the boundary with the top block layer. Accordingly, the upper compacted block part indicates a general and uniform volume increase corresponding to a final dry density equal to ρ_d=1.45 Mg/m^3.

Also the final dry density distribution of test MGR22 corresponding to full-saturated state shows a quite uniform dry density through the pellets layer close to ρ_d=1.40 Mg/m^3 and ρ_d=1.43 Mg/m^3 in the compacted block. Despite the different water hydration boundary conditions consisting in imposed water flow, the final dry density distribution is similar to the one of the strategy accounting a constant water pressure as water supply conditions.

Dry density at dismantling of test MGR27 differs noticeably from the other experimental results. The lowest dry density is found on the top and bottom parts of the sample regardless the initial dry density of the corresponding material. The densest part is detected approximately at the central part of the sample. In general, it is noticed also in this case that the bottom compacted block undergoes swelling, whereas the top pellets layer experiences compaction. The most compacted part of the sample corresponds indeed to the pellets portion in direct contact with the compacted block, similarly with the other cases, as well as the most

swollen part of the compacted block, which is the one in direct contact with the hydration front (namely the lower one). In test MGR27, the hydration front derives from the water source, whereas for all the other tests it arrives from the pellets layer.

Water content distributions and evolutions account the same dry density properties as a result of the strongly-coupled hydro-mechanical phenomena taking place during bentonite hydration.

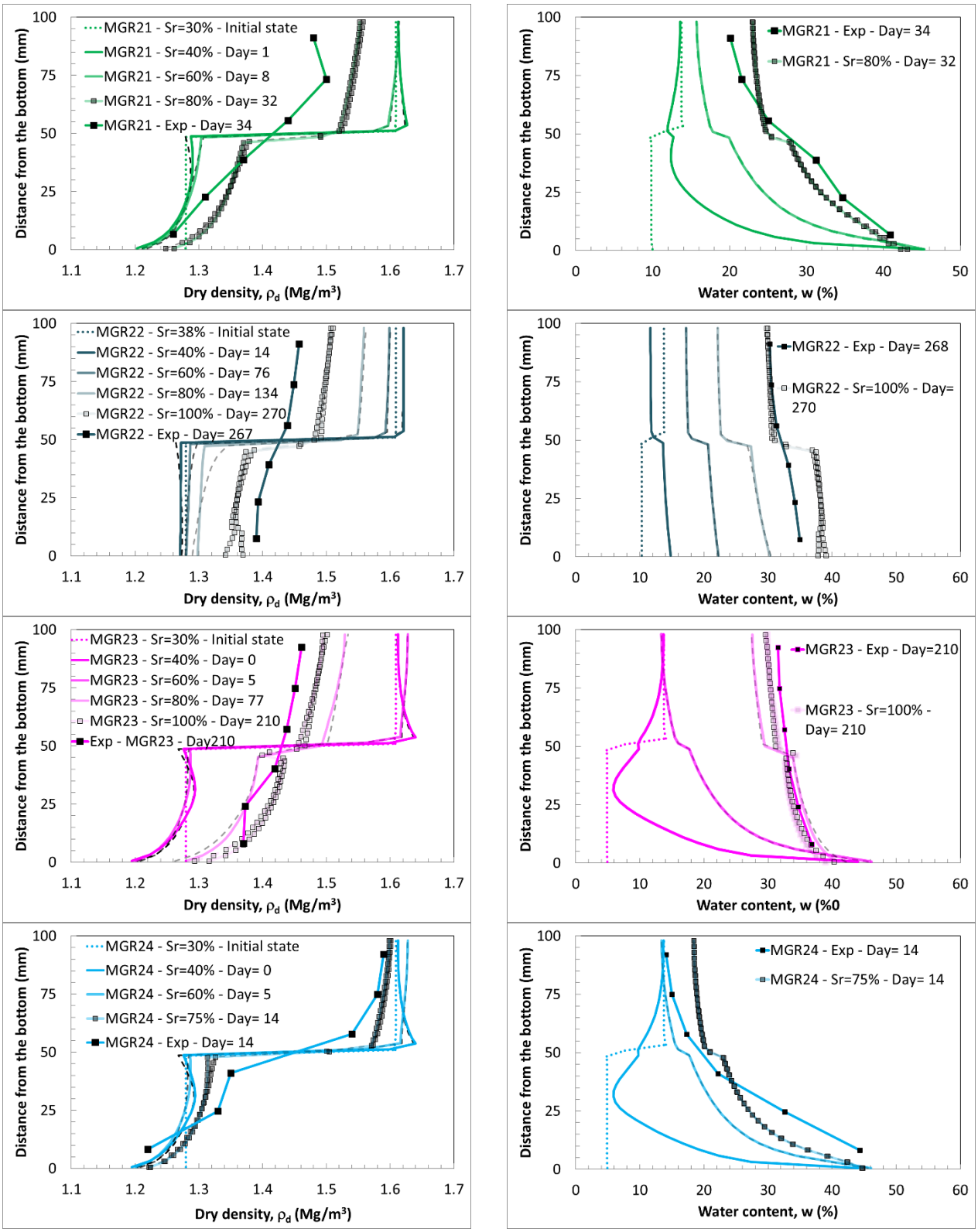

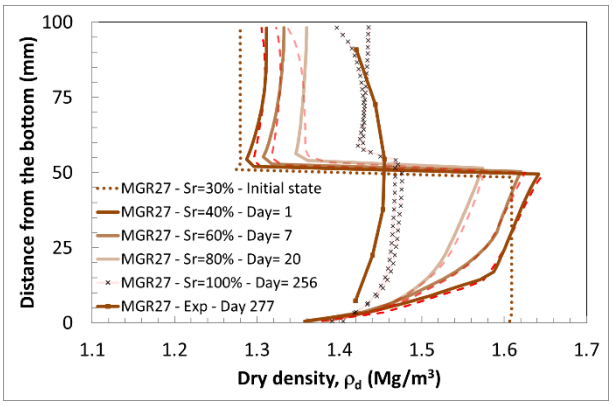

Fig. 6.25: Dry density profiles for tests MGR21, MGR22 MGR23, MGR24 and MGR27. Comparison between experimental data and numerical simulations at the final state. Time steps are selected considering the initial conditions, the 40%, 60%, 80% and the final value of each test with respect to the average saturation degree.

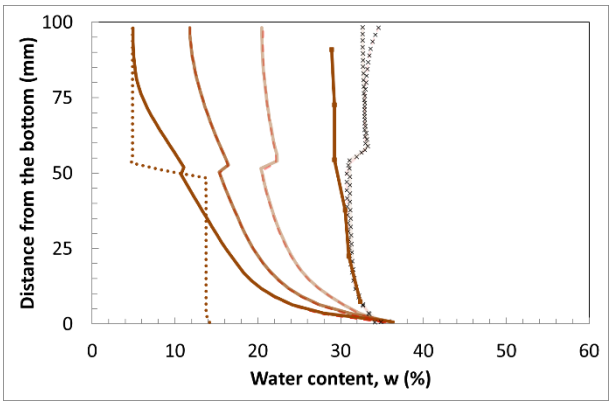

Fig. 6.26: Water content profiles for tests MGR21, MGR22 MGR23, MGR24 and MGR27. Comparison between experimental data and numerical simulations at the final state. Time steps are selected considering the initial conditions, the 40%, 60%, 80% and the final value of each test with respect to the average saturation degree.

Numerical simulations allow the direct observation of the physical state of the material during intermediate saturation levels, which are actually inaccessible for experimental analyses without the complete destruction of the samples. Thus they provide complementary information to the experimental outcomes, which can only produce post-mortem results. Hence numerical results are compared to the experimental ones. Once again it appears reasonable to distinguish the different hydration strategies and layers configurations.

The dry density distribution of those tests corresponding to constant water pressure hydration strategy and lower pellets layer (namely tests MGR21, 23 and 24) as the saturation begins starts to decrease firstly in those material portions located on the bottom part of each layer. More precisely, it can be observed that both in pellets and compacted block layers, the parts which swell the most are the bottom ones. For the pellets, that material is in direct contact with the wetting surface, whereas for the compacted block, that zone is the one immediately hydrated from the pellets material. With respect to the upper pellets layer part, in direct contact with the swelling compacted bentonite block, compaction is observed. The upper part of the compacted block layer is the one that swells the last. As a result, a certain dry density gradient in the hydration direction is established. While the saturation process continues, with the concomitant swelling of the upper block and compaction of the bottom pellets layer, the dry density gradient almost disappears. It is possible to observe that the numerical results compare remarkably well the experimental dry density distributions for all the tests (MGR21, 23 and 24), corresponding to different average saturation degrees.

On the other hand, the numerical results concerning the dry density evolution of test MGR22 show a completely different process with respect to the previous ones. This numerical simulation is characterised by a hydration strategy equal to the experimental one (i.e. imposed low water inflow of 0.05 g/h). The dry density of each layer evolves uniformly in the central part of the sample, whereas the effect of friction with the cell wall is evident and underlines the presence of a certain dry density gradient. Consistently with the other tests, the pellets layer presents a general volume reduction and the compacted block a volume expansion. The numerical and experimental final results show this similar feature, in which the dry density distribution is almost constant both for the pellets and block with a discrepancy related to the final values.

Test MGR27 dry density evolution is characterised by an immediate development of dry density gradient differently from tests MGR21, 22 and 23. The compacted block portion in direct contact with the wetting surface immediately swells. This swelling does not cause the compaction of the top compacted block part but its sliding. Once again, the pellets layer is the most compacted given the lower swelling capacity related to

the lower initial dry density. As the saturation front recedes from the bottom, all the bentonite compacted block experiences a general and quite uniform volume increase. The concomitant volume reduction in the top pellets layer appear uniform in the central part, but with a small dry density layer at the contact with the cell wall due to friction. In great correspondence with experimental results, the numerical final saturated state of test MGR27 presents the lowest dry density in the top and bottom part of the sample, with a general compaction of the central part.

As observed for experimental results, water content distributions and evolutions account the same dry density properties as a result of the strongly-coupled hydro-mechanical phenomena taking place during bentonite hydration.

Moreover, numerical results allow the distinction of additional dry density and water content profiles in the same sample. Specifically, it is possible to highlight the effects of friction phenomena between the material samples and the cell wall in several locations. Even though the effect of friction on dry density and water content is not as noticeable as the one for the swelling pressure numerical measurements, it is still possible to differentiate the dry density profile corresponding to the vertical axis of the sample from the one taken in direct contact with the cell wall. Namely, in the first case, in general, the dry density gradient is not as that visible as the one observed for the borders. On the other hand, water content profiles look less influenced by friction development with respect to dry density states.

Mercury intrusion porosimetry

The experimental campaign included Mercury Intrusion Porosimetry (MIP) measurements performed on freeze-dried subsamples taken at several distance from the wetting surface of tests MGR21, 22, 23 and 24 after dismantling (Fig. 6.28) and also measurements on the initial state of the material, i.e. compacted block and pellets mixture. For sake of completeness,

Fig. 6.29 presents the final state appearance of each tests.

For the initial state, the block part characterisation of the samples, the curve corresponding to a sample compacted at dry density 1.59 Mg/m^3 with a water content of 14% is considered (equal to the compacted block water content of all the tests). For the pellets layer, a mixture of pellets having approximately a Fuller's curve grain size distribution equal to the one considered for tests MGR21 and 22 is given, with a resulting dry density of 1.29 Mg/m^3 and a water content of 10%.

At the initial state, the denser compacted block presents two predominant pore families: one with a very small pore entry diameter between 2 and 3 nm, another with a pore entry diameter between 10 and 20 µm, which is 4 orders of magnitude larger than the first one. The looser pellets mixture shows similarly two predominant pore families: one with a very small pore entry diameter between 10 and 20 nm, one order of magnitude larger than the pore entry diameter characterising the small pore structures of the compacted bentonite block. The second pore family shows a pore entry diameter between 200 and 300 µm, which is 4 orders of magnitude larger than the first one and one order of magnitude larger than the big pore structures one characterising the compacted block. Given the very heterogeneous pores structure distribution of the pellets mixture layer, it may be possible to distinguish the presence of very large diameters pores, which cannot be detected by MIP. Those pores present a size comparable to the "grains" diameter (Fig. 6.27, beginning and

Fig. 6.29 day 14). However, as soon as the water hydration begins, they are immediately clogged and disappear (Fig. 6.27, 1 hour). Thus, the resulting very high permeability immediately reduces.

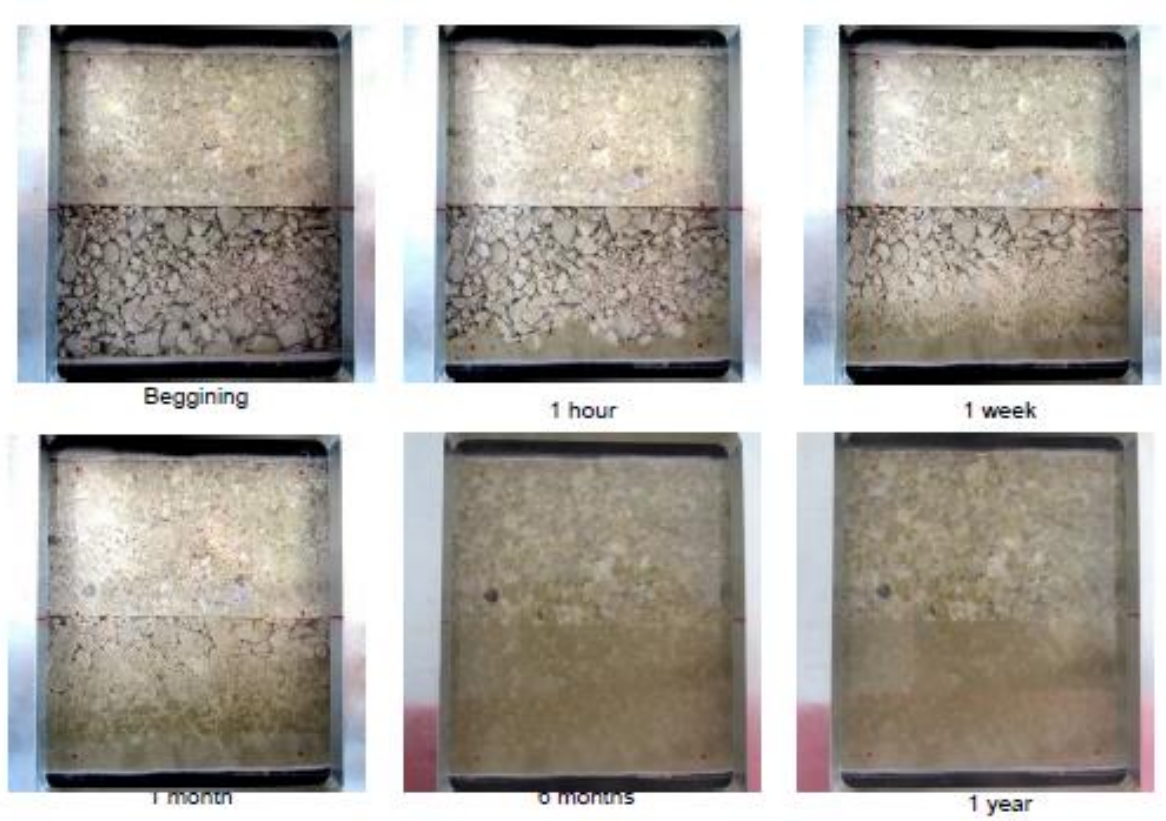

Fig. 6.27: CW1 swelling pressure hydration test performed in a rectangular glass cell on the same assembly analysed in this study (Villar et al. 2021).

Thanks to the analysis of tests MGR21, 23 and 24, it is possible to reconstruct the micro and macro pore structures evolutions upon hydration. This is possible due to the fact that those experimental tests present similar initial physical states and are stopped at different average saturations levels.

In test MGR24, stopped after 14 days, the pore size distribution of the subsamples taken from the block half is similar to the one of the initial block. Accordingly to the negligible variation observed in the dry density and water content already commented. On the contrary, the pore size distribution of the pellet half significantly changed. Although most of the porosity still corresponded to pores larger than 200 nm, the size of these pores decreased with respect to the initial pellets mixture, particularly for the subsamples taken farther away from the hydration surface. Thus, it is possible to distinguish three separated phenomena:

1. The green line corresponding to the pore size distribution of the material taken 1 cm from the wetting surface indicates that the pore entry diameter corresponding to the larger pore structures family (inter-pellet void space) has decreased of 1 order of magnitude, whereas no sensitive variations are reported for the smaller diameter family (intra-pellets void space). As the post-mortem results underline this material portion has experienced a general volume increase (Fig. 6.25).
2. The red line representing the pore size distribution of the material taken 2 cm from the wetting surface shows that the pore entry diameter of larger pore structures family has decreased of 1 order of magnitude as the material at 1 cm but also its amplitude has become half the initial value. Also in this case the smaller diameter family is not subjected to any evident change. This material portion has undergone to a certain volume reduction due to the swelling of the preceding wetted material.
3. The blue line gives information with respect to the pore size distribution of the material taken 4 cm from the wetting surface very close to the boundary with the upper compacted block layer. The MIP

measurements show that the larger pore structures family has basically disappeared but the physical appearance (

4. Fig. 6.29 day 14) clearly underlines the presence of very large pores structures. Thus, an evident limitation of the experimental set-up arises in such occurrence. As before, in this case the smaller diameter family is not subjected to any evident change. This pellets material has undergone to a clear volume reduction due to the swelling of the preceding wetted pellets material but also to the one of the upper compacted bentonite block.

Similarly, the pore size distribution of test MGR21 is described. This test was stopped after 34 days and a number of sub-samples were taken through the height of the sample. Consistently with the very small volume increase detected in the dry density and water content profiles of the upper compacted block, the pore entry diameter of the larger pore structure family corresponding to the compacted bentonite material has increased its dimension of one order of magnitude, with no clear evolution of the smaller pore structures family. The pore size distribution of the pellet half has further evolved:

1. The green line corresponding to the pore size distribution of the material taken 0.8 cm from the wetting surface shows that the pore entry diameter corresponding to the larger pore structures family has decreased of about 1 order of magnitude since the beginning of hydration, reporting two distinct peak values. It is also clear that the initial incremental volume intruded is half the initial one and the preceding one (test MGR24). For the smaller diameter family (intra-pellets void space) is not possible to distinguish any evident variation. As the post-mortem results underline this material portion has experienced a general volume increase, not as big as the one observed for test MGR24, because the upper compacted block exerted a definite compaction due to its swelling (Fig. 6.25).
2. The red line representing the pore size distribution of the material taken 2.3 cm from the wetting surface shows that the pore entry diameter of larger pore structures family has decreased of 1 order of magnitude as the material at 1 cm but also its amplitude has become half the initial value (and similar to the one at the same height of test MGR24). Also in this case the smaller diameter family is not subjected to any evident change. This material portion has undergone to a certain volume reduction due to the initial swelling of the preceding wetted material but its actual dry density is comparable to the one of the corresponding material portion of test MGR24 (ρ_d~1.32 Mg/m^3).
3. The blue line gives information with respect to the pore size distribution of the material taken 4 cm from the wetting surface very close to the boundary with the upper compacted block layer. Differently from the corresponding portion of test MGR24, the larger pore structures family is distinguishable with a pore entry diameter and intruded volume smaller with respect to the zones closer to the wetting surface. As before, in this case the smaller diameter family is not subjected to any evident change. This pellets material has undergone to a clear volume reduction due to the swelling of the preceding wetted pellets material but also to the one of the upper compacted bentonite block. Nevertheless, its dry density is comparable to the one the one of the corresponding material portion of test MGR24 (ρ_d~1.37 Mg/m^3), even though the water content has become equal to w=30% (in test MGR24 it was w=20%).

Finally, the pore size distribution of test MGR23 is reported. This test was stopped after 210 days and in the corresponding full-saturated state. A number of sub-samples were cut through the height of the sample also in this case. Despite the volume increase detected in the dry density and water content profiles of the upper compacted block, the pore entry diameter of the larger pore structure family corresponding to the compacted bentonite material has decreased its diameter and amplitude (especially for z=6 cm green line) with respect to the previous time step (namely MGR21), with no clear evolution of the smaller pore structures family. The pore size distribution of the pellet half has varied but this time for the three different heights similar features are reported:

1. The larger pore structures present a mean diameter value equal to 20 μm with homogeneous volume intruded distribution equal to 0.005 mL/g. A larger intruded volume equal to 0.010 mL/g is detected for the repetition of the measurement at z=0.7 cm;
2. The small pore structures show the same diameter as the initial state but with almost doubled volume intruded.

The pellets portion presents in this saturated state quite homogeneous and uniform dry density and water content distributions, which justify the homogeneous and uniform pore size distributions showed by the MIP and by the physical appearance. Moreover, the mean pore diameter and in general the pore size distribution of the pellets layer in the final state is remarkably similar to the one of the compacted block layer. Namely, the two initially different assemblies present in the final saturated state the same pore structure distributions, characterized by two visible pore families of 20 μm and 10 nm of mean pore diameter and intruded volume respectively about 0.004 mL/g and 0.0045 mL/g.

For test MGR22, no intermediate states information are available, thus final MIP results show similar features with respect to test MGR23. Namely, despite the general volume increase detected in the dry density and water content profiles of the upper compacted block, the pore entry diameter of the larger pore structure family corresponding to the compacted bentonite material has increased its diameter and amplitude (especially for z=6 cm green line) with respect to the initial state, with no clear evolution of the smaller pore structures family. The pore size distribution of the pellet half has changed consistently showing similar features for the three different heights. Specifically:

1. The larger pore structures present a mean diameter value equal to 20 μm with volume intruded equal to 0.008 mL/g for z=0.7 and 2.3 cm (corresponding dry density equal to ρ_d=1.39 Mg/m^3) and 0.006 mL/g for z=3.9 cm (ρ_d=1.42 Mg/m^3).
2. The small pore structures show the same diameter as the initial state but with almost doubled volume intruded.

Also in this test, it is possible to see that both compacted bentonite and pellets materials present the same mean entry pore diameter for the larger and smaller pore structures. Differently from test MGR23, the intruded volume for the larger diameter pore family of the pellets layer is higher. Numerical results (Fig. 6.24) show macro-void ratio (i.e. large-pore volume structure) distributions in remarkably good agreement with all these experimental results, despite the numerous simplifications implied by the numerical model.

It is important to mention that due to technical characteristics of the porosimeter used, mercury did not intrude pores of a size of less than 6 nm, and in clay materials the percentage of pores smaller than this size can be relevant. Thus, it is worth to report the percentage of pores intruded by mercury in these subsamples, which was between 35 and 70%.

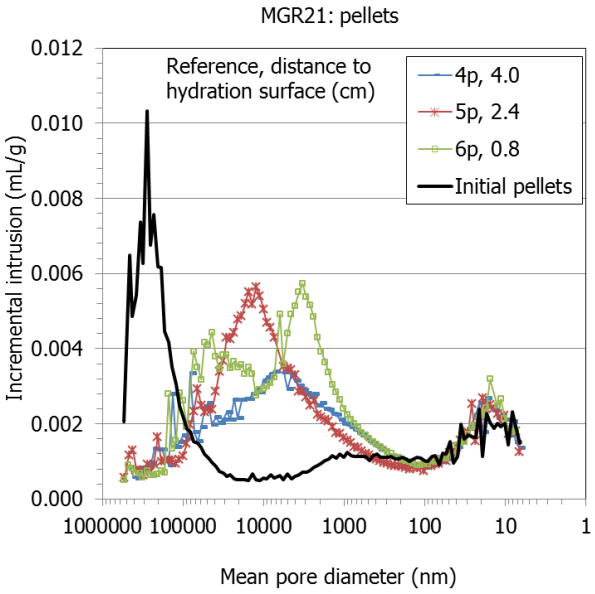
MGR21: pellets
Reference, distance to hydration surface (cm)
4p, 4.0
5p, 2.4
6p, 0.8
Initial pellets
Incremental intrusion (mL/g)
0.012
0.010
0.008
0.006
0.004
0.002
0.000
1000000 100000 10000 1000 100 10 1
Mean pore diameter (nm)

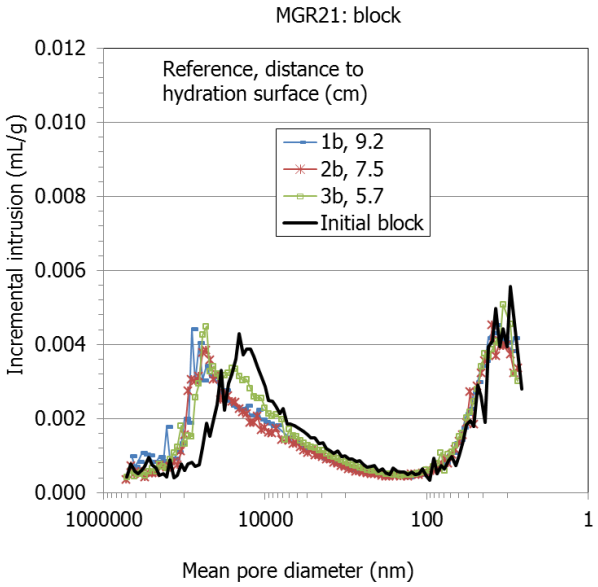
MGR21: block
Reference, distance to hydration surface (cm)
1b, 9.2
2b, 7.5
3b, 5.7
Initial block
Incremental intrusion (mL/g)
0.012
0.010
0.008
0.006
0.004
0.002
0.000
1000000 10000 100 1
Mean pore diameter (nm)

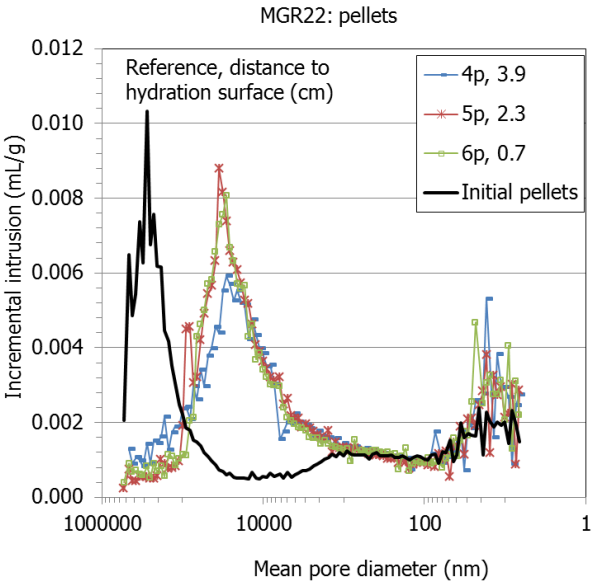
MGR22: pellets
Reference, distance to hydration surface (cm)
4p, 3.9
5p, 2.3
6p, 0.7
Initial pellets
Incremental intrusion (mL/g)
0.012
0.010
0.008
0.006
0.004
0.002
0.000
1000000 10000 100 1
Mean pore diameter (nm)

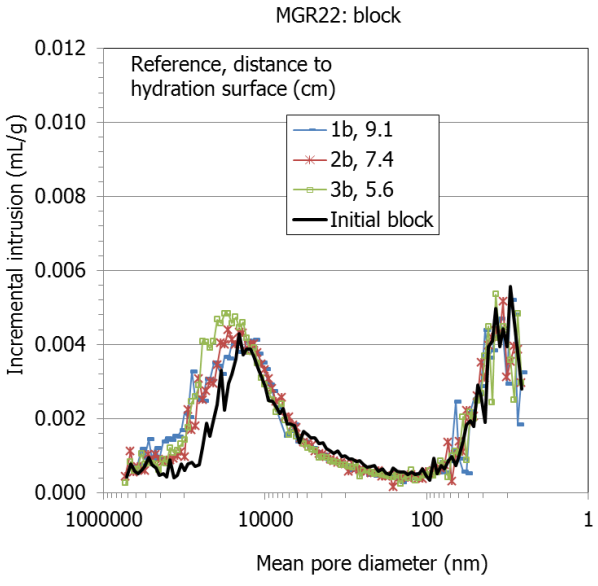
MGR22: block
Reference, distance to hydration surface (cm)
1b, 9.1
2b, 7.4
3b, 5.6
Initial block
Incremental intrusion (mL/g)
0.012
0.010
0.008
0.006
0.004
0.002
0.000
1000000 10000 100 1
Mean pore diameter (nm)

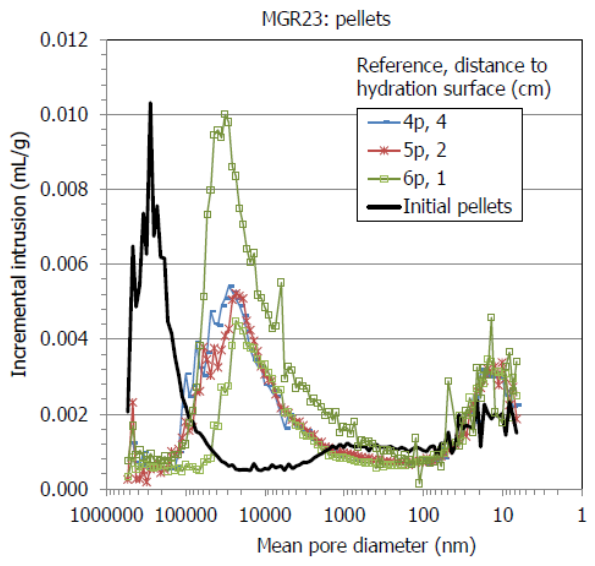
MGR23: pellets
Reference, distance to hydration surface (cm)
4p, 4
5p, 2
6p, 1
Initial pellets
Incremental intrusion (mL/g)
0.012
0.010
0.008
0.006
0.004
0.002
0.000
1000000 100000 10000 1000 100 10 1
Mean pore diameter (nm)

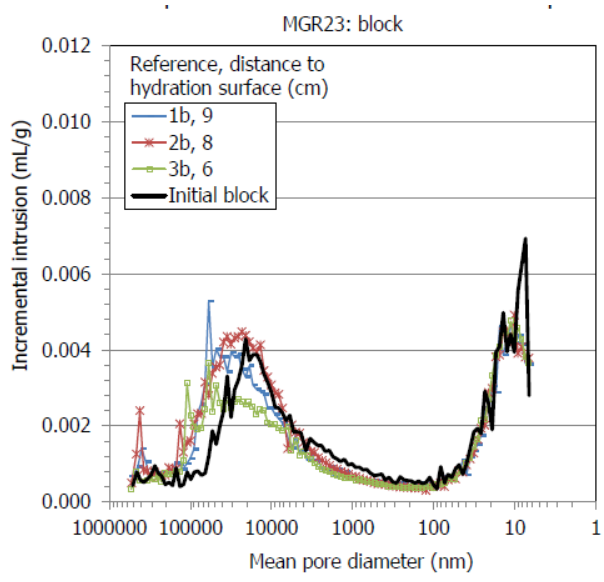
MGR23: block
Reference, distance to hydration surface (cm)
1b, 9
2b, 8
3b, 6
Initial block
Incremental intrusion (mL/g)
0.012
0.010
0.008
0.006
0.004
0.002
0.000
1000000 100000 10000 1000 100 10 1
Mean pore diameter (nm)

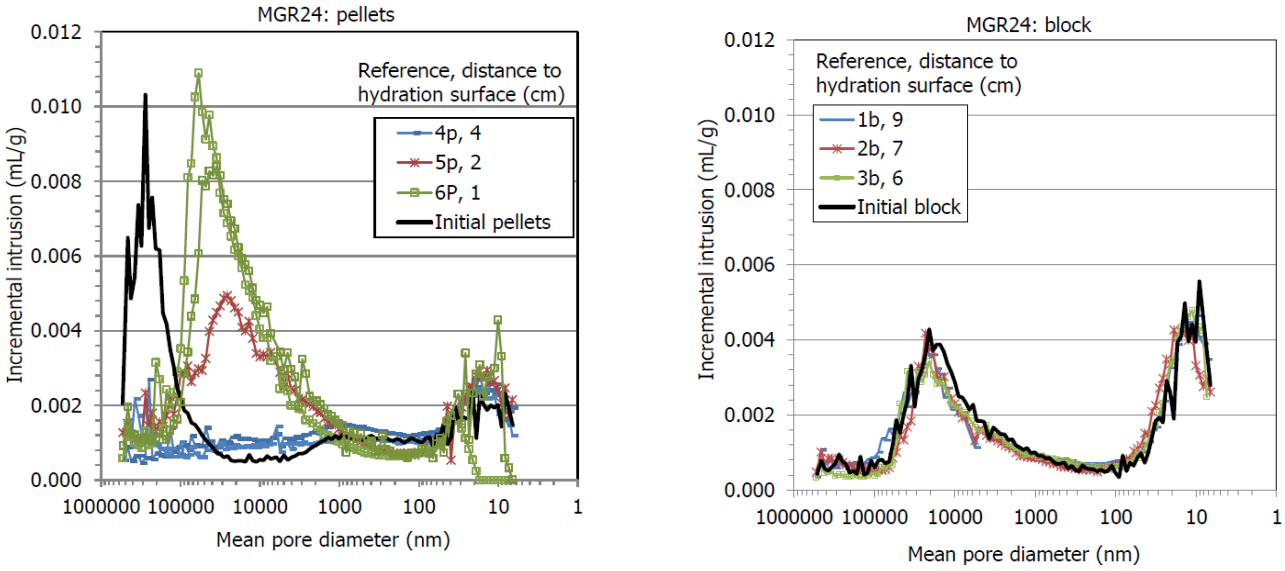

Fig. 6.28: MIP characterisation of compacted block material and pellets layer components at initial state and at several locations through the height of the sample at the end of the tests for MGR21, 22, 23 and 24.

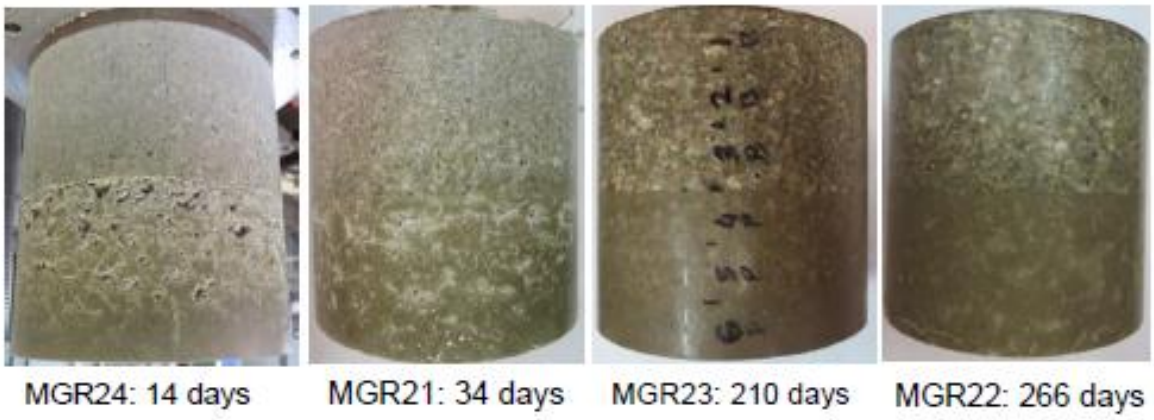

Fig. 6.29: Appearance of the MGR samples at the end of the tests (Villar et al. 2021)

From Table 6.8 to Table 6.10, the experimental large pores diameter structures and the numerical macro void ratios values are reported, together with the experimental and numerical dry density and water content. The MIP measurements are largely confirmed by the physical appearance of the samples at dismantling, in which it becomes difficult to distinguish the boundary between the two layers as the saturation progresses. Despite the numerical model does not distinguish the volume and the diameter of each pore family, it is possible to see that the macro void ratio evolution is consistent with the experimental data. The physical state evolution in terms of dry density and water content is also very well reproduced by the numerical model. Those consist in evident heterogeneities distribution migrating toward a homogenised structure. Consequentially, all these evidences represent a strong validation of the adopted numerical model.

Table 6.8: Summary comparisons between experimental large diameter pores and numerical macro void ratio together with experimental and numerical dry density and water content. Day 0 (initial state) and day 14 (MGR24).

Initial state and MGR24 (day 0 and 14)																
	Distance from the wetting face	**Large diameter pores (Macro void ratio)**						**Dry density**				**Water content**				
	Z [mm]	**e_M [-]**						**ρ_d [Mg/m^3]**				**w [%]**				
		Exp				**Num**		**Exp**		**Num**		**Exp**		**Num**		
		Pore Diameter [µm]		**Volume [mL/g]**												
Time [day]		0	14	0	14	0	14	0	14	0	14	0	14	0	14	
Compacted Block Layer	92	20	20	0.004	0.004	0.22	0.19	1.62	1.59	1.6	1.59	13.7	14.1	13.6	19	
		↔		↔		↘		↘		↘		↗		↗		
	75	20	20	0.004	0.004	0.22	0.19	1.62	1.58	1.6	1.58	13.7	15	13.6	18	
		↔		↔		↘		↘		↘		↗		↗		
	57	20	20	0.004	0.004	0.22	0.19	1.62	1.54	1.6	1.58	13.7	17.3	13.6	20	
		↔		↔		↘		↘		↘		↗		↗		
Pellets Mixture Layer	40	200	[-]	0.01	[-]	0.72	0.50	1.28	1.35	1.28	1.31	5.7	22.2	4.9	30	
		↘		↘		↘		↗		↗		↗		↗		
	2.4	200	10	0.01	0.005	0.72	0.43	1.28	1.33	1.28	1.30	5.7	32.6	4.9	35	
		↘		↘		↘		↗		↗		↗		↗		
	8	200	20	0.01	0.01	0.72	0.33	1.28	1.22	1.28	1.29	5.7	44.3	4.9	45	
		↘		↔		↘		↘		↗		↗		↗		

Table 6.9: Summary comparisons between experimental large diameter pores and numerical macro void ratio together with experimental and numerical dry density and water content. Day 14 (MGR24) and day 34 (MGR21).

MGR24 and MGR21 (day 14 and 34)																
	Distance from the wetting face	**Large diameter pores (Macro void ratio)**						**Dry density**				**Water content**				
	Z [mm]	**e_M [-]**						**ρ_d [Mg/m^3]**				**w [%]**				
		Exp				**Num**		**Exp**		**Num**		**Exp**		**Num**		
		Pore Diameter [µm]		**Volume [mL/g]**												
Time [day]		**14**	**34**	**14**	**34**	**14**	**34**	**14**	**34**	**14**	**34**	**14**	**34**	**14**	**34**	
Compacted Block Layer	92	20	100	0.004	0.004	0.19	0.19	1.59	1.48	1.59	1.55	14.1	20.1	19	25	
		↗		↔		↔		↘		↘		↗		↗		
	75	20	100	0.004	0.004	0.19	0.19	1.58	1.50	1.58	1.54	15	21.6	18	25	
		↗		↔		↔		↘		↘		↗		↗		
	57	20	100	0.004	0.004	0.19	0.19	1.54	1.44	1.58	1.53	17.3	25.1	20	25	
		↗		↔		↔		↘		↘		↗		↗		
Pellets Mixture Layer	40	[-]	4	[-]	0.0035	0.50	0.35	1.35	1.37	1.31	1.48	22.2	31.3	30	31	
		↗		↗		↘		↗		↗		↗		↗		
	2.4	10	10	0.005	0.006	0.43	0.34	1.33	1.31	1.30	1.45	32.6	34.7	35	35	
		↔		↗		↘		↗		↗		↗		↗		
	8	20	3/30	0.01	0.006	0.33	0.33	1.22	1.25	1.29	1.30	44.3	40.9	45	40	
		↘		↘		↔		↘		↗		↗		↗		

Table 6.10: Summary comparisons between experimental large diameter pores and numerical macro void ratio together with experimental and numerical dry density and water content. Day 34 (MGR21) and day 210 (MGR23).

MGR21 and MGR23 (day 34 and 240)																
	Distance from the wetting face	Large diameter pores (Macro void ratio)						Dry density				Water content				
	Z [mm]	e_M [-]						ρ_d [Mg/m^3]				w [%]				
		Exp				Num		Exp		Num		Exp		Num		
		Pore Diameter [µm]		Volume [mL/g]												
Time [day]		34	210	34	210	34	210	34	210	34	210	34	210	34	210	
Compacted Block Layer	92	100	30	0.004	0.004	0.19	0.18	1.48	1.46	1.55	1.50	20.1	31.6	25	31.6	
		↘		↔		↘		↘		↘		↗		↗		
	75	100	30	0.004	0.004	0.19	0.18	1.50	1.45	1.54	1.47	21.6	31.8	25	31.8	
		↘		↔		↘		↘		↘		↗		↗		
	57	100	300	0.004	0.003	0.19	0.19	1.44	1.44	1.53	1.45	25.1	32.5	25	32.5	
		↘		↘		↔		↔		↘		↗		↗		
Pellets Mixture Layer	40	4	20	0.0035	0.005	0.35	0.20	1.37	1.42	1.48	1.48	31.3	33.3	31	42	
		↗		↗		↘		↗		↔		↗		↗		
	2.4	10	20	0.006	0.005	0.34	0.25	1.31	1.37	1.45	1.40	34.7	34.7	35	45	
		↗		↘		↘		↗		↘		↗		↗		
	8	3/30	20	0.006	0.010/ 0.0045	0.33	0.28	1.25	1.37	1.30	1.30	40.9	36.8	40	46	
		↗		↗		↘		↗		↔		↗		↗		

6.3.4. Sensitivity analysis on the influence of friction coefficient

The influence of frictional phenomena development between bentonite materials and laboratory equipment on swelling capacity measurements during hydration are not fully understood yet. Accordingly to the very complex experimental characterisation, holding highly coupled hydro-mechanical mechanisms, very few experimental data are available.

In general friction phenomena are modelled via the Mohr-Coulomb criteria, in which the resistance to sliding is given by a friction coefficient (μ=$tg\phi$) multiplying the normal pressure exerted on a surface (possibly summed up with the cohesion) (Eq. 6.1). Namely, this coefficient, proportionally to the radial stress exerted on the cell wall, controls the maximum exerted tangential stress value before failure.

$$\tau \leq p_N tan\phi + c \qquad \text{Eq. 6.1}$$

Thus, it is logical that radial pressure at several location and top and bottom axial pressure measurements are needed in order to determine experimentally the friction coefficient in oedometer conditions. Nevertheless, in the considered experimental campaign, only the top axial swelling pressure is recorded.

Due to this a numerical sensitivity analysis is performed in order to determine the influence of the friction coefficient between the bentonite material and the cell wall on experimental and numerical responses neglecting the role of radial stress.

For this purpose tests MGR23 and 27 are considered. Those tests present exactly the same initial conditions and characteristic, but they differ for the layers configuration. Test MGR23 is composed of a bottom pellets layer in direct contact with the hydration surface and an upper compacted bentonite block, whereas test MGR27 is composed of a bottom compacted block bentonite layer in direct contact with the hydration surface and an upper pellets layer. The total axial pressure is measured on the top face of the sample, in the compacted block layer for test MGR23 and in the pellets layer for test MGR27, with final swelling pressure values respectively equal to 3 MPa and 1.5 MPa.

These experimental outcomes result in open contradiction with a number of experimental swelling pressure tests showing that the final swelling pressure value is proportional to the average initial dry density of the bentonite assembly, regardless the initial pore structures distribution or materials configurations.

However, the following analysis on friction phenomena aims to justify the experimental results and to propose a complementary numerical procedure to determine the friction coefficient.

The four cases are analysed: a model in which friction is not considered and the material is free to slide with respect to the cell wall (i.e. μ=0); a model in which infinitive friction is modelled and the material is glued to the cell wall (i.e. μ=∞); two intermediate cases in which μ=0.360 and μ=0.180 (respectively ϕ=20° and ϕ=10°) and the material can slide with respect to the cell wall only if the failure criteria is met. The friction coefficient is considered constant on the entire cell wall surface regardless the material with which it is in contact (i.e. compacted block or pellets).

Fig. 6.30 and Fig. 6.31 show the comparison between numerical results accounting different friction coefficients with the cell wall with respect to the total axial swelling pressure measured on the top and bottom faces through time. For the case μ=0, in which friction between material and the cell wall is not considered, the axial top and bottom swelling pressure measurements overlap for both tests MGR23 and MGR27, reaching final stabilised swelling pressure values equal approximately to 2 MPa in both cases. This result is in complete agreement with the above-mentioned experimental observations. On the other hand, when infinite friction is assumed between the material and the cell wall, the top and bottom axial swelling pressure measurements differ noticeably. In general, the measurements recorded in the compacted block

sides present much higher values with respect to the measurements of the pellets layer sides. For test MGR23, the axial pressure stabilised value is equal to 4 MPa in top compacted block layer and 1.20 MPa in the bottom pellets one, with ~3 MPa of discrepancy. In test MGR27, the axial pressure stabilised value in bottom compacted block layer is equal to 3 MPa and 1 MPa in the top pellets one, with 2 MPa final difference. In the intermediate cases, as the friction coefficient increases the axial swelling pressure measurements recede from the non-frictional case toward the infinite friction one, showing an evident similarity and almost correspondence with this latter one when ϕ=20° (namely $\mu = tg20° = 0.360$). Therefore, as the friction increases the axial swelling pressure measurements recorded in the compacted bentonite block and pellets layers diverge. As a consequence, the recorded top axial swelling pressures differ for tests MGR23 and MGR27. This is due to the fact that those measurements are relative respectively to the compacted block layer and to the pellets one. Measurements recorded in the same material type are however similar with values ranging between the maximum (4 MPa) exerted in the block part of test MGR23 and minimum (1 MPa) exerted in the pellets part of test MGR27 for the sticking case and the value equal to 2 MPa of the non-frictional case.

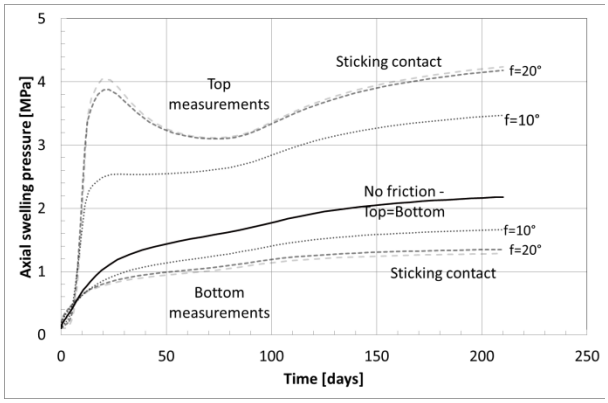

Fig. 6.30: Total axial top and bottom swelling pressure evolution for tests MGR23. Comparison between numerical results with different friction coefficients with the cell wall.

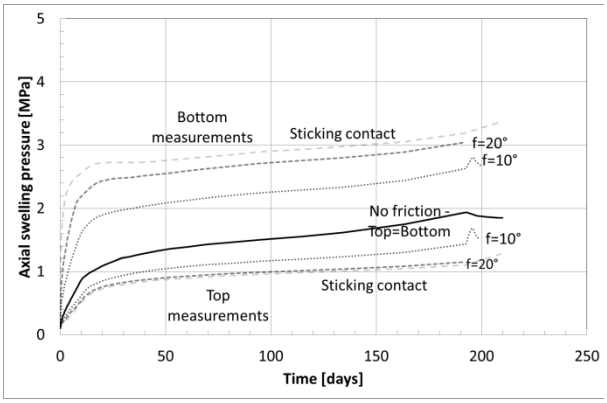

Fig. 6.31: Total axial top and bottom swelling pressure evolution for tests MGR27. Comparison between numerical results with different friction coefficients with the cell wall.

Fig. 6.32 and Fig. 6.33 present the comparison between numerical results accounting different friction coefficients with the cell wall with respect to the total radial swelling pressure measured on z=75 mm from the wetting surface (named “top measurements” in the compacted block layer for test MGR23 and pellets layer for test MGR27) and on z=25 mm from the wetting surface (named “bottom measurements” in the pellets layer for test MGR23 and compacted block layer for test MGR27) through time. It is relevant to analyse the radial stress at different locations because it multiplies the friction coefficient resulting in the maximum resistance to sliding accordingly to the selected failure criteria. Tests MGR23 and 27 present similar features. For all the friction coefficients, an evident radial swelling pressure gradient can be detected, characterised by the maximum value recorded in the compacted block part (namely on the top for test MGR23 and on the bottom for test MGR27) and a minimum one in pellets one. The amplitude of this gradient is proportional to the selected friction coefficient being maximum for $\mu = \infty$ and minimum for $\mu = 0$. The maximum radial pressure is recorded in the block layer for the sticking case with a value equal to 4 MPa and the minimum one in the pellets layer with 1 MPa for both tests MGR23 and 27. Indeed, radial pressure measurements for tests MGR23 and 27 report similar time evolution and final stabilised values if corresponding block or pellets layers are considered. Moreover, it can be observed that in the pellets layer no relevant discrepancy can be detected in the radial pressure measurements, whereas clear differences are recorded in the compacted block layer for the distinct friction coefficients (except for ϕ=20°, which overlaps the sticking case outputs). Also in this case, it is possible to notice that as the friction coefficient increases, the radial swelling pressure recorded in the block layer recedes from the non-frictional case towards the

sticking contact one for intermediate friction coefficient values. It looks particularly interesting that the axial and radial swelling pressure values recorded during test MGR23 for the sticking contact case ($\mu=\infty$) are similar also with respect to their values, highlighting an isotropic stress state similar to the one detected in the pellets part for tests MGR23 and 27 for all the μ.

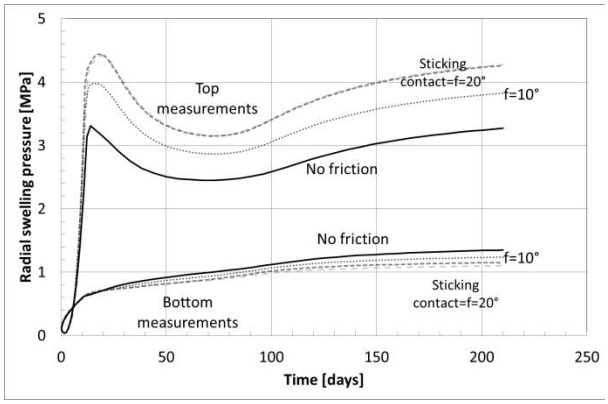

Fig. 6.32: Total radial top (z=75 mm from the wetting surface) and bottom (z=25 mm from the wetting surface) swelling pressure evolution for tests MGR23. Comparison between numerical results with different friction coefficients with the cell wall.

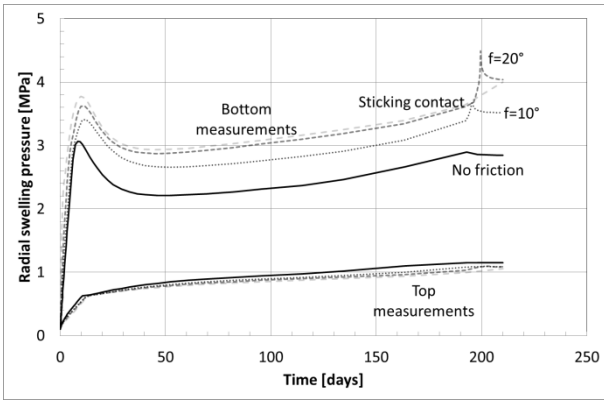

Fig. 6.33: Total radial top (z=75 mm from the wetting surface) and bottom (z=25 mm from the wetting surface) swelling pressure evolution for tests MGR27. Comparison between numerical results with different friction coefficients with the cell wall.

Fig. 6.34 and Fig. 6.35 exhibit the comparison between experimental numerical results accounting different friction coefficients with the cell wall with respect to the total top axial swelling pressure measured in the compacted block layer for test MGR23 and in the pellets one for test MGR27. It is possible to see that the experimental records lay between the non-frictional case pressure evolution and the one concerning ϕ=10° for test MGR23 and for ϕ=20° for test MGR27, not only from a values point of view but also with respect to the non-monotonic swelling pressure evolution for transient saturation states.

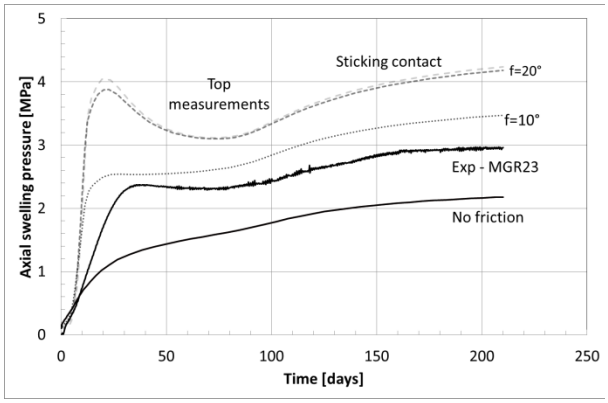

Fig. 6.34: Top swelling pressure in axial time evolution for test MGR23. Comparisons between experimental data and model predictions with different friction coefficients with the cell wall.

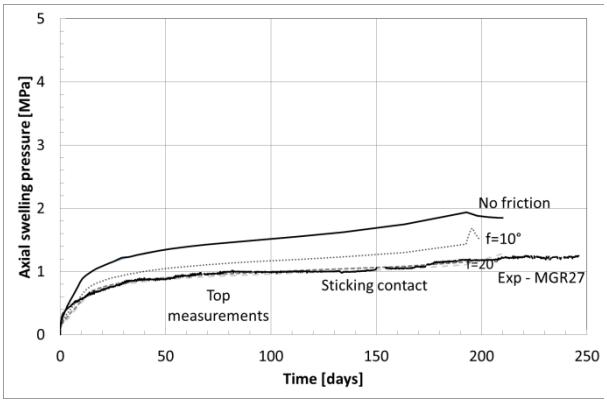

Fig. 6.35: Top swelling pressure in axial time evolution for test MGR27. Comparisons between experimental data and model predictions with different friction coefficients with the cell wall.

Fig. 6.36 and Fig. 6.37 show the sliding at the interface between the bentonite sample and the cell wall for the material placed at z=50 mm from the wetting surface (i.e. at the boundary between the pellets and compacted block layers). It is evident that the sliding occurs in the direction of the swelling of the compacted block, which always takes place toward the pellets layer. Namely, for test MGR23, the sliding direction is toward the bottom, whereas for test MGR27 it occurs toward the top. Fig. 6.36 also indicates that at the very beginning of the saturation process, a small sliding less than 1 mm occurs in the compacted block direction. This is related to the desaturation of the compacted block caused by the very high initial suction level of the

pellets and it is immediately dissipated. Obviously, the sliding magnitude is inversely proportional to the sliding resistance, hence to the selected friction coefficient. Indeed, the sliding at the interface between the material sample and the cell wall for intermediate cases ranges between 0 mm for the sticking contact strategy and 6 mm for the free sliding one.

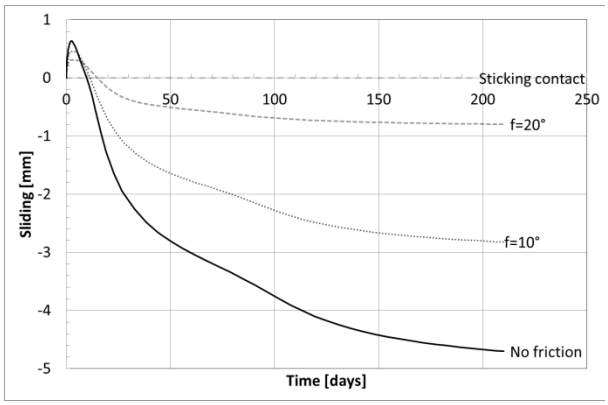

Fig. 6.36: Sliding at the interface between the bentonite sample and the cell wall for the material placed at z=50 mm from the wetting surface (i.e. at the boundary between the pellets and compacted block layers). Model predictions for test MGR23 with different friction coefficients with the cell wall.

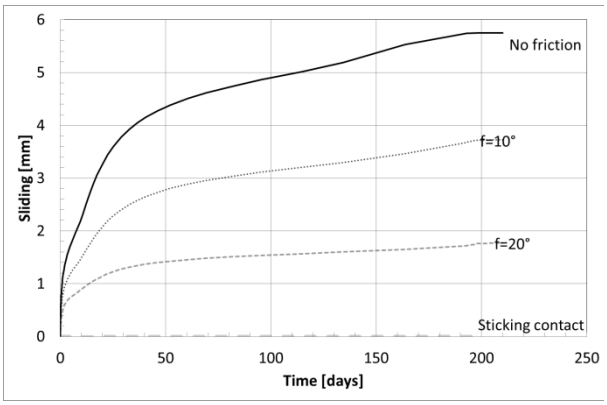

Fig. 6.37: Sliding at the interface between the bentonite sample and the cell wall for the material placed at z=50 mm from the wetting surface (i.e. at the boundary between the pellets and compacted block layers). Model predictions for test MGR27 with different friction coefficients with the cell wall.

Fig. 6.38 and Fig. 6.39 compare the experimental and numerical dry density distributions for different friction coefficient between the materials and the cell wall through the height of the sample at dismantling for tests MGR23 and 27. The final dry density distributions were already discussed in the previous paragraph thus special attention is given to the effect of friction. In both cases, increasing friction enhances the amplitude of the dry density gradient. Indeed, it can be observed that for μ=0 the dry density profiles are most uniform through the sample. In test MGR23, the experimental results look the closest to the infinitive friction case for the pellets layer part and to the non-frictional case for the compacted block layer. Similarly, post-mortem experimental results of test MGR27 are the closest to the non-frictional case for the compacted block layer and very near to the one of ϕ=10° for the pellets layer. This circumstance arises the suspect that friction is not homogeneously distributed through the height of the sample but distinguish incontrovertibly the material in contact with the cell wall.

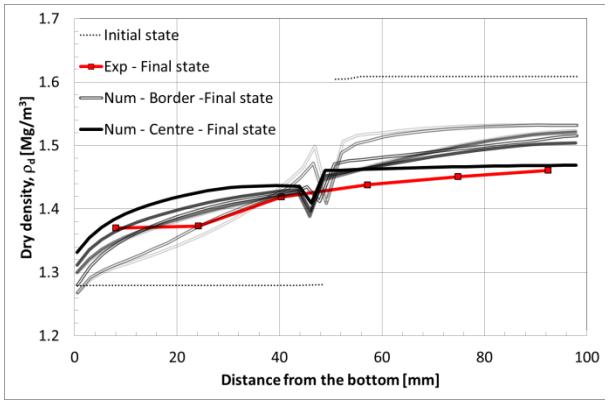

Fig. 6.38: Dry density profiles for tests MGR23. Comparison between experimental data and numerical simulations with different friction coefficients with the cell wall at the final state.

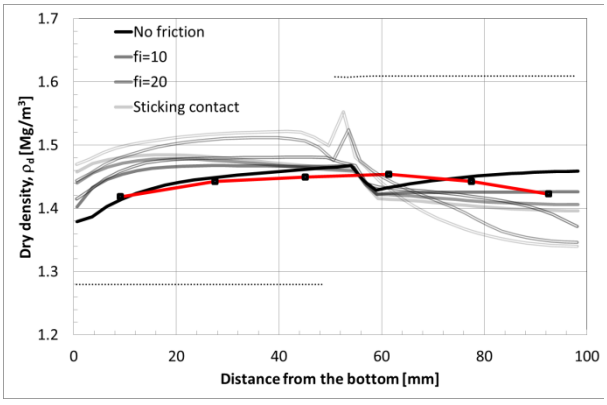

Fig. 6.39: Dry density profiles for tests MGR27. Comparison between experimental data and numerical simulations with different friction coefficients with the cell wall at the final state.

Following the previous observations, two last numerical simulations were performed and compared to the reference results presented in the previous paragraphs, which considered uniform and unique friction coefficient regardless the material (equal to μ=0.125, i.e. ϕ=7°). These modelling strategies hold a different value of the friction coefficient considering the material in contact with the cell wall, instead of the uniform reference one. Namely:

- μ=0.125 (i.e. ϕ=7°) for the interface between the cell wall and the compacted block layer;
- μ=0.360 (i.e. ϕ=20°) for the interface between the cell wall and the pellets layer.

The numerical results presented in Fig. 6.40 and Fig. 6.41 show that the "uniform friction" strategy reproduces test MGR23 top axial swelling pressure time evolution slightly better than the "differential friction" one. On the other hand, the "differential friction" strategy reproduces test MGR27 top axial swelling pressure time evolution better than the "uniform friction" model. Negligible differences with respect to dry density at dismantling are found for the two modelling strategies for test MGR23 (Fig. 6.42). Improved correspondence can be observed between the experimental and numerical results of the "differential friction" of test MGR27 (Fig. 6.43).

However, a better understanding of the friction phenomena occurring during experimental tests would be provided by radial stress measurements. Namely for higher (lower) radial stress, lower (higher) friction angle would be predicted. Radial pressure measurements were not recorded in this case and in general those are not as reliable as the axial ones (Gramegna et al. 2020). Nevertheless, a number of experimental campaigns like the one analysed in the preceeding chapter ((Bernachy-Barbe et al. 2020),(Bernachy-Barbe 2020)) showed that the radial stress is comparable to the axial one. At the same time, the numerical analysis performed in Chapter 4 showed that the radial stress depends on the Poisson ratio ν and on the material friction angle ϕ in the elastic state and on the shape of the yielding surface in the plastic one. In this analysis, both elastic and plastic stress paths are very nicely reproduced and compared for the top axial swelling pressure of tests MGR21, 23, 24 and 27. Thus the selected mechanical parameters ν and ϕ and the yielding surface shape represent the most suitable calibrated set and, finally, since no further experimental information is available, the uniform friction coefficient set equal to μ=0.125 (ϕ=7°) is assumed to be the most reasonable.

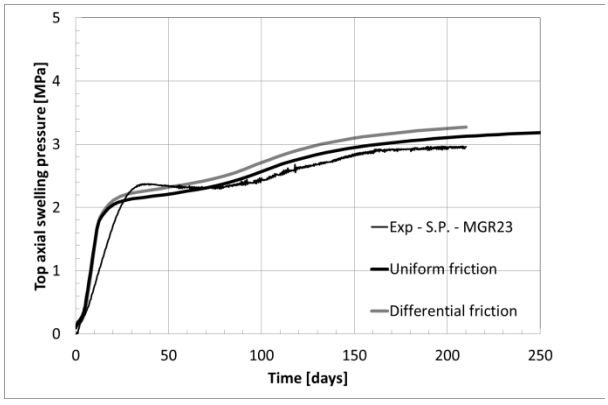

Fig. 6.40: Top swelling pressure in axial time evolution for test MGR23. Comparisons between experimental data and model predictions with different friction coefficients distribution with the cell wall.

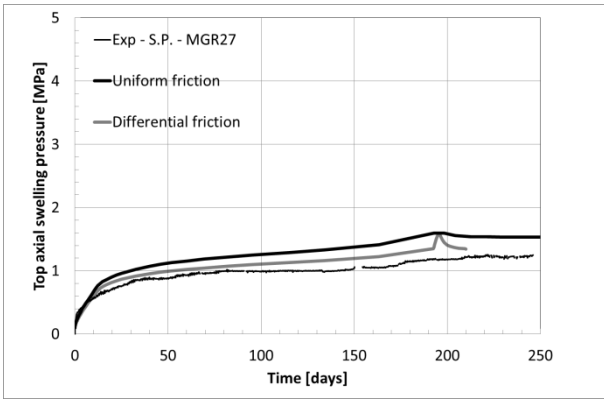

Fig. 6.41: Top swelling pressure in axial time evolution for test MGR27. Comparisons between experimental data and model predictions with different friction coefficients distribution with the cell wall.

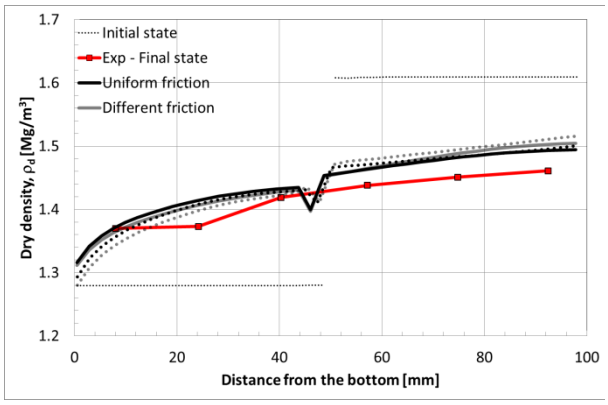

Fig. 6.42: Dry density profiles for tests MGR23. Comparison between experimental data and numerical simulations with different friction coefficients distributions with the cell wall at the final state.

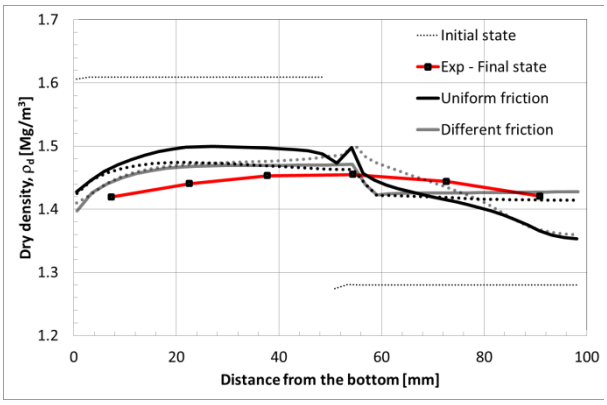

Fig. 6.43: Dry density profiles for tests MGR27. Comparison between experimental data and numerical simulations with different friction coefficients distribution with the cell wall at the final state.

For sake of completeness, it is necessary to underline that the selected friction angle values determined thanks to this numerical analysis are strongly dependent on the radial stress distributions and development. In general, for lower radial stress, higher friction angle value would be required and vice versa. However, it was possible to see in CHAPTER 5, that radial stress measurements recorded close to the top face are comparable to the axial swelling pressure measured at that location. Thus, if the numerical and experimental top axial swelling pressures coincide and numerical axial and radial swelling pressures are similar, the obtained friction angle value should also be reasonably close to the reality.

6.3.5. Analysis on the influence of boundary conditions on numerical results

In the previous sections, the presented modelling strategies involved the calibration of the permeability law evolutions based on the water inflow as function of time of test MGR23. The validation of such hypothesis was performed via the comparisons between the numerical and experimental results of swelling pressure time evolution, dry density and water content distributions at the final states for all the five analysed tests. The selected water transfer mechanism showed its capability to reproduce not only the final states but also the transient e non-monotonic hydro-mechanical features of the tests. However, a possible limitation was represented by the experimental water inflow plateau occurring approximately between the 10th and the 28th days of the test time, which was not represented by the model. It resulted quite surprising to observe that to this "plateau" corresponded, however, a certain swelling pressure increase (Fig. 6.44)5. Consequentially, the goals of this paragraph are to evaluate the quality of the experimental water inflow time evolution of test MGR23 and to analyse the test response with respect to this.

For this purpose, the experimental water supply development is modelled by imposing an injected water volume time evolution similar to the experimental one. Thanks to this alternative strategy, it is possible to reproduce the experimental water intake plateau (Fig. 6.44), to assess the influence of the numerical water supply boundary conditions on the results and to deeply analyse the strongly coupled interactions of the hydro-mechanical processes taking place during water saturation.

In the following, this additional strategy will be named "Plateau", whereas the one taking advantage of the permeability law evolution calibration giving as result the water intake time evolution will be indeed indicated as "Reference", which was extensively described in all this work.

Fig. 6.44 and Fig. 6.45 show the total swelling pressure time evolution. With respect to the comparisons between the experimental and numerical top axial swelling pressure measurements (Fig. 6.44) it is possible to note that the three curves correspond remarkably well in the transient phases as well as in the stabilised final value. The "Plateau" outcomes are slightly lower with respect to the experimental and "Reference" ones, however no remarkable discrepancies can be described.

Fig. 6.45 shows the comparison between the axial and radial numerical swelling pressure measurements of the two numerical strategies, which do not differ significantly. The "Reference" strategy swelling pressure time evolutions look more regular than the "Plateau" one. Especially at the 10th day of the simulation time, irregularities are detected in the swelling pressure development of the pellets layer measurements. At this point, the numerical water inflow plateau begins. It was decided to stop the water intake slightly before the experimental one because numerical instabilities were met. Indeed, at this stage, as Fig. 6.46 shows, the numerical "Plateau" injected water mass is equal to 135 g instead of the experimental 150 g. Despite this small discrepancy, the average saturation of the numerical and experimental samples is the same (Fig. 6.47).

The numerical strategy "Plateau" confirms that despite any further water quantity is injected in the sample, swelling pressure can still evidently increase due to the water transfer from the pellets layer to the compacted block one, main responsible of the development top axial swelling pressure.

After the 28th day of the test and simulations time (i.e. after the plateau), the trend of the top axial and water intake time evolution is the same in the three cases as the saturation process continues: a change of slope, almost constant swelling pressure values (or also decrease) and a final pressure increase are observed (from Fig. 6.44 to Fig. 6.47).

5 Further discussions with experimentalists confirmed that the plateau was an experimental artefact.

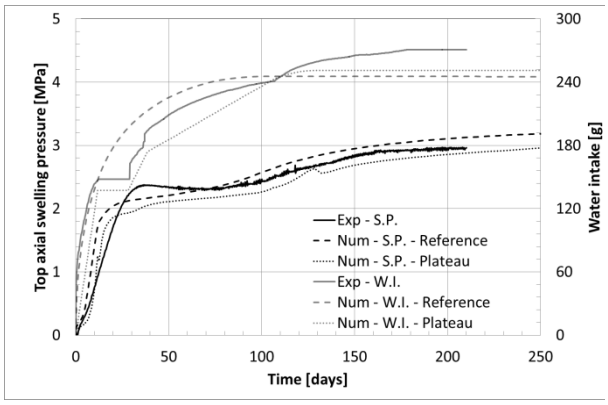

Fig. 6.44: Top swelling pressure in axial direction and water mass injection time evolution for test MGR23. Comparisons between experimental data and model predictions.

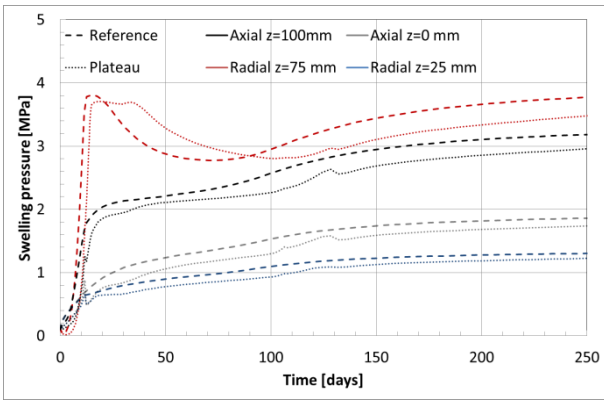

Fig. 6.45: Total swelling pressure evolution for test MGR23. Comparison between experimental results on the top axial measurement of the sample and numerical simulations at the axial top and bottom face of the sample and radial at the cell wall at z=25 mm and z=75 mm from the wetting surface.

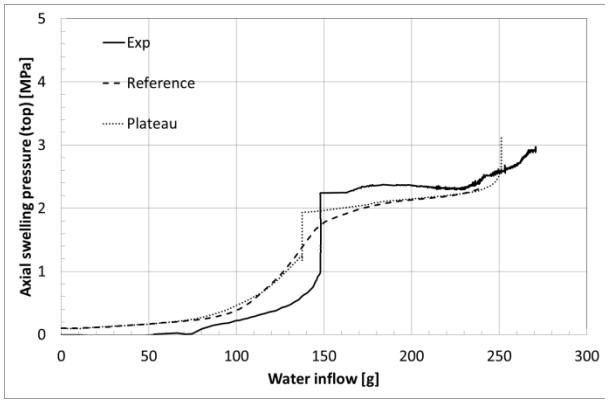

Fig. 6.46: Swelling pressure in axial direction as water inflow of the sample function for test MGR23. Comparisons between experimental data and model predictions.

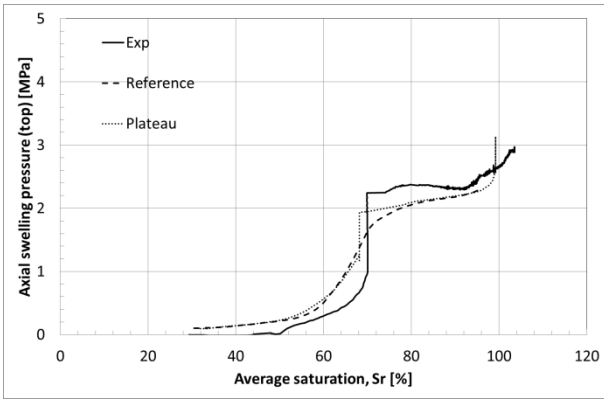

Fig. 6.47: Swelling pressure in axial direction as average saturation degree of the sample function for test MGR23. Comparisons between experimental data and model predictions.

In Fig. 6.48 and Fig. 6.49, the numerical suction and saturation profiles are showed for days 11, ~36 and ~210 of the simulations time (before and after the plateau and at the dismantling). In the "Reference" case (a), as the water is injected from the bottom, suction decreases showing a certain gradient, with the immediate full saturation of the material in direct contact with the hydration source. In the "Plateau" strategy (b), at day 11, the bottom material seems similarly fully saturated, but it can be seen that suction is not equal to zero at the 36th day of the simulation time. Moreover, the suction distribution is quite different during both time steps. The gradient of suction of "Plateau" is much more pronounced with respect to the "Reference one". This circumstance is particularly interesting because at this time the two numerical samples present the same average water quantity (i.e. 135 g) and average saturation (60%). It appears clear that the numerical hydration strategy affects undeniably the numerical results. On the other hand, the saturation profiles are quite similar. The pellets layer of the "plateau" strategy seem to contain more water than the "reference" one and, complementary, the compacted block layer less. The saturation results are consistent with the suction distribution because those are linked via the adopted water retention constitutive behaviour.

a)

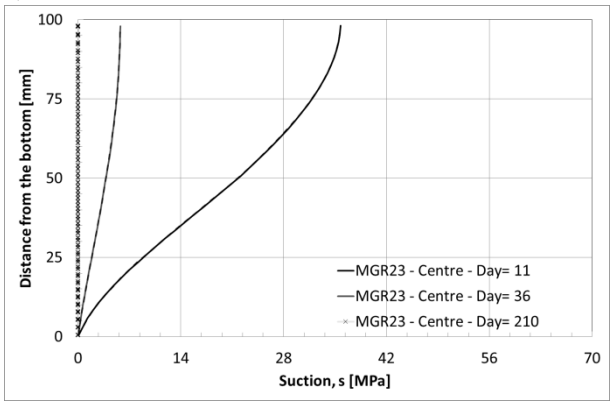

b)

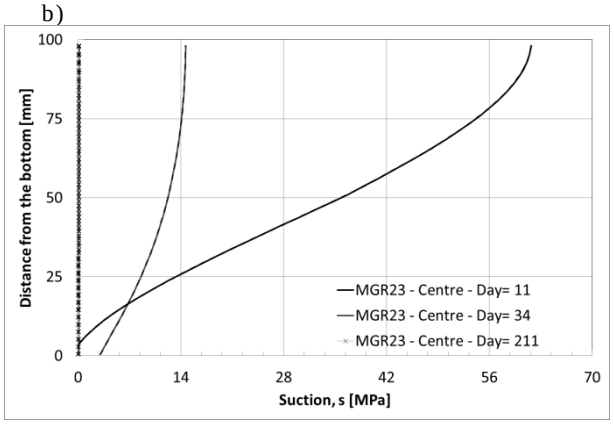

Fig. 6.48: Suction profiles for test MGR23. Comparison between numerical simulations a) "Reference" and b) "Plateau". Time steps are selected considering the beginning and the end of the experimental water intake plateau.

a)

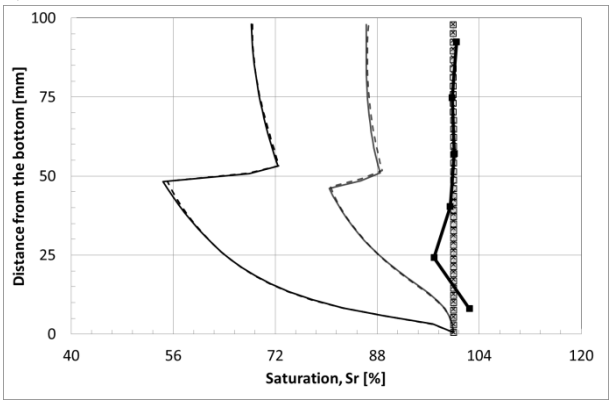

b)

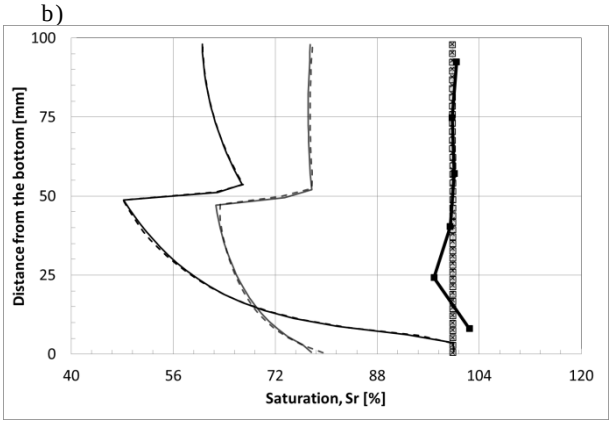

Fig. 6.49: Saturation profiles for test MGR23. Comparison between experimental data and numerical simulations at the final state. a) "Reference" and b) "Plateau. Time steps are selected considering the beginning and the end of the experimental water intake plateau.

The permeability and macro and total void ratio profiles are given in Fig. 6.50 and Fig. 6.51. The "Reference" macro void ratio decreases as saturation proceeds causing permeability decrease according to Eq. 3.29. The total and macro void ratios and permeability evolution of the "Reference" strategy was already described. Fig. 6.50 and Fig. 6.51 focus on the "Plateau" case. The very high void ratio (e=2) that is observed at the 11th simulation day suggests that a-kind-of liquefaction occurred in the pellets layer. At this stage, water is injected with a quite high rate, thus, the overpressure development could be expected. The permeability of the upper compacted block is much lower with respect to the one of the pellets part. Consequentially, water cannot be immediately transferred and it is all stored in the bottom part. Then, accordingly to the different permeabilities of the two layers, the water transfer mechanism takes place and overpressure is dissipated.

Hence, permeability profiles show that the intrinsic permeabilities of the block and pellets layers are quite different. Water is injected and mostly stored in the pellets part, which experiences the development of overpressure, a quite noticeable mechanical pressure decrease and a consequential void ratio increase. This latter occurrence generates a remarkable increase of macro void ratio and permeability. It can be noted that after the water intake plateau (i.e. 34th simulation day), this phenomenon disappears with the redistribution of pore-water pressure accordingly to a-kind-of Terzaghi consolidation theory.

The final permeability and macro and total void ratios distributions are similar in the two cases.

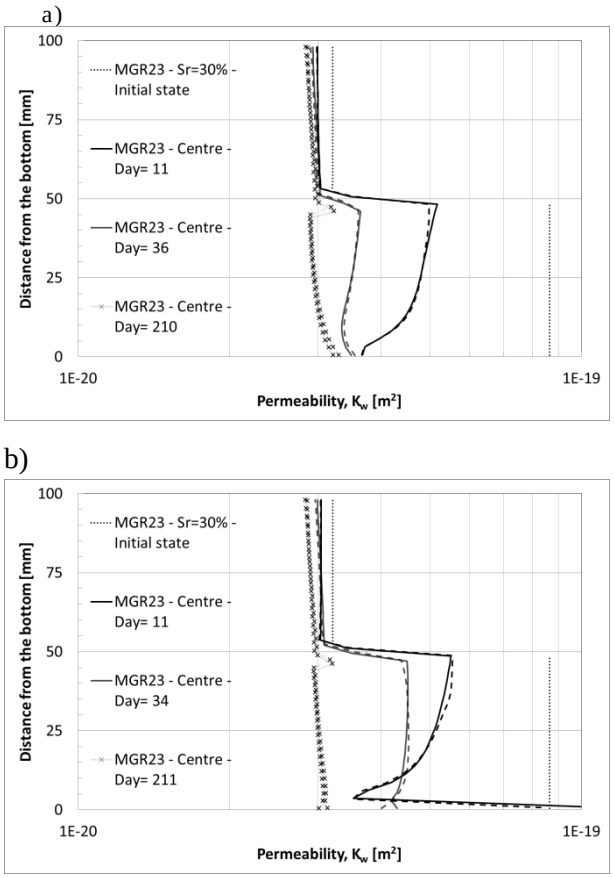

Fig. 6.50: Permeability profiles for test MGR23. Comparison between numerical simulations a) "Reference" and b) "Plateau". Time steps are selected considering the beginning and the end of the experimental water intake plateau.

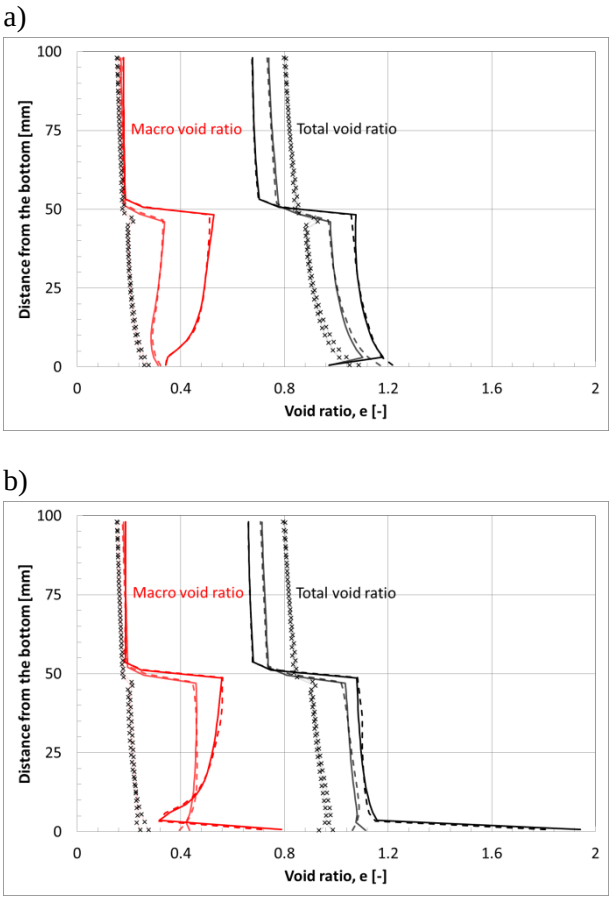

Fig. 6.51: Total and macro void ratios profiles for test MGR23. Comparison between experimental data and numerical simulations at the final state a) "Reference" and b) "Plateau". Time steps are selected considering the beginning and the end of the experimental water intake plateau.

Fig. 6.52 and Fig. 6.53 present the dry density and water content distributions. Experimental results for the final state and numerical outcomes for intermediate and final are compared. The block layer dry density and water content evolutions are quite similar in the two numerical strategies. The pellets part is characterised by different features. For the "Plateau" strategy, the above-mentioned liquefaction leading to an incredibly volume increase can be observed at the 11th simulation day. At day 34, this phenomenon has dissipated. Apart from this strongly localised event, differently from the "Reference" case, this numerical strategy implies a more homogeneous dry density (and water content) evolution, which does not account the gradients characterising the other cases. This numerical strategy provides results in terms of features development mostly similar to the ones related to test MGR22.

The final numerical distributions of dry density and water content are quite similar but slightly closer to the experimental ones for the "Plateau" strategy.

a)

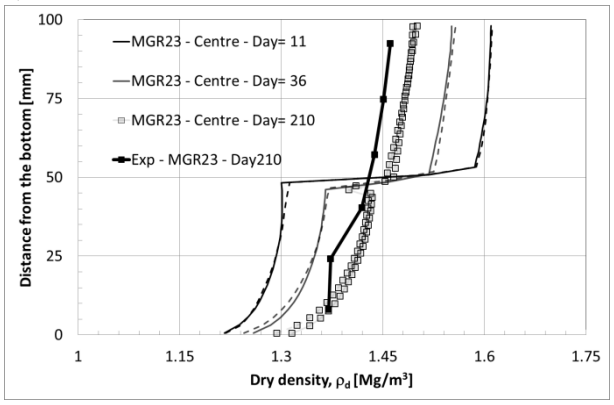

b)

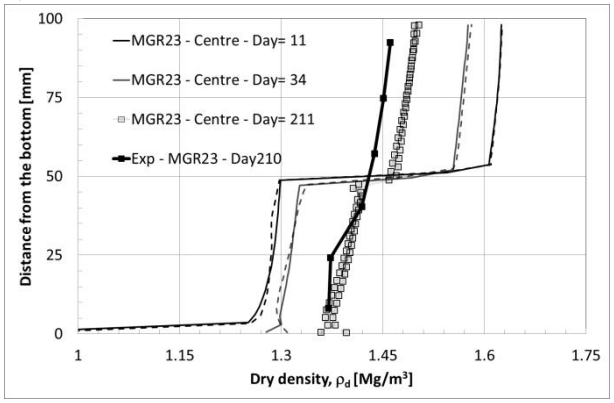

Fig. 6.52: Dry density profiles for test MGR23. Comparison between experimental data and numerical simulations at the final state a) "Reference" and b) "Plateau". Time steps are selected considering the beginning and the end of the experimental water intake plateau.

a)

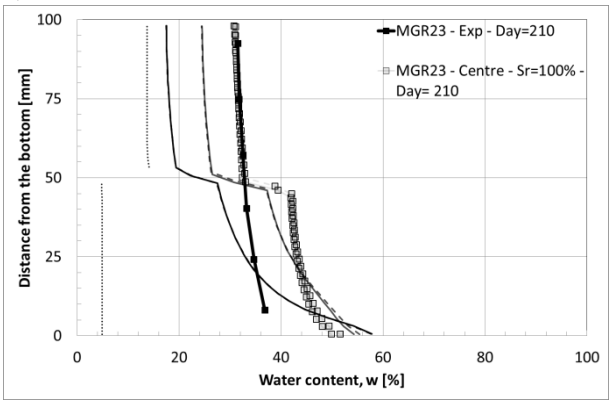

b)

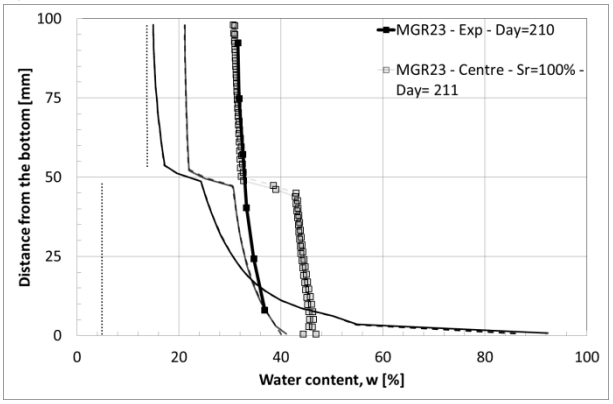

Fig. 6.53: Water content profiles for test MGR23. Comparison between experimental data and numerical simulations at the final state a) "Reference" and b) "Plateau". Time steps are selected considering the beginning and the end of the experimental water intake plateau.

6.4. Conclusions

The aim of the present research was to examine hydro-mechanical phenomena taking place during the interaction of the different assemblies between them and with the experimental tools upon hydration. This was done by taking advantage of a combined experimental and numerical approach. Such a study was performed especially to assess the combination in the same barrier of pellets and blocks of compacted bentonite, whose initial dry densities and structures noticeably differ as one of the possible sources of bentonite heterogeneity.

The analysed CIEMAT experimental campaign considered a variety of material configurations and hydration boundary conditions, as well as provided interesting clues about intermediate saturation states.

In parallel, exhaustive numerical analyses were proposed. Those allowed a precise comprehension of the dispersion related to swelling pressure measurements of the laboratory tests especially thanks to the modelling of friction between the material samples and the cell wall.

The results of this investigation showed that such heterogeneous material combinations affect undoubtedly the distribution and the development of swelling pressure of a given bentonite assembly with respect to the constraining environmental. The location of the measurement instruments, in particular, is highly influenced by such a stress distribution, resulting, sometimes, in unpredictable results. The water transfer mechanism (i.e. the permeability) clearly depicts that the combination of pellets and block layers plays a major role in the determination of the full-saturation time. In line with this, the dry density and water content evolutions and distributions were affected by the initial heterogeneity configurations. This also could be particularly observed by the comparison between tests MGR23 and 27.

Together with the preceding findings, the numerical analysis mainly focused on the role of friction development between the material samples and the cell wall. This study provided an improved understanding on the dispersion of experimental data by highlighting the relevance of frictional phenomena on the pressure measurements results. A sensitivity analysis on the influence of the friction coefficient was performed resulting in the proposition of a given friction coefficient in the framework of the adopted Mohr-Coulomb modelling strategy.

Also the effects of the numerical boundary conditions were studied. This particular numerical choice implies different evolution kinetics of the intermediate physical states of the samples.

The good agreement between the numerical results and the experimental data, both qualitatively and quantitatively, allowed validating the developed hypothesis and the prediction capability of the model especially with respect the hypothesis of friction development between the sample and cell wall during the tests.

However, it is important to remind that the adopted numerical models represent a simplification of the reality complexity, which provide interesting and complementary information, those have to be completed with further and more advanced experimental campaigns.

CHAPTER 6: MULTI-STRUCTURE ASSEMBLIES COMBINATIONS AT LABORATORY SCALE

CHAPTER 7: MULTI-STRUCTURE ASSEMBLIES COMBINATION AT REAL SCALE

– THE EB EXPERIMENT -

CHAPTER 7: MULTI-STRUCTURE ASSEMBLIES COMBINATIONS AT REAL SCALE

– THE EB EXPERIMENT -

7.1. Introduction

The aim of this chapter is to analyse and replicate a large-scale in-situ test in order to assess the feasibility of the numerical model for the nuclear waste disposal safety evaluation and long-term sealing behaviour prediction.

It was shown in the previous chapters how heterogeneous density distribution, porosities structures distribution, hydraulic boundary conditions and swelling pressure development result already at the lab scale of difficult prediction.

Consequentially, since laboratory tests and constitutive numerical models are mainly developed for the safety assessment of large scale sealing structures in the context of nuclear waste disposals, the gained understanding is employed for the analysis of a real scale test.

For this purpose the Engineered Barrier (EB) test was selected. This experiment was a demonstration test accounting for the simultaneous combination of granular bentonite mixture (also indicated as pellets mixture in the following) and bentonite compacted blocks, run in Mont Terri URL between 2000 and 2014.

Very few large scale tests are available due to the very long testing time and emplacement difficulties.

The EB test presented a quite extensive instrumentation system, which recorded the bentonite buffer response during hydration. Further post-mortem in-situ and laboratory analyses were performed for the evaluation of the saturated buffer homogenisation state.

The hydro-mechanical numerical model presented in the previous chapters is adopted. Since the EB test considered the same Febex bentonite in pellet mixtures and compacted blocks already analysed in the CIEMAT tests, the same calibrated set of hydro-mechanical parameters is taken in consideration.

Hence, the EB test is modelled. The numerical strategy considers a simplified configuration in order to emphasise the hydro-mechanical processes taking place inside the bentonite plug and the interaction between the different bentonite assemblies (i.e. the host-rock is not modelled).

The capabilities of the numerical model are evaluated as well as the suitability of the selected hypotheses thanks to the comparison with the experimental data. A number of scenarios are also presented: the role of permeability and initial heterogeneous dry density distributions are emphasised.

The complexity of large scale structures numerical modelling is clearly represented.

7.2. Materials

This large scale test presents the same materials combination as the one considered in CHAPTER 6. Hence, Febex bentonite pellets mixtures and compacted blocks, whose initial dry densities (1.35 Mg/m^3 and 1.7 Mg/m^3) and structures noticeably differ are analysed (Lloret and Villar 2007a).

Febex bentonite pellets consisted in powder that is preheated and then compacted by a roller press. The compaction results in the formation of very high dry density granules of various sizes (between 0.4 mm and 15 mm). Accordingly to the formation of such granules, this pellets mixture is also often named ***granular bentonite mixtures (GBM)***. Hence, both terminologies will be adopted indiscriminately. The pellets material presented low water content equal to w=3.3%. The Febex compacted blocks were obtained via compaction from the granulate material with its hygroscopic water content, which was ~14%.

7.2.1. Water retention behaviour

The selected double porosity dry density dependent water retention model does not distinguish the initial pore structure distributions of the considered assemblies, thus a unique set of parameters corresponding to the calibration proposed by (Dieudonné, Della Vecchia, and Charlier 2017) for Febex bentonite is selected (Fig. 7.1 and Table 7.1).

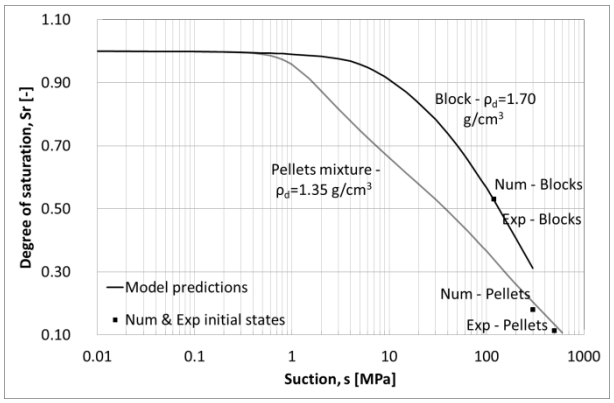

Fig. 7.1: Model prediction for the water retention curve. Initial experimental data and initial numerical data.

Table 7.1: Parameters of the water retention curve model.

		Compacted block	Pellets mixtures
ρ_d	$[Mg/m^3]$	1.70	1.35
e_{m0}	[-]	0.35	
β_0	[-]	0.15	
β_1	[-]	0.35	
C_{ads}	$[MPa^{-1}]$	0.0028	
n_{ads}	[-]	0.78	
n	[-]	3	
m	[-]	0.15	

A	***[MPa]***	0.24

7.2.2. Flow properties

In the context of EB laboratory tests, it was found that during early saturation, the pellets mixture presented a very high initial permeability, but as the pellets swelled and the large pores structures of the mixture collapsed, the permeability dropped dramatically. The selected permeability law evolution reproduces this feature. Moreover, according to the laboratory measurements, the saturated hydraulic conductivity of the pellets mixture was identified lower than 5×10^{-19} m^2 for a dry density of ρ_d=1.35 Mg/m^3.

Consequentially, in order to study the influence of permeability on the model response, this work accounts several strategies concerning the permeability evolution of the buffer components.

The parameters for the macro-void ratio water permeability dependent law (Table 7.2 and Fig. 7.2) were calibrated by best-fitting the responses of the water intake time evolution of test MGR23 of the CHAPTER 6, which considered the same materials type. Constant permeabilities are also considered in alternative simulations as it will be seen in the follow.

Finally, the model is validated by comparing the swelling pressure kinetics and final dry density and water content distributions.

Table 7.2: Parameters of the permeability evolution model for each numerical strategy(named in the following Num – 1, Num – 2 and Num – 3).

		Compacted block		**Pellets mixtures**	
		Num – 1 & 2	**Num – 3**	**Num – 1**	**Num – 2 & 3**
C_k	**[m^2]**	2.8×10^{-20}	1×10^{-21}	2.8×10^{-20}	1×10^{-15}
expm	**[-]**	1.2	-	0.9	-
expn	**[-]**	0.1	-	0.1	-
γ	**[-]**	3.4	3.4	3	3

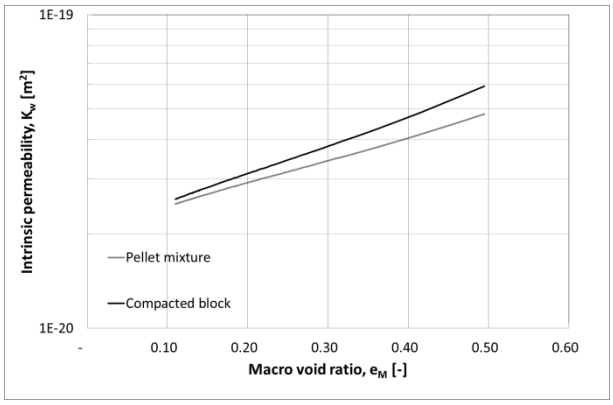

Fig. 7.2: Intrinsic permeability evolution with macro-void ratio accordingly to **Eq. 3.29** and Table 7.2.

7.2.3. Mechanical behaviour

The mechanical parameters (for this and for the preceding chapter, in this and in the preceding chapters.

Table 7.3) were derived in CHAPTER 4 from the experimental campaign performed by (Lloret et al. 2003) on a similar dry density compacted Febex bentonite, whereas for the Pellets layer, data from (Hoffmann, Alonso, and Romero 2007) were adapted. The selection of these mechanical parameters was also validated in CHAPTER 6. In this test case, preliminary simulations evidenced the occurrence of softening at the interface between the blocks and the pellets mixture. At this location very large shear strain was found. Consequentially, it was decided to modify the cohesion and the parameter *k* (parameter controlling the increase of cohesion for increase in suction) for one row of elements in the compacted blocks domain at the boundary with the pellets mixture. The yielding surface for these elements resulted in a much larger ellipse with respect to the reference one. This bentonite portion is quite limited with respect to the overall sealing surface, thus, it was assumed that likely it does not affect the global response of the buffer.

Mechanical parameters such as the friction angle, Poisson ratio and cohesion are in general very difficult to measure during experimental campaigns on swelling unsaturated bentonites (especially with respect to pellets mixtures) and very few data are available. Due to this, a trial and error procedure was adopted to reproduce the target results in terms of the swelling pressure measurements presented in this work in this and in the preceding chapters.

Table 7.3: Parameters of the mechanical model.

		Compacted block	**Compacted block (1 row elements at the border with pellets)**	**Pellets mixture**
ρ_d	[Mg/m^3]	1.70		1.35
κ	[-]	0.012		0.074
κ_s	[-]	0.12		0.075
α_p	[-]	4.4×10^{-8}		3×10^{-6}
p_0^*	[MPa]	1.6		0.65
p_c	[MPa]	0.395		0.325
$\lambda(0)$	[-]	0.12		0.20
r	[-]	0.55		0.70
ω	[MPa^{-1}]	0.25		0.008
φ	[°]	20		26
ν	[-]	0.25		0.35
$c(0)$	[MPa]	0	1	0
k	[-]	0.0046	0.046	0.0046

7.3. The EB experiment

7.3.1. Description of the tests

The EB Experiment was one of the first basic tests to demonstrate the feasibility of the proposed design of combining bentonite blocks and pellets mixture in real scale structures. It was carried out in a 6-m-long portion of a niche excavated in the Mont Terri URL (Mayor et al. 2005). The EB Experiment implied the emplacement of a bentonite buffer consisting of pellets in the upper part and bentonite blocks at the bottom in a horizontal drift (Fig. 7.3). The test included a steel dummy canister that was placed on top of the bentonite blocks and had the same dimensions and weight as in the Swiss concept. An artificial hydration system was installed to speed up the bentonite saturation process. A concrete plug was used to seal the test section. The Experiment began in October 2000 and was completed between October 2012 and February 2013 (Villar, Campos, and Gutiérrez-Nebot 2014).

The EB Experiment's goals were:

- to describe the GBM (composition and grain size distribution) and demonstrate its development at a semi-industrial scale;

- to investigate the GBM's hydro-mechanical properties;

- to design GBM emplacement technique and demonstration;

- to ensure at a sufficiently high dry density at GBM emplacement and that the disposal concept is technically feasible;

- to characterise the evolution of the Opalinus Clay EDZ;

- to track the clay barrier's and rock's hydro-mechanical behaviour during the hydration phase.

In this chapter, attention is focused on the large scale in-situ hydration of bentonite based materials composing the buffers. Thus, all the prior laboratory and emplacement tests on GBM will not be exhaustively detailed but only mentioned to explain some relevant analysis characteristics.

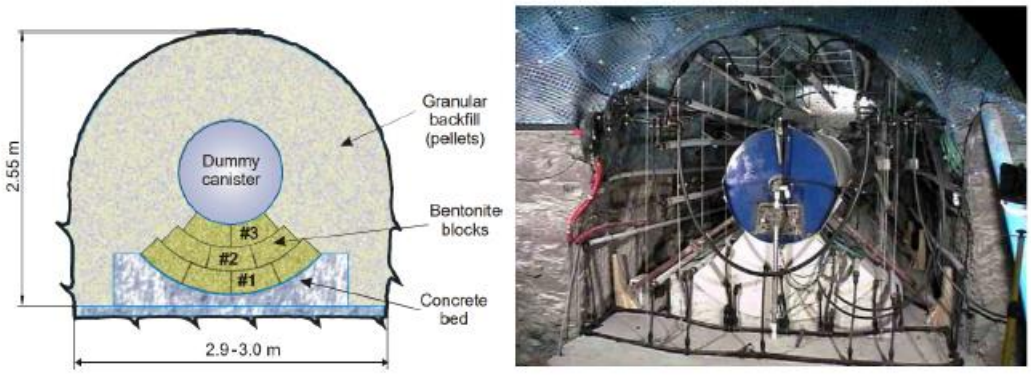

Fig. 7.3: Layout of the EB Experiment and photograph of the experiment prior to installation of the GBM (Mayor et al. 2005).

Similarly, the host-rock OPA features will not be taken into consideration. It is considered as very rigid, so not affecting the displacements, and with a very low permeability, with a much lower contribution to the hydration with respect to the artificial system.

For the pellets casting, in trials, conveyor, auger, and pneumatic emplacement methods were tested. The use of auger systems was preferred with respect to the conveyor and pneumatic methods. Indeed, a significantly higher dry density of ρ_d=1.45 Mg/m^3 was obtained for GBM emplaced using auger, avoiding dust issues. With the chosen auger, the GBM emplacement in the EB Experiment was completed in four days. The total mass displaced was 40.2 tons in a volume of approximately 28.4 m^3. Since the GBM had an average water content of 4.2%, the emplaced material presented an approximate dry density of ρ_d=1.36 Mg/m^3. The existence of artificial hydration tubing and other technological obstacles in the test section, which limited auger movements and activity, was thought to be the cause of the lower dry density obtained in the Experiment compared to the trials and its inhomogeneous distribution in the section. This feature was has also been observed during the emplacement of GBM in another large scale test (Köhler et al. 2015). Dry density heterogeneous distribution could be observed thanks to gamma-gamma and dielectric measurements, which were mostly due to the emplacement technique. It could be indeed observed that the lowest dry density value was detected for a narrow material portion (10-20 cm) at the upper part of the barrier in the vertical direction (equal to ρ_d=1.20 Mg/m^3), while, quite homogeneous dry density values were found for the remaining height toward the bottom equal to ρ_d=1.50 Mg/m^3 (80-90 cm).

The bottom bentonite blocks, coming from the FEBEX project, presented dry density of ρ_d=1.69 Mg/m^3 and water content w=14.36 %. The bentonite blocks bed was composed by three layers as Fig. 7.3 shows.

The artificial EB hydration system was divided into two parts: a test area and a service area. Hydration tubes and geotextile hydration mats composed the hydration system. Namely, in a three-layer configuration, 37 injection tubes were used. In order to favour water distribution, a pervious mat was used to cover the tubes, canister, and bentonite blocks. The hydration process consisted in four phases:

- first stage: 6.7 m^3 of water were injected inside the tunnel in two days. Leakage was observed.
- second stage: artificial hydration was stopped for 126 days. Moisture redistribution was allowed inside the plug.
- third stage, artificial hydration was resumed under controlled flux conditions;
- fourth stage: only natural hydration from the Opalinus was allowed.

It is evident that such hydration system would be very complex to reproduce with accuracy in a numerical model. Moreover, it would be characterised by a large uncertainties level.

The water used was synthetic and its composition was chemically equivalent to the Opalinus Clay formation water.

To monitor the relative humidity, temperature, pore and total pressure and displacements, sensors were installed in different sections along the niche (instrumented sections in Fig. 7.4). The idea was to be able to monitor buffer evolution and also the rock mass evolution around the niche. So, several types of sensors were installed. For instance, in the buffer there could be found:

- 8 Capacitive humidity sensors in sections B1 and B2;
- 8 Total pressure cells in section E;
- Extensometers in sections A1 and A2 (for canister displacements);

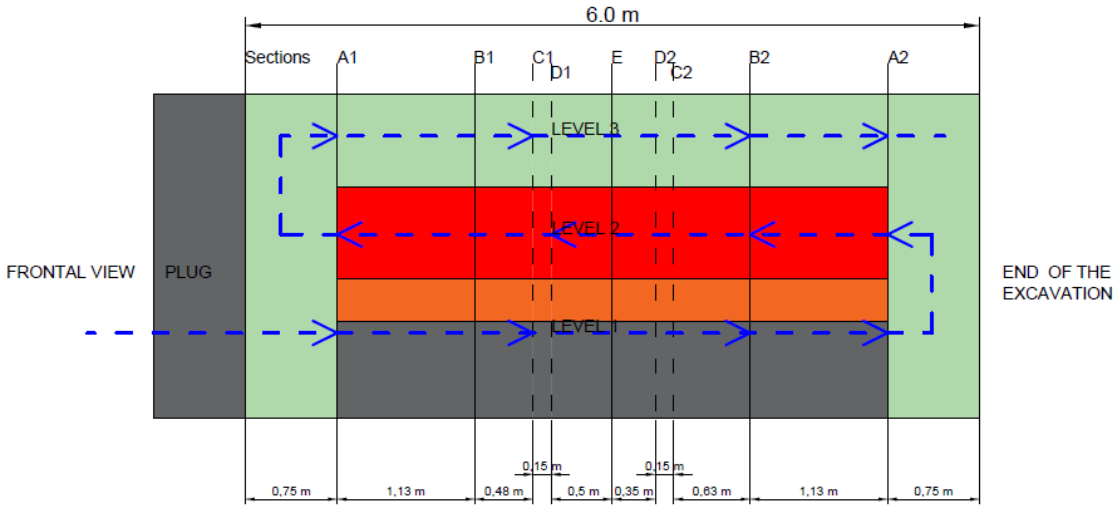

Fig. 7.4: Longitudinal section of the barrier.

7.3.2. Features of the analysis

The EB configuration consists in a horse-shoe shape excavation, 2.65 m high, 2.9 m large and 6 m long.

The EB experiment's real geometry is complex and three-dimensional effects exist. Because of gravity and emplacement techniques, the pellets mixture sealing distribution homogeneity is not guaranteed in real conditions. In addition, the presence/absence of the canister and concrete bed affects the action of the bentonite plug longitudinally.

In this modelling strategy, plane strain conditions are taken into account and only half domain is considered, with a vertical symmetry axis coinciding with the plane cutting the buffer at the centre. Given the 2-D geometry of the problem, only one cross section is modelled and the results are relative to that representative section.

The current modelling strategies focus on the strongly coupled hydro-mechanical processes taking place during bentonite buffer saturation. Thus, the Opalinus clay and the tunnel excavation phase are not considered and the buffer hydration takes place directly. It is considered that the water exchanges between the buffer and the Opalinus Clay do not play a major role. Moreover, Opalinus clay is considered rigid. Gravity is not taken into consideration either. Its driving force is assumed to be much lower with respect to the suction one.

The concrete is considered as a perfectly rigid element representing a mechanical constraint for the bentonite materials. water exchanges between the bentonite buffer and the concrete bed can be neglected due to the very low permeability of the concrete and to the major relevance of the artificial hydration system.

Consequentially, it is decided to model the mechanical interaction between the bentonite-based materials and concrete bed via an interface element (Fig. 7.5). With such a strategy, the bentonite elements can slide in the tangential direction of the interface, so that possible shear and tensile stresses, which would occur with a sticking contact with a very rigid concrete bed, are avoided. The interface element is described in (Cerfontaine et al. 2015) and APPENDIX B.

The choice to consider only the bentonite components has been made in order to focus only on the processes taking place during the artificial hydration,

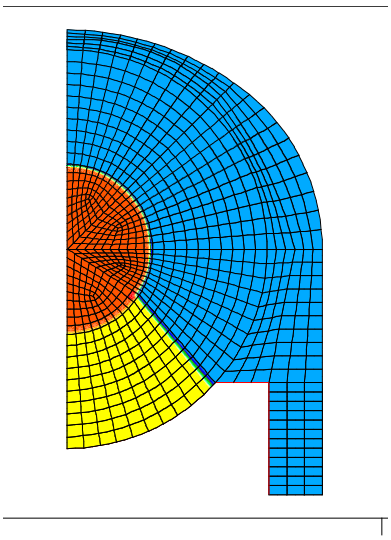

Fig. 7.5: FE mesh of the modelled domain of the EB test.

The mesh consists in 1532 8-noded iso-parametric elements. The 8-noded iso-parametric elements represent the canister, the bentonite blocks, the bentonite pellet mixture and the SUCHT elements allowing the

application of the uniform water flux on the bentonite surface. This modelling strategy considers also 25 2-noded iso-parametric elements representing the interface itself. Table 7.4 reports the number of element of the mesh.

Table 7.4: Number of elements of each component of the EB modelled test.

	Number of elements
Canister	3006
Interface element	25
Bentonite blocks	100
Bentonite pellet mixture	516
Sucht	616
Total	1557

Canister

The mechanical behaviour of the canister used in the numerical simulation is considered as linear elastic. The input mechanical parameters are presented (Table 7.5).

Table 7.5: Mechanical parameter selected for the canister.

	Young modulus	**Poisson ratio**
	E	**ν**
	[GPa]	**[-]**
Canister	0.3	0.3

Concerning the hydraulic constitutive behaviour of the canister, it is considered impermeable. This component does not provide water to the buffer. Namely, there is not water exchange.

Interface element

An interface (Cerfontaine et al. 2015) is modelled with 25 2-noded iso-parametric elements in order to reproduce the interaction between the bentonite materials and the concrete bed (green line Fig. 7.7).

Friction is considered, so that, the interface at the same moment represents a normal constraint and prevents the bentonite blocks to freely slide in the tangential direction.

The longitudinal and transversal transmittivity of the interface is supposed to be null. (i.e. there is no water exchange between the interface and the bentonite nor longitudinal flux into the interface itself).

Hence, the total stress formulation is selected for the mechanical constitutive model of the interface element. The interface mechanical parameters are presented.

Table 7.6: Interface mechanical properties.

Penalty coefficient in the normal direction	K_t	**[N/m^3]**	10^8
Penalty coefficient in the longitudinal direction	K_l	**[N/m^3]**	10^8
Friction angle	φ	**[°]**	14

6 The canister element number choice derives from mesh priorities. It does not affect the computation time.

Friction coefficient	μ	**[-]**	0.250
Cohesion	c'	**[MPa]**	0

Initial and boundary conditions

The presented numerical modelling of EB considers only the artificial hydration phase of the barrier.

A horizontal zero-displacement condition is imposed on the vertical boundary on the symmetry axis and the straight right side of the domain. On the curved area of the excavation the displacement is equal to zero in both vertical and horizontal direction. This means that no sliding can occur in this zone. On the interface, which is defined on the lower boundary of the domain, the bentonite can slide during the deformation (Fig. 7.7).

The pellets mixture presents an initial suction equal s=300 MPa and a corresponding initial saturation Sr=18%, whereas the blocks report a value equal to 120 MPa and an initial saturation Sr=53%. The numerical and experimental initial states of the pellets mixture components slightly differ (s=500 MPa and Sr=11% for pellets mixture experimental initial state). This numerical choice was done due to the fact that such high suction level could lead to numerical computation instabilities. With respect to the initial water content, it was computed that in the entire buffer only 1 m^3 of water of initial difference was found due to the different saturation levels in the pellets (Num S_r=18% and Exp S_r=11%).

The initial stress is set equal to zero.

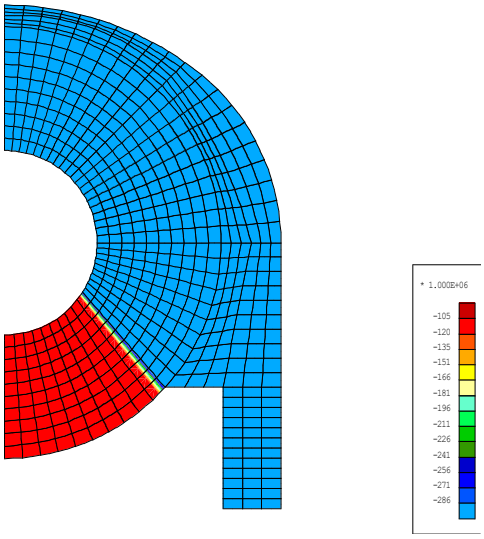

Fig. 7.6: Pore water pressure initial conditions in the barrier [Pa].

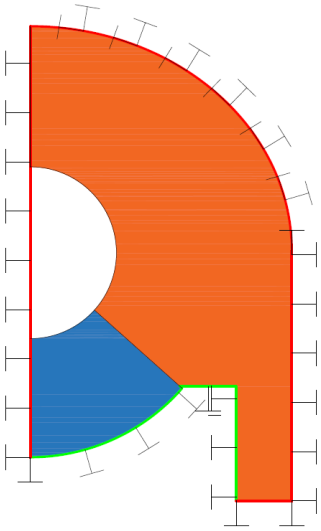

Fig. 7.7: Displacement boundary conditions.

The driving force of the bentonite buffer evolution is the water intake. However, the experimental conditions are not easy to interpret. During a first short phase, a quick hydration was applied, but some leakage was observed. As the water is injected trough tubes with opening, it is very concentrated, but the exact repartition in the whole domain is not known. For these reasons, it is decided to inject a reasonable volume of water, following a time history and a spatial repartition as credible as possible, but without trying to reproduce all the experimental hydration complexity. The re-saturation of the barrier has been modelled considering the hypothesis of a uniform surface hydration of the buffer with imposed injection rate (neglecting the system of

tubes and the geotextile). The experimental water intake records of the barrier and the numerical ones are represented in Fig. 7.8. The evaluation of the amount of water to be injected is detailed in APPENDIX C.

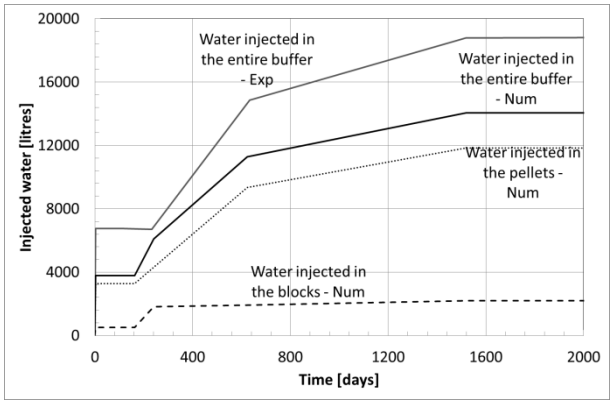

Fig. 7.8: Experimental and numerical water intake time evolution.

The final total water amount injected in the buffer is equal to ~14 m^3 and not equal to 19 m^3 as the experimental measurements suggest. This discrepancy corresponds to the fact that the system that is modelled in this numerical strategy is closed and does not consider water exchange with the surrounding components. On the other hand, it is not negligible that during the EB experiment, it was not possible to carefully control the water injection. The available experimental data correspond to the injection of water in the entire system (i.e. bentonite components, concrete bed and plug, host-rock…), in which it can be easily demonstrated (also from post-mortem analyses) that the hydration process takes place in a non-uniform way due to the non–controllable hydration system but also due to the non–controllable heterogeneity of the buffer itself (which for example presents heterogeneous dry density distribution).

The following analysis offers 3 cases with different initial and boundary conditions both for pellets permeability evolution and the dry density distribution in the pellets mixture. Comparisons between reference case and alternative formulations will allow investigating the effects of non-uniform dry density distribution and non-uniform hydration evolution in order to better understand the role of potential heterogeneity in the barrier. Hence, the following scenarios will be analysed and compared:

- **Case 1** (reference case). This modelling strategy presents uniform dry density distribution with an initial value equal to ρ_d=1.35 Mg/m^3 and macro-void ratio permeability dependence in both pellets and compacted blocks (Fig. 7.9).The permeability laws evolution were calibrated in the CHAPTER 6 on the same material types.

- **Case 2** also accounts for uniform dry density distribution with an initial value equal to ρ_d=1.35 Mg/m^3 and macro-void ratio permeability dependence in compacted blocks, but constant permeability value equal to $K_w=1\times10^{-15}$ m^2 in pellets (Fig. 7.10). This value for the pellets permeability was suggested by a number of previous researches ((Alonso, Hoffmann, and Romero 2010),(Hoffmann, Alonso, and Romero 2007)). This case aims to demonstrate the influence of pellets permeability in the response of the full barrier;

- **Case 3** concerns a case in which a non-uniform dry density distribution in the pellets mixture is assumed (ρ_d=1.28 Mg/m^3 for the red zones in Fig. 7.11 and ρ_d=1.36 Mg/m^3 for the yellow ones) in order to simulate the non-homogeneous initial state due to the mixture emplacement. (Köhler et al. 2015) demonstrated indeed that automatized emplacement techniques lead low density material on

the top of the sealing (ρ_d=1.20 Mg/m^3) and quite constant distribution in the central part (ρ_d=1.50 Mg/m^3) of the buffer in the vertical direction. Homogeneous initial and final dry density distribution is a key issue for the safety assessment of nuclear waste disposals sealing and it was shown that it is not often reached in real scale structures. Constant permeability in blocks and pellets equal respectively to $K_w=1\times10^{-21}$ m^2 and $K_w=1\times10^{-15}$ m^2 are adopted.

Despite the uniform hydration surface analysis allows minimizing the role of bentonite permeability, it represents a very important point to be discussed.

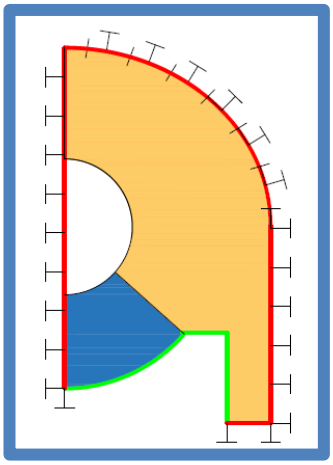

Fig. 7.9: Configuration Case 1 (reference case).

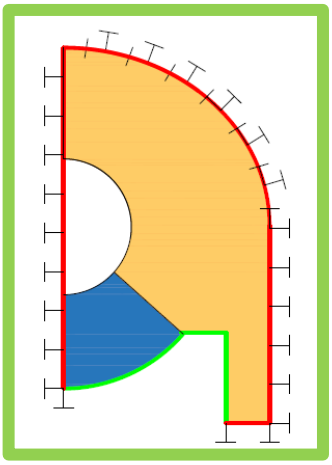

Fig. 7.10: Configuration Case 2 (constant permeability in pellets).

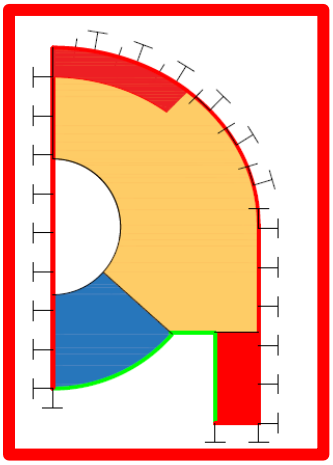

Fig. 7.11: Configuration Case 3 (non-uniform dry density distribution).

7.3.3. Experimental and numerical results

Suction and saturation degree

8 relative humidity sensors were placed into the buffer, 4 in section B1 and 4 in section B2 (Fig. 7.4) respectively, 4 in blocks and 4 in pellets. Section B1 and section B2 are far 1.90 m and 4.20 m from frontal view of the excavation and so from the hydration system "beginning" and 2.26 m distant one from each other. Fig. 7.12 and Fig. 7.13 report the suction evolution of the measurements point placed in the compacted blocks and the pellets mixture respectively for section B1 and B2.

Experimental results - Pellets (sensors 11, 12, 21, 22)

In section B1 (Fig. 7.13), the suction in the pellets mixture immediately decreases. This means that a remarkable quantity of water arrives in this location. This occurrence is not consistent with the hydration system design. The hydration occurs from the bottom, so the points to be immediately hydrated are the ones located in the compacted blocks (level 1, firstly WB13 and WB14 and then WB23 and WB24). Successively, the hydrations continues on level 2, from the end of excavation toward the concrete plug (therefore WB21 and WB22 first and successively WB11 and WB12). Contrarily, it can be observed that the points in which the suction immediately decreases are WB11 and WB12, those ones should be the last to get full saturation. The suction decreases from 500 MPa to 50 MPa. Successively, the suction increases probably due to water redistribution inside the sealing. For point WB11 the full saturation occurs after 900 days whereas for point WB11 after 170 days, i.e. just after the beginning of the second injection phase (the one in which the pore water pressure is fixed, starting 130 days after the backfill emplacement).

During the first injection of 6.7 m^3, the hydration system fails and this could represent the reason why points WB11 and WB12 present such different full-saturation time despite they are at the same level and they should be hydrated simultaneously. The reason could also be related to the different proximity to the water injection points. However, the experimental suction measurements recorded in the pellets mixture do not seem to be reliable.

Concerning section B2, for WB21 and WB22 (pellets), the suction does not decrease immediately as observed for section B1. The hydration is slower with respect to WB11 and WB12. In WB21, the suction decreases slightly after the first injection then it reaches the steady state until the second injection (130 days after the emplacement). The full saturation is reached after 400 days. For WB22, the suction decreases continuously until the 400^{th} day in which the suction starts to decrease faster. For the points WB23 and WB24 located between the compacted blocks, the trend is actually the same with respect to WB13 and WB14.

Experimental results - Blocks (sensors 13, 14, 23, 24)

For points WB13 and WB14, the suction decreases slowly and similarly. There is a first phase, just after the 6.7 m^3 injection, in which the suction decreases until the 100th day. Then the suction stabilises to an almost steady value and it decreases again when the second hydration phase begins (130th day after the backfill emplacement). The full saturation of these locations occurs approximately after 200 days since the emplacement. Point WB13 saturates slightly later with respect to point WB14 (probably because of gravity effect). However, despite point WB13 and WB14 present suction s≈0 MPa, the whole assembly of the compacted blocks is far from hydration. In this context, it is worth to mention two things: the first one is that the sensors are immersed into the mat layers (preferential pathway for water) between the blocks (where water is injected). The second is that the compacted blocks present a dry density ρ_d=1.7 Mg/m^3, with a very low permeability (K_w=1×10^{-20}±1×10^{-21} m^2). Therefore, in order to obtain the full saturation of the blocks assembly larger time is needed and surely the full saturation does not occur in the first 2 days of hydration.

Numerical results

The numerical results are able to well reproduce the experimental data. The water injection in the compacted blocks has been calibrated in order to reproduce the average experimental suction decrease in the compacted blocks. The numerical suction decrease in the pellets mixture reports a value in between the experimental measurements, testifying the fact that the pellets mixture presents in reality a permeability that allows an immediate and almost uniform water distribution. The numerical measurements points in the compacted blocks (WB3 & WB4) and in the pellets mixture (WB1 & WB2) present the same suction time evolution due to the adopted uniform hydration strategy, which allows reducing the importance of the permeability in the strong hydro-mechanical couplings taking place during the hydration of a bentonite buffer.

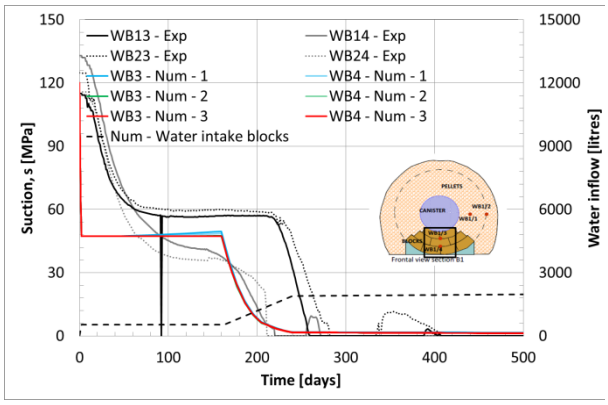

Fig. 7.12: Suction and numerical water inflow time evolution of sensors located in the compacted blocks. Comparison experimental VS numerical.

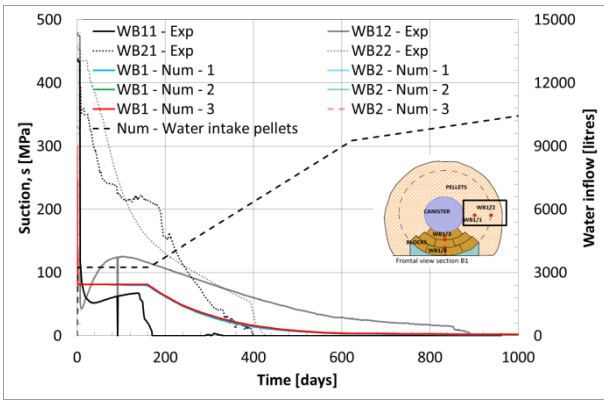

Fig. 7.13: Suction and numerical water inflow time evolution of sensors located in the pellets mixture. Comparison experimental VS numerical.

However, it is worth noting that the 3 strategies suction evolutions do not differ one from each other, even though the permeability of the pellets is different from case 1 to cases 2 and 3 and the permeability of the block differs from cases 1 and 2 to case 3 of several orders of magnitude (Fig. 7.14 and Fig. 7.15). Namely in cases 1 and 2, the compacted blocks permeability increases from K_w=2.8×10^{-20} m^2 to K_w=3×10^{-20} m^2 due to the volume increase. On the other hand, for case 3 it is constant and equal to K_w=1×10^{-21} m^2. The permeability of the pellets mixtures decreases from K_w=6×10^{-20} m^2 to K_w=3.1×10^{-20} m^2 due to the micro-structure evolution for case 1. For cases 2 and 3, the permeability is constant and equal to K_w=1×10^{-15} m^2. This means that the adopted numerical strategy for injecting water is fully controlling the time evolution of the hydration, and that permeability does not play any significant role with respect to suction decrease. However, the numerical time evolution seems consistent with experimental observations.

Fig. 7.14 and Fig. 7.15 also show the numerical saturation time evolution for the compacted blocks and the pellets mixture material, which is perfectly consistent with the imposed numerical water inflow (Fig. 7.12 and Fig. 7.13). The numerical strategy shows that the compacted blocks reach the saturation degree of 95% at the 240th day of the simulation time (far earlier than the pellets mixture).

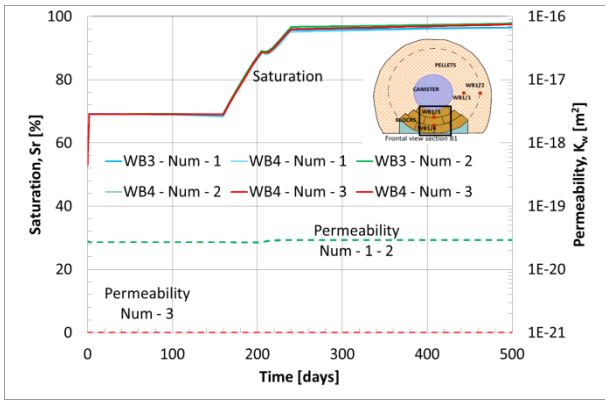

Fig. 7.14: Saturation and permeability time evolution of sensors located in the compacted blocks. Comparison numerical results.

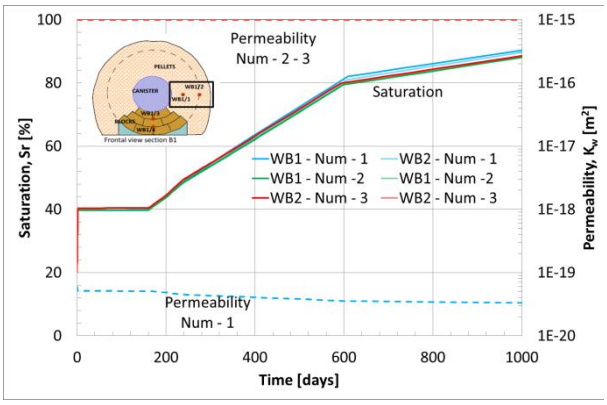

Fig. 7.15: Saturation and permeability time evolution of sensors located in the pellets mixture. Comparison numerical results.

Swelling pressure

8 total pressure cells are located in section E (Fig. 7.4). Section E is placed just in the middle between section B1 and section B2. Fig. 7.16 and Fig. 7.17 analyses the vertical total pressure measurements, whereas Fig. 7.18 and Fig. 7.19 the horizontal total pressure measurements. All the sensors show similar features: a quick pressure increase, a change of slope with slower or also negative pressure evolution and a final pressure increase up to stabilisation. Vertical measurements of PE1, PE2, PE5 and PE6 (Fig. 7.16 and Fig. 7.17) span between 1.75 and 2.25 MPa of total swelling pressure. Horizontal records of PE3, PE4, PE7 and PE8 (Fig. 7.18 and Fig. 7.19) are in general lower than the vertical measurements and show values ranging between 1.5 and 1.8 MPa. This is logical, as on a horizontal line only pellets with initial low density swell, while on a vertical line blocks with high initial density swell also. From a general point of view, it can be observed that all the total pressures stabilise after 1500 days since the emplacement of the sealing. Therefore, it can be assumed that the backfill is fully saturated at this stage (and not when the RH sensors detect full saturation). However, as depicted in Fig. 7.8, there is still water injection at low pore-water pressure (0.02 MPa kept constant for approximately one year).

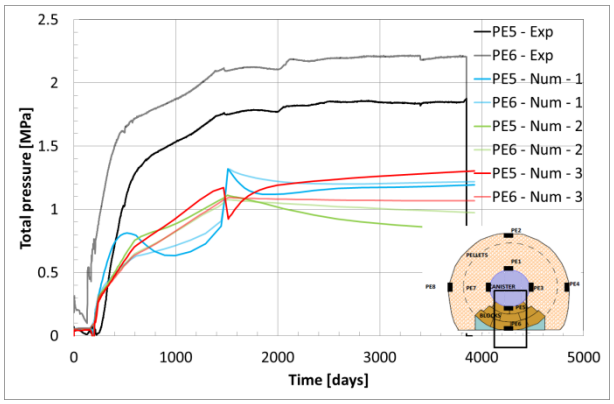

Fig. 7.16: Vertical total stress time evolution for sensors PE5 and PE6. Comparison experimental VS numerical.

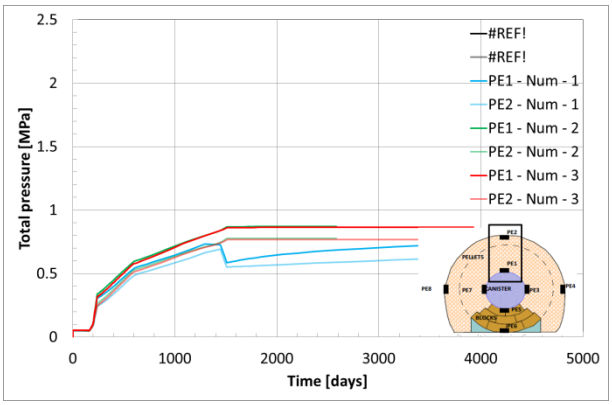

Fig. 7.17: Vertical total stress time evolution for sensors PE1 and PE2. Comparison experimental VS numerical.

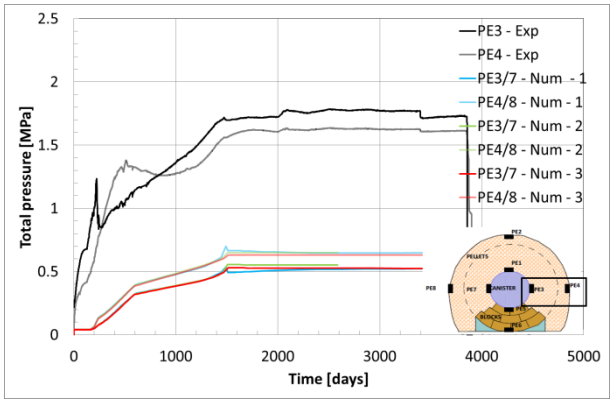

Fig. 7.18: Horizontal total stress time evolution for sensors PE3 and PE4. Comparison experimental VS numerical.

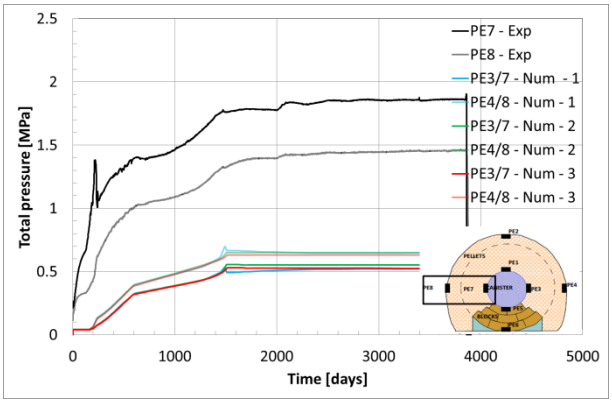

Fig. 7.19: Horizontal total stress time evolution for sensors PE7 and PE8. Comparison experimental VS numerical.

The numerical results are quite able to well reproduce the non-monotonic increase of the swelling pressure in the buffer but the final values are different. The final pressures are underestimated of half of the measured ones. The final stabilised values do not differ sensitively between the three strategies. Vertical stresses in PE5 and PE6 range between 0.8 and 1.25 MPa. The numerical sensors PE1 and PE2 present values between 0.6 and 0.9 MPa. Horizontal records are all equal to 0.5 and 0.6 MPa. Measurements in PE1, PE2, PE3/7 and PE4/8 are also characterised by the same evolution. The strongly underestimated pellets swelling pressure values may be possibly related to an erroneous compressibility pellets features selection. If one side, predictions for laboratory tests presented in CHAPTER 6 provided remarkably results, due to the fact that swelling mechanisms were mainly controlled by Febex compacted blocks, in this case the swelling capabilities of the pellets mixtures cannot be neglected. It is worth to mention that Febex pellets mechanical properties are very difficult to determine. Moreover, those are assumed constant with dry density, while it was demonstrated in CHAPTER 4 that mechanical features evolve remarkably with dry density change. Hence, a more exhaustive pellets characterisation would be needed to improve the numerical predictions.

The vertical total stress development of sensor PE5 – Num 1 (Fig. 7.16) appears quite interesting. After the very quick pressure increase, differently from the other numerical strategies and experimental records, it undergoes pressure decrease followed by a pressure increase in the second phase. Let us focus on the comparison between strategies Num – 1 and Num – 2. The two differ only for the permeability of the pellets component, which is macro-void ratio dependent and equal to $K_w=6\times10^{-20}$ m^2 in the initial state and to $K_w=3.1\times10^{-20}$ m^2 in the saturated final state for case 1. Whereas in case 2 the permeability is constant and equal to $K_w=1\times10^{-15}$ m^2, namely 5 orders of magnitude higher than the one adopted in case 1. When the bottom compacted bentonite blocks are hydrated (PE5 and PE6 sensors location), they swell. This causes the compaction of the top pellets material (i.e. namely where sensors PE1 and PE2 are placed). As the compaction takes place in the pellets components, water flow towards the less dense zones is induced. This water flow is also controlled by the time evolution of the swelling in the compacted blocks (i.e. water injection rate) and of course by the permeability of the pellets. Considering the saturation level of the pellets (Fig. 7.15), that is higher than S_r=80%, compaction (i.e. consolidation) can take place simultaneously to water expulsion. This latter is controlled by permeability, which finally affects the compaction mechanism of the pellets and their void ratio evolution (Fig. 7.20). Indirectly, the permeability of the pellets controls the swelling pressure evolution of the bottom compacted blocks as follows: in the BBM Bulk compressibility also depends on void ratio. Pellets compressibility depends thus on their void ratio, which depends on permeability. When the permeability of the pellets mixture is equal to $K_w=1*10^{-15}$ m^2 (case 2), it can be assumed that the compaction occurs in drained conditions. On the other hand, when the permeability is much lower, the water transfer mechanisms taking place during pellets compaction control the swelling pressure and deformation evolution in the compacted blocks (Num – 1). Hence, only when the hydraulic equilibrium

is reached and water is transferred to looser zones, the swelling pressure of the compacted blocks can increase again.

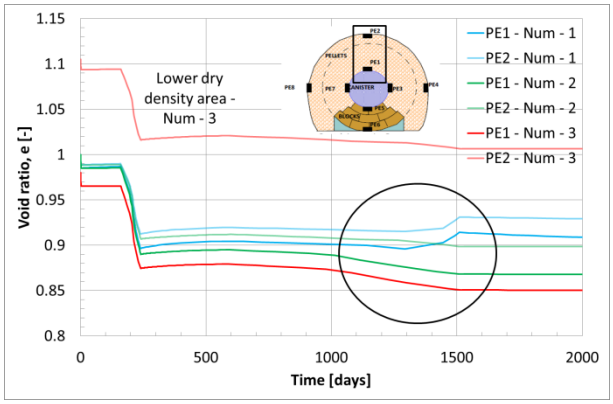

Fig. 7.20 Numerical void ratio evolutions for pellets material at PE1 and PE2 sensors locations. Comparison numerical results.

Fig. 7.21 shows the numerical vertical total stress for sensors PE5 and PE6 and water inflow time evolution. There is a clear link between the hydration of the pellets and the mechanical processes occurring in the blocks. This link is as strong as the one relating the hydration of the compacted blocks and the mechanical compaction occurring in the pellets. After the water injection end, both strategies Num -1 and Num – 2 show a swelling pressure decrease in PE5. On one side, Num – 1 immediately stabilises, whereas Num – 2 records a pressure decrease due to desaturation caused by pellets. The permeability of blocks and pellets in Num – 1 is quite similar ($K_w=3\times10^{-20}$ m^2), so the water transfer mechanisms is not controlled by this latter. With respect to case 3 (Num – 3), until the end of water injection it is similar to case Num – 2 and then it shows a swelling pressure increase instead of Num – 2 desaturation. This is related to the permeability of the blocks, which is constant equal to $K_w=1\times10^{-21}$ m^2 and much lower than the one of Num – 1 and Num 2 (increasing from $K_w=2.8\times10^{-20}$ m^2 to from $K_w=3\times10^{-20}$ m^2 due to the swelling). These observations suggest that the permeability of the pellets mixture has to be very high at the initial state of hydration and similar to the compacted block one when saturation is reached (Hoffmann, Alonso, and Romero 2007). The role of permeability is known to be relevant in the framework of Terzaghi consolidation theory, but it is quite common to assume that unsaturated soils compaction processes are not as affected as saturated ones by this feature. However, this study aims to show that not only the permeability of the unsaturated soils is relevant with respect to consolidation processes, but also that it affects undeniably the mechanical responses of the interacting materials. In general, one may erroneously conclude that only suction affects the swelling pressure development of bentonite. However, compressibilities also play a relevant role. Those are related to both mechanical properties (compressibility coefficients for change in net stress and suction κ and κ_s) but also on void ratio, *e*, which is affected by hydraulic processes.

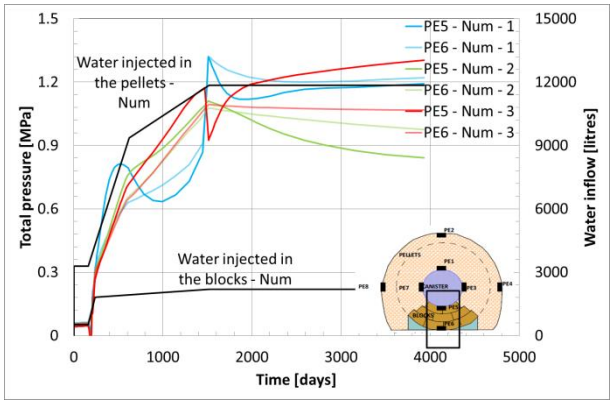

Fig. 7.21 Numerical vertical total stress for sensors PE5 and PE6 and water inflow time evolution. Comparison numerical results.

Displacement

Extensometers are located in sections A1 and A2 (for canister displacements). Despite the apparent symmetry of the configuration, horizontal displacements of the order of 6 mm (section A1) and 18 mm (section A2) are detected (Fig. 7.22 and Fig. 7.23). The vertical displacements are 9 mm (section A1) and 7 mm (section A2).

The numerical results do not provide any horizontal displacement of the canister because symmetry conditions are assumed (Fig. 7.22). Similarly, swelling cannot take place in the longitudinal direction of the gallery due to the modelled plain strain conditions.

Hence, only vertical displacement can be considered on the vertical axis. The vertical displacement reproduces similar behaviour with respect to the experimental one: there is a quick increase of vertical displacement due to the first injection phase followed by a steady state due to the natural water redistribution, then a second increase during the second injection phase and final stabilisation (Fig. 7.23). However, it seems that the whole 3D displacement history of the canister is impossible to model with a 2D symmetric model. It follows, indeed, a strong overestimation of vertical displacement.

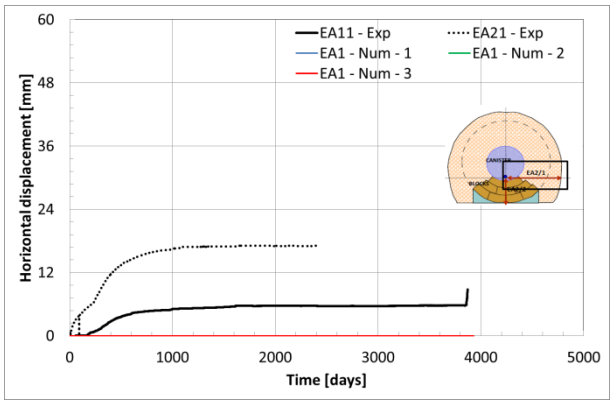

Fig. 7.22: Horizontal displacement time evolution of extensometer located in the canister. Comparison experimental VS numerical.

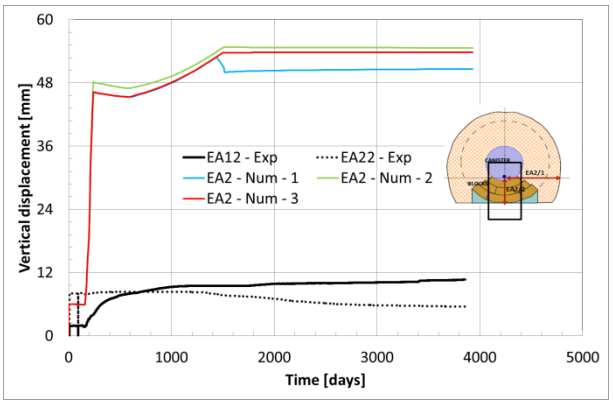

Fig. 7.23: Vertical displacement time evolution of extensometer located in the canister. Comparison experimental VS numerical.

Dry density and water content

From Fig. 7.24 to Fig. 7.27 the numerical dry density distribution and the final deformed configuration are reported. The model predicts a very small variation of dry density after the first injection phase (Fig. 7.24), relevant modifications are obtained with a strong decrease on dry density in the blocks ad a strong increase in the upper pellets mixture. Also in the portion of pellets mixture placed on the lateral side of the concrete bed there is a decrease in dry density. In the final state (Fig. 7.26), the dry density of the blocks is lower than the dry density of the upper pellets mixture with a further decrease also in the lateral side material. The deformation of the buffer occurs mainly in the vertical direction but the model allows also a horizontal swelling thanks to the sliding between the block and the concrete support (Fig. 7.27).

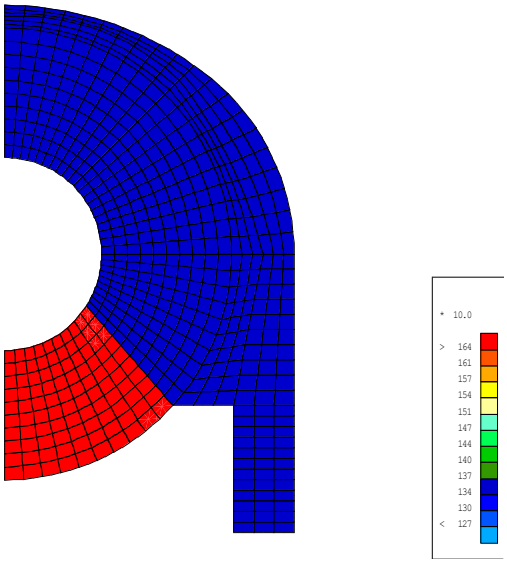

Fig. 7.24: Dry density distribution after the first injection phase (Case 1) (day 2 of the simulation time) [min-max value in the legend 1300 kg/m^3 and 1700 kg/m^3].

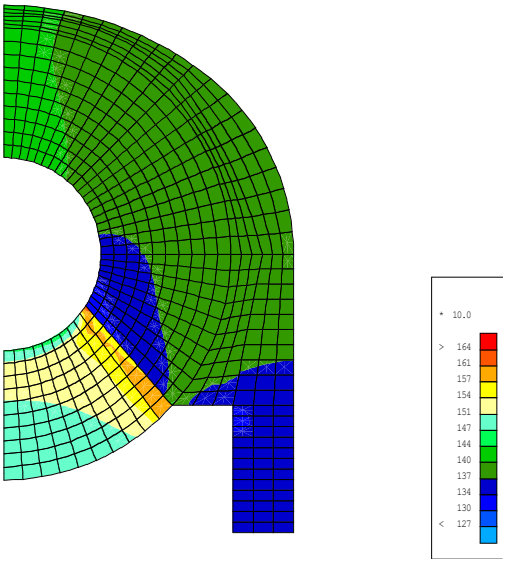

Fig. 7.25: Dry density distribution during the second injection phase (Case 1) (day 240 of the simulation time) [min-max value in the legend 1300 kg/m^3 and 1700 kg/m^3].

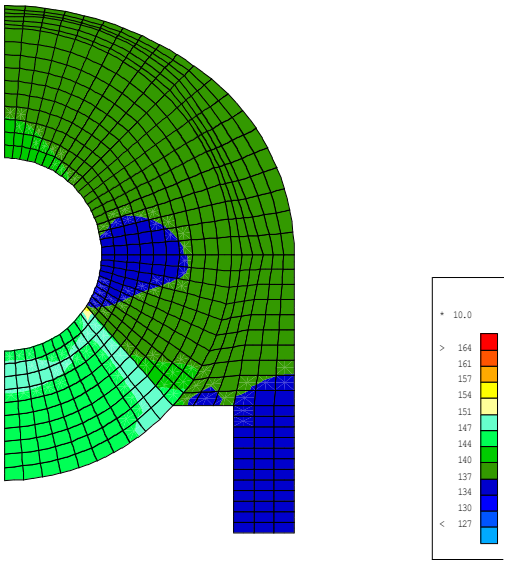

Fig. 7.26: Dry density distribution at the end of the experiment (Case 1) (day 3929 of the simulation time) [min-max value in the legend 1300 kg/m3 and 1700 kg/m3].

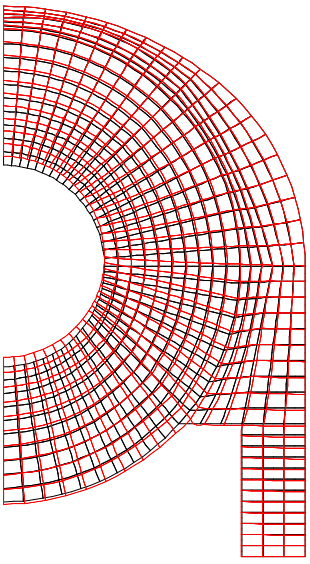

Fig. 7.27: Deformed configuration at the end of the simulation (Case 1) (day 3929 of the simulation time).

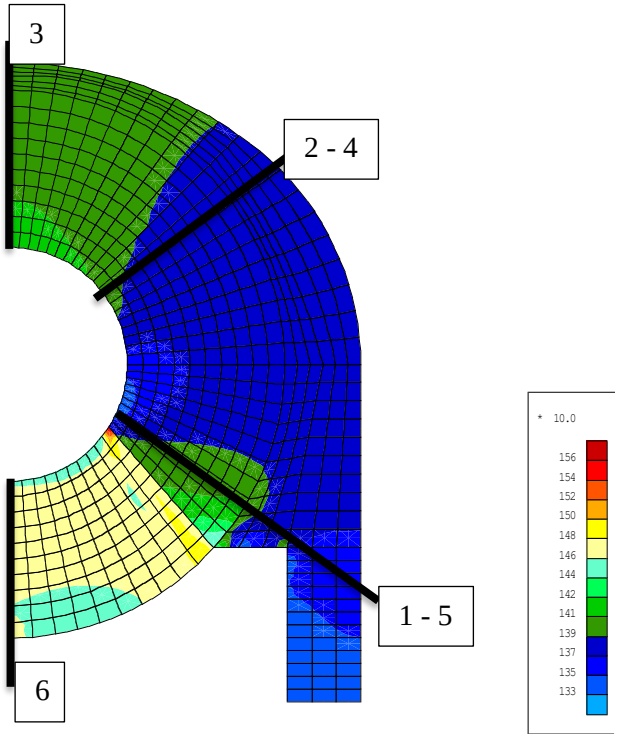

Fig. 7.28: Numerical final dry density distribution (Case 1) [min-max value in the legend 1280 kg/m^3 and 1570 kg/m^3].

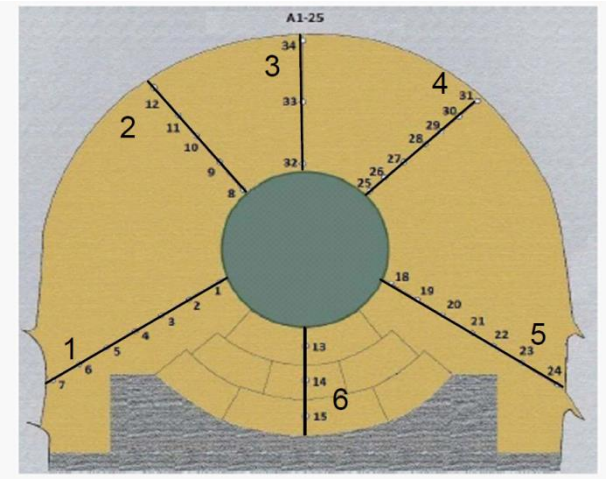

Fig. 7.29: Profiles reference (Palacios, Rey, and García-Siñeriz 2014).

Post-mortem analyses on water content (Fig. 7.31) and dry density (Fig. 7.30) in a number of sections (Fig. 7.4) allowed the determination of the spatial distribution of these quantities (Villar, Campos, and Gutiérrez-Nebot 2014). (All the distances in the following plots refer to the centre of the canister). The final computed dry density state is reported (Fig. 7.28 and Fig. 7.30). The model is able to well reproduce the final state of the barrier, in which the compacted blocks (presenting an initial state of ρ_d=1.7 Mg/m^3) swell up to a dry density equal to ρ_d≈1.4 Mg/m^3 (profile 6) compacting the upper pellets material (initial ρ_d=1.35 Mg/m^3) to a dry density equal ρ_d≈1.45 Mg/m^3 (profile 3). Despite the simplicity of the numerical strategy, which considers a uniform initial state for Case 1 and 2, the non-uniform final dry density distribution is well reproduced in all the directions, apart from profile 1 and 5 and 6. At this location the numerical predictions overestimate the final dry density distribution. However, it is not negligible that the initial state of the barrier, in which the dry density distribution of the pellets material is far from being uniform and homogeneous, and the hydration system could play a relevant role in its final state. Indeed, it can be noticed that case 3, which accounts a non-uniform initial dry density distribution, preserves the discontinuity until the full saturation (Profiles 2, 4 and 3, Fig. 7.30). More precisely, overestimations for profiles 1 and 5 are likely related to initial dry density overestimation. As strategy Num – 3 shows, dry density gradients are quite well preserved during hydration, as experimental dry density gradients are found with respect to post-mortem results.

The strongest dry density discrepancy between numerical and experimental results is related to profile 6. Numerical results predict higher swelling deformation in the vertical direction consistently with vertical displacement overestimation.

It is clear that in large scale test numerical modelling a larger complexity has to be taken into account with respect to laboratory tests. If in CHAPTER 6, the numerical modelling of the same materials combination and type provided remarkably good results, this study case is affected by an elevated uncertainty level and

possibly excessive simplification, related to 3D phenomena that cannot be reduced to plain strain conditions modelling. Moreover, it is worth to say that the imposed boundary conditions (i.e. closed system in which the overall bentonite volume cannot vary) do not allow better dry density estimation.

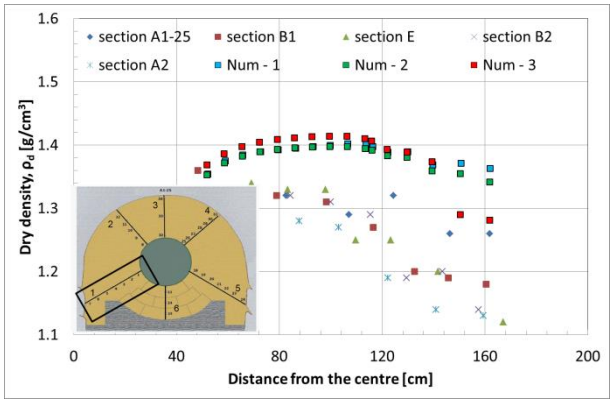

Profile 1

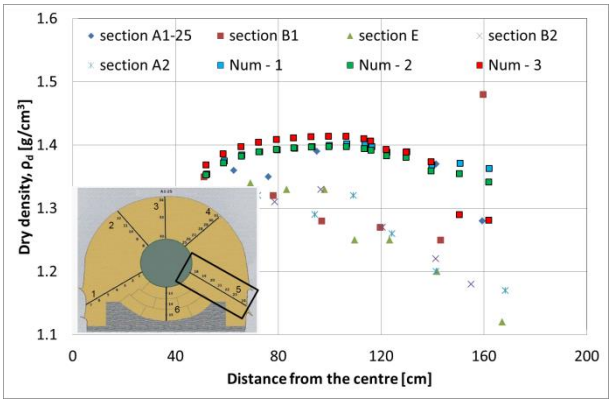

Profile 5

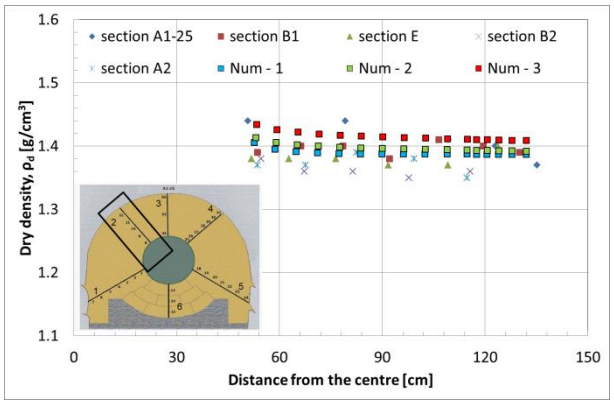

Profile 2

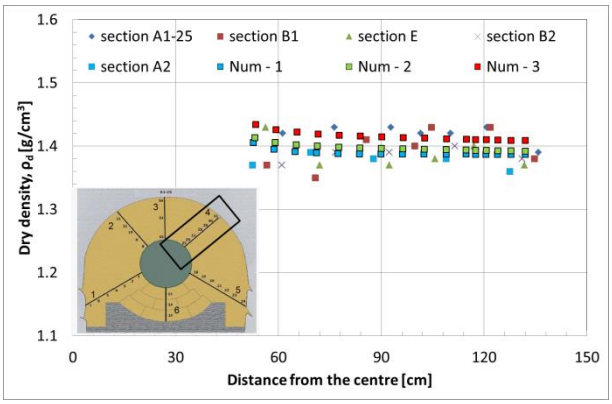

Profile 4

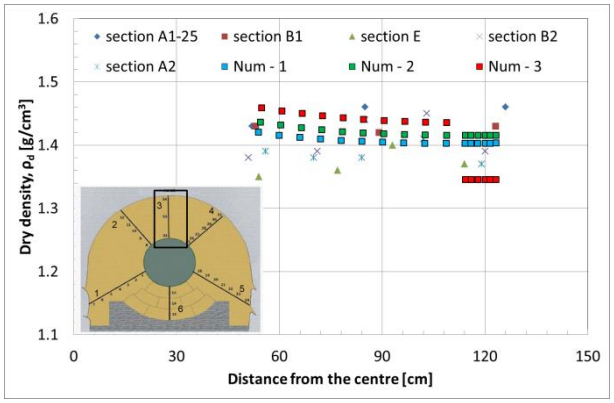

Profile 3

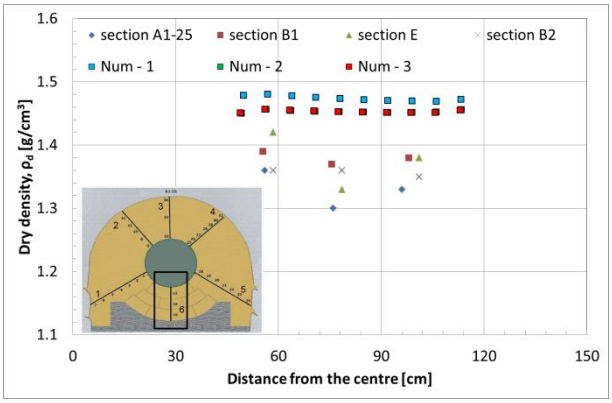

Profile 6

Fig. 7.30: Dry density profiles. Comparison experimental vs numerical final states.

The numerical strategy imposes the full saturation of the barrier, however, the numerical results reproduce remarkably well the water content distribution for each of the analysed radii (Fig. 7.31), apart from comparisons of profile 2 and 4, which underline a small overestimation.

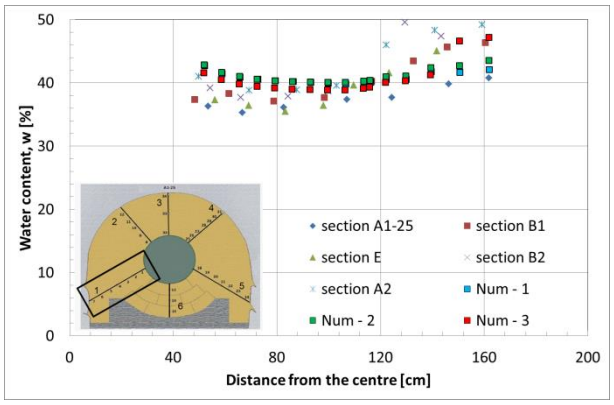

Profile 1

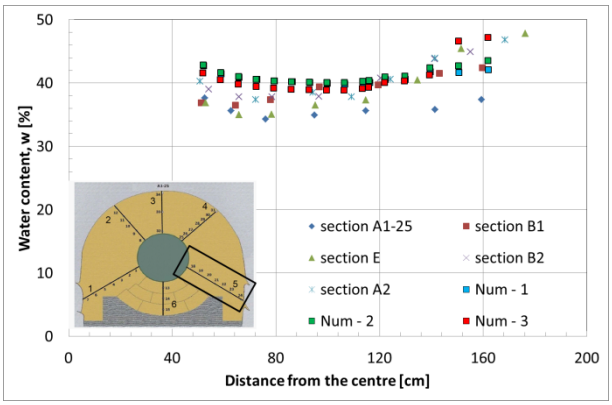

Profile 5

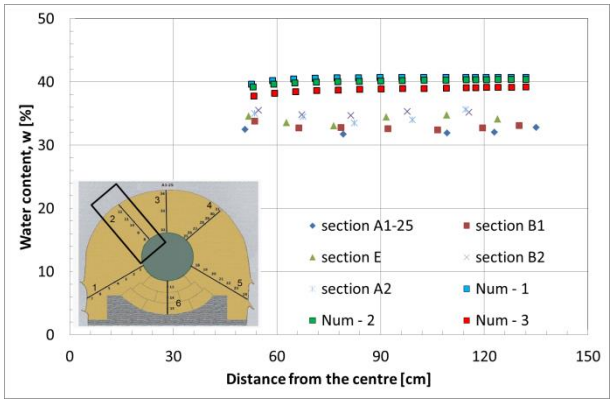

Profile 2

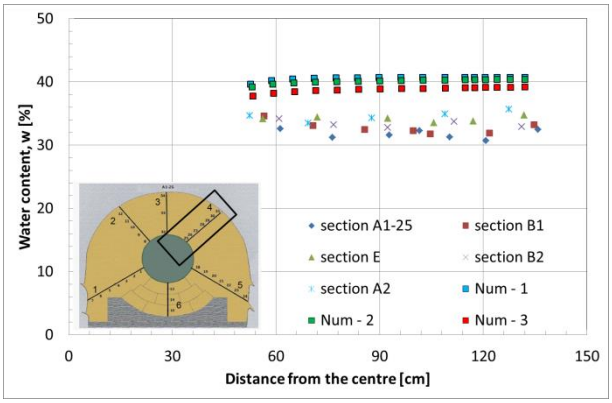

Profile 4

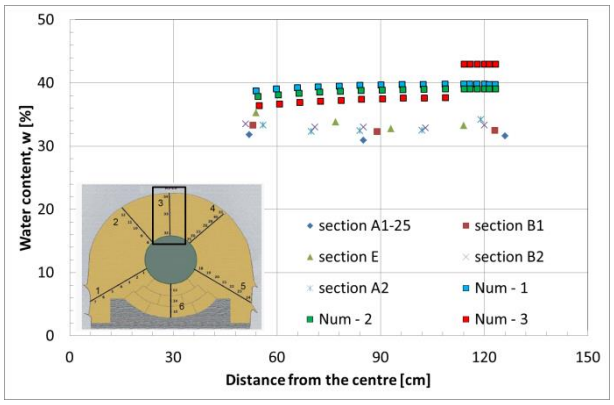

Profile 3

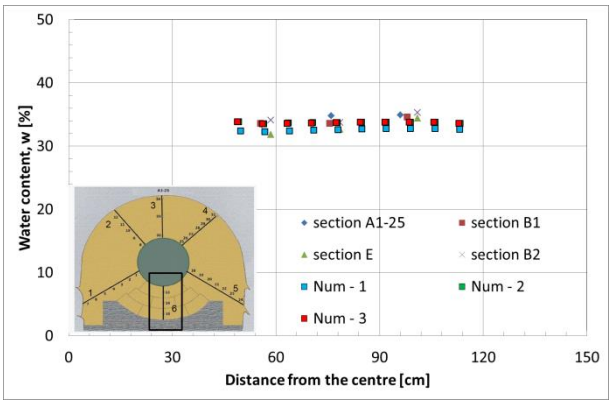

Profile 6

Fig. 7.31: Water content profiles. Comparison experimental vs numerical final states.

7.4. Conclusions

The hydro-mechanical model already implied for laboratory tests analyses has been adopted to model the large scale test EB. The numerical strategy considers a uniform surface hydration of a symmetric plane strain domain, which allows a simplified analysis of the complex phenomena occurring during saturation.

The imposed hydraulic boundary conditions allow the reproduction of the suction decrease recorded by the relative humidity sensors placed inside the buffer in section B1 and B2.

With respect to the total pressure sensors placed in section E, the model is able to satisfactorily reproduce the non-monotonic time evolution of the total swelling pressure (despite the obtained values are lower than the recorded ones). In this context, the strongly hydro-mechanical coupled processes occurring in the each barrier components are far more complex to take into account. Namely, it was observed how, for instance, not only the pellets compressibility (i.e. mechanical feature depending on void ratio) but also and especially, the hydraulic processes inside the barrier itself likely affect the bentonite sealing's response.

Moreover, the symmetric plane strain conditions evidently influence the numerical simulations results. Since the model considers a vertical symmetry axis, it is not possible to obtain the horizontal displacement of the canister recorded by the extensometers placed in sections A1 and A2. The numerical vertical displacement results 5 times larger than the experimental one. Experimental longitudinal swelling of the compacted block is also suspected, but not reproduced in this analysis.

The experimental post-mortem analysis results have been compared with the numerical ones, underlining remarkable similarities. The numerical results of dry density and water content are nevertheless located in a good range of the variability of the experimental results, being able to reproduce the heterogeneous final state of the barrier (starting from a homogeneous state). Predictions may be further improved by considering initial more heterogeneous dry density distributions.

Indeed, it was demonstrated that when a small heterogeneity is considered in the initial state, it is preserved until the full-saturation stage. Heterogeneity is crucial to produce reliable predictions for nuclear waste disposals. Real structure heterogeneity is huge and is translated in heterogeneous density distribution, evolution and final state. Concurrently, water storage, water permeability and swelling pressure inhomogeneity come along with saturation. All these phenomena were precisely reproduced in the preceding chapters where boundary conditions were well interpreted and implemented in the numerical model. Consequentially, it can be assumed that the model allows considering increasing complexity configurations providing good results. If larger complexity is correctly considered, better predictions will be provided.

Concerning the modelling tools, it can be concluded that the constitutive law for the bentonite has allowed an excellent simulation of the observed final densities. It is much difficult to analyse the transient aspects, as few experimental results exist and they are largely scattered. The measured stresses were not well reproduced and this will be analysed in the future considering lab scale experiments with layers of different densities. Large deviatoric strains could be less well calibrated.

CHAPTER 8: CONCLUSIONS

CHAPTER 8: CONCLUSIONS

8.1. Summary

The multi- barrier concept is being considered in order to create safe and sustainable repositories for the radioactive high level and long-life nuclear waste. In this framework, underground geological disposals constitute the most promising storage solution in most countries and represent the geological barrier of the system designs. The sealing of such underground galleries, drifts and shafts, where the stabilised vitrified radioactive waste (chemical barrier) will be casted in special canisters (i.e. physical barriers), implies several technologies. These technologies account for the engineered barrier, which differ from one country to another. Among other components, unsaturated swelling clays play a significant role in the sealing system. With special regards to the French CIGEO concept, bentonite-based materials result particularly suitable for the safe and permanent sealing of in-situ structures because, among other reasons and requirements, bentonite:

- is available in different types (Febex, MX80…) and forms (powder, pellets, compacted blocks…) (i.e. pores structure distribution under the same pores volume);
- has important radionuclides retardation and retention capacities.
- has extremely low permeability to prevent radionuclides leakage;
- presents remarkable swelling capacity upon hydration important to close technological gaps and to ensure tight contact with the surrounding host rock.

All these features are essential to provide the safest sealing design solution. Thus a deep understanding of each bentonite characteristic is needed not only as an independent quality but also and especially with respect to the development and evolution of the other interacting elements. Indeed, in this work, there was an attempt to show the importance of such hydro-mechanical and multi-structural coupled processes taking place in bentonite during hydration. Coupled processes and phenomena always yield significant complexity and uncertainties, which increase as the considered domain size and number of components increases. It follows that, whereas engineering structure designs (several meters and numerous components) rely on laboratory test characterisations (a few centimetres and material-experimental tool duality), the former accounts for a far larger degree of complexity and less controllable conditions than the latter. Hence, the main goals of this thesis were clarifying, simplifying and untangling the existing knowledge and providing an improved understanding about bentonite materials behaviour employed in the context of nuclear waste disposals. This was done starting the analysis from laboratory scale observations up to real engineering structures.

For this purpose, the several structures and porosities characterising bentonite materials are presented in Chapter 2. The thorough comprehension of the bentonite response at laboratory and engineering scales (naked eye observation scales) and its features cannot disregard to an adequate knowledge of the structural changes upon hydration taking place at the nanometres and micron scales. Hence, experimental multi-scale observations of bentonite multi structures behaviour are presented. The role of water on bentonite response immediately appears significant. Thus, among other experimental techniques, emphasis is given to the analysis of MIP experimental results of Febex and MX80 bentonites. MIP analyses allow quantifying most of the bentonite pore structures and their evolution upon different hydro-mechanical stress paths and linking the nanometres and micro scales to the laboratory one, clarifying some interactions between the several pores structure families. Successively, the micro-structure evolution constitutive model adopted in this work to account for the presented structural interactions is presented.

At the light of this multi-porosities structure, experimental evidences on bentonite water retention capacities and water transfer mechanisms are successively presented and explained in Chapter 3. Special attention is

paid to the distinction between pellets mixtures and compacted block water storage mechanism and permeability evolution. The suitability of the double porosity dry density dependent constitutive models implemented in LAGAMINE is tested. Thus, the models are adopted for the following experimental interpretations and numerical analyses.

Similarly, the most important mechanical properties of bentonite-based materials, as well as their reproducibility within the framework of constitutive models, were described sequentially in Chapter 4. Classical and original experimental observations and characterisations obtained via simple but robust experimental tests were shown. Existing mechanical constitutive models were then introduced and compared. Among those, emphasis was given to Barcelona Basic Model implemented by (Alonso, Gens, and Josa 1990). Despite this model has appeared 3 decades ago, it remains central in the framework of constitutive models for unsaturated geomaterials, including swelling clays. Among numerous qualities, it is (relatively) simple, robust and efficient. Its conscious employment returned remarkably good performances in terms of additional materials characterisations, experimental observations reproducibility and long-terms behaviour predictions of bentonite seals. As a consequence, the BBM implemented in LAGAMINE was adopted for the successive numerical analyses.

Therefore, the information supplied by the presented experimental observations, as well as the adopted hydro-mechanical constitutive models capabilities to reproduce bentonite behaviour, was employed and assessed to perform an in-depth analysis of recent laboratory and large scales tests.

This combined experimental and numerical approach was firstly applied (Chapter 5) to examine the hydro-mechanical response of laboratory tests concerning MX80 bentonite samples. These samples presented equal global dry density but differed for the pore structures distribution (i.e. assembly type such as pellet mixtures and compacted block bentonites) and sample sizes.

Successively (Chapter 6), the combination of multi-structural assemblies of Febex bentonite with similar initial characteristics at laboratory scale was investigated in the same fashion. The initial non uniform dry density (and features) distribution evolving towards to a-more homogenised global physical state and properties came along the development of non-uniform stress-strain states, which resulted in unexpected experimental mechanical responses discrepancies. Hence, the numerical simulations succeeded in the modelling of such surprising records especially thanks to the consideration of the interaction between the material samples and the testing cell, via a mechanical interface element and also considering the real hydraulic water supply conditions.

In both cases, the numerical simulations predictions capacities were evaluated not only in terms of hydro-mechanical response time evolution and development (i.e. swelling pressure, water intake, suction…) but also with respect to final samples physical states (i.e. dry density, water content and saturation distributions) and multi-structural porosity states, which were also available for intermediate states for some tests. This provided a better understanding of the material behaviour, which could be finally applied to the study of the bentonites behaviour in large-scale in-situ experimental tests.

This latter investigation highlighted the larger complexity arising when dealing with large scale structures (Chapter 7), in which bentonite components are subjected to various hydro-mechanical conditions and to the interaction of several other barrier elements. Thus, it allowed gaining an improved comprehension of the complicated bentonite response with respect to the limitation of constitutive models.

8.2. Original contributions

The main goals of this work could be summarised as to provide new elements for the prediction and understanding of the hydro-mechanical behaviour of bentonite-based materials and of the coupling between the different phenomena taking place simultaneously in the repository. For this purpose, the importance of hydro-mechanical and multi-structural coupled processes was highlighted and additional understanding delivered by numerical analyses of laboratory tests and large scale in-situ structures was supplied. Even though, each individual phenomenon could be considered as well understood and implemented, also simple laboratory tests results can become of difficult prediction and reproduction. Thus, taking advantage of the hydro-mechanical model implemented in LAGAMINE, numerous experimental tests have been deeply investigated and their responses have been clarified.

Among others, the main original contributions of this PhD work concerns:

- most significant characteristics identification and consequential comparison between pellet mixtures and compacted blocks assemblies features and responses allowed determining dissimilarities (such as in compressibility properties as well as in permeability discrepancies). Even though several experimental campaigns showed that the final swelling pressure exerted by bentonite is related mostly to its dry density, the transient unsaturated phases of pellet mixtures and compacted bentonite completely differ. It was demonstrated that the adopted hydro-mechanical constitutive models succeed in the reproduction of a wide range of bentonite assemblies responses (i.e. pellets or granular or compacted bentonites…). However, for the satisfactorily simulations of different type assemblies behaviour presenting the same global dry density, the model parameters were each time calibrated on the different experimental tests, when available, or consistently modified in order to obtain the target results. Undeniably, differences among such parameters derive from the various pore size distributions, which also account for the manifest dry density dependence that actually every hydro-mechanical bentonite property presents. The transient behaviour of bentonite seals under hydration is determined on the combination of these hydro-mechanical properties and was perfectly reproduced;

- Assessment of BBM capabilities on several stress paths. Model performances exploitation was done for analysis of oedometer test conditions and methodology validation on several lab tests. Calibration, comparison and analysis on bentonites BBM parameters were presented. The model performances were improved by considering alternative formulation with respect to the modelling of material swelling capacities related to some stress conditions. This permitted analysing various boundary problems types accounting for the presence of bentonite sealing of various dimensions (from few centimetres to several meters);

- in particular, the numerical modelling and analysis of laboratory and large-scale in-situ tests considering different bentonite type (Febex and MX80), bentonite assemblies (pellets and compacted block) and their combination, boundary conditions (for instance water hydration supply but also friction development or technological gap modelling) and experimental results in-depth analysis contributed to a better understanding of bentonite behaviour. Specifically, it was showed that the effect of hydration boundary conditions and friction development account for heterogeneous hydro-mechanical properties development (such as pressure distributions inside the sealing) and/or dry density and water content final states, among others.

8.3. Perspectives

Experimental investigation

During the development of this thesis it was intensively highlighted that bentonite-based materials hydro-mechanical features manifestation was mostly related to multi-level structures and porosities state and evolution.

With respect to hydraulic properties determination, such as unsaturated permeability, very few data are available at the present state. It is important to remind that the full saturation of the in-situ bentonite plug would require several thousand years, in which fluids transfer mechanisms will be mostly controlled by bentonite unsaturated permeability. Hence, its determination is crucial.

Also the bentonite response along deviatoric stress-paths has always been poorly investigated. Features as friction angle and cohesion are rarely found in literature. Those results particularly useful when analysing frictional interactions between bentonite assemblies and testing tools. This latter question affects remarkably the already scattered laboratory pressure measurements, thus should be further investigated.

Constitutive modelling

The conclusions of this work allowed defining some important features related to pores structure distributions characterising pellet mixtures and compacted bentonite. Compressibility and permeability resulted particularly affected by the pore entry diameter of large pore. Hence, constitutive models should directly account for the effect that such porosity distributions has on the development of all the hydro-mechanical features.

Moreover, a smooth transition from the unsaturated to saturated states should also be considered fundamental in the development of future constitutive models. Recognized the difficulty to investigate experimentally such domain, efforts should be done in the framework of theoretical analysis.

REFERENCES

Agus, S. S., Y. F. Arifin, S. Tripathy, and T. Schanz. 2013. “Swelling Pressure-Suction Relationship of Heavily Compacted Bentonite-Sand Mixtures.” *Acta Geotechnica* 8(2): 155–65.

Ahn, H. S., and H. Y. Jo. 2009. “Influence of Exchangeable Cations on Hydraulic Conductivity of Compacted Bentonite.” *Applied Clay Science* 44(1–2): 144–50. http://www.scopus.com/inward/record.url?scp=62349084315&partnerID=8YFLogxK.

Aitchison, G, K Russam, and B Richards. 1966. “Engineering Concepts of Moisture Equilibria and Moisture Changes in Soils.”

Alonso, E. E., A. Gens, and A. Josa. 1990. “A Constitutive Model for Partially Saturated Soils.” *Géotechnique* 40(3): 405–30.

Alonso, E. E., C. Hoffmann, and E. Romero. 2010. “Pellet Mixtures in Isolation Barriers.” *Journal of Rock Mechanics and Geotechnical Engineering* 2(1): 12–31. http://dx.doi.org/10.3724/SP.J.1235.2010.00012.

Alonso, E. E., J. Vaunat, and A. Gens. 1999. “Modelling the Mechanical Behaviour of Expansive Clays.” *Engineering Geology* 54(1–2): 173–83.

Andra. 2005. *Dossier Argile 2005. Synthèse Argile: Evaluation de La Faisabilité Du Stockage Géologique En Formation Argileuse.*

ASTM. 2004. “Standard Test Method for Compressive Strength and Elastic Moduli of Intact Rock Core Specimens under Varying States of Stress And.” *American Society for Testing and Materials* (February): 4–11.

Barnichon, J. D. 1998. “Finite Element Modelling in Structural and Petroleum Geology.” Ph.D. thesis - Université de Liège.

Baryla, P. et al. 2018. *Bentonite Mechanical Evolution – Experimental Work for the Support of Model Development and Validation*. Technical Report - BEACON Project.

Bernachy-Barbe, F. 2020. “Homogenization of Bentonite upon Resaturation: Density and Pressure Fields.” *(Under peer review)*.

Bernachy-Barbe, F., N. Conil, W. Guillot, and J. Talandier. 2020. “Observed Heterogeneities after Hydration of MX-80 Bentonite under Pellet / Powder Form.” *Applied Clay Science* 189. https://doi.org/10.1016/j.clay.2020.105542.

Bernachy-Barbe, F., C. Imbert, G Touzé, and C. Gatabin. 2016. *Caractérisation Hydrique et Mécanique Du Matériau NSC*.

Bishop, A. W. 1959. “The Principle of Effective Stress.” *Tecnisk Ukeblad* 39: 859–63.

Blight, G. E. 1966. “Strength Characteristics of Desiccated Clays.” *Journal of the Soil Mechanics and Foundations Division* 92(6): 18–388.

Börgesson, L., D. Broc, and F. Plas. 1990. “Mechanical Properties of Dense Ca-Smectite Clay.” *Engineering Geology* 28(3–4): 419–29.

Börgesson, L., O. Karnland, and L. E. Johannesson. 1996. “Modelling of the Physical Behaviour of Clay Barriers Close to Water Saturation.” *Engineering Geology* 41(1): 127–44. https://www.sciencedirect.com/science/article/pii/0013795295000305.

Bosch, J. A., A. Ferrari, and L. Laloui. 2020. “A Numerical Study on the Coupled Hydro-Mechanical Behaviour of Compacted Bentonite.” *E3S Web of Conferences* 205: 0–4.

Bosch, Jose A., Alessio Ferrari, and Lyesse Laloui. 2021. "Coupled Hydro-Mechanical Analysis of Compacted Bentonite Behaviour during Hydration." *Computers and Geotechnics* 140: 104447. https://doi.org/10.1016/j.compgeo.2021.104447.

Brooks, R. N., and A. T. Corey. 1964. *Hydraulic Properties of Porous Media. Technical Report*.

Cerfontaine, B. et al. 2015. "3D Zero-Thickness Coupled Interface Finite Element: Formulation and Application." *Computers and Geotechnics* 69: 124–40.

Charlier, R. 1987. "Approche Unifiée de Quelques Problèmes Non Linéaires de Mécanique Des Milieux Continus Par La Méthode Des Éléments Finis (Grandes Déformations Des Métaux et Des Sols, Contact Unilatéral de Solides, Conduction Thermique et Écoulements En Milieu Poreux)." Ph.D. thesis, Université de Liège.

Chavant, C., and R. Fernandez. 2005. "Evaluating the Reliability of Hydro-Mechanical Simulation: A Benchmark of Numerical Techniques Carried out by Research Group OfMoMas." In *2nd International Meeting Clays in Natural and Engineer- Ing Barriers for Radioactive Waste Confinement*, Tours, 249–250.

Collin, F. 2003. "Couplages Thermo-Hydro-Mécaniques Dans Les Sols et Les Roches Tendres Partiellement Saturés. Thèse de Doctorat. Université de Liège, Belgique, 300p." University of Liege.

Cui, Y. J. 1993. "Etude Du Comportement d'un Limon Compacté Non Saturé et Da Sa Modelisation Dans Un Cadre Elasto-Plastique." Ecole Nationale des Ponts et Chaussée.

———. 2017. "On the Hydro-Mechanical Behaviour of MX80 Bentonite-Based Materials." *Journal of Rock Mechanics and Geotechnical Engineering* 9(3): 565–74. http://dx.doi.org/10.1016/j.jrmge.2016.09.003.

Cui, Y. J., A. M. Tang, C. Loiseau, and P. Delage. 2008. "Determining the Unsaturated Hydraulic Conductivity of a Compacted Sand-Bentonite Mixture under Constant-Volume and Free-Swell Conditions." *Physics and Chemistry of the Earth, Parts A/B/C* 33: S462–S471.

Dananaj, I., J. Frankovská, and I. Janotka. 2005. "The Influence of Smectite Content on Microstructure and Geotechnical Properties of Calcium and Sodium Bentonites." *Applied Clay Science* 28(1): 223–32. https://www.sciencedirect.com/science/article/pii/S0169131704000766.

Darcy, H. 1865. "Les Fontaines Publiques de La Ville de Dijon: Exposition et Application Des Principes à Suivre et Des Formules à Employer Dans Les Questions de Distribution d'eau." : 343.

Dardé, B. 2019. "Experimental and Numerical Study of the Hydromechanical Behaviour of Bentonite Pellet-Powder Mixtures." Ph.D. thesis - École des Ponts ParisTech.

Dieudonné, A. C. 2016. "Hydromechanical Behaviour of Compacted Bentonite : From Micro-Scale Analysis to Macro-Scale Modelling." University of Liege.

Dieudonné, A. C., G. Della Vecchia, and R. Charlier. 2017. "Water Retention Model for Compacted Bentonites." *Canadian Geotechnical Journal* 54(7): 915–25.

Di Donna, A., and L. Laloui. 2015. "Numerical Analysis of the Geotechnical Behaviour of Energy Piles AIice." *International Journal for Numerical and Analytical Methods in Geomechanics* 39: 861–888. http://onlinelibrary.wiley.com/doi/10.1002/nag.527/abstract%5Cnhttps://web.natur.cuni.cz/uhigug/masin/download/MTVC_IJNAMG06-pp.pdf.

Dor, M. et al. 2020. "Assembly of Clay Mineral Platelets , Tactoids , and Aggregates : Effect of Mineral Structure and Solution Salinity." *Journal of Colloid And Interface Science* 566: 163–70. https://doi.org/10.1016/j.jcis.2020.01.084.

Dueck, A. et al. 2019. *Bentonite Homogenisation Laboratory Study, Model Development and Modelling of Homogenisation Processes*. www.skb.se.

REFERENCES

Dueck, A., and U. Nilsson. 2010. Tr-10-55 *Thermo-Hydro-Mechanical Properties of MX-80. Results from Advanced Laboratory Tests*. Technical Report - SKB.

van Eekelen, H. A. M. 1980. "Isotropic Yield Surfaces in Three Dimensions for Use in Soil Mechanics." *International Journal for Numerical and Analytical Methods in Geomechanics* 4(1): 89–101.

ENRESA. 2000. *FEBEX Project Full-Scale Engineered Barriers Experiment for a Deep Geological Repository for High Level Radioactive Waste in Crystalline Host Rock*.

Escario, V, and J Sáez. 1986. "The Shear Strength of Partly Saturated Soils." *Géotechnique* 36(3): 453–56. https://doi.org/10.1680/geot.1986.36.3.453.

Fredlund, D G, N R Morgenstern, and R A Widger. 1978. "The Shear Strength of Unsaturated Soils." *Canadian Geotechnical Journal* 15(3): 313–21. https://doi.org/10.1139/t78-029.

Gatabin, C. et al. 2006. *ESDRED PROJECT - MODULE : Selection and THM Characterisation of the Buffer Material*.

———. 2016. "Competing Effects of Volume Change and Water Uptake on the Water Retention Behaviour of a Compacted MX-80 Bentonite/Sand Mixture." *Applied Clay Science* 121–122: 57–62. https://www.sciencedirect.com/science/article/pii/S016913171530209X.

Gatabin, C., W. Guillot, and F. Bernachy-Barbe. 2016. *F.T. Caractérisation Bentonite REM : Essais de Gonflement à l'échelle Du Laboratoire Avec Différentes Eaux d'imbibition*.

Van Geet, M., G. Volckaert, and S. Roels. 2005. "The Use of Microfocus X-Ray Computed Tomography in Characterising the Hydration of a Clay Pellet/Powder Mixture." *Applied Clay Science* 29(2): 73–87.

Gens, A. 2010. "Soil-Environment Interactions in Geotechnical Engineering." *Geotechnique* 60(1): 3–74.

———. 2011. "Hydromechanical Behaviour of a Heterogeneous Compacted Soil: Experimental Observations and Modelling." *Geotechnique* 61(5): 367–86.

Gens, A., and E. E. Alonso. 1992. "A Framework for the Behaviour of Unsaturated Expansive Clays." *Canadian Geotechnical Journal* 29: 1013–32.

Gens, A., and M. Sanchez. 2014. *Formulation of a Model Suitable for Long Term Predictions. Technical Report, PEBS Deliverable D3.5-2*.

van Genuchten, M. T. 1980. "A Closed-Form Equation for Predicting the Hydraulic Conductivity of Unsaturated Soils." *Soil Science Society of America Journal* 44(5): 892–98.

Gerard, P., R. Charlier, and F. Collin. 2008. "On Boundary Condition in Tunnels under Partial Saturation." *Unsaturated Soils: Advances in Geo-Engineering - Proceedings of the 1st European Conference on Unsaturated Soils, E-UNSAT 2008*: 779–84.

Ghiadistri, G., L. Zdravkovic, D. Potts, and A. Tsiampousi. 2019. "Calibration of a Double Structure Constitutive Model for Unsaturated Compacted Soils." *E3S Web of Conferences* 92: 15002.

Gramegna, L. et al. 2020. "Hydro-Mechanical Behaviour of a Pellets Based Bentonite Seal: Numerical Modelling of Lab Scale Experiments." *E3S Web of Conferences* 195: 04009.

Hoffmann, C., E. E. Alonso, and E. Romero. 2007. "Hydro-Mechanical Behaviour of Bentonite Pellet Mixtures." *Physics and Chemistry of the Earth* 32: 832–49.

Imbert, C., P. Billaud, G Touzé, and K. D. Dang. 2004. *Acquisition Des Paramètres de Comportement Hydraulique et Hydromécanique de Base de l'argile MX80 à l'état Saturé.*

Imbert, C., and M. V. Villar. 2006. "Hydro-Mechanical Response of a Bentonite Pellets / Powder Mixture upon Infiltration." *Applied Clay Science* 32: 197–209.

ISRM. 1977. “Suggested Methods for Determining the Uniaxial Compressive Strength and Deformability of Rock Materials.” *International Society for Rock Mechanics* (December): 0–3.

Jacinto, A. C., M. V. Villar, R. Gómez-Espina, and A. Ledesma. 2009. “Adaptation of the van Genuchten Expression to the Effects of Temperature and Density for Compacted Bentonites.” *Applied Clay Science* 42(3–4): 575–82. http://dx.doi.org/10.1016/j.clay.2008.04.001.

Jacinto, A. C., M. V. Villar, and A. Ledesma. 2012. “Influence of Water Density on the Water-Retention Curve of Expansive Clays.” *Géotechnique* 62(8): 657–67. https://doi.org/10.1680/geot.7.00127.

Karnland, O., U. Nilsson, H.P. Weber, and P. Wersin. 2008. “Sealing Ability of Wyoming Bentonite Pellets Foreseen as Buffer Material – Laboratory Results.” *Physics and Chemistry of the Earth, Parts A/B/C* 33: S472–75. https://www.sciencedirect.com/science/article/pii/S1474706508003070.

Kiviranta, L. et al. 2018. 31 *Characterization of Bentonite and Clay Materials 2012-2015*.

Köhler, S., B. Garitte, H.P. Weber, and H.R. Müller. 2015. *Arbeitsbericht NAB 15-27*. Wettingen.

Komine, Hideo, Kazuya Yasuhara, and Satoshi Murakami. 2009. “Swelling Characteristics of Bentonites in Artificial Seawater.” *Canadian Geotechnical Journal* 46(2): 177–89.

Labalette, T., A. Harman, M. C. Dupuis, and G. Ouzounian. 2009. “Cigeo, the French Geological Repository Project.” In *Waste Management Conference,WM2013,* Phoenix, USA, 9.

Lajudie, A., J. Raynal, J. C. Petit, and P. Toulhoat. 1994a. “Clay-Based Materials for Engineered Barriers: A Review.” *MRS Online Proceedings Library* 353(1): 221–30. https://doi.org/10.1557/PROC-353-221.

Lajudie, A., J. Raynal, J.C. Petit, and P. Toulhoat. 1994b. *Clay-Based Materials for Engineered Barriers: A Review*.

Laloui, L., and C. Cekerevac. 2003. “Thermo-Plasticity of Clays: An Isotropic Yield Mechanism.” *Computers and Geotechnics* 30(8): 649–60.

Laloui, L., and B. François. 2009. “ACMEG-T: Soil Thermoplasticity Model.” *Journal of Engineering Mechanics* 135(9): 932–44.

Lewis, R. W., and B. A. Schrefler. 1998. *The Finite Element Method in the Static and Dynamic Deformation and Consolidation of Porous Media.* ed. John Wiley & Sons.

Lloret, A. et al. 2003. “Mechanical Behaviour of Heavily Compacted Bentonite under High Suction Changes.” *Géotechnique* 53(1): 27–40. http://www.icevirtuallibrary.com/doi/10.1680/geot.2003.53.1.27.

Lloret, A., E. Romero, and M. V. Villar. 2004. Empresa Nacional de Residuos Radiactivos *FEBEX II Project Final Report on Thermo-Hydro-Mechanical Laboratory Tests*.

Lloret, A., and M. V. Villar. 2007a. “Advances on the Knowledge of the Thermo-Hydro-Mechanical Behaviour of Heavily Compacted ‘FEBEX’ Bentonite.” *Physics and Chemistry of the Earth* 32(8–14): 701–15. https://doi.org/10.1016/j.apgeochem.2018.08.013.

———. 2007b. “Advances on the Knowledge of the Thermo-Hydro-Mechanical Behaviour of Heavily Compacted ‘“FEBEX”’ Bentonite.” *Physics and Chemistry of the Earth* 32: 701–15. https://doi.org/10.1016/j.apgeochem.2018.08.013.

Machatschki, F. 1928. “Zur Frage Der Struktur Und Konstitution Der Feldspäte.” *Zentralbl. f. Min.*: 97–100.

Madsen, F. T. 1998. “Clay Mineralogical Investigations Related to Nuclear Waste Disposal.” *Clay Minerals* 33(1): 109–29. https://www.cambridge.org/core/article/clay-mineralogical-investigations-related-to-nuclear-waste-disposal/9E51F165C95A2310514E26435F9931E5.

REFERENCES

Marcial, D. 2003. “Comportement Hydromécanique et Microstructural Des Matériaux de Barrière Ouvragée.” Ph.D. thesis, Ecole Nationale des Ponts et Chaussées.

Mašín, D. 2005. “A Hypoplastic Constitutive Model for Clays.” *International Journal for Numerical and Analytical Methods in Geomechanics* 29(4): 311–36.

———. 2017. “Coupled Thermohydromechanical Double-Structure Model for Expansive Soils.” *Journal of Engineering Mechanics* 143(9): 04017067.

Mayor, J et al. 2005. “Engineered Barrier Emplacement Experiment in Opalinus Clay for the Disposal of Radioactive Waste in Underground Repositories.” *ENRESA: Empresa Nacional de Residuos Radiactivos* (March 2017): 1–101.

Molinero, A. et al. 2017. “In-Depth Characterisation of a Mixture Composed of Powder / Pellets MX80 Bentonite.” *Applied Clay Science* 135: 538–46.

———. 2018. “Investigation of the Hydro-Mechanical Behaviour of a Pellet/Powder MX80 Bentonite Mixture Using an Infiltration Column.” *Engineering Geology* 243(June): 18–25. https://doi.org/10.1016/j.enggeo.2018.06.006.

———. 2019. “Characterization of Water Retention , Compressibility and Swelling Properties of a Pellet / Powder Bentonite Mixture.” *Engineering Geology* 248: 14–21. https://doi.org/10.1016/j.enggeo.2018.11.005.

———. “Experimental and Digital Characterisations of the Hydro-Mechanical Behaviour of a Heterogeneous Powder / Pellet Bentonite Material.” c: 67–70.

Montes-H, G. 2002. “Etude Expérimentale de La Sorption d’eau et Du Gonflement Des Argiles Par Microscopie Électronique à Balayage Environnementale (ESEM).” Ph.D. thesis, Université Louis Pasteur.

Moore, D. M., and R. C. Jr. Reynolds. 1997. *X-Ray Diffraction and the Identification and Analysis of Clay Minerals*. Cambridge University Press. https://www.cambridge.org/core/article/moore-d-m-reynolds-r-c-jr-1997-xray-diffraction-and-the-identification-and-analysis-of-clay-minerals-2nd-ed-xviii-378-pp-oxford-new-york-oxford-university-press-price-2795-spiralbound-paperback-isbn-0-19-508713-5/36D.

Narasimha Rao, S., and Paul K. Mathew. 1995. “Effects of Exchangeable Cations on Hydraulic Conductivity of a Marine Clay.” *Clays and Clay Minerals* 43(4): 433–37.

Navarro, V. et al. 2020. “From Double to Triple Porosity Modelling of Bentonite Pellet Mixtures.” *Engineering Geology* 274(April): 105714. https://doi.org/10.1016/j.enggeo.2020.105714.

Nuth, M., and L. Laloui. 2008. “Effective Stress Concept in Unsaturated Soils: Clarification and Validation of a Unified Framework.” *International Journal for Numerical and Analytical Methods in Geomechanics* 32(2008): 189–213.

Palacios, B., M. Rey, and J García-Siñeriz. 2014. *Long-Term Performance of Engineered Barrier Systems PEBS Engineered Barrier Emplacement Experiment in Opalinus Clay: “EB” Experiment*.

Pardoen, B. 2015. “Hydro-Mechanical Analysis of the Fracturing Induced by the Excavation of Nuclear Waste Repository Galleries Using Shear Banding.” University of Liege.

Potts, D., and L. Zdravkovic. 1999. *Finite Element Analysis in Geotechnical Engineering: Volume One - Theory*. ed. Thomas Telford.

Pusch, R. 2001. *Experimental Study of the Effect of High Porewater Salinity on the Physical Properties of a Natural Smectitic Clay*.

———. 2019. “Microstructure Controls Physical Properties of Smectite Clay.” 9(3): 65–100.

Pusch, R., and R. N. Yong. 2006. *Microstructure of Smectite Clays and Engineering Performance*. CRC Press.

Raynal, J. 2005. "Mesure de La Masse Volumique de l'eau Interfoliaire Dans Les Smectites; Application Aux Courbes Capillaires." *REVUE FRANÇAISE DE GÉOTECHNIQUE* 1(110): 69–76.

Romero, E. 2012. *Complementary Triaxial Compression and Direct Shear Tests under High Matric Suctions on Low-Density Kunigel V1*. Technical report.

———. 2013. "A Microstructural Insight into Compacted Clayey Soils and Their Hydraulic Properties." *Engineering Geology* 165: 3–19.

Romero, E., A. Gens, and A. Lloret. 1999. "Water Permeability, Water Retention and Microstructure of Unsaturated Compacted Boom Clay." *Engineering Geology* 54(1–2): 117–27.

Romero, E., and P. H. Simms. 2008. "Microstructure Investigation in Unsaturated Soils: A Review with Special Attention to Contribution of Mercury Intrusion Porosimetry and Environmental Scanning Electron Microscopy." *Geotechnical and Geological Engineering* 26(6): 705–27.

Romero, E., G. Della Vecchia, and C. Jommi. 2011. "An Insight into the Water Retention Properties of Compacted Clayey Soils." *Géotechnique* 61(4): 313–28. http://www.icevirtuallibrary.com/doi/10.1680/geot.2011.61.4.313.

Roscoe, K. H., and J. B. Burland. 1968. "On the Generalized Stress–Strain Behaviour of the 'Wet' Clay." *Engineering plasticity (Heyman, J. & Leckic, F., Eds.)*: 535–609.

Saba, S. et al. 2014. "Further Insight into the Microstructure of Compacted Bentonite-Sand Mixture." *Engineering Geology* 168: 141–48. http://dx.doi.org/10.1016/j.enggeo.2013.11.007.

Saiyouri, N., P. Y. Hicher, and D. Tessier. 2000. "Microstructural Approach and Transfer Water in Highly Compacted Unsaturated Swelling Clays." *Mechanics of Cohesive-frictional Materials* 5((1)): 41–60.

Saiyouri, N., D. Tessier, and P. Y. Hicher. 2004. "Experimental Study of Swelling in Unsaturated Compacted Clays." *Clay Minerals* 39(4): 469–79.

Sanchez, M., A. Gens, L. Do Nascimento Guimaraes, and S. Olivella. 2005. "A Double Structure Generalized Plasticity Model for Expansive Materials." *Numerical and Analytical Methods in Geomechanics* 29(8): 751–87.

Sanchez, M., A. Gens, and S. Olivella. 2012. "THManalysis of a Large-Scale Heating Test Incorporating Material Fabric Changes." *International Journal for Numerical and Analytical Methods in Geomechanics* 36: 391–421. http://onlinelibrary.wiley.com/doi/10.1002/nag.527/abstract%5Cnhttps://web.natur.cuni.cz/uhigug/masin/download/MTVC_IJNAMG06-pp.pdf.

Sauzeat, E. et al. 2001. *Caracterisation Mineralogique, Cristallochimique et Texturale de l'argile MX-80*. Paris, France.

Seiphoori, A. et al. 2016. "Water Retention and Swelling Behaviour of Granular Bentonites for Application in Geosynthetic Clay Liner (GCL) Systems." *Soils and Foundations* 56(3): 449–59. http://dx.doi.org/10.1016/j.sandf.2016.04.011.

Seiphoori, A., A. Ferrari, and L. Laloui. 2014. "Water Retention Behaviour and Microstructural Evolution of MX-80 Bentonite during Wetting and Drying Cycles." *Géotechnique* 64(9): 721–34. http://www.icevirtuallibrary.com/doi/10.1680/geot.14.P.017.

Sellin, P. et al. 2020. "Beacon: Bentonite Mechanical Evolution." *EPJ Nuclear Sciences & Technologies* 6: 23.

REFERENCES

Sellin, P., and O. X. Leupin. 2014. “The Use of Clay as an Engineered Barrier in Radioactive-Waste Management - A Review.” *Clays and Clay Minerals* 61(6): 477–98.

Som, N. N., and N. E. Simons. 1969. “The Influence of Lateral Stresses on the Stress Deformation Characteristics of London Clay.” *7th International Conference on Soil Mechanics and Foundation Engineering (Mexico)* 1: 161-.

Talandier, J. 2018. *Specifications for BEACON WP5: Testing, Verification and Validation of Models Step 1-Verification Cases*. Technical Report - BEACON Project.

———. 2019. *Synthesis of Results from Task 5.1. Deliverable D5.1.2*. BEACON PROJECT.

Tang, A. M., and Y. J. Cui. 2010. “Effects of Mineralogy on Thermo-Hydro-Mechanical Parameters of MX80 Bentonite.” *Journal of Rock Mechanics and Geotechnical Engineering* 2(1): 91–96. http://dx.doi.org/10.3724/SP.J.1235.2010.00091.

Tang, A. M., Y. J. Cui, and N. Barnel. 2008. “Thermo-Mechanical Behaviour of a Compacted Swelling Clay.” *Géotechnique* 58(1): 45–54.

Tarantino, A. 2009. “A Water Retention Model for Deformable Soils.” *Geotechnique* 59(9): 751–62.

Thatcher, K. 2017. *Contractor Report to RWM FEBEX-DP : THM Modelling*.

Villar, M. V. 2000. “Caracterizacion Thermo-Hidro-Mecanica de Una Bentonita de Cabo Gata.” Universidad Complutense de Madrid.

———. 2002. *Thermo-Hydro-Mechanical Characterisation of a Bentonite from Cabo de Gata. A Study Applied to the Use of Bentonite as Sealing Material in High Level Radioactive Waste Repositories*.

———. 2005. Informes Técnicos Ciemat 1053 (2001-2004) *MX-80 Bentonite. Thermo-Hydro-Mechanical Characterisation Performed at CIEMAT in the Context of the Prototype Project*.

Villar, M. V., R. Campos, and L. Gutiérrez-Nebot. 2014. *Long-Term Performance of Engineered Barrier Systems PEBS EB Experiment Laboratory Post-Mortem Analyses Report (DELIVERABLE-N°: D2.1-7)*. Madrid.

Villar, M. V., R. Gómez-Espina, and L. Gutiérrez-Nebot. 2012. “Basal Spacings of Smectite in Compacted Bentonite.” *Applied Clay Science* 65–66: 95–105. https://www.sciencedirect.com/science/article/pii/S0169131712001561.

Villar, M. V., R.J. Iglesias, C. Gutiérrez-Álvarez, and B. Carbonell. 2021. “Pellets/Block Bentonite Barriers: Laboratory Study of Their Evolution upon Hydration.” *Engineering Geology* 292.

Wang, Q., Y. J. Cui, et al. 2013. “Hydraulic Conductivity and Microstructure Changes of Compacted Bentonite / Sand Mixture during Hydration.” *Engineering Geology* 164: 67–76. http://dx.doi.org/10.1016/j.enggeo.2013.06.013.

Wang, Q., A. M. Tang, et al. 2013. “The Effects of Technological Voids on the Hydro-Mechanical Behaviour of Compacted Bentonite-Sand Mixture.” *Soils and Foundations* 53(2): 232–45. http://dx.doi.org/10.1016/j.sandf.2013.02.004.

Wang, Q. et al. 2014. “Time- and Density-Dependent Microstructure Features of Compacted Bentonite.” *Soils and Foundations* 54(4): 657–66.

Zhang, F., Y. J. Cui, and W. M. Ye. 2018. “Distinguishing Macro- and Micro-Pores for Materials with Different Pore Populations.” *Geotechnique Letters* 8: 1–9.

Zhou, A. N., D. Sheng, S. W. Sloan, and A. Gens. 2012. “Interpretation of Unsaturated Soil Behaviour in the Stress - Saturation Space, I: Volume Change and Water Retention Behaviour.” *Computers and*

Geotechnics 43: 178–87. http://dx.doi.org/10.1016/j.compgeo.2012.04.010.

Zhou, B., M. Sanchez, and M. V. Villar. 2020. “Impact of Dry Density, Saturation, and Confinement on Gas Permeability of Clay-Barrier Materials.” *E3S Web of Conferences* 205.

APPENDIX A: Analytical mechanical response for axial swelling upon hydration under oedometer conditions

APPENDIX A: Analytical mechanical response for axial swelling upon hydration under oedometer conditions

The general definition of a soil mechanical deformative and stress state at constant suction s can be provided by the volumetric strain ε_{vol}, deviatoric strain ε_d, mean net stress p and deviatoric stress q, which can read as follow in principal stress and strain directions:

$$\varepsilon_{vol} = \varepsilon_1 + \varepsilon_2 + \varepsilon_3 \quad \text{Eq. A.1}$$

$$\varepsilon_d = \frac{\sqrt{2}}{3}\sqrt{(\varepsilon_1 - \varepsilon_2)^2 + (\varepsilon_1 - \varepsilon_3)^2 + (\varepsilon_2 - \varepsilon_3)^2} \quad \text{Eq. A.2}$$

$$p = \frac{\sigma_1 + \sigma_2 + \sigma_3}{3} \quad \text{Eq. A.3}$$

$$q = \sqrt{\frac{1}{2}[(\sigma_1 - \sigma_2)^2 + (\sigma_1 - \sigma_3)^2 + (\sigma_2 - \sigma_3)^2]} \quad \text{Eq. A.4}$$

Where ε_1, $\varepsilon_2$and ε_3 and σ_1, $\sigma_2$and σ_3 are respectively the strains and the stresses in the principal directions 1, 2 and 3.

Constitutive relationships link the elastic volumetric and deviatoric strains to mean and deviatoric stresses via:

$$d\varepsilon_{vol} = \frac{dp}{K} \quad \text{Eq. A.5} \qquad d\varepsilon_d = \frac{dq}{3G} \quad \text{Eq. A.6}$$

Where *K* and *G* are respectively the Bulk and the Shear moduli.

When axisymmetric conditions are considered (Fig. A.1), principal stress and strain directions coincide with axial and radial directions. Thus, it is possible to write:

$$\varepsilon_a = \varepsilon_1 \quad \text{Eq. A.7} \qquad \varepsilon_2 = \varepsilon_3 = \varepsilon_r \quad \text{Eq. A.8}$$

And

$$\sigma_a = \sigma_1 \quad \text{Eq. A.9} \qquad \sigma_2 = \sigma_3 = \sigma_r \quad \text{Eq. A.10}$$

APPENDIX A: Analytical mechanical response for axial swelling upon hydration under oedometer conditions

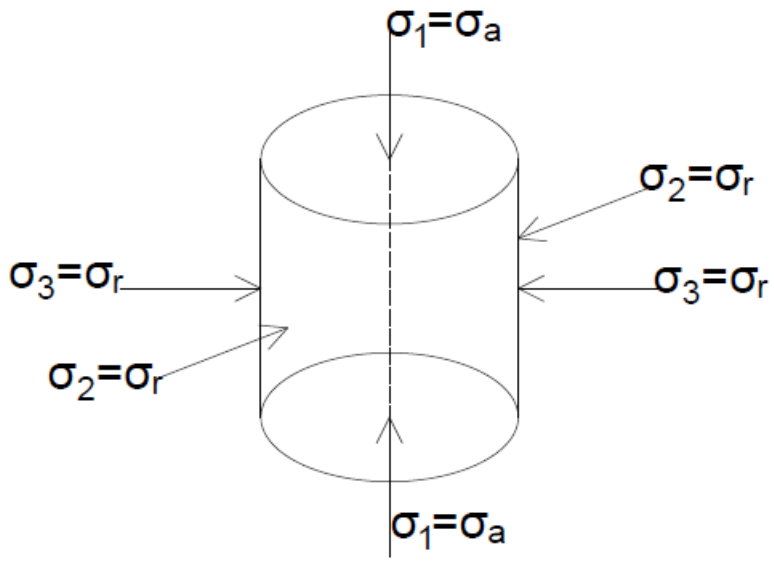

Fig. A.1: Axisymmetric conditions statement.

Hence Eq. A.1, Eq. A.2, Eq. A.3 and Eq. A.4 can be formulated as:

$$\varepsilon_{vol} = \varepsilon_a + 2\varepsilon_r \quad \text{Eq. A.11}$$

$$\varepsilon_d = \frac{\sqrt{2}}{3}\sqrt{(\varepsilon_a - \varepsilon_r)^2 + (\varepsilon_a - \varepsilon_r)^2 + (\varepsilon_r - \varepsilon_r)^2} \quad \text{Eq. A.12}$$

$$\varepsilon_d = \frac{2}{3}(\varepsilon_a - \varepsilon_r) \quad \text{Eq. A.13}$$

$$p = \frac{\sigma_a + 2\sigma_r}{3} \quad \text{Eq. A.14}$$

$$q = \sigma_a - \sigma_r \quad \text{Eq. A.15}$$

In the framework of unsaturated swelling clay, when BBM is adopted for the modelling of hydration in oedometer conditions at constant vertical stress, the problem formulation reads:

$$d\varepsilon_a \neq 0 \quad \text{Eq. A.16} \qquad d\varepsilon_r = 0 \quad \text{Eq. A.17}$$

$$d\sigma_a = 0 \quad \text{Eq. A.18} \qquad d\sigma_r \neq 0 \quad \text{Eq. A.19}$$

Namely, the suction decrease produces swelling deformation in the vertical direction (Eq. A.16) and radial stress development (Eq. A.19), while the external applied axial stress remains constant (Eq. A.18) and radial deformation cannot take place due to the oedometer boundary conditions (Eq. A.17).

Eq. A.11, Eq. A.13, Eq. A.14 and Eq. A.15 can be rewritten accounting for the specific oedometer case as:

APPENDIX A: Analytical mechanical response for axial swelling upon hydration under oedometer conditions

$$d\varepsilon_{vol} = d\varepsilon_a \quad \text{Eq. A.20} \qquad d\varepsilon_d = \frac{2}{3} d\varepsilon_a \quad \text{Eq. A.21}$$

$$dp = \frac{2d\sigma_r}{3} \quad \text{Eq. A.22} \qquad dq = -d\sigma_r \quad \text{Eq. A.23}$$

The volumetric elastic strain defined by the BBM, which reads:

$$d\varepsilon_{vol} = \frac{dp}{K} + \frac{ds}{K_s} \quad \text{Eq. A.24}$$

Is then redefined considering Eq. A.20 and Eq. A.22 as:

$$d\varepsilon_a = \frac{2d\sigma_r}{3K} + \frac{ds}{K_s} \quad \text{Eq. A.25}$$

Where K_s is the Bulk modulus for change in suction *s*.

Eq. A.6 is also reformulated via Eq. A.21 and Eq. A.23

$$\frac{2}{3} d\varepsilon_a = \frac{-d\sigma_r}{3G} \quad \text{Eq. A.26} \qquad d\varepsilon_a = \frac{-d\sigma_r}{2G} \quad \text{Eq. A.27}$$

The Bulk moduli are selected as follows:

$$K = \frac{(1+e)p}{\kappa} \quad \text{Eq. A.28}$$

$$K_s = \frac{(1+e)(s+u_{atm})}{\kappa_s} \quad \text{Eq. A.29}$$

Where *e* is the total void ratio, *p* the mean net stress, *s* the suction, u_{atm} the atmospheric pressure, κ and κ_s the compressibility coefficients for change in mean net stress and suction respectively.

The Shear modulus is selected as function of the elastic Bulk modulus *K* and of the Poisson coefficient ν:

$$G = \frac{3(1-2\nu)K}{2(1+\nu)} \quad \text{Eq. A.30}$$

Elastic radial stress development following axial swelling upon hydration in oedometer condition is obtained as follows. The axial strain increment at the first member of Eq. A.25 is substituted by Eq. A.27:

$$\frac{-d\sigma_r}{2G} = \frac{2d\sigma_r}{3K} + \frac{ds}{K_s} \quad \text{Eq. A.31}$$

The radial stress increments are moved at the left side and put in evidence:

APPENDIX A: Analytical mechanical response for axial swelling upon hydration under oedometer conditions

$$-\frac{d\sigma_r}{2G}-\frac{2d\sigma_r}{3K}=\frac{ds}{K_s} \quad \text{Eq. A.32} \qquad -d\sigma_r\left(\frac{1}{2G}+\frac{2}{3K}\right)=\frac{ds}{K_s} \quad \text{Eq. A.33}$$

The shear modulus *G* is written as Eq. A.30:

$$-d\sigma_r\left(\frac{2(1+\nu)}{3(1-2\nu)2K}+\frac{2}{3K}\right)=\frac{ds}{K_s} \quad \text{Eq. A.34}$$

The left side of Eq. A.34 is reorganised and simplifications are showed:

$$-d\sigma_r\frac{2}{3K}\left(\frac{(1+\nu)}{2(1-2\nu)}+1\right)=\frac{ds}{K_s} \quad \text{Eq. A.35} \qquad -d\sigma_r\frac{2}{3K}\left(\frac{1+\nu+2-4\nu}{2(1-2\nu)}\right)=\frac{ds}{K_s} \quad \text{Eq. A.36}$$

$$-d\sigma_r\frac{2}{3K}\left(\frac{3-3\nu}{2(1-2\nu)}\right)=\frac{ds}{K_s} \quad \text{Eq. A.37} \qquad -d\sigma_r\frac{2}{3K}\left(\frac{3}{2}\frac{1-\nu}{(1-2\nu)}\right)=\frac{ds}{K_s} \quad \text{Eq. A.38}$$

Elastic radial stress increment $d\sigma_r$ is written as function of mean net stress via Eq. A.22 and the sign is changed:

$$\frac{-dp}{K}\frac{3(1-\nu)}{2(1-2\nu)}=\frac{ds}{K_s} \quad \text{Eq. A.39} \qquad \frac{dp}{K}\frac{3(1-\nu)}{2(1-2\nu)}=-\frac{ds}{K_s} \quad \text{Eq. A.40}$$

The elastic Bulk moduli for change in net stress and suction *K* and K_s are written via Eq. A.28 and Eq. A.29 and simplifications are performed:

$$\frac{\kappa}{\cancel{1+e}}\frac{dp}{p}\frac{3(1-\nu)}{2(1-2\nu)}=-\frac{\kappa_s}{\cancel{1+e}}\frac{ds}{s+u_{atm}} \quad \text{Eq. A.41}$$

Eq. A.41 is then integrated:

$$p_B=p_A\left(\frac{s_A+u_{atm}}{s_B+u_{atm}}\right)^{\frac{\kappa_s}{\kappa}\frac{2(1-2\nu)}{3(1-\nu)}} \quad \text{Eq. A.42}$$

And the mean net stress p is substituted via Eq. A.14

$$\frac{\sigma_{a,0}+2\sigma_{rB}}{\cancel{3}}=\frac{\sigma_{a,0}+2\sigma_{rA}}{\cancel{3}}\left(\frac{s_A+u_{atm}}{s_B+u_{atm}}\right)^{\frac{\kappa_s}{\kappa}\frac{2(1-2\nu)}{3(1-\nu)}} \quad \text{Eq. A.43}$$

$$\sigma_{a,0}+2\sigma_{rB}=\left(\sigma_{a,0}+2\sigma_{rA}\right)\left(\frac{s_A+u_{atm}}{s_B+u_{atm}}\right)^{\frac{\kappa_s}{\kappa}\frac{2(1-2\nu)}{3(1-\nu)}} \quad \text{Eq. A.44}$$

As the axial stress remains constant, the elastic radial stress resulting from a suction variation is obtained:

$$\sigma_{rB}=\frac{1}{2}\left[\left(\sigma_{a,0}+2\sigma_{rA}\right)\left(\frac{s_A+u_{atm}}{s_B+u_{atm}}\right)^{\frac{\kappa_s}{\kappa}\frac{2(1-2\nu)}{3(1-\nu)}}-\sigma_{a,0}\right] \quad \text{Eq. A.45}$$

APPENDIX A: Analytical mechanical response for axial swelling upon hydration under oedometer conditions

Accordingly to Eq. A.45 and BBM, the development of the radial stress in oedometric conditions in the elastic state depends essentially on 3 parameters:

- κ_s, elastic coefficient for change in suction: the higher radial stress is obtained for the higher κ_s;
- κ, elastic coefficient for change in pressure: the higher radial stress is obtained for the lower κ (stiffer material);
- ν, Poisson modulus: the higher radial stress is obtained for the lower ν and the lower radial stress is obtained for the higher ν.

Similarly the explicit development of axial swelling upon hydration in oedometer conditions is obtained combining Eq. A.27 and Eq. A.22:

$$d\varepsilon_a = -\frac{\cancel{3}}{\cancel{2}} dp \frac{\cancel{2}(1+\nu)}{\cancel{3}(1-2\nu)2K} \quad \text{Eq. A.46} \qquad d\varepsilon_a = -dp\frac{(1+\nu)}{2(1-2\nu)K} \quad \text{Eq. A.47}$$

The elastic Bulk modulus for change in net stress *K* is written as Eq. A.28:

$$d\varepsilon_a = -\frac{\kappa}{1+e}\frac{dp}{p}\frac{(1+\nu)}{2(1-2\nu)} \quad \text{Eq. A.48}$$

and the elastic strain increment is written as function of void ratio *e*: allowing simplyfing:

$$\frac{de}{\cancel{1+e}} = -\frac{\kappa}{\cancel{1+e}}\frac{dp}{p}\frac{(1+\nu)}{2(1-2\nu)} \quad \text{Eq. A.49}$$

Eq. A.49 is integrated:

$$e_B = -\kappa\frac{(1+\nu)}{2(1-2\nu)}\ln\left(\frac{p_B}{p_A}\right) + e_A \quad \text{Eq. A.50}$$

And Eq. A.41 is considered for p_b definition:

$$e_B = -\kappa\frac{(1+\nu)}{2(1-2\nu)}\ln\left(\frac{\cancel{p_A}\left(\frac{s_A+u_{atm}}{s_B+u_{atm}}\right)^{\frac{\kappa_s}{\kappa}\frac{2(1-2\nu)}{3(1-\nu)}}}{\cancel{p_A}}\right) + e_A \quad \text{Eq. A.51}$$

The right side exponent is moved outside the logarithmic operator and simplified:

$$e_B = -\cancel{\kappa}\frac{\kappa_s}{\cancel{\kappa}}\frac{\cancel{2(1-2\nu)}}{3(1-\nu)}\frac{(1+\nu)}{\cancel{2(1-2\nu)}}\ln\left(\frac{s_A+u_{atm}}{s_B+u_{atm}}\right) + e_A \quad \text{Eq. A.52}$$

Finally the void ratio following the axial deformation upon hydration in oedometer conditions can be written:

APPENDIX A: Analytical mechanical response for axial swelling upon hydration under oedometer conditions

$$e_B = -\kappa_s \frac{(1+\nu)}{3(1-\nu)} \ln\left(\frac{s_A + u_{atm}}{s_B + u_{atm}}\right) + e_A \qquad \text{Eq. A.53}$$

The void ratio (or axial deformation in this case) depends only on κ_s and ν, whereas κ does not play any role and it affects directly only the radial stress.

The equation of the evolution of void ratio with respect to suction in the case of free swelling in oedometric conditions (Eq. A.53) is similar to the one for the isotropic case (Eq. A.54), it only differs for the ratio $\frac{(1+\nu)}{3(1-\nu)}$ depending on the Poisson ratio. It means that in oedometric condition, considering the same κ_s, the swelling deformation will be lower with respect to the isotropic case (considering κ_s, κ and ν constant and not depending on stress for example).

$$e_B = -\kappa_s \ln\left(\frac{s_A + u_{atm}}{s_B + u_{atm}}\right) + e_A \qquad \text{Eq. A.54}$$

Accordingly to Eq. A.53 during axial swelling upon hydration in oedometer conditions:

- the higher void ratio increase (i.e. axial deformation) is obtained for the higher ν. Let's remind that the lower radial stress is obtained for the higher ν;
- the higher void ratio increase (higher axial deformation) is obtained for the higher κ_s.

Therefore if the target is to maximize the axial deformation and minimize the radial stress, high value of Poisson modulus ν should be adopted.

Increasing κ_s means to increase both radial swelling stress and axial deformation. Increasing κ (making the material more compressible) means to reduce the radial swelling stress and it does not have any effect on the axial deformation.

APPENDIX B: Interface element

APPENDIX B: Interface element

Geometrical and/or physical discontinuities between interacting bodies are frequently found in the realm of geotechnical engineering. Each side of the discontinuity may in fact present different mechanical displacements, water pressure and gas pressure. However, due to the fact that one side of the interface interacts with the other, their mechanical and hydraulic evolutions cannot be considered separately.

For large scale structures, one can mention for instance fault sliding or technological gaps, in which the above mentioned phenomena are quite evident. On the other hand, several researches suggest that it is critical to consider the interaction between the material samples and the experimental devices in laboratory experiments as well. To this regards, friction between the laboratory sample and the cell wall may develop (i.e. a purely mechanical interaction). Such occurrences can have an impact on the measurement's reliability, resulting in an incorrect material characterisation.

As a consequence, a computational tool that can replicate a wide range of phenomena is required. The hydro-mechanical zero-thickness element implemented in LAGAMINE (Cerfontaine et al. 2015) is briefly described with respect in this paragraph with regard to its application in this study. The element's classification is limited to two-dimensional analysis under isothermal conditions, as well as, in its mechanical characteristics.

Two deformable porous bodies (Fig. B.1), denoted $\mathcal{B}_1$ and $\mathcal{B}_2$, in their current configuration at time t, are considered in the description of a general mechanical problem.

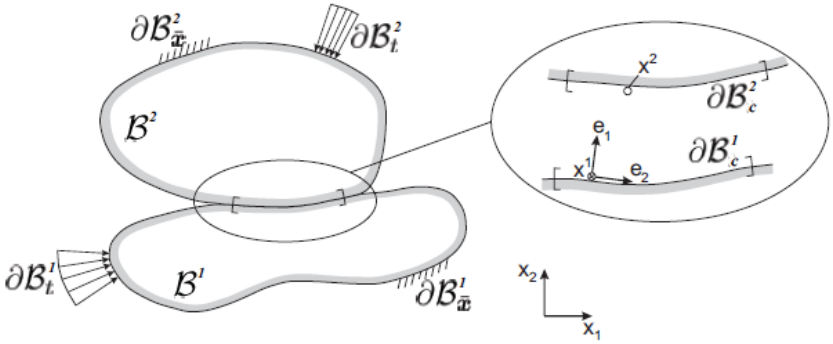

Fig. B.1: Statement of the mechanical problem (Cerfontaine et al. 2015).

Between $\mathcal{B}_1$ and $\mathcal{B}_2$, a gap function can be defined. It is denoted g_N:

$$g_N = (\boldsymbol{x}^2 - \bar{\boldsymbol{x}}^1) \cdot \boldsymbol{e}_1 \qquad \text{Eq. B.1}$$

Where $\bar{\boldsymbol{x}}^{\boldsymbol{1}}$ represents the projection of the point $\boldsymbol{x}^{\boldsymbol{2}}$ belonging to the boundary of $\mathcal{B}_2$ on the closest point on the boundary of $\mathcal{B}_1$. $\bar{\boldsymbol{e}}_{\boldsymbol{1}}$ is a unit normal vector at point $\bar{x}^1$. If there is no contact g_N is positive, for g_N equal to zero the contact is termed ideal (i.e. no interpenetration of the solid bodies) and for g_N negative interpenetration distance is defined. Interpenetration is necessary to produce contact pressure when the penalty method is used. Contact between two solids gives birth to non-zero stress vectors $\boldsymbol{\sigma_c}$ along their common boundary. The vector $\boldsymbol{\sigma_c}$ is described in the corresponding local system of coordinates at each contacting point such that:

$$\boldsymbol{\sigma_c} = -p_N \boldsymbol{e}_1 + \tau \boldsymbol{e}_2 = [-p_N \quad \tau]^T \qquad \text{Eq. B.2}$$

where p_N is the normal pressure and τ is the shear stress in the plane of the interface. The ideal contact constraint is summarised into the Hertz-Signorini-Moreau condition but, from a computational point of view, this relationship may be difficult to ensure. Hence, the penalty method is used. In case of contact, the relation between the pressure and the gap function reads:

$$\dot{p}_N = -K_N \dot{g}_N \qquad \text{Eq. B.3}$$

where the minus sign ensures the contact pressure is positive when interpenetration increases, i.e. g_N<0 and $\dot{g}_N$<0. If the penalty method is employed, interpenetration is necessary to generate contact pressure and the gap function becomes negative. While interacting with geomaterials, it's worth noting that the physical basis for interpenetration of two bodies is the gradual crushing of interface asperities [Fig. B.2].

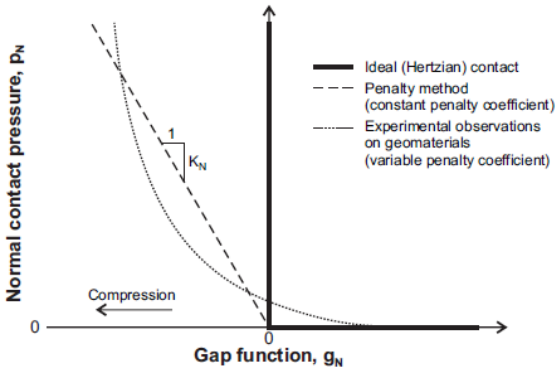

Fig. B.2: Relationship between the gap function $\boldsymbol{g_N}$ and the normal contact pressure $\boldsymbol{p_N}$.

When solids are in contact, the ideal tangential behaviour of the interface distinguishes between the stick and slip states. In the stick state, two points in contact are not allowed to move in the tangential direction, so that $\dot{g}_T = 0$ and they keep stuck together. On the other hand, in the slip state, a relative tangential displacement exists between both sides of the interface. From a computational point of view, this statement reads:

$$\dot{g}_T^{sl} \geq 0 \qquad f_c(\boldsymbol{\sigma}_c) \geq 0 \qquad \dot{g}_T^{sl} f_c(\boldsymbol{\sigma}_c) = 0 \qquad \text{Eq. B.4}$$

where $\dot{g}_T^{sl}$ is the variation of the non-recoverable displacement in the tangential direction. It is related to the variation of tangential displacement:

$$\dot{g}_T = sign(\dot{\tau}) \dot{g}_T^{sl} \qquad \text{Eq. B.5}$$

with sign($\dot{\tau}$) the sign function of $\dot{\tau}$.

Stick and slip states are distinguished by the plasticity criterion $f_c(\sigma_c)$, defining a threshold of admissible shear stress. The slip state involves a relative tangential displacement in the plane of the interface. The Coulomb criterion is adopted as relatively smooth interfaces are considered. It reads:

$$f_c(\boldsymbol{\sigma}_c) = |\tau| - \mu p_N \qquad \text{Eq. B.6}$$

where $|\tau|$ is the norm of the shear stress τ and μ is the friction coefficient. Perfect plasticity is considered. Accordingly, once that the Coulomb criterion is reached, relative displacement of the interfaces continues without any further increase of the shear stress, unless the normal stress is increased

The penalty method allows relative elastic displacement for the stick state. Shear stress and tangential variation of displacement are linked linearly by the penalty coefficient K_T:

$$\dot{\tau} = K_T \dot{g}_T \qquad \text{Eq. B.7}$$

Consequently, the mechanical behaviour of the interface is described by the incremental relationship between stress and displacements:

$$\dot{\boldsymbol{\sigma}}_c = \dot{\boldsymbol{\sigma}}_c(g, \boldsymbol{\sigma}_c) \qquad \text{Eq. B.8}$$

APPENDIX C: Clarifications on EB test numerical hydraulic boundary conditions

APPENDIX C: Clarification on EB test numerical hydraulic boundary conditions

In order to justify the numerical boundary conditions adopted in CHAPTER 7 for the EB test simulation, a number of considerations are presented.

Let us consider the length of the tunnel (i.e. 6 m Fig. 7.4) composed only by cross sections as the one depicted in Fig. C.2.

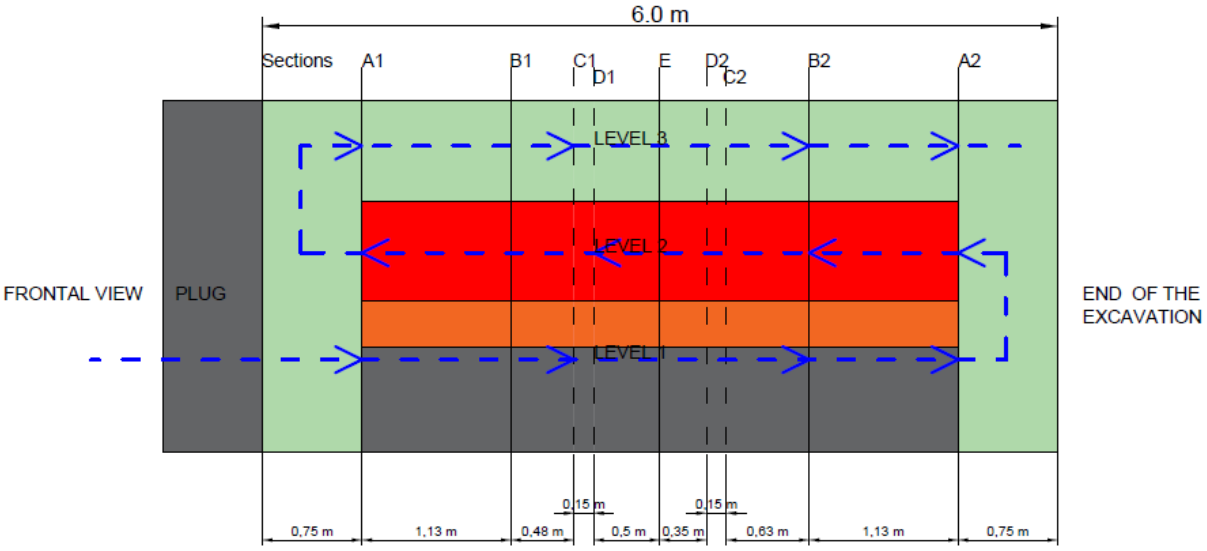

Fig. C.1: Longitudinal section of the EB barrier.

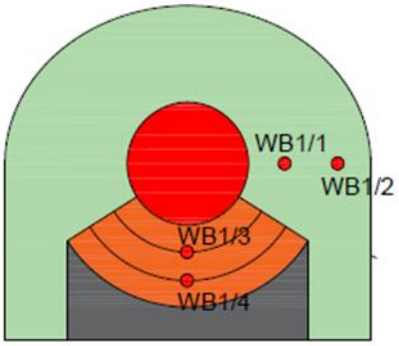

Fig. C.2: Example of cross section of the analysed barrier.

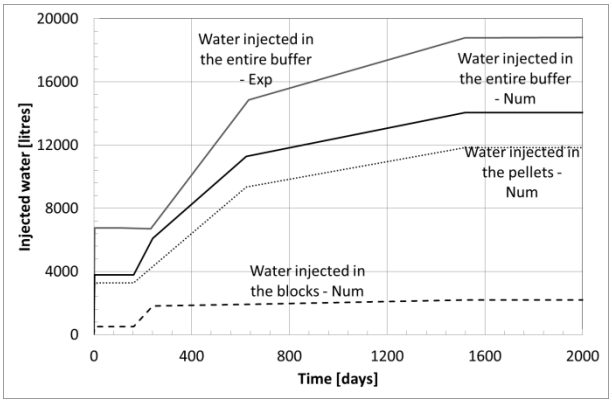

Fig. C.3: Experimental and numerical water intake time evolution.

With this configuration the total volume of pellets mixture is equal to 25.86 m^3 (in (Mayor et al. 2005) a volume equal to 28.4 m^3 was reported) and the total volume of the compacted blocks equal to 6.33 m^3 (Eq. C.1).

$$V[m^3] = A[m^2] \times L[m] \qquad \begin{aligned} V_{tot,pellets} &= 4.31\ m^2 \times 6\ m = 25.86\ m^3 \\ V_{tot,blocks} &= 1.055\ m^2 \times 6\ m = 6.33\ m^3 \end{aligned} \qquad \text{Eq. C.1}$$

The pellets represent the 80% of the total volume to be hydrated, whereas the blocks the 20%.

APPENDIX C: Clarification on EB test numerical hydraulic boundary conditions

The water content, dry density and saturation degree of the pellet mixture are equal to w=4.17%, ρ_d=1.35 Mg/m^3 and S_r=11.27%, whereas for the compacted blocks w=11.55 %, ρ_d=1.70 Mg/m^3 and S_r=53% (Eq. C.2).

$$S_r[-] = \frac{w[-]}{\frac{1}{\varrho_d\left[\frac{Mg}{m^3}\right]} - \frac{1}{\varrho_s\left[\frac{Mg}{m^3}\right]}} \qquad S_{r,pellets} = \frac{0.0417}{\frac{1}{1.35\left[\frac{Mg}{m^3}\right]} - \frac{1}{2.7\left[\frac{Mg}{m^3}\right]}} = 0.1127\ [-]$$

$$S_{r,blocks} = \frac{0.1155}{\frac{1}{1.7\left[\frac{Mg}{m^3}\right]} - \frac{1}{2.7\left[\frac{Mg}{m^3}\right]}} = 0.53\ [-] \qquad \text{Eq. C.2}$$

Firstly the porosity is computed (Eq. C.3). Via the porosity, the total volume of void is obtained (Eq. C.4). Finally, the saturation represents the volume of water on the volume of voids (Eq. C.5).

At the initial state, the volumes of water in the pellets mixtures and in the blocks are respectively equal to 1.46 m^3 and 1.24 m^3.

$$n[-] = 1 - \frac{\varrho_d\left[\frac{Mg}{m^3}\right]}{\varrho_s\left[\frac{Mg}{m^3}\right]} = \frac{V_V[m^3]}{V_{TOT}[m^3]} \qquad n_{pellets} = 1 - \frac{1.35\left[\frac{Mg}{m^3}\right]}{2.7\left[\frac{Mg}{m^3}\right]} = 0.5\ [-]$$

$$n_{blocks} = 1 - \frac{1.7\left[\frac{Mg}{m^3}\right]}{2.7\left[\frac{Mg}{m^3}\right]} = 0.37\ [-] \qquad \text{Eq. C.3}$$

$$V_v[m^3] = n[-] * V_{TOT}[m^3] \qquad V_{v,pellets} = 0.5 * 25.86\ [m^3] = 12.93\ [m^3]$$

$$V_{v,blocks} = 0.37 * 6.33\ [m^3] = 2.3421\ [m^3] \qquad \text{Eq. C.4}$$

$$S_r[-] = \frac{V_w[m^3]}{V_V[m^3]} \rightarrow V_w[m^3] = S_r[-] \times V_V[m^3] \qquad V_{w,pellets} = 0.1127 \times 12.93[m^3] = 1.46\ [m^3]$$

$$V_{w,blocks} = 0.53 \times 2.3421[m^3] = 1.24\ [m^3] \qquad \text{Eq. C.5}$$

Let us consider the first hydration phase with the water injection of 6.7 m^3 in 2 days (Fig. C.3). Let us assume that the material is uniformly hydrated, so that the 80% of 6.7 m^3 of water will go into the pellets and the 20% in the compacted blocks and let us compute the degree of saturation for the two components, which is 52.7% for the pellets and 110% for the compacted blocks (Eq. C.6). The value of 110% is reasonable because this is not the case of a constant volume hydration but during wetting the material swells, therefore the dry density decreases and the volume of voids increases.

$$S_r[-] = \frac{V_w[m^3]}{V_V[m^3]} \qquad S_{r,pellets}[-] = \frac{1.46\ [m^3] + 0.80 * 6.7[m^3]}{12.93[m^3]} = 0.527$$

$$S_{r,blocks}[-] = \frac{1.24\ [m^3] + 0.20 * 6.7[m^3]}{2.3421\ [m^3]} = 1.10 \qquad \text{Eq. C.6}$$

The water volume required to fully saturate the buffer can be calculated in a first approximation with Eq. C.7. Finally, it can be assumed that the total volume of water needed to obtain the total saturation of the buffer is equal to 12 m^3.

APPENDIX C: Clarification on EB test numerical hydraulic boundary conditions

$$V_w[m^3] = (1 - S_r[-]) * V_V[m^3] \quad V_w[m^3] = (1 - 0.527) * 12.93\ [m^3] = 6.12\ [m^3] \qquad \text{Eq. C.7}$$

However, it is worth to note that after the first injection phase the suction level in the compacted bentonite blocks does not reach a value corresponding to an almost saturated state (experimental measurements show values ranging between 40 and 60 MPa). Moreover, leakage was observed during the injection. Consequentially, it can be assumed that, during the first injection phase, only a percentage equal to the 8% of 6.7 m^3 of water is injected in the blocks with a uniform water flux equal to 0.00045 $l*m^2*m*s^{-1}$ (~0.5 m^3) in 2 days in a surface of 1.055 m^2 times a length of 6 m, Fig. C.3). This amount of water has been compared with the available experimental suction measurements in CHAPTER 7.

After the natural re-distribution phase of water, a uniform water flux has been set in the bentonite compacted blocks equal to 0.0000324 $l*m^2*m*s^{-1}$ between the 163rd and 240th day of the simulation time. This value of flux was selected in order to reproduce the experimental suction decrease at this location. Finally a flux equal to $5.2*10^{-7}$ $l*m^2*m*s^{-1}$ between the 240th and 1517th day was imposed in order to obtain a final pore pressure value approximately equal to 2 kPa.

The total water amount injected uniformly in the volume of the bentonite compacted blocks resulted equal to 2.19 m^3 considering a surface of 1.055 m^2 times a length of 6 m.

With respect to the pellets mixture, the initial flux was selected in order to consider the leakage experimentally observed. Despite it was not possible to precisely quantify this water loss, it was assumed equal to ≈2 m^3. The uniform flux imposed in the first injection phase was then set equal to $7.2*10^{-4}$ $l*m^2*m*s^{-1}$ with a total water amount injected in the pellet mixture in the first 2 days equal to ≈3.3 m^3 (in a surface of 4.30 m^2 times a length of 6 m, Fig. C.3). After the natural re-distribution phase, in order to reproduce the experimental injection rate, fluxes equal to $5.8*10^{-6}$ $l*m^2*m*s^{-1}$ between 163rd and 623rd day of the simulation time and $1.30*10^{-6}$ $l*m^2*m*s^{-1}$ between 623rd and 1517th day, with a total water amount injected in the pellets mixture equal to ≈11.8 m^3.